

## Electrochemical Ammonia Synthesis: Hydrogen Permeable Electrodes as Alternative Pathway for Nitrogen Reduction

Ripepi, D.

**DOI**

[10.4233/uuid:e75408f4-b1f3-446a-bfd5-19d9465f7038](https://doi.org/10.4233/uuid:e75408f4-b1f3-446a-bfd5-19d9465f7038)

**Publication date**

2023

**Document Version**

Final published version

**Citation (APA)**

Ripepi, D. (2023). *Electrochemical Ammonia Synthesis: Hydrogen Permeable Electrodes as Alternative Pathway for Nitrogen Reduction*. [Dissertation (TU Delft), Delft University of Technology].  
<https://doi.org/10.4233/uuid:e75408f4-b1f3-446a-bfd5-19d9465f7038>

**Important note**

To cite this publication, please use the final published version (if applicable).  
Please check the document version above.

**Copyright**

Other than for strictly personal use, it is not permitted to download, forward or distribute the text or part of it, without the consent of the author(s) and/or copyright holder(s), unless the work is under an open content license such as Creative Commons.

**Takedown policy**

Please contact us and provide details if you believe this document breaches copyrights.  
We will remove access to the work immediately and investigate your claim.

Electrochemical ammonia synthesis: hydrogen permeable electrodes as alternative pathway for nitrogen reduction

**Davide Ripepi**



# Electrochemical ammonia synthesis: hydrogen permeable electrodes as alternative pathway for nitrogen reduction

Dissertation

for the purpose of obtaining the degree of doctor  
at Delft University of Technology,  
by the authority of the Rector Magnificus prof.dr.ir. T.H.J.J. van der Hagen,  
chair of the Board for Doctorates,  
to be defended publicly on  
Friday 3 February 2023 at 12.30 o'clock

by

**Davide RIPEPI**

Master of Science in Sustainable Energy Technology  
Delft University of Technology, the Netherlands  
Born in Reggio di Calabria, Italy

This dissertation has been approved by:

promotor: Prof. dr. F.M. Mulder

promotor: Prof. dr. W.A. Smith

Composition of the doctoral committee:

Rector Magnificus, chairman

Prof. dr. F.M. Mulder, Delft University of Technology, promotor

Prof. dr. W.A. Smith, Delft University of Technology, promotor

*Independent members:*

Prof. dr. E. Skúlason University of Iceland

Prof. dr. M.T. Tromp University of Groningen

Prof. dr. G. Mul University of Twente

Prof. dr.ir. J.J.C. Geerlings Delft University of Technology

Prof. dr.ir. A. Urakawa Delft University of Technology

The research described in this thesis was carried out in the Materials for Energy Conversion and Storage (MECS) group, Department of Chemical Engineering, Faculty of Applied Sciences, Delft University of Technology. The research received funding from the Open Technology research program under the project number 15234, which is partially financed by the Netherlands Organization for Scientific Research (NWO).



*Printed by:* Proefschrift specialist

*Cover design by:* Davide Ripepi and Tamira Theunissen

Copyright © 2022 by Davide Ripepi

ISBN: 978-94-6366-633-6

An electronic version of this dissertation is available at  
<http://repository.tudelft.nl/>.

*To family and friends.*



# Table of contents

<b>1</b>	<b>Introduction</b>	<b>1</b>
1.1	The necessity for renewable energy	2
1.2	Ammonia: essential commodity and future energy carrier	5
1.3	Challenges in electrochemical ammonia synthesis	7
1.4	Outline of the thesis	8
	References	10
<b>2</b>	<b>Gas chromatographic method for <i>in situ</i> ammonia quantification at ppb levels</b>	<b>15</b>
2.1	Introduction	16
2.2	Experimental	19
2.3	Results and discussion	20
2.4	Conclusions	26
	Appendix A.2	27
	References	34
<b>3</b>	<b>Operando isotope selective ammonia quantification in nitrogen reduction studies via gas chromatography-mass spectrometry</b>	<b>37</b>
3.1	Introduction	38
3.2	Experimental	40
3.3	Results and discussion	43
3.4	Conclusions	48
	Appendix A.3	49
	References	56
<b>4</b>	<b>Determination and effective NO<sub>x</sub> and NH<sub>3</sub> removal for quantitative electrochemical nitrogen reduction</b>	<b>59</b>
4.1	Introduction	60
4.2	Experimental	62
4.3	Results and discussion	66
4.4	Conclusions	78
	Appendix A.4	80
	References	85



<b>5</b>	<b>Ammonia synthesis at ambient conditions via electrochemical atomic hydrogen permeation</b>	<b>91</b>
5.1	Introduction	92
5.2	Experimental	94
5.3	Results and discussion	99
5.4	Conclusions	108
	Appendix A.5	109
	References	124
<b>6</b>	<b><i>In situ</i> study of hydrogen permeable electrodes for electrolytic ammonia synthesis using near ambient pressure XPS</b>	<b>129</b>
6.1	Introduction	130
6.2	Experimental	132
6.3	Results and discussion	138
6.4	Conclusions	151
	Appendix A.6	153
	References	162
<b>7</b>	<b>Effect of temperature and H flux on the NH<sub>3</sub> synthesis via electrochemical hydrogen permeation</b>	<b>169</b>
7.1	Introduction	170
7.2	Experimental	171
7.3	Results and discussion	174
7.4	Conclusions	178
	Appendix A.7	179
	References	186
	<b>Summary</b>	<b>191</b>
	<b>Samenvatting</b>	<b>195</b>
	<b>Acknowledgements</b>	<b>199</b>
	<b>List of publications</b>	<b>203</b>
	<b>Curriculum Vitae</b>	<b>205</b>







## 1.1 The necessity for renewable energy

Today the average Earth's surface temperature is approximately  $1.0 \pm 0.2$  °C higher compared to pre-industrial level (**Figure 1.1**).<sup>1-3</sup> Extreme alterations in weather and climate have deleterious impacts on environmental, social and economic sectors.<sup>4</sup> The emission of greenhouse gases (GHG) from human activities is considered the leading cause of climate change, which is thus mostly anthropogenic (**Figure 1.2**).<sup>5,6</sup>

To limit, and possibly arrest, this climate change, the Intergovernmental Panel on Climate Change (IPCC) predicted that the increase of temperature should not exceed the 1.5 °C above pre-industrial level. Beyond this threshold, irreversible and catastrophic events will be unavoidable, threatening the existence of life.<sup>7</sup>

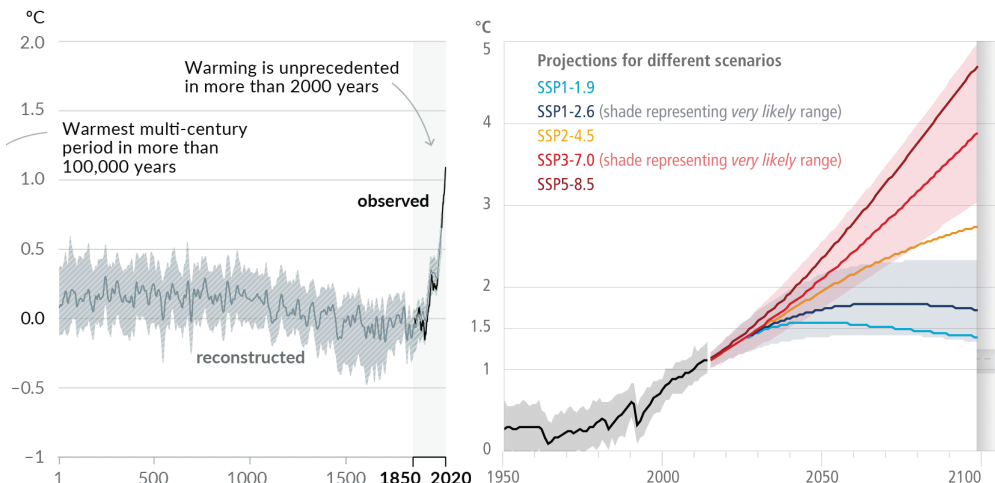


**Figure 1.1** Changes in global average surface temperature (on the left). Projections of global average surface temperature corresponding to different scenarios, where SSP1-1.9 represents the *net-zero* in 2050 scenario (on the right).<sup>6</sup>

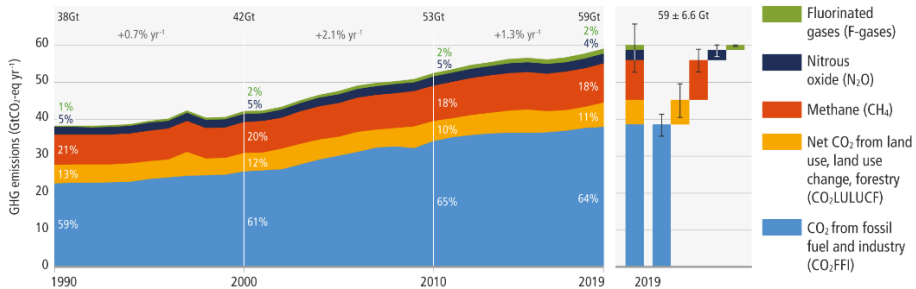


**Figure 1.2** Global net anthropogenic greenhouse gases emissions from 1990 to 2019.<sup>8</sup>

Based on the IPCC report, a drastic reduction in GHG emissions, i.e. *net-zero* within 2050, is needed to achieve this goal.<sup>8</sup> Anthropogenic GHG emissions are generated from human activities, mostly from burning fossil resources in the energy (electricity, heat and transport), agriculture and industrial sectors.<sup>9</sup> Undoubtedly, the resolution of the global warming requires the decarbonisation of these sectors, as well as the capture of past emissions from the atmosphere.

The electricity generated from renewables is a sustainable alternative to fossil fuels. Therefore, to address the issue of anthropogenic GHG emissions, a transition to a renewable electricity-based society is already taking place, ultimately leading to the direct or indirect electrification of most of the processes. Renewable energy sources, as wind, solar, geothermal and hydropower, can provide vast amounts of clean and cheap energy. The cost of renewable power generation has fallen sharply in the last decade, being now competitive with fossil-based electricity (**Figure 1.3**).<sup>10</sup> Besides being an environmentally friendly solution, renewable energy does not suffer from geopolitical instability. An additional factor in the drive to renewable energies implementation is that the price and availability of the intrinsically limited, and not equally distributed, fossil resources are highly sensitive to geopolitics; as demonstrated by the recent record high price of natural gas due to the recent perturbation of international trade equilibria by armed conflict (**Figure 1.4**). Of further importance is that renewables, like solar and wind power, produce electricity directly. This is a high value form of energy that can lead to efficiency gains and reductions in energy use, compared to fossil fuel use, for applications such as electrical transport and heating via heat pumps.

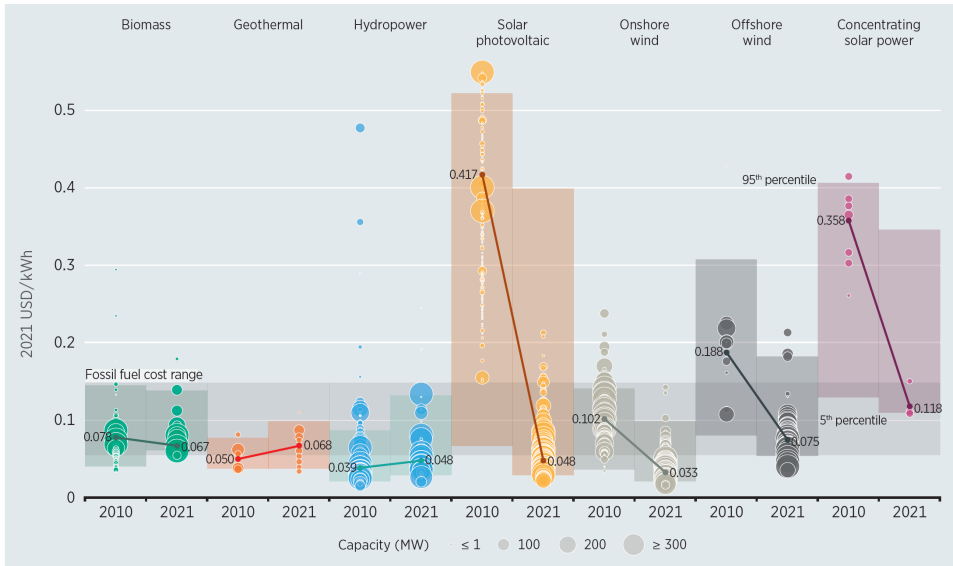


**Figure 1.3** The weighted average levelized cost of electricity (LCOE) of utility scale renewable power generation technologies compared to fossil fuel cost range in the years 2010 and 2021.<sup>10</sup>

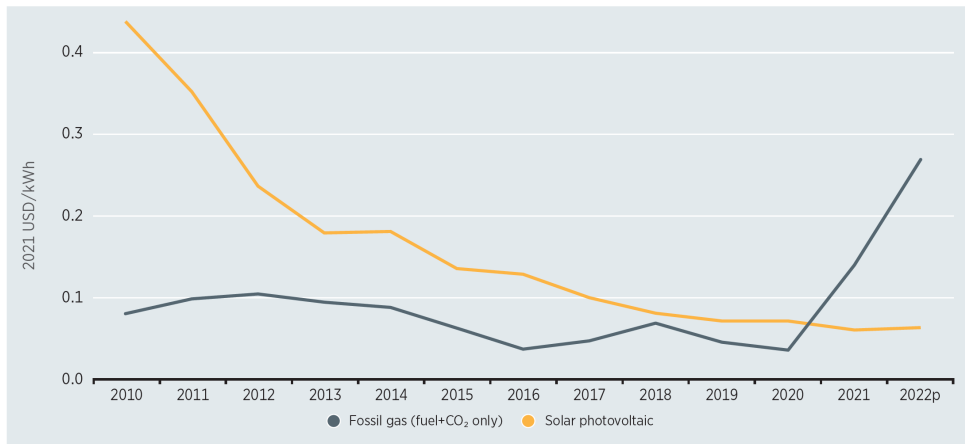


**Figure 1.4** The weighted average LCOE of utility scale solar PV compared to fuel and CO<sub>2</sub> cost only for fossil gas in Europe from 2010 to 2022. The values for 2022 are possible outcomes and not a forecast.<sup>10</sup>

One of the major limitations of renewables is their systematic daily and seasonal variation combined with intrinsic intermittent and poorly predictable local weather conditions. To ensure grid stability and constantly match production and demand of electricity, daily and seasonal fluctuations in renewable power generation need to be balanced with proper short- and long-term energy storage. It is likely that the future energy system will include a combination of multiple storage technologies, with a wide range of applications depending on energy and power density.

Among other strategies for storing renewable electricity, electrochemical processes offer the possibility of converting and storing electricity into chemical bonds. Electrochemistry can be used to temporarily store electricity, to then be reconverted back to electrons, or it can be used to produce chemicals, which can find direct application or be further refined in final products. As such, the electrification of the chemical industry offers the opportunity to reduce its GHG footprint. The flexible supply of renewable electricity can be used by the chemical industry, establishing a key synergy between the chemical industry and the energy sector, which can boost market access, scale and competitiveness.

## 1.2 Ammonia: essential commodity and future energy carrier

Ammonia ( $\text{NH}_3$ ), with an annual production of 178 million tons,<sup>11</sup> is an essential commodity at the base of modern agriculture, ranking among the highest produced bulk chemicals in the world. About a century ago, one of the main challenges chemists had to tackle was the conversion of atmospheric nitrogen to ammonia. This process became an urgent necessity to meet the increasingly higher demand of nitrogen containing fertilizers to ultimately sustain food production for the exponentially growing world population. The Haber-Bosch process, operating ever since, brings nitrogen fixation among the top large scale catalytic processes operating on the planet, next to photosynthesis and respiration.<sup>12</sup> Today, it is estimated that half of the population is sustained by synthetic nitrogen fertilisers (**Figure 1.5**).<sup>13, 14</sup> Currently, the Haber-Bosch process produces  $\text{NH}_3$  at large scale from dinitrogen ( $\text{N}_2$ ) and hydrogen ( $\text{H}_2$ ) derived from steam-methane reforming. The overall ammonia synthesis process demands high pressure and temperature operating conditions and it has a



significant impact on the world-wide energy consumption (1-2%) and carbon dioxide emissions (1.4%), equivalent to about 300 million metric tons of CO<sub>2</sub>.<sup>15-17</sup>

Other than being a unique chemical intermediate in fertilizers synthesis, ammonia is also a promising candidate as next generation sustainable carbon free energy carrier,<sup>18-21</sup> because of its high energy density (22.5 MJ kg<sup>-1</sup>) and hydrogen content (17.6 wt%).<sup>22</sup> Ammonia can be easily liquefied (8 bar and RT, or 1 bar and -33° C),<sup>19, 20</sup> stored and transported at large scale. As today, these infrastructures are already available in the fertiliser field. However, ramping-up ammonia production with the current state of the art Haber-Bosch technology, to meet both fertilizers and fuel production, would have a profound unsustainable impact on the environment due to the usage of natural gas as hydrogen source.<sup>23</sup> To meet the *net-zero* GHG emissions goal by 2050, established in the latest IPCC report,<sup>1</sup> ammonia must be produced via a sustainable pathway.<sup>24</sup>

In this context, direct electrochemical nitrogen reduction to ammonia, when powered by renewable energy sources, would have negligible carbon footprint and may represent a more flexible and decentralised option. In a future characterised by a large number of distributed renewable energy generation sites, such electrochemical approaches may provide an environmentally friendly solution to the growing demand for green ammonia.

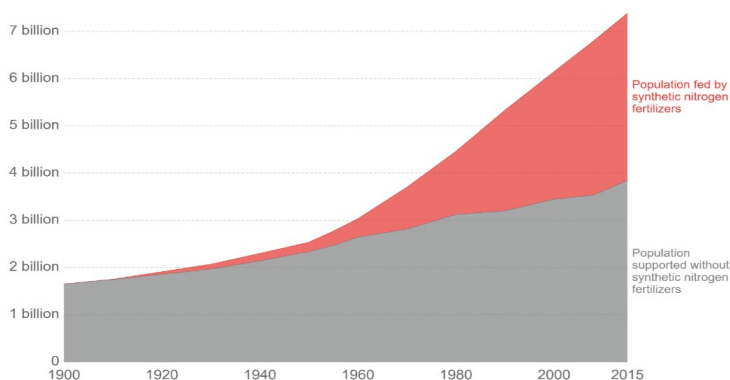


**Figure 1.5** Growth in population over the last century. The estimated portion of the human population fed with and without synthetic nitrogen fertilisers are shown in red and grey, respectively.<sup>25</sup>

### 1.3 Challenges in electrochemical ammonia synthesis

The conventional electrochemical conversion of  $N_2$  to  $NH_3$  in aqueous electrolyte involves, among other challenges,<sup>26, 27</sup> the low solubility of  $N_2$  (0.7 mM at ambient conditions),<sup>27</sup> the competition with the kinetically more favoured hydrogen evolution reaction (HER), the arduous activation and stepwise hydrogenation of the apolar  $N_2$  molecule and its triple bond (941 kJ mol<sup>-1</sup>). Conventional electrochemistry is carried out in the presence of an aqueous electrolyte, which contains an excess of hydrogen species (as  $H_2O$ ,  $H^+$  or  $OH^-$ ). As a consequence, in an aqueous solution and at negative polarization, hydrogen reduction and adsorption on the catalyst's active sites easily prevail over nitrogen adsorption.<sup>26-29</sup> This results in sluggish ammonia production rates and poor faradaic efficiency (FE).<sup>30</sup>

Despite the stable N-N triple bond, dissociative chemisorption of dinitrogen at room temperature has been reported to happen spontaneously on several clean transition metal surfaces.<sup>31-44</sup> This is possible when  $N_2$  is not in competition with other adsorbate molecules, as hydrogen or oxygen species from the electrolyte.<sup>35, 45-48</sup> Furthermore, one of the major limitations of ambient condition (catalytic) ammonia synthesis is the formation of stable N and  $NH_x$  (with  $x = 1, 2$  or  $3$ ) intermediates at the catalytic surface, hampering the advancement of the reaction due to the lack of available sites for both  $H_2$  and  $N_2$  activation.<sup>47, 49</sup> Therefore, these evidences point to the fact that the challenging electrolytic ambient temperature ammonia synthesis derives from the competition between H and N species, and catalyst poisoning by oxides, rather than solely from the activation of dinitrogen.

Besides these fundamental challenges, the practical challenges of reliable quantification of low ammonia yields have raised several concerns in the scientific community. As such, an increasing number of false positives, led to mispending of time and resources in pursuing misleading or irreproducible results.<sup>50, 51</sup>

The following chapters of this thesis address both these fundamental and practical challenges.

## 1.4 Outline of the thesis

The organisation of the thesis is given below.

Chapter 2 provides a fast and reliable ammonia detection method to speed-up catalyst screening and development of novel sustainable ammonia evolution devices, as it requires significantly less sample handling and preparation compared to other reported methods. The proposed method is based on a gas chromatography technique, and it allows for *in situ* monitoring of ammonia evolution, down to 150 ppb, from -but not limited to- electrochemical devices.

Chapter 3 presents an isotope sensitive gas chromatography-mass spectrometry method for the quantification of  $\text{NH}_3$  at low concentration level, typically encountered in electrochemical ammonia synthesis applications. This method allows the discrimination of  $^{15/14}\text{NH}_3$ , necessary for the required  $^{15}\text{N}_2$  isotope labelling control experiments. Additionally, this method can directly and simultaneously measure other species in the analyte, thus it allows researchers to directly assess reaction selectivity by measuring reaction by-products, as well as the presence of gaseous/volatile contaminants in the experimental setup.

Chapter 4 investigates the impact of contaminations on electrochemical nitrogen reduction experiments. This chapter not only provides a comprehensive identification and quantification of the contaminations, but it also critically analyses the effectiveness of different cleaning strategies, establishing a series of guidelines to perform reliable experiments.

Chapter 5 demonstrates a novel strategy for ambient condition ammonia synthesis from water and dinitrogen designed to limit the competition between nitrogen activation and other competing adsorbates. As such, a hydrogen permeable nickel membrane electrode is used to spatially separate the electrolyte and hydrogen activation side from the nitrogen activation and hydrogenation sites. With this approach, ammonia is produced catalytically directly in the gas phase and in the absence of electrolyte. Gaseous nitrogen activation at the nickel electrode is confirmed with  $^{15}\text{N}$  isotope labelling control experiments and it is attributed to a Mars-van Krevelen mechanism enabled by the formation of N-vacancies upon hydrogenation of surface nitrides.

Chapter 6 reports on the interactions of adsorbing N and permeating H at the catalytic interface of nickel, iron and ruthenium based hydrogen permeable electrodes during electrolytic ammonia synthesis. *In situ* near ambient pressure X-ray photoelectron spectroscopy (XPS) is used to measure modifications in the surface electronic structure of the catalyst and the nature of the adsorbed molecules. This chapter shows that permeating atomic hydrogen reduces surface Ni oxide and hydroxide species, under conditions at which gaseous H<sub>2</sub> does not. Moreover, the results demonstrate that the availability of surface Ni<sup>0</sup> sites is a primary requirement for the chemisorption of gaseous N<sub>2</sub>. *In situ* XPS measurements reveal that nitrogen gas chemisorbs on the generated metallic sites, followed by hydrogenation via permeating H, as adsorbed N and NH<sub>3</sub> are found on the Ni surface. Our findings suggest that the first hydrogenation step to NH and the last NH<sub>3</sub> desorption step might be limiting at the utilised operating conditions. Finally, the study was then extended to Fe and Ru surfaces. However, the formation of surface iron oxide and nitride species on iron blocks the H permeation and prevents the reaction to advance; while on ruthenium the stronger Ru-N bond might favour the recombination of permeating hydrogen to H<sub>2</sub> over the hydrogenation of adsorbed nitrogen.

Chapter 7 provides a systematic investigation of the effect of operating temperature (in the range 25 to 120 °C) and H permeation flux on the N<sub>2</sub> reduction reaction on Ni, leading to a considerably improved NH<sub>3</sub> synthesis process. At 120 °C a stable operation was achieved for over 12 h with a 10 times higher cumulative NH<sub>3</sub> production and almost 40-fold increase in faradaic efficiency compared to the room temperature operation reported in chapter 5. The results obtained in this chapter indicate that increasing operating temperatures enhances nitrogen adsorption and NH<sub>3</sub> desorption, maintaining a steady N surface coverage throughout the NH<sub>3</sub> synthesis cycle. Moreover, to operate the nitrogen reduction reaction in a stable and efficient manner, the control over the population of N, NH<sub>x</sub> and H species at the catalyst surface is critical. As such, the adoption of H permeable electrodes allows to independently controlled the N activation and H permeation, by a large extent.

This thesis is concluded by a short summary.

## References

1. Arias, P. A., N. Bellouin, E. Coppola, R.G. Jones, G. Krinner, J. Marotzke, V. Naik, M.D. Palmer, G.-K. Plattner, J. Rogelj,; M. Rojas, J. S., T. Storelvmo, P.W. Thorne, B. Trewin, K. Achuta Rao, B. Adhikary, R.P. Allan, K. Armour, G. Bala,; R. Barimalala, S. B., J.G. Canadell, C. Cassou, A. Cherchi, W. Collins, W.D. Collins, S.L. Connors, S. Corti, F. Cruz,; F.J. Dentener, C. D., A. Di Luca, A. Diongue Niang, F.J. Doblas-Reyes, A. Dosio, H. Douville, F. Engelbrecht,; V. Eyring, E. F., P. Forster, B. Fox-Kemper, J.S. Fuglestad, J.C. Fyfe, N.P. Gillett, L. Goldfarb, I. Gorodetskaya,; J.M. Gutierrez, R. H., E. Hawkins, H.T. Hewitt, P. Hope, A.S. Islam, C. Jones, D.S. Kaufman, R.E. Kopp, Y. Kosaka,; J. Kossin, S. K., J.-Y. Lee, J. Li, T. Mauritsen, T.K. Maycock, M. Meinshausen, S.-K. Min, P.M.S. Monteiro,; T. Ngo-Duc, F. O., I. Pinto, A. Pirani, K. Raghavan, R. Ranasinghe, A.C. Ruane, L. Ruiz, J.-B. Sallée, B.H. Samset,; S. Sathyendranath, S. I. S., A.A. Sörensson, S. Szopa, I. Takayabu, A.-M. Tréguier, B. van den Hurk, R. Vautard,; K. von Schuckmann, S. Z., X. Zhang, and K. Zickfeld, *Technical Summary. In Climate Change 2021: The Physical Science Basis. Contribution of Working Group I to the Sixth Assessment Report of the Intergovernmental Panel on Climate Change 2021*; pp 33-144.
2. Seneviratne, S. I.; Zhang, X.; Adnan, M.; Badi, W.; Dereczynski, C.; Di Luca, A.; Vicente-Serrano, S. M.; Wehner, M.; Zhou, B., 11 Chapter 11: Weather and climate extreme events in a changing climate. **2021**.
3. State of the Climate: Monthly Global Climate Report for Annual 2020. <https://www.ncei.noaa.gov/access/monitoring/monthly-report/global/202013> (accessed 18-07-2022).
4. Carleton, T. A.; Hsiang, S. M., Social and economic impacts of climate. *Science* **2016**, 353 (6304), aad9837.
5. Mikhaylov, A.; Moiseev, N.; Aleshin, K.; Burkhardt, T., Global climate change and greenhouse effect. *Entrepreneurship and Sustainability Issues* **2020**, 7 (4), 2897.
6. Masson-Delmotte, V.; Zhai, P.; Pirani, A.; Connors, S. L.; Péan, C.; Berger, S.; Caud, N.; Chen, Y.; Goldfarb, L.; Gomis, M., Climate change 2021: the physical science basis. *Contribution of working group I to the sixth assessment report of the intergovernmental panel on climate change* **2021**, 2.
7. Masson-Delmotte, V.; Zhai, P.; Pörtner, H.-O.; Roberts, D.; Skea, J.; Shukla, P. R.; Pirani, A.; Moufouma-Okia, W.; Péan, C.; Pidcock, R., Global warming of 1.5 C. *An IPCC Special Report on the impacts of global warming of* **2018**, 1 (5).
8. P.R., S. J., Skea, R., Slade, A., Al Khourdajie, R., van Diemen, D., McCollum, M., Pathak, S., Some, P., Vyas, R., Fradera, M., Belkacemi, A., Hasija, G., Lisboa, S., Luz, J., Malley, IPCC, 2022: Summary for Policymakers. In: Climate Change 2022: Mitigation of Climate Change. Contribution of Working Group III to the Sixth Assessment Report of the Intergovernmental Panel on Climate Change. *Cambridge University Press* **2022**.
9. Hannah, R. M., Roser, Pablo, Rosado, CO<sub>2</sub> and Greenhouse Gas Emissions. *Our World in Data* **2020**.
10. Renewable Power Generation Costs in 2021. *International Renewable Energy Agency. IRENA* **2022**.
11. World fertilizer trends and outlook to 2022. *Food and Agriculture Organization of the United Nations* **2019**.

12. Habibzadeh, F.; Miller, S. L.; Hamann, T. W.; Smith, M. R., Homogeneous electrocatalytic oxidation of ammonia to  $N_2$  under mild conditions. *Proc. Natl. Acad. Sci. U.S.A.* **2019**, *116* (8), 2849-2853.
13. Erisman, J. W.; Sutton, M. A.; Galloway, J.; Klimont, Z.; Winiwarter, W., How a century of ammonia synthesis changed the world. *Nature Geoscience* **2008**, *1*, 636.
14. Smil, V., Detonator of the population explosion. *Nature* **1999**, *400* (6743), 415-415.
15. Rafiqul, I.; Weber, C.; Lehmann, B.; Voss, A., Energy efficiency improvements in ammonia production—perspectives and uncertainties. *Energy* **2005**, *30* (13), 2487-2504.
16. Tanabe, Y.; Nishibayashi, Y., Developing more sustainable processes for ammonia synthesis. *Coord. Chem. Rev.* **2013**, *257* (17), 2551-2564.
17. MacFarlane, D. R.; Cherepanov, P. V.; Choi, J.; Suryanto, B. H. R.; Hodgetts, R. Y.; Bakker, J. M.; Ferrero Vallana, F. M.; Simonov, A. N., A Roadmap to the Ammonia Economy. *Joule* **2020**, *4* (6), 1186-1205.
18. Zamfirescu, C.; Dincer, I., Using ammonia as a sustainable fuel. *J. Power Sources* **2008**, *185* (1), 459-465.
19. Avery, W. H., A role for ammonia in the hydrogen economy. *International Journal of Hydrogen Energy* **1988**, *13* (12), 761-773.
20. Lan, R.; Irvine, J. T. S.; Tao, S. W., Ammonia and related chemicals as potential indirect hydrogen storage materials. *International Journal of Hydrogen Energy* **2012**, *37* (2), 1482-1494.
21. Mulder, F. M., Implications of diurnal and seasonal variations in renewable energy generation for large scale energy storage. *J. Renew. Sustain. Energy* **2014**, *6*, 033105.
22. Mulder, F. M., Implications of diurnal and seasonal variations in renewable energy generation for large scale energy storage. *Journal of Renewable and Sustainable Energy* **2014**, *6* (3), 033105.
23. Smith, C.; Hill, A. K.; Torrente-Murciano, L., Current and future role of Haber–Bosch ammonia in a carbon-free energy landscape. *Energy & Environmental Science* **2020**, *13* (2), 331-344.
24. Lim, J.; Fernández, C. A.; Lee, S. W.; Hatzell, M. C., Ammonia and Nitric Acid Demands for Fertilizer Use in 2050. *ACS Energy Letters* **2021**, *6* (10), 3676-3685.
25. Hanna, R., How many people does synthetic fertilizer feed? *Our World in Data* **2017**.
26. Singh, A. R.; Rohr, B. A.; Schwalbe, J. A.; Cargnello, M.; Chan, K.; Jaramillo, T. F.; Chorkendorff, I.; Nørskov, J. K., Electrochemical Ammonia Synthesis—The Selectivity Challenge. *ACS Catalysis* **2017**, *7* (1), 706-709.
27. Hu, L.; Xing, Z.; Feng, X., Understanding the Electrocatalytic Interface for Ambient Ammonia Synthesis. *ACS Energy Letters* **2020**, *5* (2), 430-436.
28. Kibsgaard, J.; Nørskov, J. K.; Chorkendorff, I., The Difficulty of Proving Electrochemical Ammonia Synthesis. *ACS Energy Letters* **2019**, *4* (12), 2986-2988.
29. Abghoui, Y.; Skúlason, E., Computational Predictions of Catalytic Activity of Zincblende (110) Surfaces of Metal Nitrides for Electrochemical Ammonia Synthesis. *The Journal of Physical Chemistry C* **2017**, *121* (11), 6141-6151.
30. Yang, B.; Ding, W.; Zhang, H.; Zhang, S., Recent progress in electrochemical synthesis of ammonia from nitrogen: strategies to improve the catalytic activity and selectivity. *Energy & Environmental Science* **2021**, *14* (2), 672-687.

31. Jacobi, K.; Dietrich, H.; Ertl, G., Nitrogen chemistry on ruthenium single-crystal surfaces. *Applied Surface Science* **1997**, 121-122, 558-561.
32. Hinrichsen, O.; Rosowski, F.; Hornung, A.; Muhler, M.; Ertl, G., The Kinetics of Ammonia Synthesis over Ru-Based Catalysts: 1. The Dissociative Chemisorption and Associative Desorption of N<sub>2</sub>. *Journal of Catalysis* **1997**, 165 (1), 33-44.
33. Dietrich, H.; Geng, P.; Jacobi, K.; Ertl, G., Sticking coefficient for dissociative adsorption of N<sub>2</sub> on Ru single-crystal surfaces. *The Journal of Chemical Physics* **1996**, 104 (1), 375-381.
34. Muhler, M.; Rosowski, F.; Hinrichsen, O.; Hornung, A.; Ertl, G., Ruthenium as catalyst for ammonia synthesis. In *Studies in Surface Science and Catalysis*, Hightower, J. W.; Nicholas Delgass, W.; Iglesia, E.; Bell, A. T., Eds. Elsevier: 1996; Vol. 101, pp 317-326.
35. Shi, H.; Jacobi, K.; Ertl, G., Interaction of hydrogen with nitrogen atoms chemisorbed on a Ru(0001) surface. *The Journal of Chemical Physics* **1995**, 102 (3), 1432-1439.
36. Ertl, G.; Lee, S. B.; Weiss, M., Adsorption of nitrogen on potassium promoted Fe(111) and (100) surfaces. *Surface Science* **1982**, 114 (2), 527-545.
37. Ertl, G.; Lee, S. B.; Weiss, M., Kinetics of nitrogen adsorption on Fe(111). *Surface Science* **1982**, 114 (2), 515-526.
38. Ertl, G.; Huber, M.; Thiele, N., Formation and Decomposition of Nitrides on Iron Surfaces. In *Zeitschrift für Naturforschung A*, 1979; Vol. 34, p 30.
39. Bozso, F.; Ertl, G.; Grunze, M.; Weiss, M., Interaction of nitrogen with iron surfaces: I. Fe(100) and Fe(111). *Journal of Catalysis* **1977**, 49 (1), 18-41.
40. Bozso, F.; Ertl, G.; Weiss, M., Interaction of nitrogen with iron surfaces: II. Fe(110). *Journal of Catalysis* **1977**, 50 (3), 519-529.
41. Rao, C. N. R.; Ranga Rao, G., Nature of nitrogen adsorbed on transition metal surfaces as revealed by electron spectroscopy and cognate techniques. *Surface Science Reports* **1991**, 13 (7), 223-263.
42. Grunze, M.; Driscoll, R. K.; Burland, G. N.; Cornish, J. C. L.; Pritchard, J., Molecular and dissociative chemisorption of N<sub>2</sub> on Ni(110). *Surface Science* **1979**, 89 (1), 381-390.
43. Rao, G. R.; Rao, C. N. R., Adsorption of nitrogen on clean and modified single-crystal Ni surfaces. *Applied Surface Science* **1990**, 45 (1), 65-69.
44. Wedler, G.; Alshorachi, G., Adsorption of Nitrogen on Polycrystalline Nickel Films between 77 K and 333 K. *Berichte der Bunsengesellschaft für physikalische Chemie* **1980**, 84 (3), 277-281.
45. Abghoui, Y.; Garden, A. L.; Hlynsson, V. F.; Björgvinsdóttir, S.; Ólafsdóttir, H.; Skúlason, E., Enabling electrochemical reduction of nitrogen to ammonia at ambient conditions through rational catalyst design. *Physical Chemistry Chemical Physics* **2015**, 17 (7), 4909-4918.
46. Howalt, J. G.; Vegge, T., The role of oxygen and water on molybdenum nanoclusters for electro catalytic ammonia production. *Beilstein Journal of Nanotechnology* **2014**, 5, 111-120.
47. Ertl, G.; Huber, M.; Lee, S. B.; Paál, Z.; Weiss, M., Interactions of nitrogen and hydrogen on iron surfaces. *Applications of Surface Science* **1981**, 8 (4), 373-386.
48. Ertl, G.; Huber, M., Interaction of Nitrogen and Oxygen on Iron Surfaces. *Zeitschrift für Physikalische Chemie* **1980**, 119 (1), 97.

49. Vojvodic, A.; Medford, A. J.; Studt, F.; Abild-Pedersen, F.; Khan, T. S.; Bligaard, T.; Nørskov, J. K., Exploring the limits: A low-pressure, low-temperature Haber–Bosch process. *Chemical Physics Letters* **2014**, *598*, 108-112.
50. Choi, J.; Du, H.-L.; Nguyen, C. K.; Suryanto, B. H. R.; Simonov, A. N.; MacFarlane, D. R., Electroreduction of Nitrates, Nitrites, and Gaseous Nitrogen Oxides: A Potential Source of Ammonia in Dinitrogen Reduction Studies. *ACS Energy Letters* **2020**, *5* (6), 2095-2097.
51. Licht, S.; Cui, B.; Wang, B.; Li, F.-F.; Lau, J.; Liu, S., Retraction. *Science* **2020**, *369* (6505), 780-780.

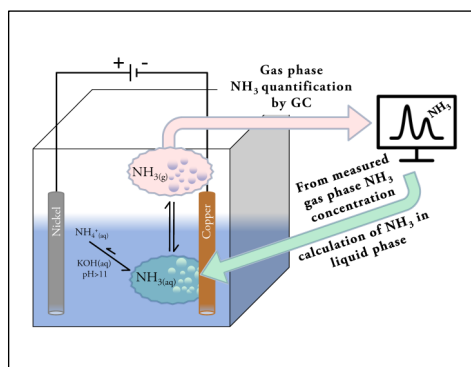




# Gas chromatographic method for *in situ* ammonia quantification at ppb levels

# 2

Ammonia, a commodity chemical, is recently gaining attention as next generation carbon free sustainable fuel. The Haber-Bosch process excels at ammonia synthesis but this process remains largely unsustainable due to massive use of fossil methane resources as main energy input. Electrochemistry has already demonstrated some potential at small scale sustainable ammonia production using renewable energy, but more fundamental research and development is needed to compete with the large scale Haber-Bosch process. In this context, quantification of ammonia produced electrochemically is fundamental for fast catalyst and device optimization and the few analytical methods reported to date are typically impractically laborious and time consuming. In this contribution we report an *in line* gas chromatographic method useful for *in situ* electrochemical ammonia detection in the gas phase with a lower detection limit of 150 ppb. We further show that this method can be used to also calculate ammonia concentrations in solution, thus obtaining full  $\text{NH}_3$  quantification in only a few minutes. The method is demonstrated by *in line* monitoring of electrochemically generated ammonia from the nitrate reduction reaction chosen as model system.

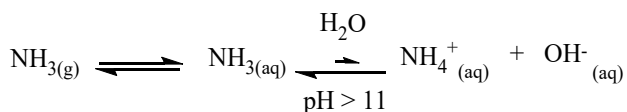


## 2.1 Introduction

Recently, novel promising and sustainable electrochemical approaches at nitrogen reduction are starting to populate the literature, yet more fundamental research and improvements are essential.<sup>1-8</sup> In the context of novel (electrochemical)  $\text{NH}_3$  technology development, the ability to detect ammonia, even at trace levels, is of crucial importance for fast catalyst screening and for their implementation into working devices.

Typically, ammonia is detected by the Berthelot method (or indophenol method); a water based colorimetric analysis. This method is well established, widely used and allows for low ammonia detection limit but it is heavily dependent on experimental conditions such as pH and presence of other species in solution. The major drawback of this method is the laborious and time consuming sample preparation. Among other techniques aimed at sensitive ammonia detection, ion chromatography (IC) has undoubtedly advantages over the indophenol method as the analysis can be automatized. Unfortunately, electrochemically generated ammonia solutions typically contain high concentrations of salts used as supporting electrolyte which may interfere with the analytical IC measurement e.g. sodium or potassium ions. Other techniques shown to be powerful analytical tools in this field are quantitative  $^1\text{H-NMR}$ <sup>9, 10</sup> and UPLC-MS<sup>11</sup> (ultrahigh performance liquid chromatography–mass spectrometry).<sup>12</sup> They detect ammonium ions derived from acidification of ammonia containing solutions or derivatize ammonia with suitable chemicals such as dansyl chloride.<sup>11</sup> Nonetheless, often, ammonia is produced in a basic aqueous media and due to its gaseous nature at typical electrochemical experimental conditions, it partitions between the gaseous head space and liquid phase as dissolved gas as shown in **Scheme 2.1**. For this reason, ammonia solutions are difficult to store for subsequent quantitative analysis and the laborious and time consuming sample preparation must be done immediately after sampling procedures. For IC and quantitative  $^1\text{H-NMR}$ , trapping the ammonia in an acidic medium as ammonium ion is essential for its quantitative detection. Similarly, for UPLC-MS, ammonia derivatization should be done quickly to obtain a representative sample containing now a more stable compound that can be analyzed at later times. As such, ammonia present in the liquid phase can be trapped or derivatized rather easily, yet quantitative analysis of the ammonia that equilibrates with the head space remains challenging to address, especially in open systems. Furthermore, the mentioned techniques

involve a discrete degree of sampling, sample handling and sample preparation that require manual dexterity, great attention from the experimentalist and time dedication in order to be successful. All the above can also potentially introduce errors and contaminations in the measurements.



**Scheme 2.1.** Equilibrium reaction between gas phase ammonia ( $\text{NH}_{3(g)}$ ), dissolved ammonia ( $\text{NH}_{3(aq)}$ ) and ammonium ion ( $\text{NH}_4^+$ ). When pH is higher than 11 the equilibrium is fully shifted to the left side of the equation thus the only relevant equilibrium to be considered is between ammonia in the gas phase ( $\text{NH}_{3(g)}$ ) and ammonia as dissolved gas ( $\text{NH}_{3(aq)}$ ).

As a consequence, time resolved information becomes unfortunately difficult to acquire leading to poor catalyst/system/device characterization and to large errors in the calculation of relevant catalyst parameters, chief among which rate constants, turn over frequencies and efficiency parameters. In this chapter we propose a gas chromatographic (GC) method for *in situ* ammonia detection that can be applied to any (electrochemical) device operating under a wide range of conditions. The *in situ* GC method quantifies ammonia present in the gas phase in under 5 minutes analysis time with a lower detection limit of about 150 ppb v/v ( $\sim 110 \text{ ng l}^{-1} \text{ NH}_3$  or  $6.5 \text{ nM NH}_3$  in the gas phase) a threshold level relevant to study and screen (electro)catalysts. We further show that the ammonia concentration in the gas phase, directly measured by GC, can be used to calculate the ammonia concentration in the liquid electrolyte solution thus enabling full quantification of the analyte under interest as depicted in **Figure 2.1**, including ammonia stripped from the system due to GC carrier gas. The method allows for collection of time resolved data giving access to relevant parameters to measure catalysts performance. Importantly, ammonia quantification is done *in situ* thus avoiding altogether sample manipulations and time consuming sample preparations.

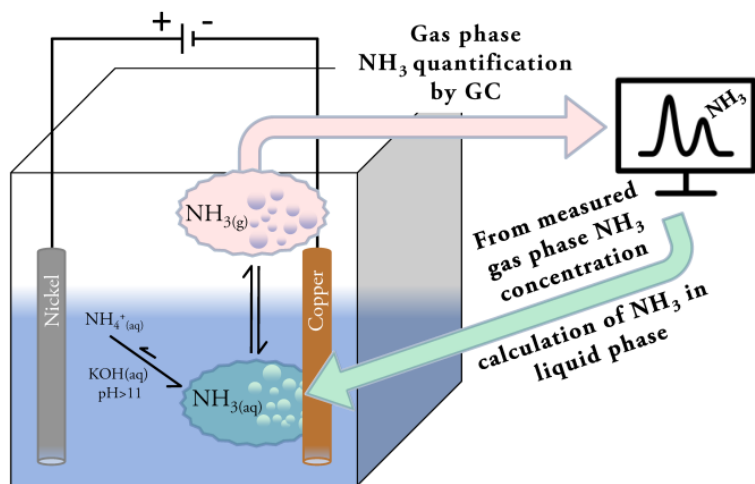


**Figure 2.1** Representation of electrochemical ammonia generation device and equilibrium between ( $\text{NH}_3(\text{aq})$ ) and gas phase ammonia ( $\text{NH}_3(\text{g})$ ) provided pH is basic. Gas phase ammonia concentration is addressed directly by GC while dissolved ammonia concentration is calculated from gas phase ammonia concentration.

## 2.2 Experimental

All commercially available chemicals were used as received without further purification. Milli-Q water was used for preparation of standard solutions and for electrolyte solutions. Electrochemical experiments at constant current were performed using Ametek PARSTAT potentiostat using a copper wire coil working electrode (diameter 2 mm) and nickel wire coil counter electrode (diameter 1 mm) with a 3 M KOH solution as electrolyte and 100 mM KNO<sub>3</sub> as substrate. Chromatographic experiments were performed using a custom assembled gas chromatographer based on a Trace GC 1300 chromatographer from Thermo Scientific. The instrument was assembled by Interscience BV (Breda, Netherlands). Channel 1 was equipped with a 250  $\mu$ L sample loop, a Select Low Ammonia capillary column from Agilent and a PDD detector using He as carrier gas. The column was located in the GC oven compartment. This channel is dedicated to ammonia detection. Channel 2 was equipped with a 250  $\mu$ L sample loop, a series of packed columns (Hayesep N, 60-80, 0.5 m, XL Sulfurum 60-80, 2m and Molsieve 5 Å, 60-80 3 m) and a TCD detector using He as carrier gas. The columns were located in the GC valve compartment at fixed temperature (100 °C). This channel is dedicated to detection of other gases such as H<sub>2</sub>, O<sub>2</sub>, N<sub>2</sub> and Ar. Channel 3 was equipped with a 250  $\mu$ L sample loop and a series of packed columns (Hayesep N, 60-80, 1 m, CBS 60-80, 3 m) and a TCD detector using N<sub>2</sub> as carrier gas. The columns were located in the GC valve compartment at fixed temperature (100 °C). This channel is dedicated to detection of H<sub>2</sub>.

Ammonium quantification in solution was carried out using Berthelot indophenol colorimetric method. Three different solutions were freshly prepared prior to the analysis. Solution 1 was prepared placing 40 g (0.25 mol) of sodium salicylate and 4 g (0.10 mol) of sodium hydroxide in a beaker and dissolved in a minimal amount of water. The solution was transferred to a 100 mL volumetric flask and brought to volume. Final concentration of sodium salicylate 2.5 M and sodium hydroxide 1 M. Solution 2 was prepared placing 0.465 g (1.82 mmol) of dichloroisocyanuric acid sodium salt dihydrate and 10 g (34 mmol) of trisodium citrate in a beaker and dissolved in a minimal amount of water. The solution was transferred to a 100 mL volumetric flask and brought to volume. Final concentration of dichloroisocyanuric acid sodium salt dihydrate 0.018 M and trisodium citrate 0.34 M. Solution 3 was prepared placing 0.136g of sodium nitroprussiate dihydrate in a 100 mL

volumetric flask and brought to volume with a final concentration of 4.5 mM. For the analyte preparation, 100  $\mu\text{L}$  of sample to be analysed were transferred to a glass vial followed by 0.9 mL of Solution 1. After mixing for few seconds, 1 mL of Solution 2 was added and the vial was again mixed for few seconds. Lastly 1 mL of Solution 3 was added to the glass vial. The vial was shaken and placed in an oven at 50 °C for 30 minutes. After this time the vial was shaken for few seconds and incubated at 50 °C for additional 30 minutes. After this time the solutions were analysed at the UV-vis at 650 nm.

## 2.3 Results and discussion

*Ammonia gas chromatography and calibration curve.* Few key aspects are fundamental to establish quantitative GC ammonia detection. Ammonia gas is well known for its tendency to physisorb onto most materials including stainless steel tubing, often used to connect experimental setups to the GC inlet and sometimes also for GC internal connections.<sup>13</sup> Physisorption onto tubing and valves becomes a very relevant issue when ammonia concentration approaches sub-ppm range, as most analyte would be lost due to physisorption with drastic implications for quantitative detection. In this regard, some materials are best used to minimize this issue. Stainless steel coated with an inert layer of SilcoNert®2000 (Sulfinert®) minimizes ammonia physisorption to around  $5.7 \cdot 10^{12}$  molecules  $\text{cm}^{-2}$ .<sup>14</sup> In comparison, bare stainless steel adsorbs over two orders of magnitude more ammonia;  $1.50 \cdot 10^{14}$  molecules  $\text{cm}^{-2}$ . Among materials with low ammonia adsorption that can be useful for setup fabrication are PVDF (polyvinylidene difluoride), LDPE (low-density polyethylene), PTFE (polytetrafluoroethylene) and PFA (perfluoroalkoxy alkanes) ranging from  $1 \cdot 10^{12}$  to  $14 \cdot 10^{12}$  molecules  $\text{cm}^{-2}$ .<sup>14</sup> Care should also be taken to exclude any valve that might be present along the sample path as they are unlikely to be inert towards ammonia physisorption, including those within the GC instrument such as stop flow valves typically placed before sample loops. VICI® diaphragm valves were used in our setup as their main body is inert and the sample comes in contact with only an inert membrane. The separation column chosen, Agilent Select Low Ammonia, is of primary importance to achieve good water/ammonia separation while maintaining a symmetric and sharp ammonia peak shape,

important for sensitive quantification (**Figure 2.2**). GC configuration and details of the method are compiled in the SI.

For the validity of the method it is fundamental to obtain an ammonia calibration curve which was built by nitrogen dilution of ammonia containing certified cylinders. The dilution was carried out with the aid of a mass flow controller (MFC) and a mass flow meter (MFM) as depicted in **Figure 2.3**. This simple set up allows for choosing a nitrogen flow at MFC (dilution gas) while the ammonia containing gas flow is tuned by a needle valve, positioned just after the  $\text{NH}_3$  cylinder pressure reducer, to obtain the desired total flow displayed at MFM. With such dilution setup, ammonia never passes through non-inert surfaces such as that of valves or mass flow controllers and allowed for generating ammonia containing samples ranging from 13.8ppm to 100ppb. A good linear response between ammonia concentration and area under  $\text{NH}_3$  peak was obtained as shown in **Figure 2.4**. A series of consecutive injections of samples with the same gas composition was used to calculate the standard deviation and determine the experimental error (**Table A.2.2**).

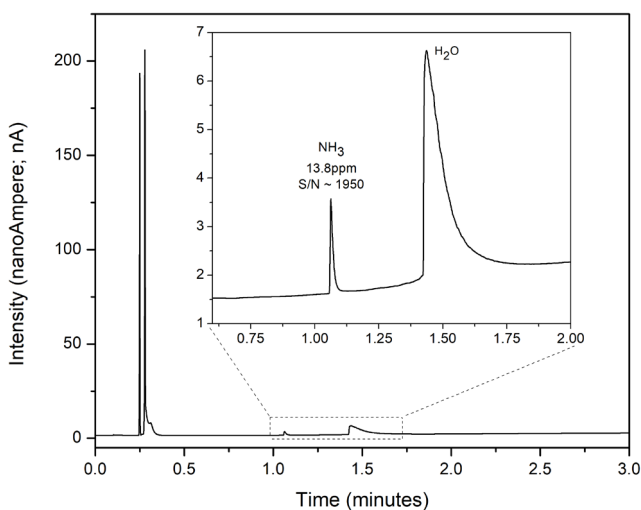


**Figure 2.2** Example of full chromatogram obtained for a sample containing 13.8 ppm ammonia in  $\text{N}_2$ . Permanent gases are eluted at 0.25 minutes, ammonia at 1.1 minutes and water at 1.3 minutes. The insert shows the nearly symmetrical peak of ammonia peak and the excellent resolution between ammonia and water peaks. The Slight background signal increase is due to temperature increase ramp.



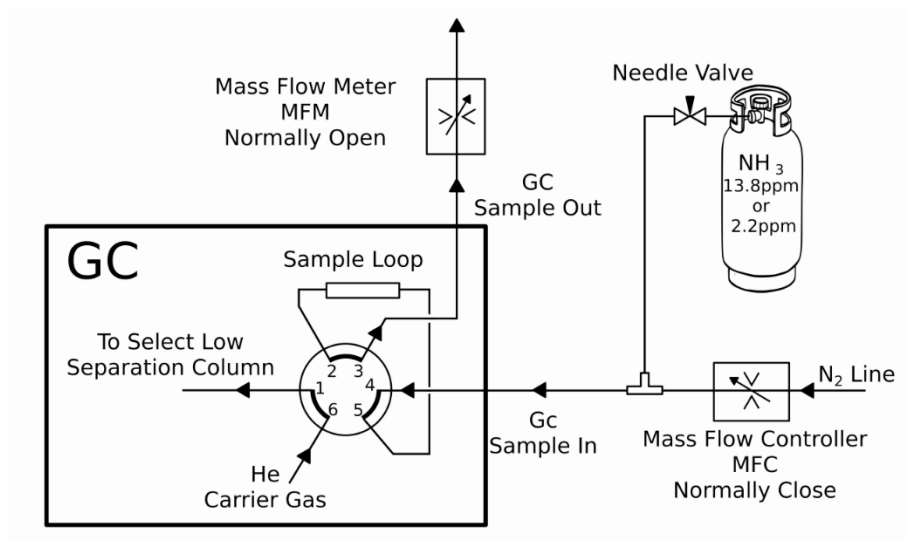


**Figure 2.3** Ammonia dilution setup comprising an ammonia cylinder with a pressure reducer and needle valve to adjust ammonia flow, a mass flow controller (MFC) in a normally closed mode to select  $\text{N}_2$  diluting gas flow and a mass flow meter (MFM) to measure total flow passing through the GC instrument.

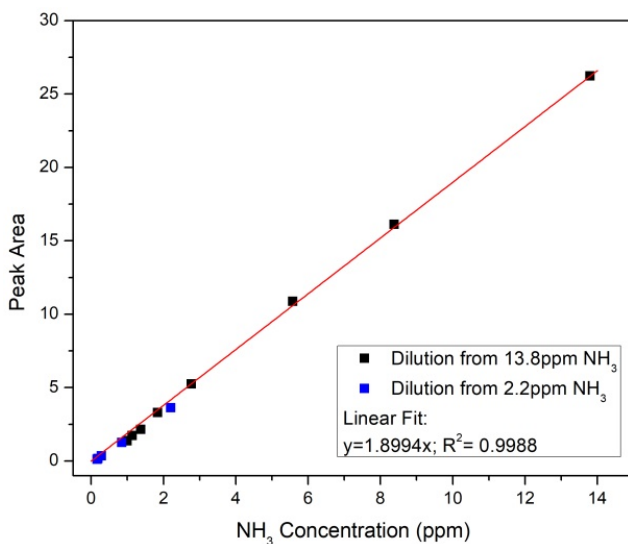


**Figure 2.4** Ammonia calibration curve in the range 150 ppb to 13.8 ppm obtained from dilution of ammonia containing streams from gas cylinders rated at 13.8 ppm and 2.2 ppm  $\text{NH}_3$  in  $\text{N}_2$  using setup shown in Figure 2.3.

*Ammonia in liquid phase.* As ammonia can be measured reliably in the gas phase, this method can be directly applied to those (electrochemical) systems that produce ammonia as gaseous product without direct contact with electrolyte e.g. gas diffusion electrodes or gas phase heterogeneous catalytic systems.<sup>15, 16</sup> However, most electrochemical systems do require aqueous electrolyte thus we set out to find a versatile method to correlate ammonia concentration in the electrolyte and ammonia concentration in the gas phase in equilibrium with it. We envision that this correlation can be easily found by plotting the concentration found in solution measured by traditional indophenol method and the concentration in gas phase measured by GC as described above.

Ammonia containing solutions at different concentrations were analyzed by Berthelot indophenol colorimetric method to accurately determine their concentration in the liquid phase by comparing their absorbance at 650 nm with a suitable UV-vis calibration curve obtained previously (**Figure A.2.1**). Secondly, aliquots of the same solutions were individually placed in a closed cell having a nitrogen inlet gas stream blowing over the ammonia solution and an outlet line connected to the GC sample inlet. After allowing time for equilibration between the liquid phase and head space, the nitrogen carrier flow was activated and the ammonia concentration in the gas phase was evaluated by comparing the ammonia peak area measured to the calibration curve shown in **Figure 2.4**. Plotting the ammonia concentration in solution obtained by Berthelot indophenol colorimetric method against the ammonia concentration in the gas phase obtained by GC, results in a linear relationship, shown in **Figure 2.5**, that allows for quickly calculating ammonia concentration in solution by simply measuring the ammonia concentration in the gas phase above the liquid electrolyte. The authors wish to point out the method can be easily applied to any set of conditions experimentally needed, provided that pH of the liquid phase is basic, in order to establish the  $\text{NH}_3/\text{NH}_4^+$  equilibrium towards the  $\text{NH}_3$  side according to **Scheme 2.1**, and that calibration curves are obtained with the experimental setup and conditions that are to be used for the experiment itself.

*In situ GC quantification of electrochemically produced ammonia.* To showcase the validity of the method, nitrate reduction operated electrochemically in basic aqueous media was chosen as model reaction as this particular electrochemical reaction is sufficiently robust and widely studied in literature.<sup>17-22</sup> For the purpose intended in this chapter, our interest relies in showing the applicability of the *in situ* ammonia detection method;

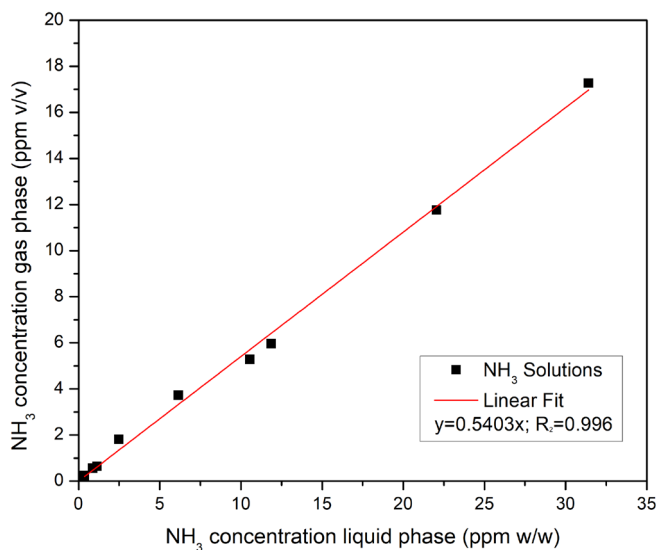


**Figure 2.5** Linear relationship between  $\text{NH}_3$  concentration in liquid phase as obtained by Berthelot indophenol colorimetric method and  $\text{NH}_3$  concentration in the gas phase as obtained by GC chromatography. The ammonia concentration in the gas phase is expressed in ppm intended as volume ratio (v/v) while ammonia concentration in the liquid phase is expressed in ppm intended as weight ratio (w/w). As such, 1 ppm in the gas phase equals to  $0.75 \mu\text{g l}^{-1} \text{NH}_3$  while 1 ppm in the liquid phase equals  $1000 \mu\text{g l}^{-1} \text{NH}_3$ .

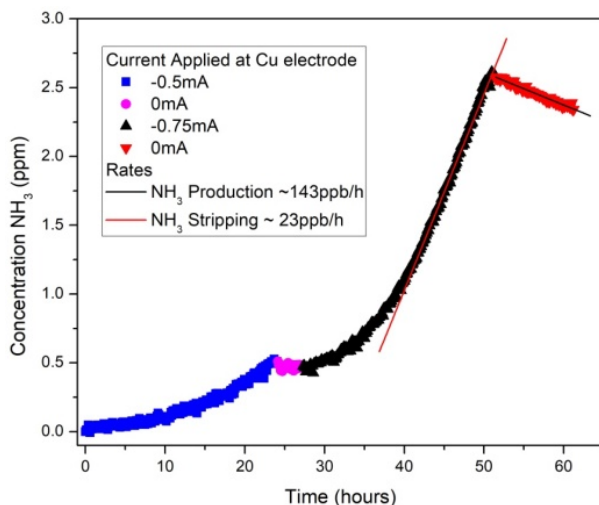


**Figure 2.6** *In line* ammonia detection from electrochemical nitrate reduction reaction at copper electrode at different currents in basic aqueous electrolyte.

therefore a simple one compartment cell, two-electrode system without ion exchange membrane was used and the array of possible reaction products compiled in **Figure A.2.2** was not investigated. Copper wire was used as working electrode and a nickel wire used as counter electrode in KOH aqueous electrolyte containing potassium nitrate as substrate. The electrodes were placed into a sealed Teflon cell equipped with a nitrogen carrier gas inlet line and an outlet line directly connected to the GC sample inlet, all controlled by MFC and MFM similarly as discussed previously.

When no current is applied to the electrodes, no ammonia is detected at the GC but as soon as the current is switched on the corresponding ammonia peak appears in the chromatograms. As shown in **Figure 2.6**, this peak increases in time, indicating that ammonia is generated electrocatalytically in solution and it quickly equilibrates with its gaseous head space as the high pH ensures that  $\text{NH}_3$  is present in solution rather than  $\text{NH}_4^+$ . As an example, when -0.75 mA current was applied the ammonia production rate in the gas phase reached about 143 ppb  $\text{h}^{-1}$ . When the current is stopped while maintaining the nitrogen carrier gas flow active, the ammonia concentration slowly decreases due to the stripping effect of the carrier gas which slowly depletes the  $\text{NH}_3$  from solution at a rate of 23 ppb  $\text{h}^{-1}$ .

Calculation of faradaic efficiency is straightforward as the ammonia concentration in solution can be derived from the concentration measured in the gas phase at the end of the experiment while integration of the plot in **Figure 2.6** gives direct access to the amount of ammonia lost due to stripping effects from the  $\text{N}_2$  carrier gas. Thus, ammonia present in liquid phase at the end of the experiment is calculated to be 5.66  $\mu\text{mol}$   $\text{NH}_3$  while stripped ammonia amounts to 9.70  $\mu\text{mol}$ ; roughly 60% of the total ammonia produced is lost due to stripping effects. The capability to measure the  $\text{NH}_3$  stripping from the system is an illustration of the directness and strength of this method. The amount of charge passed through the electrodes is easily obtained from the electrochemical experiment done at constant current and, as such, faradaic efficiency can be calculated (detailed calculations are compiled in SI). When all parameters of the system under investigation are known, other relevant information are easily calculated such as catalytic turnover frequency, turnover number and rate constants.

This set of experiments shows that electrochemically produced ammonia in basic aqueous solution quickly equilibrates with its head space and its concentration can be monitored with *in line* GC rendering this method a valuable tool for sensitive real-time ammonia detection under a wide variety of experimental conditions. Calibration plots are still

necessary for quantitative ammonia analysis but their preparation requires only limited amount of time as compared to time requirements for sample handling and preparation for other quantitative ammonia analytical techniques.

## 2.4 Conclusions

*Impact and Future Work.* This fast and reliable method has the potential to speed-up catalyst screening and development of novel sustainable ammonia evolution devices as it requires significantly less effort in sample handling and preparation compared to other reported methods. The method is unique as it allows for *in situ* monitoring of ammonia evolution from (electrochemical) devices as showcased by electrochemical nitrate reduction reaction. Furthermore, provided proper calibration curves are obtained for the set of experimental conditions employed, a simple 5-minutes gas chromatogram provides information on ammonia concentration both in gas phase and in the liquid phase in equilibrium with it. In the following chapters, we will show the employment of this method in relevant nitrogen reduction to ammonia applications that are currently under study in our laboratories.

## Appendix A.2

**Table A.2.1** Parameters used for ammonia detection.

Column	Agilent Select Low Ammonia
Pressure	Constant at 320 kPa
Split flow	1.4 mL min <sup>-1</sup>
Temperature program	60 °C for 1 min, ramp at 120 °C min <sup>-1</sup> to 200 °C, hold for 2 min at 200 °C
Sample volume	250 µL
Equilibration time	30 seconds

**Table A.2.2** Injections obtained from N<sub>2</sub> gas dilution of NH<sub>3</sub> cylinders (8 dilutions from 13.80 ppm NH<sub>3</sub> in N<sub>2</sub>, 5 from 2.2 ppm). Data are used to build calibration curve shown in Figure 2.4.

Inj.	Area												
1	26.0514	16.2076	10.8378	5.2837	3.3513	2.3204	1.6997	1.3149	3.5927	1.4272	0.3203	0.1791	0.1036
2	26.0387	16.05	10.8007	5.4127	3.182	2.0028	1.7646	1.2799	3.5704	1.3741	0.386	0.1457	0.0984
3	26.1658	16.2055	10.8748	5.4245	3.4557	2.0777	1.7072	1.3843	3.612	1.4132	0.3966	0.1634	0.1237
4	26.2171	16.0043	10.9208	5.0943	3.204	2.3423	1.7588	1.3843	3.678	1.1302	0.3926	0.1619	0.1191
5	26.374	16.1924	10.8914	5.1113	3.3943	2.1089	1.7824	1.468	3.8273	1.2225	0.3291	0.1548	0.1164
6	26.3323	16.0883	10.9273	5.3309	3.3981	2.0426	-	1.475	3.5089	1.1279	0.3356	0.1926	0.1243
7	26.3126	-	-	5.1203	3.1363	2.1785	-	-	3.6052	1.1204	0.3056	-	-
8	26.3232	-	-	-	-	-	-	-	-	1.2999	0.3763	-	-
9	26.3231	-	-	-	-	-	-	-	-	-	0.3421	-	-
10	26.1593	-	-	-	-	-	-	-	-	-	-	-	-
ppm	13.80	8.38	5.58	2.77	1.84	1.37	1.14	1.00	2.20	0.84	0.28	0.19	0.15
Area Average	26.2298	16.1247	10.8755	5.2540	3.3031	2.1533	1.7425	1.3844	3.6278	1.2644	0.3538	0.1663	0.1143
Standard Deviation Area	0.1154	0.0810	0.0447	0.1335	0.1167	0.1236	0.0329	0.0718	0.0939	0.1230	0.0323	0.0155	0.0099
Error % Area	0.44	0.50	0.41	2.54	3.53	5.74	1.89	5.19	2.59	9.73	9.14	9.32	8.63
Error % ppm	0.0607	0.0421	0.0229	0.0704	0.0649	0.0786	0.0215	0.0517	0.0570	0.0822	0.0260	0.0178	0.0144

**Standard ammonia solutions preparation.** As the indophenol method is rather sensitive to experimental conditions and as we will apply this method to detect ammonia in solutions generated electrochemically i.e. containing KOH electrolyte and  $\text{KNO}_3$  substrate, the calibration curve was built using  $\text{NH}_3$  standard solutions containing the same electrolyte and the same substrate concentration that will be used for the electrochemical experiment.

0.315g of anhydrous  $\text{NH}_4\text{Cl}$  were added to a 100 mL volumetric flask and dissolved using a solution containing 3 M KOH and 100 mM  $\text{KNO}_3$  to reach a concentration of 1000.935 ppm  $\text{NH}_3$ . All further dilutions reported in **Table A.2.3** were done using a solution containing 3 M KOH and 100 mM  $\text{KNO}_3$ .

**Table A.2.3** Summary of all standard solutions prepared by dilution of 1000.935 ppm  $\text{NH}_3$ .

Starting $\text{NH}_3$ concentration [ppm]	Volume $\text{NH}_3$ solution [mL]	Final volume [mL]	Finale $\text{NH}_3$ concentration [ppm]
1000.935	10	100	100.093
1000.935	5	100	50.047
1000.935	2.5	100	25.023
1000.935	1.5	10	15.014
1000.935	1	100	10.009
1000.935	0.75	10	7.507
50.047	1	10	5.005
25.023	1	10	2.502
10.009	1	10	1.001
7.507	1	10	0.751
5.005	1	10	0.500
5.005	0.5	10	0.250
1.001	1	10	0.100
0.751	1	10	0.075
0.500	1	10	0.050

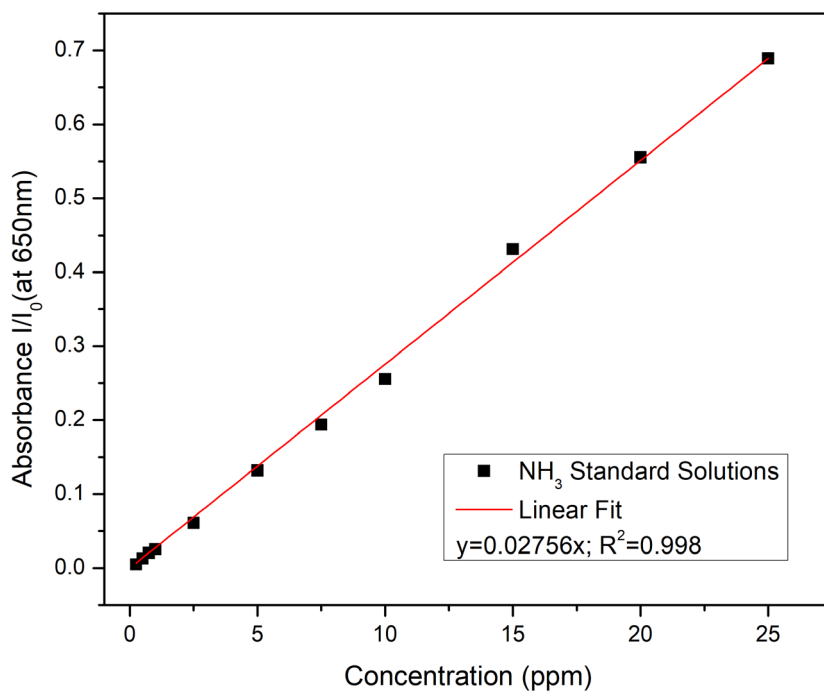


**Figure A.2.1** Calibration curve for UV-Vis colorimetric indophenol analysis of standard ammonia solutions containing 3 M KOH and 100 mM KNO<sub>3</sub>.



**Comparison NH<sub>3</sub> concentration in solution vs NH<sub>3</sub> concentration in gas phase.**

Preparation of solutions: an arbitrary amount (roughly 3 mL) of the NH<sub>3</sub> standard solution with a concentration of 1000.935 ppm prepared as described above was diluted several times with a solution containing 3 M KOH and 100 mM KNO<sub>3</sub> to obtain NH<sub>3</sub> concentrations in the range 35 ppm to 250 ppb. The exact concentration of the prepared solutions is obtained by colorimetric indophenol UV-Vis analysis by comparison of their absorbance at 650 nm with the calibration curve shown above in **Figure A.2.1**.

The same solutions were analyzed with GC chromatography to determine the NH<sub>3</sub> concentration in the gas phase that is in equilibrium with the solution phase. Data are compiled in **Table A.2.4** below.

**Table A.2.4** Summary of UV-Vis absorbance at 650 nm, calculated NH<sub>3</sub> concentration in liquid phase by indophenol method and measured concentration of NH<sub>3</sub> in gas phase by GC.

Absorbance at 650 nm	Calculated NH <sub>3</sub> concentration in solution [ppm, w/w]	NH <sub>3</sub> concentration in gas phase determined by GC [ppm, v/v]
0.0101	0.366	0.239
0.0242	0.880	0.562
0.0311	1.130	0.638
0.0684	2.482	1.809
0.1694	6.147	3.730
0.2907	10.548	5.280
0.3271	11.869	5.959
0.6076	22.046	11.762
0.8657	31.411	17.271

**Faradaic efficiency calculation.** Our electrochemical setup consists in a one compartment cell so it likely that the generated ammonia is back oxidized to nitrates at the counter electrode thus lowering the faradaic efficiency. Nitrogen formation either from nitrate reduction at the working electrode or from ammonia oxidation at the counter electrode are also likely reaction pathways that are concentration dependent and contribute to lower the faradaic efficiency (**Figure A.2.2**). This GC method has also the potential to simultaneously detect hydrogen gas, a common side product in nitrogen reduction reaction. Obtaining information on hydrogen concentrations could help corroborate calculated efficiency values. Nonetheless, in our experiments hydrogen was not detected at significant levels.

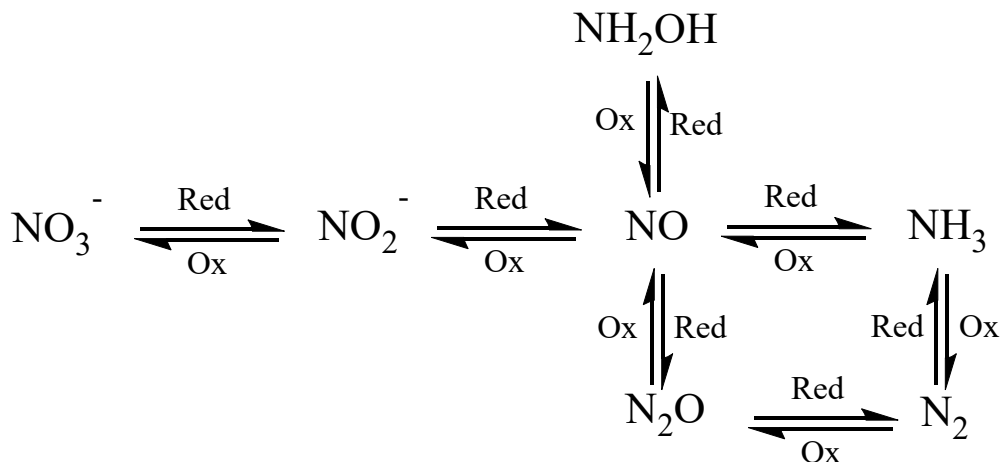


**Figure A.2.2** Scheme of possible products formed during electrochemical nitrate reduction. All the species exist as solvated species in solution and adsorbed species onto the electrodes. In a one compartment cell, two-electrode system, the reduction path happens at the working negative electrode while the oxidation path can take place at the positive counter electrode.

$$F.E. = \frac{(\text{molNH}_3(l) + \text{molNH}_3(g)) \times n \times F}{I \times t} \times 100$$

**Equation A.2.1** Faradaic efficiency (F.E.) expression: molNH<sub>3</sub>(l) are moles of NH<sub>3</sub> that stay in the liquid phase (mol), molNH<sub>3</sub>(g) are moles of NH<sub>3</sub> that go in the gas phase and slushed away by carrier gas (mol), n is the number of electrons exchanged going from nitrate (oxidation state of N in NO<sub>3</sub><sup>-</sup> is +5) to ammonia (oxidation state of N in NH<sub>3</sub> is -3) thus a 8 electron process, F is faraday constant (C mol<sup>-1</sup>), I is the current applied (A) and t is time (s).

Moles of NH<sub>3</sub>(l) are calculated from the concentration in gas phase measured at the end of the experiment (time 51.33 h) using the relationship obtained before shown in **Figure 2.5**;

$$[\text{NH}_3(l)]_{\text{ppm w/w}} = [\text{NH}_3(g)]_{\text{ppm v/v}} / 0.5403$$

$$[\text{NH}_3(l)]_{\text{ppm w/w}} = [\text{NH}_3(g)]_{\text{ppm v/v}} / 0.5403 = 2.592\text{ppm} / 0.5402 = 4.80\text{ppm NH}_3(l)$$

$$\text{molNH}_3(l) = 4.80\text{ppm NH}_3(l) = 4.8\text{mgNH}_3/\text{l in 20 ml solution} = 5.66\mu\text{molNH}_3(l)$$

Moles of NH<sub>3</sub>(g) are obtained by integration of the plot shown in **Figure 2.6** of main manuscript until time 51.33 h. The value of the integral is 26.773 mgNH<sub>3</sub> m<sup>-3</sup> while the carrier gas flow is 2 ml min<sup>-1</sup>.

$$\text{m}^3 \text{ carrier gas} = 51.33\text{h} * 2\text{ml min}^{-1} * 60\text{min h}^{-1} / 10^6 \text{ ml m}^{-3} = 0.00616 \text{ m}^3$$

$$\text{molNH}_3(g) = 26.773\text{mgNH}_3 \text{ m}^{-3} * 0.00616\text{m}^3 / 17\text{g mol}^{-1} = 9.70 \mu\text{mol NH}_3(g)$$

Total charge passed electrochemically:

$$Q = I * t = (0.75\text{mA} + 0.5\text{mA}) * 24\text{h} * 60\text{min h}^{-1} * 60\text{s min}^{-1} = 108 \text{ C}$$

$$F.E. = (5.66\mu\text{molNH}_3(l) + 9.70\mu\text{molNH}_3(g))10^{-6}\text{mol } \mu\text{mol}^{-1} * 8 * 96485\text{C mol}^{-1} / 108\text{C} * 100 = 10.98\%$$

### Comparison between SilcoNert coated tubing and bare stainless steel tubing.

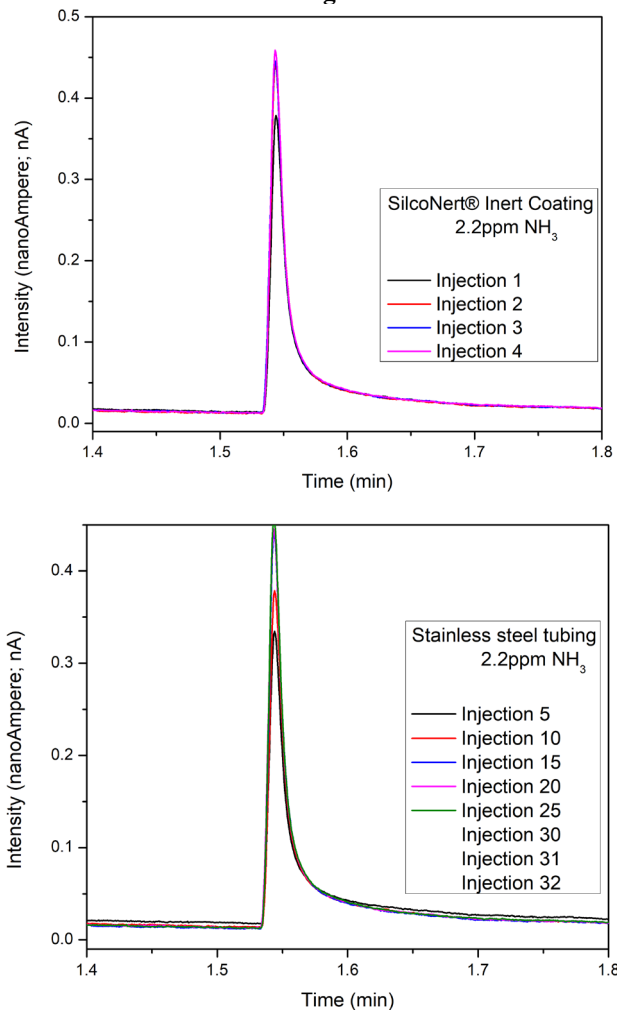


**Figure A.2.3** Comparison of injection of 2.2 ppm NH<sub>3</sub> using SilcoNert coated tubing (left) and bare stainless steel tubing (right) showing that when stainless steel is used about 30 injections are needed to reach a constant ammonia signal while when SilcoNert tubing is used a constant ammonia signal is reached already at the second injection. Injections are done every 8 minutes but the 2.2 ppm NH<sub>3</sub> sample flows constantly through the sample loop.

## References

1. Cui, X.; Tang, C.; Zhang, Q., A Review of Electrocatalytic Reduction of Dinitrogen to Ammonia under Ambient Conditions. *Advanced Energy Materials* **2018**, 8 (22), 1800369.
2. Kyriakou, V.; Garagounis, I.; Vasileiou, E.; Vourros, A.; Stoukides, M., Progress in the Electrochemical Synthesis of Ammonia. *Catal. Today* **2017**, 286, 2-13.
3. Shipman, M. A.; Symes, M. D., Recent progress towards the electrosynthesis of ammonia from sustainable resources. *Catal. Today* **2017**, 286, 57-68.
4. van der Ham, C. J. M.; Koper, M. T. M.; Hetterscheid, D. G. H., Challenges in reduction of dinitrogen by proton and electron transfer. *Chemical Society Reviews* **2014**, 43 (15), 5183-5191.
5. Tanabe, Y.; Nishibayashi, Y., Developing more sustainable processes for ammonia synthesis. *Coord. Chem. Rev.* **2013**, 257 (17), 2551-2564.
6. Smith, C.; Hill, A. K.; Torrente-Murciano, L., Current and future role of Haber–Bosch ammonia in a carbon-free energy landscape. *Energy & Environmental Science* **2020**, 13 (2), 331-344.
7. Giddey, S.; Badwal, S. P. S.; Kulkarni, A., Review of electrochemical ammonia production technologies and materials. *Int. J. Hydrogen Energy* **2013**, 38 (34), 14576-14594.
8. Amar, I. A.; Lan, R.; Petit, C. T. G.; Tao, S., Solid-state electrochemical synthesis of ammonia: a review. *J. Solid State Electrochem.* **2011**, 15 (9), 1845.
9. Nielander, A. C.; McEnaney, J. M.; Schwalbe, J. A.; Baker, J. G.; Blair, S. J.; Wang, L.; Pelton, J. G.; Andersen, S. Z.; Enemark-Rasmussen, K.; Čolić, V.; Yang, S.; Bent, S. F.; Cargnello, M.; Kibsgaard, J.; Vesborg, P. C. K.; Chorkendorff, I.; Jaramillo, T. F., A Versatile Method for Ammonia Detection in a Range of Relevant Electrolytes via Direct Nuclear Magnetic Resonance Techniques. *ACS Catalysis* **2019**, 9 (7), 5797-5802.
10. Hodgetts, R. Y.; Kiryutin, A. S.; Nichols, P.; Du, H.-L.; Bakker, J. M.; Macfarlane, D. R.; Simonov, A. N., Refining Universal Procedures for Ammonium Quantification via Rapid <sup>1</sup>H NMR Analysis for Dinitrogen Reduction Studies. *ACS Energy Letters* **2020**, 5 (3), 736-741.
11. Yu, W.; Lewis, N. S.; Gray, H. B.; Dalleska, N. F., Isotopically Selective Quantification by UPLC-MS of Aqueous Ammonia at Submicromolar Concentrations Using Dansyl Chloride Derivatization. *ACS Energy Letters* **2020**, 5 (5), 1532-1536.
12. It must be acknowledged that quantitative <sup>1</sup>H-NMR and UPLC-MS not only allow sensitive ammonia detection but they also allow for resolution and identification of nitrogen labeled species providing extremely useful information for detailed mechanistic investigations. We note that the method described here could also achieve such level of analysis when the gas chromatographer is coupled with a MS detector. Direct NH<sub>3</sub> detection at MS detectors is notoriously challenging as the couples <sup>14</sup>NH<sub>3</sub>/OH<sup>-</sup> as well as <sup>15</sup>NH<sub>3</sub>/H<sub>2</sub>O share the same m/z ratio. Yet, the chromatographic method described here allows for excellent water-ammonia separation as shown in Figure 2, thus minimizing MS detectability issues of the mentioned species as NH<sub>3</sub> and water reach the MS detector at different times. Water background at the MS detector from water present in the system such as traces amounts in the He carrier gas, should not cause detection issues as they will be constant and, as such, only cause a time independent baseline increase.

13. de Castro, A.; Alegre, D.; Tabarés, F. L., Physisorption of ammonia on AISI 304L stainless steel at different surface temperature under high vacuum conditions. *Nuclear Materials and Energy* **2016**, 9, 1-5.
14. Vaittinen, O.; Metsälä, M.; Persijn, S.; Vainio, M.; Halonen, L., Adsorption of ammonia on treated stainless steel and polymer surfaces. *Appl. Phys. B* **2014**, 115 (2), 185-196.
15. Michalsky, R.; Avram, A. M.; Peterson, B. A.; Pfromm, P. H.; Peterson, A. A., Chemical looping of metal nitride catalysts: low-pressure ammonia synthesis for energy storage. *Chemical Science* **2015**, 6 (7), 3965-3974.
16. Wang, K.; Smith, D.; Zheng, Y., Electron-driven heterogeneous catalytic synthesis of ammonia: Current states and perspective. *Carbon Resources Conversion* **2018**, 1 (1), 2-31.
17. Shih, Y.-J.; Wu, Z.-L.; Huang, Y.-H.; Huang, C.-P., Electrochemical nitrate reduction as affected by the crystal morphology and facet of copper nanoparticles supported on nickel foam electrodes (Cu/Ni). *Chem. Eng. J.* **2020**, 383, 123157.
18. Pérez-Gallent, E.; Figueiredo, M. C.; Katsounaros, I.; Koper, M. T. M., Electrocatalytic reduction of Nitrate on Copper single crystals in acidic and alkaline solutions. *Electrochim. Acta* **2017**, 227, 77-84.
19. Reyter, D.; Bélanger, D.; Roué, L., Study of the electroreduction of nitrate on copper in alkaline solution. *Electrochim. Acta* **2008**, 53, 5977-5984.
20. Abdallah, R.; Geneste, F.; Labasque, T.; Djelal, H.; Fourcade, F.; Amrane, A.; Taha, S.; Floner, D., Selective and quantitative nitrate electroreduction to ammonium using a porous copper electrode in an electrochemical flow cell. *J. Electroanal. Chem.* **2014**, 727, 148-153.
21. Bouzek, K.; Paidar, M.; Sadílková, A.; Bergmann, H., Electrochemical reduction of nitrate in weakly alkaline solutions. *J. Appl. Electrochem.* **2001**, 31 (11), 1185-1193.
22. Reyter, D., Electrochemical Reduction of Nitrate. In *Encyclopedia of Applied Electrochemistry*, Kreysa, G.; Ota, K.-i.; Savinell, R. F., Eds. Springer New York: New York, NY, 2014; pp 585-593.

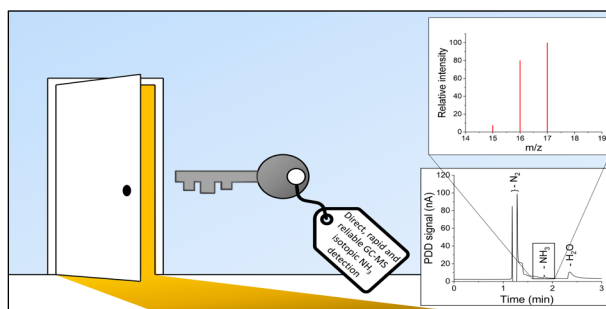


---

# Operando isotope selective ammonia quantification in nitrogen reduction studies via gas chromatography-mass spectrometry

# 3

Rapid advances in electrocatalytic ammonia synthesis are impeded by laborious detection methods commonly used in the field and by constant risk of external contaminations, which generates misleading false positives. We developed a facile real-time GC-MS method for sensitive isotope  $\text{NH}_3$  quantification, requiring no external sample manipulations. This method ensures high detection reliability paramount to accelerate (electro-)catalyst screening.





### 3.1 Introduction

The electrochemical conversion of  $\text{N}_2$  to  $\text{NH}_3$  involves, among other challenges,<sup>1, 2</sup> the arduous activation and stepwise hydrogenation of the N-N triple bond ( $941 \text{ kJ mol}^{-1}$ ) and the competition with the kinetically more favoured hydrogen evolution reaction (HER). This results in sluggish ammonia production rates (usually of the order of  $10^{-10} \text{ mol}_{\text{NH}_3} \text{ cm}^{-2} \text{ s}^{-1}$ ) and poor faradaic efficiency (FE) around 10%.<sup>3</sup> Values that are still far from the commercially relevant threshold of  $10^{-6} \text{ mol}_{\text{NH}_3} \text{ cm}^{-2} \text{ s}^{-1}$  at 90% FE,<sup>4</sup> thus revealing the relatively low maturity of current electrochemical ammonia synthesis technology and highlighting the urgent need for faster electro-catalyst development.

In recent years, the field of electrochemical nitrogen reduction reaction (NRR) to ammonia has witnessed an increasing number of published scientific reports that have been later proven to be false positives, causing mispending of time and resources in pursuing misleading results.<sup>5, 6</sup> As such, due to the limited amount of ammonia produced in typical electrocatalytic experiments, rigorous protocols must be followed to categorically exclude false positive results that might arise from extraneous  $\text{NH}_3$  contaminations or from labile nitrogen-containing compounds<sup>7-12</sup> (e.g.  $\text{NO}_x$ ). Recognised sources of contaminations in nitrogen reduction experiments include: carrier gas<sup>8</sup>, catalyst material<sup>13, 14</sup>, electrolyte<sup>15</sup>, membrane<sup>16</sup>, human breath<sup>17</sup>, ambient air<sup>18</sup> and laboratory ware<sup>19</sup>. Consequently, considerable effort and time are constantly dedicated to perform multiple control measurements and careful background quantifications. Reported ammonia synthesis results must include blank tests under argon atmosphere, under purified dinitrogen in open circuit, as well as electroreduction of purified  $^{15}\text{N}_2$  nitrogen gas. The purification is necessary to remove any  $^{14/15}\text{NH}_3$  or  $^{14/15}\text{NO}_x$  from the feed gasses. The  $^{15}\text{NH}_3$  produced from  $^{15}\text{N}_2$ , when reported over time and in quantitative agreement with the ammonia obtained with  $^{14}\text{N}_2$ , represents the ultimate validation to confirm the dinitrogen reduction to ammonia. Therefore, reliable and rapid detection methods, capable of quantitative discrimination of  $\text{NH}_3$  isotopologues, are paramount for high throughput catalyst testing and the advancement of this research field.

Conventional spectrophotometric techniques, like the Berthelot method, are not able to discriminate ammonium isotopes, and suffer from serious interferences from solvents and other species present in solution, extensive sample manipulation and instability of derivatives.

Recently, other analytical methods have been proposed with the aim to overcome the limitations of spectrophotometric ammonia detection;<sup>20, 21</sup> however, only nuclear magnetic resonance (NMR) and ultrahigh performance liquid chromatography-mass spectrometry (UPLC-MS) techniques allow selective detection of  $^{15}\text{NH}_3$  in labeling experiments.<sup>22, 23</sup>

Quantitative  $^1\text{H}$  NMR is by far the most widely used isotope-sensitive technique for  $\text{NH}_3$  detection.<sup>24</sup> Ammonia is detected in its acidified form, i.e. ammonium in solution ( $\text{NH}_4^+$ ), and isotopic discrimination is based on the different nuclear spin of  $^{14}\text{NH}_4^+$  and  $^{15}\text{NH}_4^+$ , which interacts with the four nearby protons yielding respectively a triplet and a doublet in the proton NMR spectrum. With this technique, Nielander et al. reached high sensitivity ( $1\ \mu\text{M}\ \text{NH}_4^+$ ) with a state of the art cryoprobe equipped 900 MHz NMR spectrometer, but at the expense of a prohibitive data acquisition time of about one hour.<sup>22</sup> However, a practical detection limit of about  $10\ \mu\text{M}$  has been reported for more accessible NMR spectrometers with magnetic fields ranging from 300 MHz to 400 MHz.<sup>22, 25, 26</sup> Alternatively, UPLC-MS offers the advantage of a reduced acquisition time. However, this method relies on a chemical derivatization reaction of ammonia with dansyl chloride, which is susceptible to variations in pH.

Despite being powerful analytical methods, both these isotope-sensitive techniques are indirect, via acid traps or chemical derivatization, requiring different degrees of sample manipulation, and characterised by time-consuming procedures. Each step in the preparation of the analyte solution required for NMR, or ammonia derivatization with dansyl chloride, extends the overall analysis time and it represents a potential source of contamination and external errors. Real-time data acquisition is prohibitive and unpractical. Moreover, NMR and UPLC-MS measure the concentration of ammonia present in the electrolyte. As such, extensive reaction time is required to accumulate sufficient ammonia to reach the lower limit of quantification (LOQ), above possible background contaminations, which also results in a larger consumption of expensive  $^{15}\text{N}_2$  gas ( $>500\text{€}/\text{L}$ ) during isotope labeling experiments. A single experiment can require up to several hours for reliable multiple point measurements (Appendix A.3), representing one of the main bottlenecks in current research on electrocatalytic dinitrogen reduction. A direct gas phase  $\text{NH}_3$  detection, able to distinguish  $^{14}\text{NH}_3$  from  $^{15}\text{NH}_3$ , overcomes such limitations; moreover, it becomes particularly relevant when testing high current density

electrochemical devices, such as gas diffusion electrodes, where the product of the reaction evolves in the gas stream.<sup>27-29</sup>

In this communication, we report a gas chromatography-mass spectrometry (GC-MS) method for quantitative isotope-sensitive ammonia detection in real-time and without any external sample manipulation, aiming to boost catalyst screening in NRR. Ammonia is detected directly in the gas phase, with less than 2 min chromatographic elution time, by continuous sampling of the electrochemical cell headspace and regardless of the electrolyte nature.<sup>30</sup> The proposed GC-MS method can quantify  $^{15}\text{NH}_3/^{14}\text{NH}_3$ , down to 1 ppm in the gas phase, and simultaneously detect other gaseous species, giving a complete set of relevant information to better assess reaction selectivity and the presence of contaminants. We further compare the results obtained from GC-MS with those from  $^1\text{H}$  NMR measurements for the same mixed  $^{15}\text{N}$  and  $^{14}\text{N}$  ammonia solution, confirming the consistent quantification of mixed ammonia isotope samples with the two methods.

## 3.2 Experimental

A simplified representation of the presented GC-MS system is shown in **Figure 3.1**. The sample is first introduced in a switching multiport VICI Valco diaphragm valve, kept at a constant temperature of 80°C. A sample loop of 500  $\mu\text{L}$  is filled with the analyte and then, at the moment of the injection, transported with a purified He carrier gas through two Select Low Ammonia (Agilent) capillary columns. Temperature and pressure profiles are provided in **Figure 3.2**. This ensures the best water/ammonia separation and an optimal peak shape. Once eluted out of the chromatographic column, the sample is partitioned between the pulse discharge detector (PDD) and the single quadrupole mass spectrometer (ISQ) via two restriction lines of one meter each and with internal diameter (ID) of 0.25 mm and 0.15 mm, respectively. Importantly, all the surfaces in contact with the analyte are inert or carefully passivated with inert coating (SilcoNert® 2000) to minimize any possible ammonia physisorption. The system was assembled by Interscience BV (Breda, The Netherlands).

The concentration of  $^{14}\text{NH}_3$  and  $^{15}\text{NH}_3$  in solution was quantified using an  $^1\text{H}$  NMR method with absolute quantification as previously described.<sup>25</sup> This method allows for quantification of  $^{14}\text{NH}_3$  and  $^{15}\text{NH}_3$  without requiring a calibration curve because the

interscan delay is sufficiently long ( $>5T_1$ ) to allow full relaxation of the analyte and the internal standard. To prepare the NMR sample, 510  $\mu\text{L}$  sample solution, 45  $\mu\text{L}$  2M sulfuric acid (freshly prepared) and 45  $\mu\text{L}$  detection solution were added to an NMR tube and stirred using a vortex mixer. The detection solution consists of 3.21 mM maleic acid (MA), 12.86 mM gadolinium nitrate hexahydrate diluted in DMSO- $d_6$ . Maleic acid ( $\geq 99\%$ ) and  $\text{H}_2\text{SO}_4$  ( $\geq 99.999\%$ ) were obtained from Sigma Aldrich. Gadolinium(III) nitrate hexahydrate (99.9%) was obtained from Fisher Scientific. DMSO- $d_6$  (99.9% D, 0.03 % V/V Tetramethylsilan) was obtained from Cambridge Isotope Laboratories. Ultrapure water was produced with a Milli-Q Advantage A10 water purification system (resistivity: 18.2  $\text{M}\Omega$  at  $25^\circ\text{C}$ ).  $^1\text{H}$  NMR spectra were acquired using a 400 MHz Fourier transform NMR spectrometer equipped with an autosampler and an autotunable, temperature regulated Agilent OneNMR room temperature probe. The temperature was set to  $25^\circ\text{C}$  and the receiver gain was optimized automatically. The excitation sculpting pulse sequence “waterES” was used to suppress the resonance of water during acquisition. The “waterES” pulse sequence has the following structure: waterES: d1-P90-G1-S180-P180-G1-G2-S180-P180-G2-aq; where, G1,G2 are z-gradients of different strengths, P90, P180 are hard pulses and S180 is a selective  $180^\circ$  pulse. The acquisition parameter were: 0.75 s acquisition time, 0.05 s recycle delay and 1024 number of scans. The data was processed with the software package MestReNova (version: 12.0.1-20560) using the automated tools available with this software. Unless otherwise noted an apodization of 4 Hz was applied followed by phasing and baseline correction. The peaks of  $\text{NH}_4^+$  (t/d  $\approx 6.9$  ppm, 4H) and MA (s,  $\approx 6.21$  ppm, 2H) were integrated using the line fitting tool (Lorentzian fit). The integrals of the  $^{14}\text{NH}_4^+$  triplets (or  $^{15}\text{NH}_4^+$  doublet) were added together to calculate the total  $^{14}\text{NH}_4^+$  (or  $^{15}\text{NH}_4^+$ ) integral ( $I_{\text{NH}_4^+}$ ). The concentration of  $\text{NH}_4^+$  was calculated with absolute quantification, from the ratio of the integral of  $\text{NH}_4^+$  and MA ( $I_{\text{std}}$ ), according to equation 3.1.

$$c_{\text{NH}_4^+} = \frac{I_{\text{NH}_4^+}}{I_{\text{std}}} \frac{N_{\text{std}}}{N_{\text{NH}_4^+}} c_{\text{std}} \quad (3.1)$$

where I, N and C are respectively the integral area, number of nuclei and concentration of  $\text{NH}_4^+$  and internal standard maleic acid, respectively.

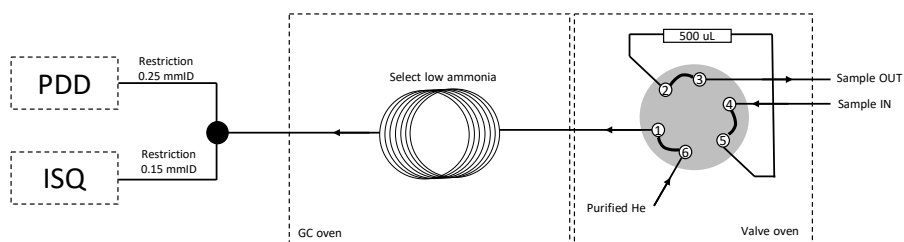


**Figure 3.1** Simplified GC-MS layout.

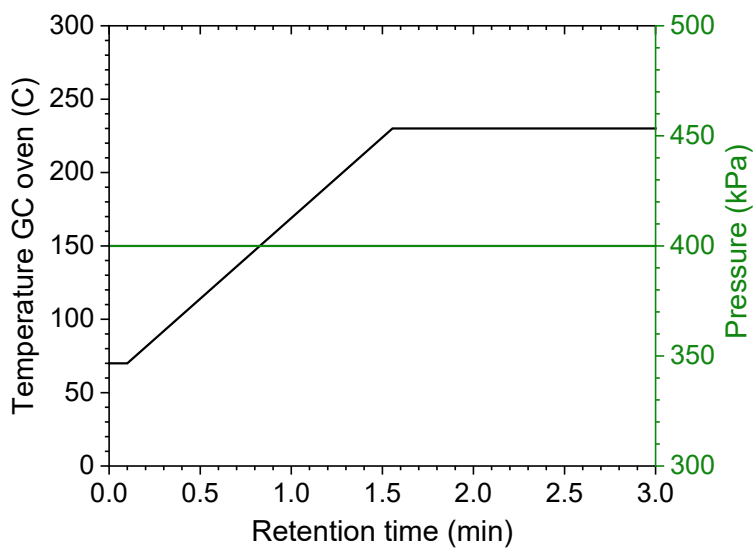


**Figure 3.2** GC oven temperature (black) and He carrier gas pressure (green) settings as function of retention time.

### 3.3 Results and discussion

Mass spectrometry is a widely used approach in real-time trace gas analysis, capable of detecting multiple species even at ppb concentration levels.<sup>31</sup> In a mass spectrometer, the ionization source converts the incoming molecules in detectable charged fragments. Ions with different mass-to-charge ( $m/z$ ) ratio are then separated by the mass analyser and measured by the detector, thus allowing isotopic discrimination. The ionised fragments of a molecule produce a distinctive pattern in the  $m/z$  spectrum, which can be used for the identification of complex mixtures. Ammonia detection by MS at low concentration is notoriously challenging, due to the overlapping  $m/z$  ratios of water and ammonia ionised fragments. Consequently, even small variations of the water background in the system impede reliable ammonia quantification. To circumvent this issue, we combined chromatographic separation with mass spectrometry. With the proposed system, aliquots of the gaseous analyte are directly collected from the reactor headspace by flowing a carrier gas, i.e. Ar,  $^{14}\text{N}_2$  or  $^{15}\text{N}_2$ , avoiding any external sample manipulations. The ammonia concentration in equilibrium in the gas phase is strongly correlated to the ammonia present in the electrolyte, allowing a complete quantification of the produced  $\text{NH}_3$  in both liquid and gas phase.<sup>21</sup> A small sample volume (500  $\mu\text{L}$ ) is then automatically injected into the GC column, via a set of switching diaphragm valves (**Figure 3.1**). The Agilent Select Low Ammonia column, with suitable temperature and pressure settings (**Figure 3.2**), offers adequate separation between ammonia and water. The two components of interest are rapidly eluted at different retention times and clearly discernible from the chromatographs in **Figure 3.3**. Once eluted from the GC column, the analyte is partitioned between a pulse discharge detector (PDD) and the single quadrupole mass spectrometer (ISQ<sup>TM</sup> from Thermo Fisher Scientific), which simultaneously analyse the sample with matching retention time. Therefore, a mass spectrum is assigned to each peak in the chromatograph (**Figure 3.3**). The optimisation of the split ratio of the analyte between the PDD and the mass spectrometer is a key aspect affecting the sensitivity of each detector. Restriction lines of suitable internal diameter and length were used to adjust the split ratio. In the present work, two 1 m long capillary lines of 0.15 mm and 0.25 mm internal diameter were connected to the MS and the PDD respectively.

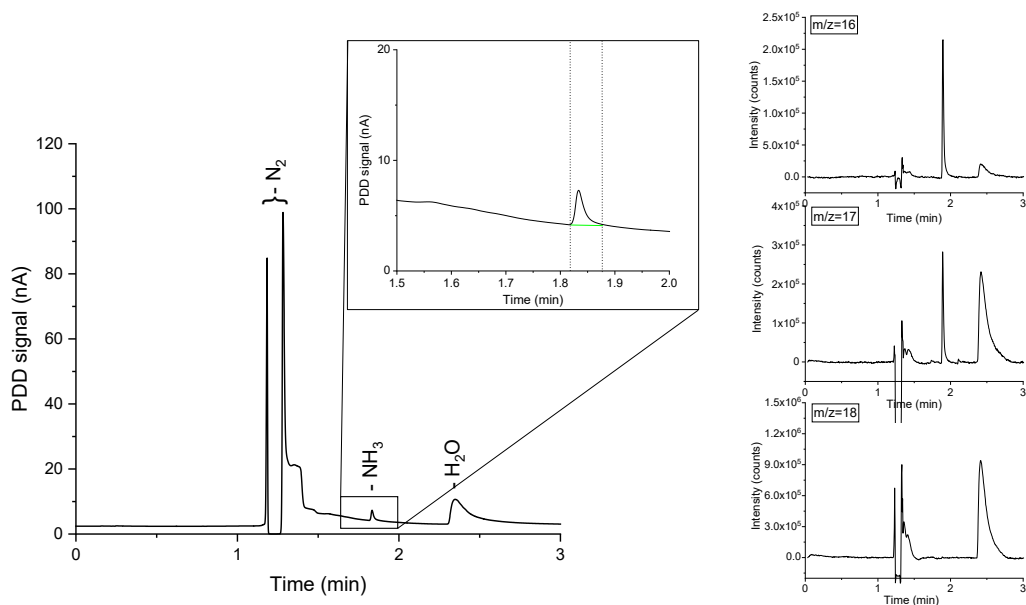


**Figure 3.3** GC oven temperature (black) and He carrier gas pressure (green) settings as function of retention time.

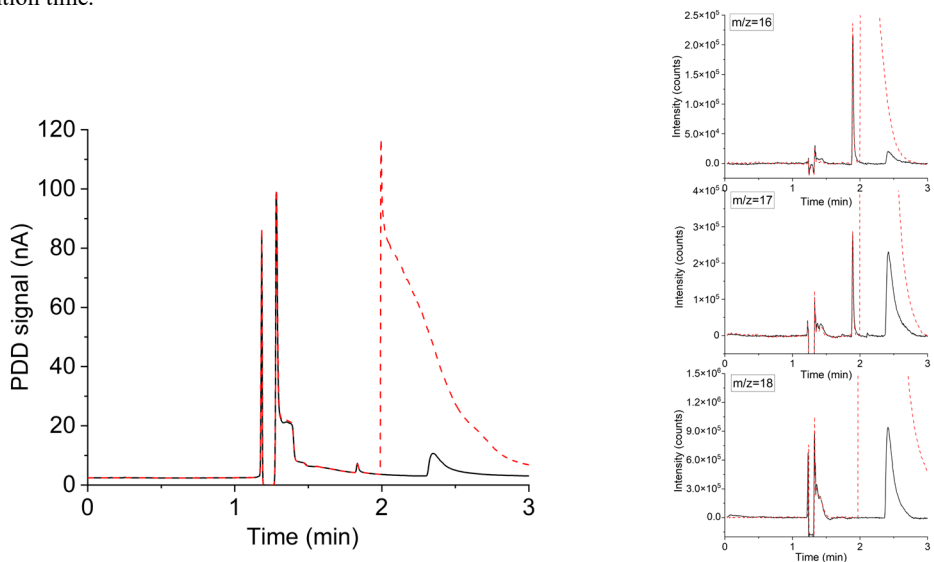


**Figure 3.4** Comparison of two GC-MS measurements of 13.8 ppm of  $NH_3$  in nitrogen, connected directly to the GC-MS (black) and feed into the headspace of a sealed vial containing Milli-Q water prior to injection to the GC-MS (red). On the left, the full chromatograph. On the right, the MS signal corresponding to  $m/z$  18, 17, 16. The significant increase in the water content of the analysed gas sample does not influence the ammonia quantification.

This configuration ensures a MS detection limit of 1 ppm of ammonia in the gas phase, allowing real time quantification of reaction rates down to a lower limit of  $10^{-13} \text{ mol cm}^{-2} \text{ s}^{-1}$  (assuming  $1 \text{ cm}^2$  catalyst area and a constant carrier gas flowrate of  $1 \text{ mL min}^{-1}$ ). This detection range is already relevant for studies on nitrogen reduction reaction. However, users have the option to tune to a large extent the ratio of MS and PDD flows to achieve even higher sensitivity either on the MS or the PDD. Compared to previous ammonia detection methods, the presented GC-MS method can directly and simultaneously measure other species in the analyte with the MS detector or with dedicated extra channels usually installed in GC instruments (e.g. flame ionization detector, thermal conductivity detector, etc.). The advantage of a single analytical method that is not exclusively ammonia sensitive allows researchers to directly assess reaction selectivity by measuring reaction by-products, as well as the presence of gaseous/volatile contaminants in the experimental setup. For instance, gaseous  $\text{NO}_x$  do not suffer from severe overlapping  $m/z$  fragments with other species commonly present in electrochemical nitrogen reduction experiments. Therefore  $\text{NO}_x$  could be potentially discriminated by their characteristic mass spectrum, without requiring a strict chromatographic separation.

The instrument calibration was conducted by carefully diluting gaseous  $\text{NH}_3$  from certified calibration gas cylinders, with starting concentrations of 13.8 ppm and 2.2 ppm in  $\text{N}_2$ . Ammonia detection is confirmed by the appearance of a peak in the chromatograph at a retention time of 1.83 min and separated from the water vapour present in the sample, which is eluted at about 2.30 min, as shown in **Figure 3.3**. The electron ionization mass spectrum at the corresponding retention time validates the presence of ammonia with two main  $m/z$  fragments, 17 and 16, with relative intensities of 100 % and 80.1 % respectively (**Table A.3.2**).<sup>32</sup> On the other hand, the ionization of water generates fragments at  $m/z$  equal to 17 (21.2 %) and 18 (100 %) at 2.30 min. A constant background of the  $m/z$  18 and 17 at the  $\text{NH}_3$  retention time (1.83 min) clearly indicates the absence of water interferences in the ammonia quantification (**Figure 3.3** and **Figure 3.4**). The integrated MS signal of both  $m/z$  ratio 16 and 17 at ammonia retention time shows a linear behaviour in the range 1 ppm to 13.8 ppm (**Figure 3.5** and **Table A.3.1**). As such, mass-sensitive ammonia detection can be achieved accurately with a coupled GC-MS, even in the presence of water vapour (**Figure 3.4** and **Figure A.3.1-A.3.3**), resolving the challenge of overlapping water/ammonia ionization fragments encountered in mass spectrometers alone.



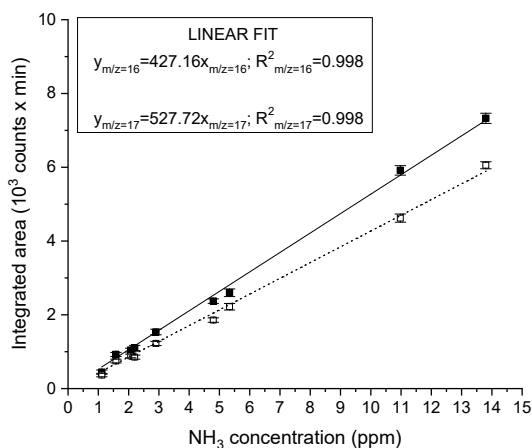


**Figure 3.5** Ammonia calibration based on the integrated MS signal at  $m/z$  17 (closed symbol) and 16 (open symbol), at 1.83 elution time. The calibration was carried out by dilution of a 13.8 ppm or 2.2 ppm certified NH<sub>3</sub> calibration gases in nitrogen with pure N<sub>2</sub>.

N-labeled control experiments in the field electrochemical ammonia synthesis require analytical methods to quantitatively discriminate between <sup>15</sup>N and <sup>14</sup>N ammonia. To demonstrate the capability of the presented GC-MS method in an environment comparable to a NRR experiment in aqueous electrolytes and in the presence of both isotopologues of NH<sub>3</sub>, we prepared a solution by mixing 28% <sup>14</sup>N (BASF) and 3M <sup>15</sup>N (Isotec, 98+ % <sup>15</sup>N) ammonia aqueous solutions, to achieve a final <sup>14</sup>NH<sub>3</sub>:<sup>15</sup>NH<sub>3</sub> concentration of 0.21:0.68 mM. This mixed ammonia solution was then enclosed in a sealed vial equipped with a gas inlet and outlet, where 2.5 mL min<sup>-1</sup> of N<sub>2</sub> (6N) were flown at the headspace of the vial (**Figure 3.6a**). The gas outlet was directly connected to the GC-MS. The chromatograph corresponding to the PDD detector shows only a single NH<sub>3</sub> peak (**Figure 3.6b**); therefore it is unable to distinguish between the ammonia derived from the two nitrogen isotopes. Yet, the contributions from <sup>15</sup>NH<sub>3</sub> and <sup>14</sup>NH<sub>3</sub> can be determined with the MS detector connected in parallel (**Figure 3.6c**). The electron ionization mass spectrum of <sup>15</sup>NH<sub>3</sub> is characterised by three main contributions at  $m/z$  18, 17 and 16, with relative intensities of 100, 80.1 and 7.5 % respectively (**Table A.3.2** and **Figure A.3.1**).<sup>32</sup> Therefore, <sup>15</sup>N and <sup>14</sup>N ammonia can be quantified from the integrated intensities corresponding to their ionised fragments (**Figure 3.6e** and **Table A.3.3**), as reported in the calculations available in the

Appendix A.3 (equations A.3.2-A.3.5). As such, the  $^{15}\text{NH}_3/^{14}\text{NH}_3$  ratio resulting from direct headspace analysis via GC-MS is equal to  $3.30 \pm 0.06$ , which is in close agreement with the  $^1\text{H}$  NMR analysis of an aliquot of the same solution ( $3.25 \pm 0.04$ , **Figure 3.6d**). The details of the NMR method used in this contribution have been presented elsewhere<sup>25</sup> and in the Appendix A.3 (**Table A.3.4**) together with the data processing of **Figure 3.6d**.

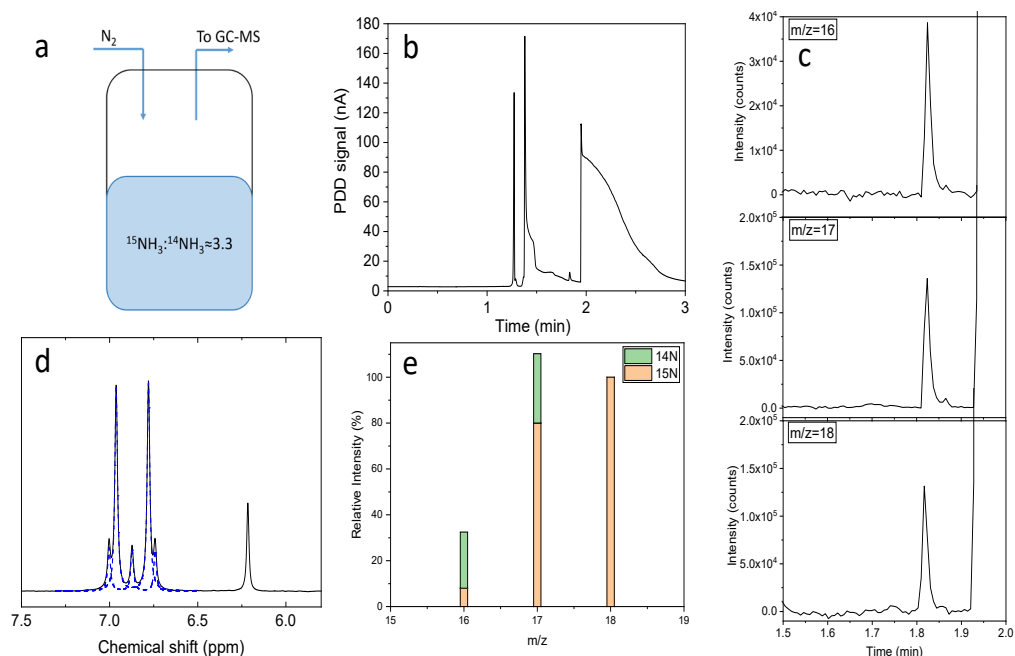


**Figure 3.6** (a) Schematic representation of headspace measurement of a  $^{15}\text{NH}_3/^{14}\text{NH}_3$  (0.21/0.68 mM) aqueous solution. (b) Full chromatograph. (c) Closed up, around the ammonia elution time (1.83 min) of the MS signal related to the  $m/z$  18, 17 and 16. (d)  $^1\text{H}$  NMR measurement of the  $^{15}\text{NH}_3/^{14}\text{NH}_3$  aqueous solution, in agreement with the GC-MS quantification. Line fitting is shown as blue dotted line. (e) Relative intensity of the integrated  $m/z$  at 1.83 min.

### 3.4 Conclusions

The aim of this study is to present an isotope sensitive method for the determination of  $\text{NH}_3$  at low concentration level, typically encountered in electrochemical ammonia synthesis applications. In this fast-growing field, the detection of  $\text{NH}_3$  is of primary relevance due to the raised concerns over the need for more reliable experiments. Compared with previously reported  $\text{NH}_3$  detection methods, which rely on extensive  $\text{NH}_3$  accumulation in a liquid medium (electrolyte or acid trap) and subsequent indirect quantification, the presented GC-MS method detects ammonia in less than 2 minutes directly from the gas phase with 1 ppm detection limit (equals to rates as low as  $10^{-13} \text{ mol}_{\text{NH}_3} \text{ cm}^{-2} \text{ s}^{-1}$  at a carrier gas flowrate of  $1 \text{ mL min}^{-1}$ ). The proposed approach requires no external sample manipulations, resulting in the lowest risk of external contaminations and reduced analysis time. GC-MS detection is mass sensitive and therefore suitable for  $^{15}\text{N}$ -labelled control experiments. As such, the direct, fast and sensitive ammonia quantification reduces the usage of expensive  $^{15}\text{N}_2$ , cutting down the, sometimes prohibitive, experimental costs both in terms of times and reagents. Contrary to conventional MS detection, the accurate quantification of a mixture of  $^{14}\text{NH}_3$  and  $^{15}\text{NH}_3$  with GC-MS is not influenced by background water, which is eluted at a different time. Importantly, this gas analysis method is not exclusively ammonia sensitive and therefore it can also provide additional information on by-products and level of contaminants.

In summary, we provide a fast and highly reliable mass and isotope sensitive  $\text{NH}_3$  detection method with unique capabilities. This approach accelerates the testing and discovery of new active catalysts for NRR and therefore it should become a standard method essential for publications involving ammonia synthesis.

## Appendix A.3

### Estimated experimental time for cumulative detection methods

The required minimum time for an electrochemical nitrogen reduction reaction (NRR) experiment can be defined as the time required to reach the limit of detection of the analytical method used to quantify ammonia.  $\text{NH}_3$  detection methods, as Berthelot method,  $^1\text{H}$  NMR or UPLC-MS, rely on extensive  $\text{NH}_3$  accumulation in a liquid medium (electrolyte or external acid trap).

As today, most reported ammonia electrochemical synthesis rate ( $r_{\text{NH}_3}$ ) are on the order of  $10^{-10} \text{ mol}_{\text{NH}_3} \text{ cm}^{-2} \text{ s}^{-1}$ ,<sup>3</sup> and electrochemical H-cells have a typical catalyst area to electrolyte volume ratio ( $\frac{A}{V}$ ) of 0.02-0.04  $\text{cm}^2 \text{ mL}^{-1}$ . Therefore, considering a practical limit of quantification (LOQ) of 10  $\mu\text{M}$ ,<sup>22</sup> the minimum time strictly necessary for a NRR experiment ( $t_{\text{LOQ}}$ ) to reach such limit would be between 0.7 and 1.4 h, as calculated from equation A.3.1. Additional time is then required for sampling, analyte preparation and analysis for multiple data points. Therefore, a single NRR experiment based on indirect cumulative detection methods can take several hours.

$$t_{\text{LOQ}} = \frac{\text{LOQ}}{r_{\text{NH}_3} \times \frac{A}{V}} \quad (\text{A.3.1})$$

## Ammonia calibration measurements

**Table A.3.1** Data set of integrated MS peak area (in  $10^3$  counts x min), average and standard deviation (STD) of mass-to-charge ratio 16 and 17 used to build the calibration curve of **Figure 3.5**.

Injection	1.02		1.58		2.07		2.20		2.91		4.80		5.33		10.98		13.80	
	m/z=17	m/z=16	m/z=17	m/z=16	m/z=17	m/z=16	m/z=17	m/z=16	m/z=17	m/z=16	m/z=17	m/z=16	m/z=17	m/z=16	m/z=17	m/z=16	m/z=17	m/z=16
1	0.5151	0.4173	0.8614	0.6752	1.0232	0.8671	0.9905	0.7831	1.4987	1.1971	2.3667	1.8549	2.6616	2.2712	6.0567	4.7315	7.1335	5.9952
2	0.4918	0.2998	1.0098	0.8801	1.0784	0.9503	1.1647	0.9026	1.6058	1.2825	2.3656	1.856	2.7801	2.3808	5.9546	4.5521	7.1356	5.8901
3	0.3401	0.2603	0.9248	0.7373	0.9938	0.8497	1.0825	0.8385	1.4853	1.1666	2.4330	1.9978	2.5300	2.2380	6.1308	4.7897	7.6352	6.0109
4	0.3677	0.3993	0.9384	0.7576	1.122	0.9138	1.0667	0.8605	1.4140	1.1262	2.3390	1.8539	2.4715	2.1899	5.6930	4.4488	7.3728	6.0930
5	0.4399	0.3669	0.9529	0.7200	1.002	0.8423	1.1948	0.9220	1.4628	1.1863	2.2645	1.7746	2.4380	2.0834	5.8011	4.5390	7.3083	6.0388
6	0.5059	0.4273	1.0150	0.8019	0.9796	0.8895	1.1998	0.9001	1.4134	1.1206	2.3348	1.8384	2.5988	2.2299	5.8816	4.5911	7.2882	6.2093
7	0.3985	0.3487	0.8835	0.7195	1.0764	0.9413	0.9984	0.7395	1.6755	1.3400	2.4714	1.91084	2.6001	2.2223	5.9064	4.7146	7.2499	6.1071
8	0.4125	0.3284	0.9044	0.7181	1.0552	0.8328	1.1000	0.8527	1.5300	1.2343	2.3464	1.8059	2.4765	2.1408	5.8939	4.5967	7.1981	5.9489
9	0.4459	0.3627	0.9118	0.7306	1.1125	0.9059	1.1084	0.8795	1.5446	1.2411	2.4215	1.8466					7.4258	6.1070
10					0.9921	0.8106			1.5445	1.2684	2.4070	1.8673					7.5660	6.2535
11									1.4893	1.1951							7.2374	5.9150
12									1.5819	1.2649							7.3217	6.1320
13									1.6245	1.2955							7.4380	6.0713
14									1.5881	1.2344							7.3047	6.0369
15																	7.2964	6.0305
Average	0.4353	0.3567	0.9336	0.7489	1.0435	0.8803	1.1006	0.8532	1.5335	1.2252	2.3750	1.8601	2.5696	2.2195	5.9148	4.6329	7.3274	6.0560
STD	0.0579	0.0316	0.0494	0.0564	0.0497	0.0449	0.0722	0.0560	0.0750	0.0613	0.0565	0.0570	0.1071	0.0827	0.1285	0.1039	0.1376	0.0969

## Additional GC-MS measurements and calculations

To further clarify the peak identification and ammonia quantification, we hereby report a series of measurements performed under the following different conditions:  $^{14}\text{NH}_3$  alone, from certified calibration gas in dry and humidified conditions (**Figure 3.4**);  $^{15}\text{NH}_3$  alone, from aqueous solution headspace (**Figure A.3.1**);  $^{14}\text{NH}_3/^{15}\text{NH}_3$  mixture from aqueous solution headspace (**Figure 3.6**); ultrapure water headspace without ammonia (**Figure A.3.2**) and direct analysis of purified (Agilent OT3-4 filter)  $\text{N}_2$  gas (**Figure A.3.3**).

When present in the analyte, ammonia ( $^{14}\text{N}$  or  $^{15}\text{N}$ ) is detected in the chromatograph as a peak with a retention time of 1.83 min, in the absence of interferences from water vapour, which is eluted at a later chromatographic elution time of about 2 min. Similarly, excellent water/ammonia separation is established at the MS detector for the  $m/z$  16, 17 and 18. The outsized amount of water vapour (compared to typical ppm levels of ammonia produced in electrochemical nitrogen reduction experiments) carried during sampling of aqueous headspace is affected by several factors and therefore can largely vary over time, making unfeasible to reliably quantify  $\text{NH}_3$  without a proper water/ammonia separation (e.g. in MS detectors without chromatographic separation).

When both  $^{14}\text{NH}_3$  and  $^{15}\text{NH}_3$  are present in the analyte, the contributions from  $^{14}\text{N}$  and  $^{15}\text{N}$  ammonia are calculated from the respective electron ionization mass spectra (**Table A.3.2**) and the integrated peak areas of  $m/z$  16, 17 and 18 (**Table A.3.3**), using the equations A.3.2-A.3.4. The estimated error based on the difference between the measured and calculated peak area at  $m/z=16$  is about 1.6% (equation A.3.5).

**Table A.3.2** The electron ionization mass spectrum of  $^{14}\text{N}$  and  $^{15}\text{N}$  ammonia. The relative intensities of the corresponding fragments are reported between brackets.

	$\text{NH}_3^+$ (100%)	$\text{NH}_2^+$ (80.1%)	$\text{NH}^+$ (7.5%)	$\text{N}^+$ (2.2%)
$m/z$ [ $^{14}\text{NH}_3$ ]	17	16	15	14
$m/z$ [ $^{15}\text{NH}_3$ ]	18	17	16	15

**Table A.3.3** Integrated peak area of the  $m/z$  equal to 16, 17 and 18 at the ammonia elution time (1.83 min) from **Figure 3.6c**. The data refers to the GC-MS analysis of the headspace of a  $^{15}\text{NH}_3/^{14}\text{NH}_3$  (0.21/0.68 mM) aqueous solution in a sealed vial, with a  $\text{N}_2$  gas flow of  $2.5 \text{ mL min}^{-1}$ .

Retention time (min)	Peak area $m/z=16$ (counts*min)	Peak area $m/z=17$ (counts*min)	Peak area $m/z=18$ (counts*min)
1.83	652.563	2305.459	2090.715

$$^{15}\text{NH}_3 = (\text{Peak area } m/z_{18}) \times 0.8 \times 527.72 \quad (\text{A.3.2})$$

$$^{14}\text{NH}_3 = [(\text{Peak area } m/z_{17}) - (\text{Peak area } m/z_{18}) \times 0.8] \times 527.72 = {}^{14}\text{N } m/z_{17} \times 527.72 \quad (\text{A.3.3})$$

$$\begin{aligned} & (\text{Peak area } m/z_{16})^{\text{calc.}} \\ &= [(\text{Peak area } m/z_{18}) \times 0.075] + \left[ \left( {}^{14}\text{N } m/z_{17} \right) \times 0.8 \right] \end{aligned} \quad (\text{A.3.4})$$

$$\begin{aligned} \text{Error (\%)} &= \frac{[(\text{Peak area } m/z_{16})^{\text{measured}} - (\text{Peak area } m/z_{16})^{\text{calc.}}]}{(\text{Peak area } m/z_{16})^{\text{measured}}} \\ &\quad \times 100 \end{aligned} \quad (\text{A.3.5})$$

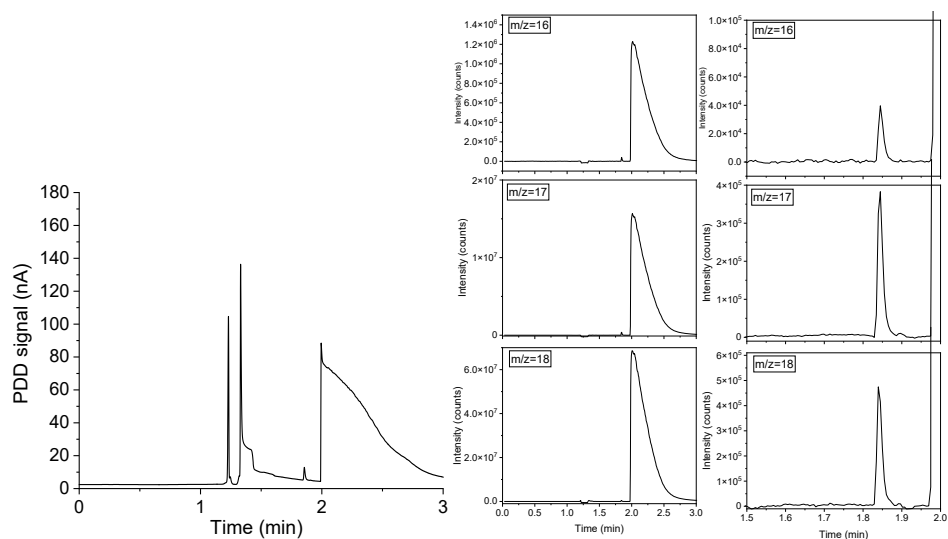


**Figure A.3.1** GC-MS analysis of the headspace of  $^{15}\text{NH}_3$  ammonia aqueous solution (without  $^{14}\text{NH}_3$ ) in a sealed vial, with a  $\text{N}_2$  gas flow of  $2.5 \text{ mL min}^{-1}$ . On the left, the full chromatograph. In the middle, the MS signal corresponding to  $m/z$  18, 17, 16. On the right, the closed up around the ammonia elution time (1.83 min) of the MS signal corresponding to  $m/z$  18, 17, 16. The integrated peak areas at 1.83 min are respectively 7668.181 ( $m/z=18$ ), 6218.650 ( $m/z=17$ ) and 565.708 ( $m/z=16$ ) counts per minutes, which correspond to the expected relative intensities of the electron ionization mass spectrum of  $^{15}\text{NH}_3$  within measurement error (1.6%).

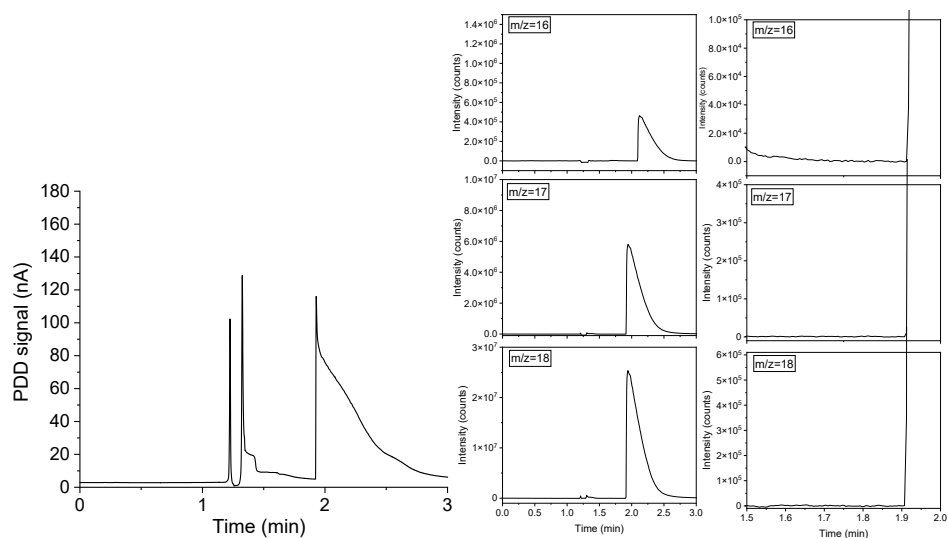


**Figure A.3.2** GC-MS analysis of the headspace of Milli-Q water (without added  $\text{NH}_3$ ) in a sealed vial, with a  $\text{N}_2$  gas flow of  $2.5 \text{ mL min}^{-1}$ . On the left, the full chromatograph. In the middle, the MS signal corresponding to  $m/z$  18, 17, 16. On the right, the closed up around the ammonia elution time (1.83 min) of the MS signal corresponding to  $m/z$  18, 17, 16. The absence of a peak at 1.83 min confirms that no ammonia is present in the analysed sample above the GC-MS detection limit.



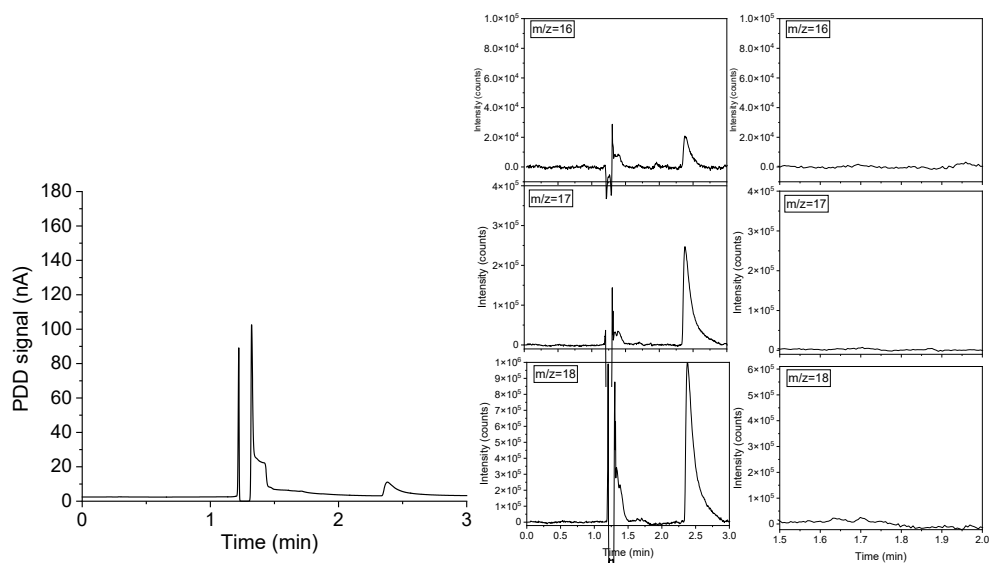


**Figure A.3.3** GC-MS analysis of purified  $\text{N}_2$  gas at  $2.5 \text{ mL min}^{-1}$  directly connected to the instrument inlet. On the left, the full chromatograph. In the middle, the MS signal corresponding to  $m/z$  18, 17, 16. On the right, the closed up around the ammonia elution time (1.83 min) of the MS signal corresponding to  $m/z$  18, 17, 16. The absence of a peak at 1.83 min confirms that no ammonia is present in the analysed sample above the GC-MS detection limit.

**Table A.3.4** Line fitting data of the  $^1\text{H}$  NMR measurement shown in **Figure 3.6d**.

	Chemical shift (ppm)	Intensity (a.u.)	Area (a.u.)	Compound
1	7.003	13.6	1410.11	$^{14}\text{NH}_4^+$
2	6.963	63.9	6113.98	$^{15}\text{NH}_4^+$
3	6.873	13.1	1276.26	$^{14}\text{NH}_4^+$
4	6.780	65.6	6417.14	$^{15}\text{NH}_4^+$
5	6.742	12.9	1170.50	$^{14}\text{NH}_4^+$
6	6.216	27.7	2207.35	$\text{C}_4\text{H}_4\text{O}_4$

## References

1. Singh, A. R.; Rohr, B. A.; Schwalbe, J. A.; Cargnello, M.; Chan, K.; Jaramillo, T. F.; Chorkendorff, I.; Nørskov, J. K., Electrochemical Ammonia Synthesis—The Selectivity Challenge. *ACS Catalysis* **2017**, 7 (1), 706-709.
2. Hu, L.; Xing, Z.; Feng, X., Understanding the Electrocatalytic Interface for Ambient Ammonia Synthesis. *ACS Energy Letters* **2020**, 5 (2), 430-436.
3. Yang, B.; Ding, W.; Zhang, H.; Zhang, S., Recent progress in electrochemical synthesis of ammonia from nitrogen: strategies to improve the catalytic activity and selectivity. *Energy & Environmental Science* **2021**, 14 (2), 672-687.
4. DOE, U. S., *Renewable Energy to Fuels Through Utilization of Energy-Dense Liquids (REFUEL) Program Overview* **2016**.
5. Choi, J.; Du, H.-L.; Nguyen, C. K.; Suryanto, B. H. R.; Simonov, A. N.; MacFarlane, D. R., Electroreduction of Nitrates, Nitrites, and Gaseous Nitrogen Oxides: A Potential Source of Ammonia in Dinitrogen Reduction Studies. *ACS Energy Letters* **2020**, 5 (6), 2095-2097.
6. Licht, S.; Cui, B.; Wang, B.; Li, F.-F.; Lau, J.; Liu, S., Retraction. *Science* **2020**, 369 (6505), 780-780.
7. Andersen, S. Z.; Čolić, V.; Yang, S.; Schwalbe, J. A.; Nielander, A. C.; McEnaney, J. M.; Enemark-Rasmussen, K.; Baker, J. G.; Singh, A. R.; Rohr, B. A.; Statt, M. J.; Blair, S. J.; Mezzavilla, S.; Kibsgaard, J.; Vesborg, P. C. K.; Cargnello, M.; Bent, S. F.; Jaramillo, T. F.; Stephens, I. E. L.; Nørskov, J. K.; Chorkendorff, I., A rigorous electrochemical ammonia synthesis protocol with quantitative isotope measurements. *Nature* **2019**, 570 (7762), 504-508.
8. Choi, J.; Suryanto, B. H. R.; Wang, D.; Du, H.-L.; Hodgetts, R. Y.; Ferrero Vallana, F. M.; MacFarlane, D. R.; Simonov, A. N., Identification and elimination of false positives in electrochemical nitrogen reduction studies. *Nature Communications* **2020**, 11 (1), 5546.
9. Zhao, Y.; Shi, R.; Bian, X.; Zhou, C.; Zhao, Y.; Zhang, S.; Wu, F.; Waterhouse, G. I. N.; Wu, L.-Z.; Tung, C.-H.; Zhang, T., Ammonia Detection Methods in Photocatalytic and Electrocatalytic Experiments: How to Improve the Reliability of NH<sub>3</sub> Production Rates? *Advanced Science* **2019**, 6 (8), 1802109.
10. Zhao, Y.; Wu, F.; Miao, Y.; Zhou, C.; Xu, N.; Shi, R.; Wu, L.-Z.; Tang, J.; Zhang, T., Revealing Ammonia Quantification Minefield in Photo/Electrocatalysis. *Angewandte Chemie International Edition* **2021**, 60 (40), 21728-21731.
11. Tang, C.; Qiao, S.-Z., True or False in Electrochemical Nitrogen Reduction. *Joule* **2019**, 3 (7), 1573-1575.
12. Shahid, U. B.; Chen, Y.; Gu, S.; Li, W.; Shao, M., Electrochemical nitrogen reduction: an intriguing but challenging quest. *Trends in Chemistry* **2022**, 4 (2), 142-156.
13. Chen, Y.; Liu, H.; Ha, N.; Licht, S.; Gu, S.; Li, W., Revealing nitrogen-containing species in commercial catalysts used for ammonia electrosynthesis. *Nature Catalysis* **2020**, 3 (12), 1055-1061.
14. Yu, W.; Buabthong, P.; Read, C. G.; Dalleska, N. F.; Lewis, N. S.; Lewerenz, H.-J.; Gray, H. B.; Brinkert, K., Cathodic NH<sub>4</sub><sup>+</sup> leaching of nitrogen impurities in CoMo thin-film electrodes in aqueous acidic solutions. *Sustainable Energy & Fuels* **2020**, 4 (10), 5080-5087.

15. Li, L.; Tang, C.; Yao, D.; Zheng, Y.; Qiao, S.-Z., Electrochemical Nitrogen Reduction: Identification and Elimination of Contamination in Electrolyte. *ACS Energy Letters* **2019**, 4 (9), 2111-2116.
16. Liu, H.; Zhang, Y.; Luo, J., The removal of inevitable NO<sub>x</sub> species in catalysts and the selection of appropriate membrane for measuring electrocatalytic ammonia synthesis accurately. *Journal of Energy Chemistry* **2020**, 49, 51-58.
17. Turner, C.; Španěl, P.; Smith, D., A longitudinal study of ammonia, acetone and propanol in the exhaled breath of 30 subjects using selected ion flow tube mass spectrometry, SIFT-MS. *Physiological Measurement* **2006**, 27 (4), 321-337.
18. Schlesinger, W. H.; Hartley, A. E., A global budget for atmospheric NH<sub>3</sub>. *Biogeochemistry* **1992**, 15 (3), 191-211.
19. Ishibashi, T.; Himeno, M.; Imaizumi, N.; Maejima, K.; Nakano, S.; Uchida, K.; Yoshida, J.; Nishio, M., NO<sub>x</sub> Contamination in Laboratory Ware and Effect of Countermeasures. *Nitric Oxide* **2000**, 4 (5), 516-525.
20. Lin, Y.-X.; Zhang, S.-N.; Xue, Z.-H.; Zhang, J.-J.; Su, H.; Zhao, T.-J.; Zhai, G.-Y.; Li, X.-H.; Antonietti, M.; Chen, J.-S., Boosting selective nitrogen reduction to ammonia on electron-deficient copper nanoparticles. *Nature Communications* **2019**, 10 (1), 4380.
21. Zaffaroni, R.; Ripepi, D.; Middelkoop, J.; Mulder, F. M., Gas Chromatographic Method for In Situ Ammonia Quantification at Parts per Billion Levels. *ACS Energy Letters* **2020**, 5 (12), 3773-3777.
22. Nielander, A. C.; McEnaney, J. M.; Schwalbe, J. A.; Baker, J. G.; Blair, S. J.; Wang, L.; Pelton, J. G.; Andersen, S. Z.; Enemark-Rasmussen, K.; Čolić, V.; Yang, S.; Bent, S. F.; Cargnello, M.; Kibsgaard, J.; Vesborg, P. C. K.; Chorkendorff, I.; Jaramillo, T. F., A Versatile Method for Ammonia Detection in a Range of Relevant Electrolytes via Direct Nuclear Magnetic Resonance Techniques. *ACS Catalysis* **2019**, 5797-5802.
23. Yu, W.; Lewis, N. S.; Gray, H. B.; Dalleska, N. F., Isotopically Selective Quantification by UPLC-MS of Aqueous Ammonia at Submicromolar Concentrations Using Dansyl Chloride Derivatization. *ACS Energy Letters* **2020**, 5 (5), 1532-1536.
24. As matter of fact, nitrogen has two NMR active nuclei; therefore N NMR could also be used to discriminate <sup>14</sup>NH<sub>3</sub> and <sup>15</sup>NH<sub>3</sub>. However, both <sup>15</sup>N and <sup>14</sup>N NMR are significantly less sensitive than the heteronuclear coupling observed in <sup>1</sup>H NMR, leaving the latter as a better option compared to N NMR.
25. Kolen, M.; Smith, W. A.; Mulder, F. M., Accelerating <sup>1</sup>H NMR Detection of Aqueous Ammonia. *ACS Omega* **2021**, 6 (8), 5698-5704.
26. Hodgetts, R. Y.; Kiryutin, A. S.; Nichols, P.; Du, H.-L.; Bakker, J. M.; Macfarlane, D. R.; Simonov, A. N., Refining Universal Procedures for Ammonium Quantification via Rapid <sup>1</sup>H NMR Analysis for Dinitrogen Reduction Studies. *ACS Energy Letters* **2020**, 5 (3), 736-741.
27. Lazouski, N.; Chung, M.; Williams, K.; Gala, M. L.; Manthiram, K., Non-aqueous gas diffusion electrodes for rapid ammonia synthesis from nitrogen and water-splitting-derived hydrogen. *Nature Catalysis* **2020**, 3 (5), 463-469.
28. Burdyny, T.; Smith, W. A., CO<sub>2</sub> reduction on gas-diffusion electrodes and why catalytic performance must be assessed at commercially-relevant conditions. *Energy & Environmental Science* **2019**, 12 (5), 1442-1453.
29. Ripepi, D.; Zaffaroni, R.; Schreuders, H.; Boshuizen, B.; Mulder, F. M., Ammonia Synthesis at Ambient Conditions via Electrochemical Atomic Hydrogen Permeation. *ACS Energy Letters* **2021**, 3817-3823.

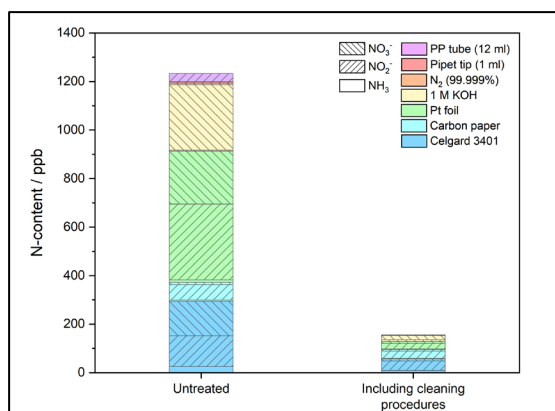
30. The proposed GC-MS method is suitable for quantification of gaseous  $\text{NH}_3$  evolving directly in the gas phase or from an electrolytic cell (with organic, inorganic, aqueous or non-aqueous electrolyte). However, the authors acknowledge that when ammonia is produced directly in the electrolyte this should have a pH above 9. On the other hand, at pH lower than 9 the chemical equilibrium is increasingly shifted towards the formation of ammonium ions ( $\text{NH}_4^+$ ), which will remain in solution requiring a liquid analysis. This limitation could be overcome by externally shifting the pH at the end of the electrochemical experiment.
31. Mowry, C. D.; Jarek, R. L.; Román-Kustas, J.; Telles, A. C.; Pimentel, A. S., Gas Analysis by Mass Spectrometry. In *Materials Characterization*, ASM International: 2019; Vol. 10, p 0.
32. William, E. W., NIST Mass Spectrometry Data Center. In *NIST Chemistry WebBook, NIST Standard Reference Database Number 69*, Linstrom, P. J.; Mallard, W. G., Eds. National Institute of Standards and Technology: Gaithersburg MD, 20899.

# Determination and effective NO<sub>x</sub> and NH<sub>3</sub> removal for reliable electrochemical nitrogen reduction

# 4

Sustainable ammonia production via electrochemical dinitrogen reduction reaction (NRR) could potentially replace the fossil fuel based Haber-Bosch process which is responsible for the emission of large amounts of carbon dioxide in the atmosphere. However, when performing electrocatalytic NRR, a careful control over extraneous N contamination is required to produce reliable studies. In this work, we carried out a systematic investigation on the origin of these contaminations and on the efficacy of multiple removal strategies.

We estimated, based on our conditions, that a typical NRR experiment could have a minimum background level of about 1200 ppb of labile N-species, which can be reduced to roughly 150 ppb with the correct implementation of the recommendations here can provide, ensuring a higher reliability of the results. The insights on the identification and elimination of N contamination facilitate a faster advancement in the field and may provide a benchmark to perform reliable electrochemical NRR studies.



## 4.1 Introduction

Ammonia ( $\text{NH}_3$ ) with an annual production of 178 million tons ranks among the most produced bulk chemical products in the world. Approximately 80% of the ammonia production is used in the fertilizer industry, with an estimated annual growth rate of 3-5% to meet the global demand of fertilizer in the agricultural sector and the increasing world population.<sup>1,2</sup> The majority of the  $\text{NH}_3$  is produced by the century old Haber-Bosch process, wherein elevated temperatures (300-500°C) and pressure (200-300 bar) are required.<sup>3</sup> Not only this is a highly energy intensive process, but additionally the current  $\text{NH}_3$  production has a major negative environmental impact due to the production of fossil-based hydrogen by steam-methane reforming, which is responsible for roughly 1 % of the global greenhouse emissions.<sup>4</sup> To meet the net-zero emissions goal by 2050, established in the latest IPCC report,<sup>5</sup> ammonia must be produced via a sustainable pathway.<sup>6</sup> Direct electrocatalytic synthesis of ammonia from nitrogen and water at mild conditions could potentially offer a carbon free alternative, resilient to intermittent renewable energy generation.<sup>7</sup> When produced entirely from renewables,  $\text{NH}_3$  may be used as green energy vector on a large scale because of its higher energy density (22.5 MJ kg<sup>-1</sup>), hydrogen content (17.7 wt.%) and liquefaction at room temperature and 10 bar, which makes it suitable for transport and long term energy storage.<sup>8</sup>

Despite the large research efforts in nitrogen electroreduction in aqueous electrolytes, current  $\text{NH}_3$  synthesis rates remain extremely low (0.003 – 14 nmol cm<sup>-2</sup> s<sup>-1</sup>),<sup>9</sup> mainly due to the lack of a suitable electrocatalyst and the competition with the hydrogen evolution reaction (HER). Besides, the reliable quantification of these low ammonia yields raised several concerns in the scientific community. In fact, the presence of traces of extraneous N species (such as,  $\text{NH}_3$ ,  $\text{NO}_x$ ,  $\text{N}_2\text{O}$ ,  $\text{NO}_2^-$ ,  $\text{NO}_3^-$  and other labile forms of N), led to an increasing number of reported false positives and non-reproducible results.<sup>9-12</sup> The electrochemical reduction of nitrogen oxide species into ammonia is more facile than the NRR on many transition metals.<sup>13-16</sup> An exception is  $\text{N}_2\text{O}$ , which has been proven to only electro-reduce to  $\text{N}_2$  on several transition metals.<sup>13-16</sup> This implies that  $\text{N}_2\text{O}$  is not a concerning source of impurity for the NRR to  $\text{NH}_3$  as proposed elsewhere,<sup>10, 17</sup> and for this reason will not be considered in the present study.<sup>18</sup> Extraneous nitrogen species were found in multiple sources.  $\text{NO}_3^-$  has been identified as the main sources of contamination in commercial metal

oxide powders,<sup>19</sup> chemically resistant gloves,<sup>20</sup> lab consumables<sup>21</sup> and Li-salt electrolytes.<sup>22</sup> Feed gases are also considered primary sources of extraneous nitrogen contaminations in NRR studies.<sup>9, 23</sup> Traces of <sup>14/15</sup>NH<sub>3</sub> and <sup>14/15</sup>NO<sub>x</sub> (NO<sub>x</sub> is intended as NO and NO<sub>2</sub> throughout the text) in <sup>15</sup>N<sub>2</sub>, <sup>14</sup>N<sub>2</sub> and Ar can result in erroneous conclusion on the electrocatalytic activity.<sup>9, 23-26</sup> Significant amounts of extraneous NH<sub>3</sub> coming from atmospheric air, human breath,<sup>25, 27</sup> Nafion membranes,<sup>25, 28</sup> catalysts and precursors<sup>12, 29-32</sup> can also accidentally be introduced in the experiment.

Strict experimental protocols have been proposed to perform reliable quantification of the NH<sub>3</sub> production by electrochemical reduced N<sub>2</sub>. Such protocols include open circuit voltammetry (OCV) and Ar blank tests,<sup>25</sup> which are now commonly applied methods. Ultimately, expensive <sup>15</sup>N<sub>2</sub>-labelled gas is used to reliably confirm the genuine electroreduction of <sup>15</sup>N<sub>2</sub> to produce, in principle, an unambiguously traceable <sup>15</sup>NH<sub>3</sub>.<sup>25</sup>

To successfully implement these protocols, a proper identification and elimination of these N impurities must be carried out. Different methods were proposed to remove N impurities from membranes,<sup>25, 33, 34</sup> catalyst materials<sup>19, 34</sup> and electrolytes<sup>22</sup>. Strategies to purify the feed gases are based on catalytic reduction or scrubbing. Certified gas purifiers (<1 ppb) are commercially available and already applied in the NRR field.<sup>12, 35-37</sup> An in-house made catalytic filter based on a Cu-Zn-Al oxide mixture was also proven to be successful.<sup>25, 38</sup> Scrubbers are to some extent more economic and are therefore more commonly applied. There are however, large variations in the design, varying from a packed column with alkaline and oxidant mixture,<sup>9</sup> to a glass washing bottle containing an acidic or alkaline solution.<sup>39-41</sup> However, the practical removal efficiency of these purification treatments has not been carefully evaluated yet.

The purpose of this work is to provide a comprehensive identification and quantification of the commonly encountered sources of impurities and to give an overview of which sources requires most attention based on their impact on NRR experiments. By means of sensitive NO<sub>x</sub> and NH<sub>3</sub> *in-line* gas analyzers, we provide a careful quantification of the contaminants present in feed gases and evaluation of gas purifications. Additionally, we analyze the effectiveness of earlier proposed cleaning strategies on commonly used electrochemical cell components, such as membranes, carbon substrates and platinum foils. This work will equip the experimentalist with specific guidelines and tools to perform reliable NRR studies.



## 4.2 Experimental

**Materials.** Ultrapure water (Millipore Milli-Q IQ 7000) was used for cleaning and solution preparation. All the materials were supplied by Sigma Aldrich unless stated otherwise:  $\text{Cu}(\text{NO}_3)_2 \cdot 2.5\text{H}_2\text{O}$  (98%, Alfa Aesar), KOH (99.99% and 85%),  $\text{NaClO}_2$  (25wt% in  $\text{H}_2\text{O}$ ), 1/8" HDPE spheres (McMaster), Hydrophobic frit (19.6 mm x 3.2 mm, Biocomma), isopropanol (98%), anion exchange membrane (Selemion), microporous membrane (Celgard 3401), carbon paper (Alfa Aesar), Pt foil (2.5 cm x 2.5 cm x 0.025 cm, Mateck) pipet tips (Thermo Fischer Scientific), polypropylene sample tubes (1.5 ml Eppendorf, 12 ml Kartell, 50 ml Falcon), Latex and Nitrile gloves (Ansell, size M).

**N-impurity assessment and removal.** All sample tubes, pipet tips, bottles, glassware and other involved materials in the sample handling and storage was always excessive prewashed with water. During a typical impurity assessment before and after an applied cleaning procedure, an experimental component with a predefined area (if applicable) was submerged in freshly prepared 0.1 M KOH (often 5 ml) in a sample tube and sonicated for 15 min. Aliquots were withdrawn from the sample tube for  $\text{NH}_3$ ,  $\text{NO}_2^-$  and  $\text{NO}_3^-$  quantification. Three main cleaning procedures were evaluated and consisted of; rinsing excessively with water; alkaline wash by submerging the material in 0.1 M KOH followed by 15 min of sonication; overnight heat treatment in a tubular furnace (Lenton Blue) at 200 °C ( $10^\circ\text{C min}^{-1}$ , 12 hour) under Ar atmosphere.

**Ammonia detection by gas chromatography-mass spectrometry.** Gaseous ammonia quantification was carried out with a gas chromatographic-mass spectrometry (GC-MS) method with about 5 minutes analysis time and a lower detection limit of about 1 ppm. A TRACE™ 1300 Gas Chromatograph (from Interscience BV - Thermo Fisher Scientific) was equipped with Agilent Select Low Ammonia column located in the GC oven chamber. Once eluted from the chromatography column, the analyte is partitioned between a pulse discharge detector (PDD) and a single quadrupole mass spectrometer (ISQ™ from Thermo Fisher Scientific), which simultaneously analyse the sample with matching retention times. Calibration standards were prepared diluting certified calibration gas mixtures of 13.8 ppm and 2.2 ppm of  $\text{NH}_3$  in  $\text{N}_2$  with purified  $\text{N}_2$ . Details of the detection method and calibration curves are available elsewhere.<sup>42, 43</sup>

**Quantification of gaseous NO<sub>x</sub> by chemiluminescence analyser.** A chemiluminescence 200E Nitric Oxides Analyser (API Teledyne) was used to measure gaseous NO and NO<sub>2</sub>. The amount of nitric oxide (NO) present in the sample gas is directly determined from the infrared light ( $h\nu_{[1200\text{ nm}]}$ ) emitted by the reaction between NO and ozone (O<sub>3</sub>), as shown in equations 4.1-4.2.



The emitted light of wavelength 1200 nm is then detected by the photo-multiplier tube light. In addition, NO<sub>2</sub> can be measured as sum of NO and NO<sub>2</sub> present in the gas sample. In this case, the gas sample passes through a molybdenum catalyst held at about 315 °C, where the NO<sub>2</sub> reacts to produce NO gas. Thus, the formed NO (together with the NO already present in the sample) is detected by reaction with ozone and generation of infrared light, following the equations 4.1-4.2. The total inlet gas flow rate of the gas chemiluminescence nitric oxides analyser was 700 mL min<sup>-1</sup>, as the instrument requires a relatively high gas flow. The gas purification scrubbers and filters were tested on a flow rate ranging between 1 and 50 mL min<sup>-1</sup>, and feeding the remaining flow aliquot as He by mean of dedicated mass flow controllers, as illustrated in **Figure A.4.2**. The detection limit of the NO analyser is 1 ppb.

**NH<sub>3(aq)</sub> and NO<sub>2</sub><sup>-</sup> spectrophotometric detection.** The quantification of ammonia was performed by the Berthelot method<sup>44</sup>. 1.33 ml of aliquot (typically 0.1 M KOH) was neutralized by adding 112 µl of 0.5 M H<sub>2</sub>SO<sub>4</sub>. Both 360 µl of phenol nitroprusside and alkaline hypochlorite (0.2% sodium hypochlorite) were added directly afterwards and stirred on a vortex shaker. An observable colour change ranging from light green to dark blue appeared after 30 min of incubation time. The coloured solutions were transferred to PMMA cuvettes (10x10x30mm<sup>3</sup>) and were inserted in the UV-Vis spectrophotometer (Hach DR6000) for analysis. Six different NH<sub>4</sub>Cl (99.99%) concentrations of 0.01, 0.05, 0.1, 0.5, 1 and 2 ppm NH<sub>3</sub> in 0.1 M KOH were prepared to construct the calibration line with the maximum absorbance at 633 nm. The fitted linear curve with  $A = 0.7279C_{\text{NH}_3} - 0.001$  and  $R^2 = 0.9999$  showed decent reproducibility (**Figure 4.1**).

Aliquots containing anion species that interfered with the NO<sub>2</sub><sup>-</sup> peak in the ion chromatogram, where quantified with the spectrophotometric Griess test. A commercially available Griess reagent mixture with a detection range between 0.007-3.28 ppm NO<sub>2</sub><sup>-</sup> (Spectroquant, Merck) was used. 2 ml Aliquots of 0.1 M KOH solutions were neutralized

with 0.5 M  $\text{H}_2\text{SO}_4$ . Approximately, 30 mg of the Griess reagent mixture was added to the neutralized aliquots and mixed thoroughly. After 10 min of incubation time the solution appears between light pink and dark magenta ranging from low to high concentration. Five different concentrations from  $\text{KNO}_2^-$  (Check purity) of 0.02, 0.05, 0.1, 0.5, 1 ppm  $\text{NO}_2^-$  were used to construct the calibration line by taking the maximum absorbance at 542 nm. The calibration line was perfectly linear with  $A = 0.8071C_{\text{NO}_2^-} - 0.0001$  and  $R^2 = 1$  (**Figure 4.2**). The spectrophotometric samples were always compared versus a fresh 0.1 M KOH solution as blank.

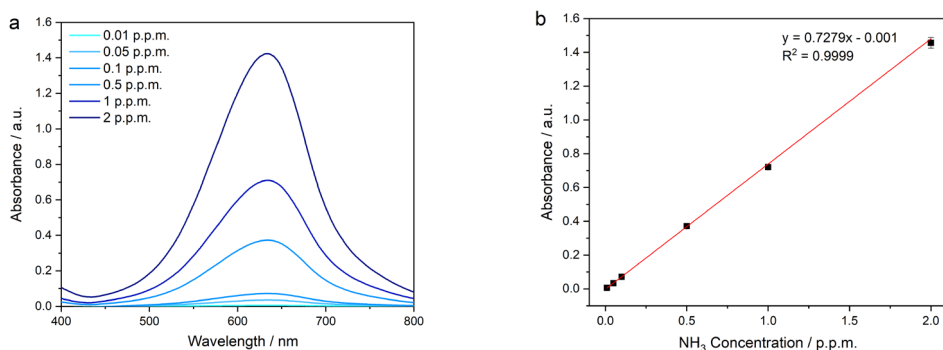


**Figure 4.1** (a) UV-Vis spectra of different  $\text{NH}_3$  concentrations in 0.1 M KOH. (b) Fitted calibration curve (red) from the absorbance at 633 nm versus different  $\text{NH}_3$  concentrations.

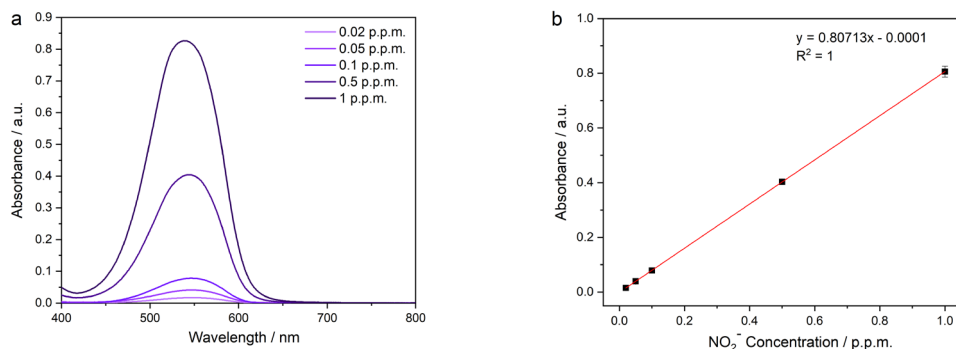


**Figure 4.2** (a) UV-Vis spectra of different  $\text{NO}_2^-$  concentrations in 0.1 M KOH. (b) Fitted calibration curve (red) from the absorbance at 542 nm versus different  $\text{NO}_2^-$  concentrations.

**NO<sub>2</sub><sup>-</sup> and NO<sub>3</sub><sup>-</sup> detection by ion chromatography.** The concentration of anions, most notably nitrite and nitrate were determined through ion chromatography (IC). The IC tests were performed by an Thermo Fischer Scientific, Dionex, Integrion HPIC System, equipped with a conductivity detector and AS18-Fast anion column. Additionally, according to application note 72481 from Thermo Fischer Scientific,<sup>45</sup> AutoNeutralization was installed to remove the KOH background. This removes the need for dilution of samples before injection and thus increases accuracy. With the used setup, a sample is manually injected, filling the sample loop (25 µL). Milli-Q water delivered from the external AXP pump and trap column (Dionex IonPac ATC-HC 500 trap column) is used to transfer the sample from the sample loop at 0.5 mL min<sup>-1</sup> to the neutralizing suppressor and collected on the concentrator column. As the sample passes through the suppressor (4 mm high capacity Dionex AERS 500 Anion Electrolytically Regenerated Suppressor), the cation (K<sup>+</sup> in our case) is exchanged with hydronium thereby neutralising the alkaline sample. The anions of interest are retained on the concentrator column while the water flows to waste, thereby also concentrating the trace anions of the sample. The anions of interest elute from the concentrator column to the guard column and separation column. Here the anions are separated using an eluent consisting of 21.8 mM KOH in milli-Q water at 0.25 mL min<sup>-1</sup> on the Dionex AS18-Fast anion column. As the analyte peaks elute from the column, they are detected by suppressed conductivity detection using a 2 mm Dionex AERS 500 Anion Electrolytically Regenerated Suppressor and conductivity detector. Two calibration lines were constructed by preparing five different concentrations of 0.02, 0.05, 0.1, 0.5 and 1 ppm NO<sub>2</sub><sup>-</sup> and NO<sub>3</sub><sup>-</sup> in 0.1 M KOH from KNO<sub>2</sub> and KNO<sub>3</sub>. **Figure 4.3** indicates a clear peak separation between different anion species, which allows accurate integration of the respective peaks. The integrated conductance vs. NO<sub>2</sub><sup>-</sup> and NO<sub>3</sub><sup>-</sup> concentration were plotted in **Figure 4.3**, which show with  $I = 0.6812 \cdot C_{\text{NO}_2^-} - 0.0036$  ( $R^2 = 0.9998$ ) and  $I = 0.4455 \cdot C_{\text{NO}_3^-} - 0.00796$  ( $R^2 = 0.9969$ ) a highly reproducible linear relationship.

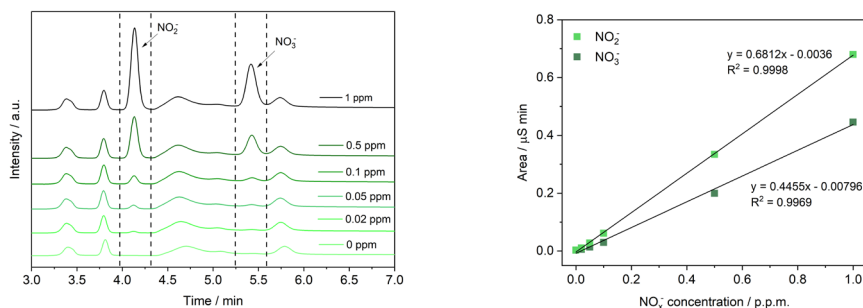


**Figure 4.3** On the left, ion chromatographs recorded at different  $\text{NO}_2^-$  and  $\text{NO}_3^-$  concentrations. On the right, ion chromatography calibration curves for  $\text{NO}_2^-$  and  $\text{NO}_3^-$ .

### 4.3 Results and discussion

**Effect of atmospheric N-species.** Atmospheric ammonia ( $\text{NH}_3$  and  $\text{NH}_4^+$ ) is caused by emissions from the agricultural sector, where ammonia volatilization occurs due to intensified herbivore production and field-applied manure.<sup>46, 47</sup> Volatilization rates can vary between day and night, which depends on multiple factors, such as wind speed, humidity and fertilization rate. A monthly average of the measured ammonia emissions in the Netherlands varied between 2–44 ppb.<sup>48</sup>  $\text{NH}_3$  adsorbs relatively easy on various surfaces, which explains its short atmospheric lifetime between 12 hours and 5 days.<sup>47, 49</sup> Although, the atmospheric ammonia concentration might seem negligible, it is expected that long term exposure of laboratory equipment will contain surface adsorbed  $\text{NH}_3$  and contributes to an unavoidable background level.<sup>12</sup>

The majority of the  $\text{NO}_x$  emissions are anthropogenic, derived by the industrial and automotive combustion of fossil fuels.<sup>50</sup> Long term laboratory equipment exposure can accumulate significant  $\text{NO}_x$  content because it has high electron affinity and can react particularly well with metals,<sup>51</sup> but also other materials.<sup>52, 53</sup>  $\text{NO}_x$  are reactive species,<sup>54</sup> and electroreduction of  $\text{NO}_x$  to ammonia has been reported.<sup>10, 55</sup> Most of the atmospheric  $\text{NO}_x$  is in the form of  $\text{NO}_2$ , as  $\text{NO}$  gas is typically less stable.  $\text{NO}_2$  has a higher solubility in water compared to  $\text{NO}$  ( $0.65 \text{ g L}^{-1}$  vs  $0.063 \text{ g L}^{-1}$  at  $20^\circ\text{C}$  and 1 atm),<sup>56, 57</sup> and it can accumulate in long term stored solutions when exposed to air similarly as ammonia. At low  $\text{NO}_2$  concentrations, it is expected that the nitrogen oxide species form mainly nitric and nitrous acid, which in case of an alkaline environment decompose into detectable  $\text{NO}_2^-$  and  $\text{NO}_3^-$ .<sup>58,</sup>

Our results show that the atmospheric  $\text{NO}_x$  concentration in our laboratory, measured by a chemiluminescence  $\text{NO}_x$  analyzer (Teledyne 200E, details available in the experimental section of this chapter), varies largely over the course of five consecutive days up to 27 ppb (**Figure 4.4**). The uptake rate of  $\text{NO}_x$  and  $\text{NH}_3$  from air in 24 hour exposed water, freshly prepared 0.1 M and 1 M KOH was yet negligible (**Figure A.4.3**). However, higher  $\text{NH}_3$  uptake rates (25-75 ppb) in similar electrolytes during 24 hour exposure have been reported earlier.<sup>25</sup> As previously mentioned, atmospheric  $\text{NH}_3$  can fluctuate depending on the time and location, therefore similar variations are expected.

Long term accumulation of  $\text{NO}_x$  impurities were observed both in low and high purity grade KOH salt (85%, 99.99%, Sigma-Aldrich) and depends solely on the storage conditions, as summarized in **Figure A.4.4**. KOH salt bottles stored in a chemical safety cabinet, hence exposed to the laboratory environment for a considerable time period (10 months) contained 270 ppb of  $\text{NO}_3^-$  in a freshly prepared 1 M KOH solution. Remarkably, when storing the KOH pellets in a vacuum desiccator for approximately 9 months, the  $\text{NO}_x$  impurities were negligible (< 20 ppb). It is, therefore, strongly advised to store chemicals in a controlled environment in for example, a desiccator or Ar glovebox.

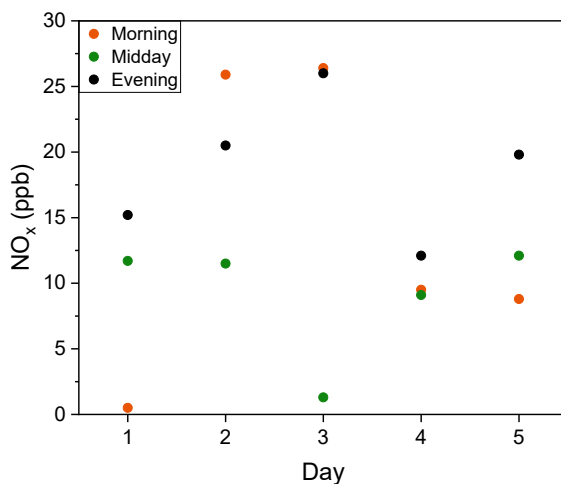


**Figure 4.4**  $\text{NO}_x$  concentration measured directly from air in our laboratory over a week (Monday-Friday). Morning (orange), midday (green) and evening (black) measurements were recorder around 9.00, 12.30 and 18.00 every day. Each data point is the average of the measured  $\text{NO}_x$  concentration over 5 minutes.

**Table 4.1** Overview of N containing contaminations in the indicated substances.

Compound	NH <sub>3</sub> (ppm)	NO <sub>x</sub> (ppm)	
Ambient air	0.002–0.044 <sup>48, b</sup>	0.0015–0.027 <sup>a</sup>	
He (99.999%)	<0.15 <sup>a</sup>	0.0011 <sup>a</sup>	
<sup>14</sup> N <sub>2</sub> (99.999%)	<0.15 <sup>a</sup>	0.0019 <sup>a</sup>	
<sup>15</sup> N <sub>2</sub> (99%)	9.8 ( <sup>15</sup> NH <sub>3</sub> ) <sup>a</sup> 0–1.61 <sup>23</sup>	0–1.03 <sup>23</sup>	
Ar (99.999%)	<0.15 <sup>a</sup>	0.0018 <sup>a</sup>	
Materials	NH <sub>4</sub> <sup>+</sup> (ppm)	NO <sub>2</sub> <sup>-</sup> (ppm)	NO <sub>3</sub> <sup>-</sup> (ppm)
Fe <sub>2</sub> O <sub>3</sub> <sup>c</sup>	295-7372 <sup>60</sup>	0 <sup>60</sup>	0-576 <sup>60</sup>
Bi <sub>2</sub> O <sub>3</sub> <sup>c</sup>		329 <sup>60</sup>	1288 <sup>60</sup>
Al <sub>2</sub> O <sub>3</sub> <sup>c</sup>		26 <sup>60</sup>	664 <sup>60</sup>
0.5 M Li <sub>2</sub> SO <sub>4</sub>			0-11 <sup>22</sup>
0.5 M LiClO <sub>4</sub>			1.39-2.38 <sup>22</sup>
15 ml tube (borosilicate) <sup>d</sup>		0.00015 <sup>21</sup>	0.088 <sup>21</sup>
15 ml tube (soda lime) <sup>d</sup>		0.00009 <sup>21</sup>	0.041 <sup>21</sup>
12 ml tube (PP) <sup>e</sup>	0.002	0.004 <sup>a</sup> , 0.00009 <sup>d, 21</sup>	0.001 <sup>a</sup> , 0.035 <sup>d, 21</sup>
1.5 ml tube (Eppendorf) <sup>e</sup>	0.002 <sup>a</sup>		0.003 <sup>a</sup>
1 ml pipet tip (PP) <sup>d,f</sup>	0.002 <sup>a,f</sup>	0.006 <sup>a,f</sup> 0.00011 <sup>d, 21</sup>	0.013 <sup>a, f</sup> 0.006 <sup>d, 21</sup>
0.2 ml pipet tip (PP) <sup>d</sup>		0.0005 <sup>21</sup>	0.004 <sup>21</sup>
0.1 ml pipet tip (PP) <sup>f</sup>	0.005 <sup>a</sup>	0.023 <sup>a</sup>	0.009 <sup>a</sup>

<sup>a</sup> Values obtained in this study. <sup>b</sup> Indicative range of the NH<sub>3</sub> emissions measured in the Netherlands over 2021.<sup>48</sup> <sup>c</sup> N-assessment of metal oxide powders by mixing 500 mg of the material under investigation with 30 ml of 0.1 M KOH and 50 mg with 100 ml H<sub>2</sub>SO<sub>4</sub> to measure the NH<sub>4</sub><sup>+</sup> content, as in ref <sup>60</sup>. <sup>d</sup> Data adopted from ref <sup>21</sup>, impurities in the 15 ml tubes were obtained by decanting, using 1 ml water, while a single aspiration-expiration procedure was applied on 0.2 and 1 ml pipet tips with 0.3 ml and 1.1 ml water, respectively. <sup>e</sup> Both 1.5 ml and 12 ml sample tube were filled completely with 0.1 M KOH and sonicated. <sup>f</sup> 0.1 ml and 1 ml pipet tips were assessed by submerging and sonicating in 6 and 12 ml 0.1 M KOH, respectively. More details about the procedures are stated in the experimental section.

**Impurities in the feed gases.** The level of earlier reported N contaminants in the feed gases are summarized in **Table 4.1**. Our analysis reveals that the NH<sub>3</sub> and NO<sub>x</sub> impurities present in high purity (5N) He, <sup>14</sup>N<sub>2</sub> and Ar are very low. As such, the NH<sub>3</sub> concentration does not exceed the lower detection limit (LOD<sub>NH3</sub> < 150 ppb) of the gas chromatograph (GC).<sup>43</sup> Similarly, the NO<sub>x</sub> content is also negligible, as it falls in the instrument's LOD (1 ppb). Conversely, <sup>15</sup>N<sub>2</sub> isotopologue is commercially available at a lower purity level than

the conventional  $^{14}\text{N}_2$ ; thus it might contain a higher concentration of contaminants. As such, we measured up to 9.8 ppm of ammonia contained in a  $^{15}\text{N}_2$  gas bottle (99 % purity, Sigma-Aldrich), by using an isotope sensitive GC-MS (**Figure 4.5**).<sup>42</sup> The totality of the measured ammonia is in the form of  $^{15}\text{NH}_3$ , as shown in **Figure 4.5b**. The presence of  $^{15}\text{NH}_3$  presumably derives from traces of unreacted  $^{15}\text{NH}_3$ , used during the catalytic oxidation process for the production of  $^{15}\text{N}_2$  gas from isotopically enriched  $^{15}\text{NH}_3$ .<sup>61</sup>

It should be noted that, to avoid underestimation of measured gaseous  $\text{NH}_3$ , it is recommended to use direct gas analysis methods,<sup>42, 43</sup> and inert materials for all the surfaces in contact with the gaseous sample, to minimize ammonia physisorption. In fact, **Figure 4.5a** shows that no ammonia was detected when the same  $^{15}\text{N}_2$  gas was dosed via mass flow controller (Bronkhorst, not surface passivated). Quantification of  $\text{NO}_x$  in  $^{15}\text{N}_2$  was not performed due to the high cost of  $^{15}\text{N}_2$  and because the  $\text{NO}_x$  chemiluminescence analyser requires high flow rates ( $1\text{ L min}^{-1}$ ) in combination with a long equilibration time ( $> 30\text{ min}$ ), as described in the methods section.

Due to the low solubility in aqueous media, prolonged  $\text{N}_2$  bubbling into the electrolyte is often required to reach saturation. Moreover, the use of cumulative detection methods requires several hours of reaction time to collect significant amounts of  $\text{NH}_3$ .<sup>11, 42</sup> This also results in accumulation of nitrogen contaminations in the electrolytic cell. This problem can be partly circumvented adopting a gas recirculation setup,<sup>62</sup> or by adopting suitable gas filters.

**Gas filter performance.** The efficiency of the adopted gas purification strategy needs to be assessed prior to its implementation in NRR studies. This is especially important for uncertified filter systems, such as in-house developed scrubbers or catalytic filters. Herein, the  $\text{NO}_x$  and  $\text{NH}_3$  impurity removal efficiency is examined for a set of different filters at experimentally relevant conditions ( $1\text{-}50\text{ mL min}^{-1}$  for 3 h). Initially, a flow rate of  $10\text{ mL min}^{-1}$  of 50 ppm NO in He is used to compare the performance of the different gas purifiers. The NO concentration is then measured at the outlet of the filter with the chemiluminescence detector. The gas purifiers with a stable (variation  $< 5\%$ ) removal efficiency throughout the duration of the experiment, are then tested over a wider range of flow rates relevant for electrochemical NRR studies ( $1\text{-}50\text{ mL min}^{-1}$ ). Additionally, the  $\text{NH}_3$  trapping is tested using a gas mixture containing 13.8 ppm  $\text{NH}_3$  in  $\text{N}_2$  and analysing the purified gas stream with a GC-MS. More details on the methods are available in the experiment section.



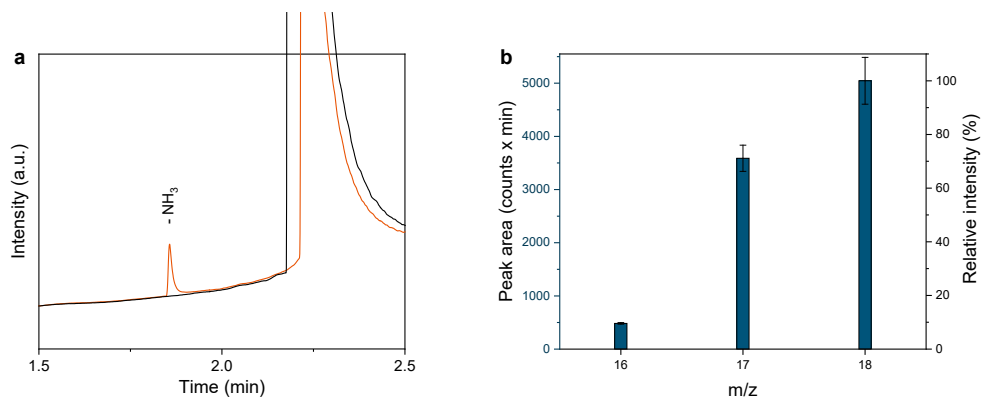


**Figure 4.5** (a) Close up of the chromatograph around the ammonia elution time of the GC from the analysis of  $^{15}\text{N}_2$  gas. Ammonia contaminations (9.8 ppm) are detected in the  $^{15}\text{N}_2$  gas directly connected to the GC inlet (orange line). Interestingly, when the  $^{15}\text{N}_2$  gas was dosed via a mass flow controller (not passivated against ammonia adsorption), no ammonia was detected. (b) Integrated peak areas of the mass-to-charge ratio (m/z) of the ions detected with GC-MS at 1.84 min retention time (i.e. ammonia retention time). The relative intensity of the m/z corresponds to the  $^{15}\text{NH}_3$  ionization fragments. Error bars correspond to the standard deviation of three independent measurements.

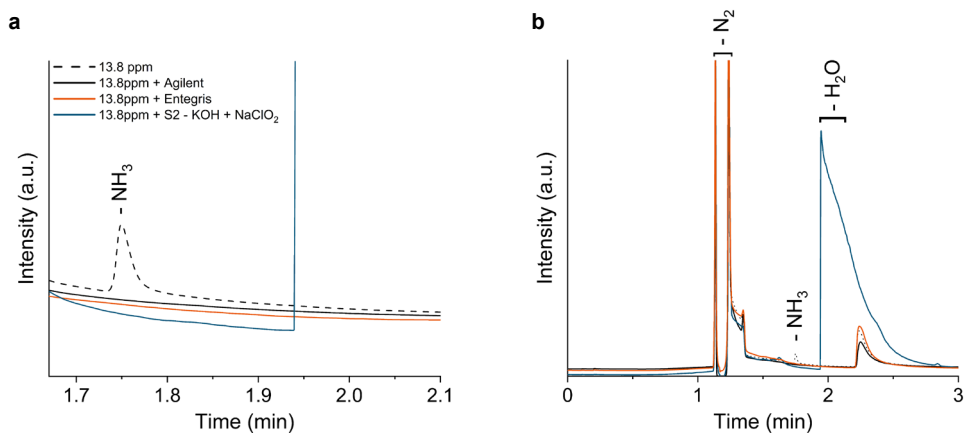


**Figure 4.6** (a) Close up of the chromatograph around the ammonia elution time obtained from the analysis of a 13.8 ppm  $\text{NH}_3$  in  $\text{N}_2$  calibration gas flowing at  $10 \text{ mL min}^{-1}$  connected directly to the GC (dashed black line) and purified with the Agilent OT3-4 filter (solid black line), Entegris GPUS35FHX filter (solid orange line) and in-house made scrubber (S2) filled with a 0.1 M KOH and 0.1 M  $\text{NaClO}_2$  trapping solution (solid blue line) prior entering the GC. All the ammonia contained in the gaseous analyte is captured by the filters. (b) Full chromatograph highlighting that the purification with the in-house made scrubber introduces a significant amount of water into the feed gas.

The most commonly applied method to remove impurities consists of flowing the feed gas through one or more scrubbers containing a liquid trap, prior the introduction to the electrochemical cell. Scrubbers can vary in volume, geometry and liquid solution. We first tested two standard 20 mL scrubbers with a glass frit (Supelco Analytical, 6-4835) connected in series. The poor solubility of NO in aqueous media results in less than 25% NO removal efficiency when using MilliQ water (**Figure A.4.5**). Alkaline solutions are a common choice because gaseous NO<sub>x</sub> can be trapped in the form of NO<sub>x</sub><sup>-</sup>, while the absorption rate is generally lower in neutral to acidic media at low NO<sub>x</sub> concentrations.<sup>58, 59</sup> Previous studies recommended the use of strong oxidizing agents, such as KMnO<sub>4</sub> or NaClO<sub>2</sub> to convert NO directly into NO<sub>2</sub><sup>-</sup> or NO<sub>3</sub><sup>-</sup>, and improve the overall NO<sub>x</sub> removal efficiency.<sup>17</sup> It is recommended to operate the oxidizing agent in combination with alkaline conditions because it enhances the oxidation effect.<sup>58, 63, 64</sup> NaClO<sub>2</sub> seems to be one of the most effective oxidants and its effectiveness is evaluated in the present work.<sup>63</sup>

Substituting water with 0.1 M KOH enhances the removal efficiency up to 78%, while using a solution of 0.1 M NaClO<sub>2</sub> and 0.1 M KOH removed 88% of NO after 3 hours purging time (**Figure 4.7**). The scrubbing efficiency can be increased by optimizing the gas residence time and the bubble contact area between the gas-liquid interface. For these purposes, common strategies consist of: (1) inserting packing material to increase the tortuosity; (2) extending the length of the column. As such, inert polytetrafluoroethylene (PTFE) beads were inserted into a 30 cm long 25 mL in-house made scrubber (further details are given in the experimental section). This results in a further improvement in the removal efficiency, up to 98 % over a course of three hours at 10 mL min<sup>-1</sup> (**Figure 4.7**). However, when the flow rate is increased, the efficiency drops drastically (**Figure 4.8**); making this NO removal strategy not suitable for flow rates higher than 10 mL min<sup>-1</sup>. Remarkably, the commercially available gas filters (Agilent OT3-4 and Entegris GPUS35FHX) show a consistent excellent removal efficiency, within the 1-50 mL min<sup>-1</sup> range (**Figure 4.7**, **Figure 4.8** and **Figure A.4.6**).

The results from the NH<sub>3</sub> removal experiments show that both commercial gas filter can effectively trap NH<sub>3</sub> contaminations with 100 % (**Figure 4.6**). Similarly, also the scrubber containing a 0.1 M NaClO<sub>2</sub> and 0.1 M KOH solution, shows complete NH<sub>3</sub> removal (**Figure 4.6**). The difference in NO<sub>x</sub> and NH<sub>3</sub> removal efficiency in scrubbers is expected, due to the higher ammonia solubility in water.

Based on this analysis commercial packed filters appear to be the most efficient and durable solution for feed gas purification. Both the tested commercial packed filters have been extensively used for over one year without showing any sign of decay in performance. On the other hand, scrubbers require daily preparation and filling of the liquid trapping solution. Lastly, commercial filters are widely accessible and affordable, often with the possibility of being conveniently regenerable via  $H_2$  treatments.

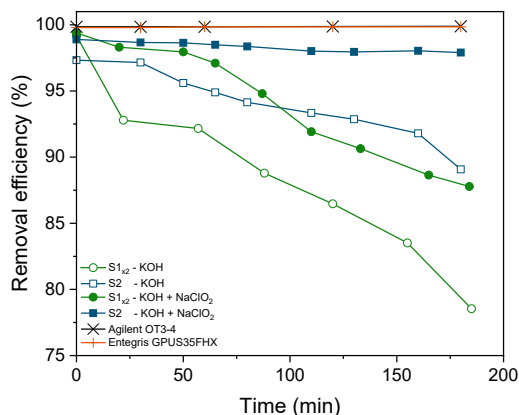


**Figure 4.7** NO<sub>x</sub> removal efficiency over time, measured for an inlet gas mixture of 50 ppm NO in He at 10 mL min<sup>-1</sup> for different scrubbers and liquid trap solutions. S1<sub>x2</sub> and S2 indicate the two standard scrubbers (Supelco Analytical, 6-4835) connected in series and the in-house made scrubber, respectively.

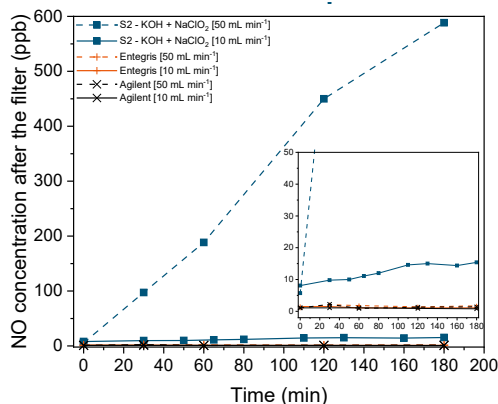


**Figure 4.8** NO concentration measured over time at the outlet of each gas filter tested with an inlet gas mixture of 50 ppm NO in He at 50 (dashed line) and 10 (solid line) mL min<sup>-1</sup>. In-house made scrubber (S2) filled with a 0.1 M KOH and 0.1 M NaClO<sub>2</sub> trapping solution is shown in blue, while the commercial Entegris and Agilent packed filters are shown in orange and black, respectively. The complete dataset with flowrates from 1 to 50 mL min<sup>-1</sup> is given in **Figure A.4.6**.

**Lab consumables.** Based on our analysis, lab consumables made from polypropylene, including 0.1-1 ml pipet tips, 1.5ml and 12 ml samples tubes that were stored in our laboratory supply cabinets, contained relatively low levels of impurities (**Table 4.1**, **Figure 4.9a** and **Figure A.4.7**). Several 1.5 ml tubes were also analysed directly after arrival, and appeared to be free of N-impurities. This suggests that the consumables stored for longer periods of time in typical supply cabinets undergoes build-up of atmospheric impurities, but remains within an acceptable range. Although not assessed here, glassware appears to be more problematic where NO<sub>3</sub><sup>-</sup> was identified as a potential source, but varied between different manufacturers.<sup>20, 21</sup> These surface impurities, both for glassware and plastic consumables, were effectively removed by rinsing several times with water.

Chemically resistant gloves must be used with caution as N-impurities contained in the material have the potential to contaminate lab consumables, but also cell components during handling and cleaning.<sup>20, 25</sup> Gloves made from latex rubber or synthetic nitrile- or vinyl-based rubber might contain remaining trace impurities from the coagulant material, such as calcium nitrate, used on the glove formers to harden the rubber during the manufacturing process. Not all manufacturers use calcium nitrate as a coagulant, which explains the NO<sub>x</sub><sup>-</sup> variations.<sup>20</sup> Latex and nitrile-based gloves, both commonly used in our laboratory were screened by ultrasonication of a piece of 6 cm x 6 cm in 0.1 M KOH for 15 min (more details in **Figure 4.9b**). Both gloves released excessive quantities of NO<sub>3</sub><sup>-</sup>; latex 614 ±43 ppb and nitrile 1757 ±27 ppb.

These values are in fair agreement with other studies which reported N-impurities in both latex (0-0.7 ppm NO<sub>2</sub><sup>-</sup>, 0.06-94.2 ppm NO<sub>3</sub><sup>-</sup>) and nitrile-based gloves (2.8 ppm NH<sub>3</sub>).<sup>20, 25</sup> It is however difficult to assess the impact of gloves on routine NRR measurements because it depends on the impurity level (which differs per manufacturer and batch), including the amount of interaction with electrolyte exposed surfaces, such as membranes, electrodes, glassware, etc. Nevertheless, we performed a qualitative assessment by rubbing both thumb and forefinger of a nitrile glove in 5 circular movements over the front and back of a Celgard membrane surface and observed repeatable release of 13 ±1 ppb NH<sub>3</sub>, 36 ±11 ppb NO<sub>2</sub><sup>-</sup> and 948±163 ppb NO<sub>3</sub><sup>-</sup>. This demonstrates that ppm levels of NO<sub>3</sub><sup>-</sup> can be unintentionally released during a NRR experiment.

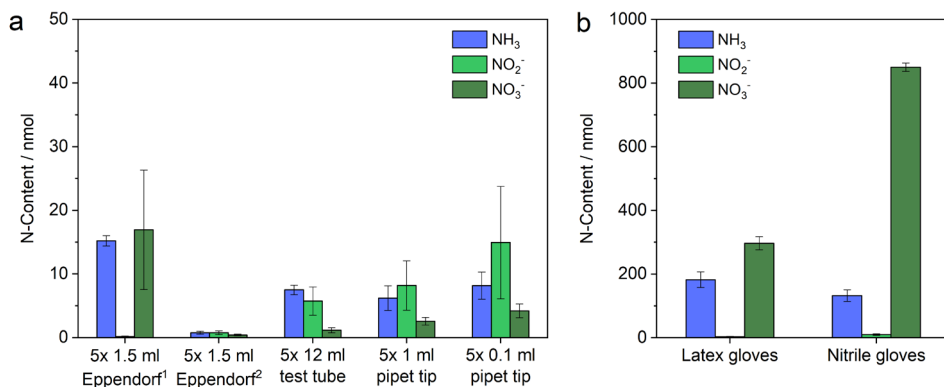


**Figure 4.9** Screening of various lab consumables stocked in our laboratory. (a) 1.5 ml and 12 ml sample tubes were completely filled with 0.1 M KOH. The 0.1 ml and 1 ml pipet tips were transferred into a sample tube filled with 12 ml and 6 ml of 0.1 M KOH, respectively. All consumables were sonicated for 15 min. This procedure was repeated 5 times using the same solution. <sup>1</sup> Stored for a longer period of time, <sup>2</sup> directly analysed after arrival. (b) For the latex and nitrile gloves, pieces of 6x6cm<sup>2</sup> were cut from the centre of each glove and cut into smaller chunks to be subsequently transferred to a 50 ml sample tube filled with 30 ml 0.1 M KOH and sonicated for 15 min. The error bars indicate the standard deviation of three individual experiments.

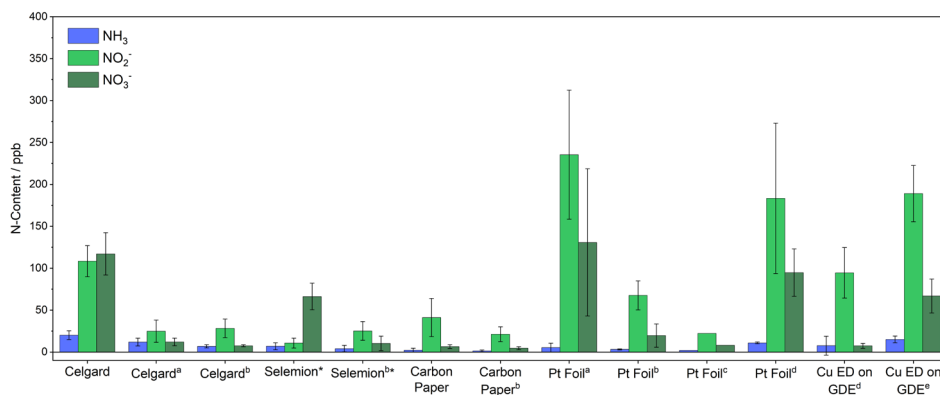


**Figure 4.10** Release of extraneous NH<sub>3</sub>, NO<sub>2</sub><sup>-</sup> and NO<sub>3</sub><sup>-</sup> sources from common used electrochemical cell components during ultra-sonicating in 5 ml of 0.1 M KOH for 15 min using different pre-treatment steps. All components, except the carbon paper had a 2.5 cm x 2.5 cm dimension. The carbon paper and Cu GDE were finely cutted discs with a diameter of 1.2 cm. Indicated as unlabelled is untreated and fetched from the as received package. (a) rinsed excessively with H<sub>2</sub>O, (b) sonicated for 15 min in 0.1 M KOH, (c) sonicated for 15 min in 0.1 M KOH plus flame annealing with butane flame torch, (d) heat treatment in Ar at 200 °C overnight (12 hours), (e) rinsed with H<sub>2</sub>O and isopropanol, than electrochemical treatment by performing 10 cyclic voltammetry scans with only reductive currents (-0.2 V to -0.7 V vs. RHE) and rinsed with H<sub>2</sub>O afterwards as elaborately described in ref <sup>35</sup>. \* NO<sub>2</sub><sup>-</sup> assay with the Griess test. Every component is measured in triplicates. N-content in nmol normalized by the geometric surface area is given in **Figure A.4.8**.

**Impurity screening of cell components.** The use of Nafion membranes in NRR studies have become controversial. NH<sub>4</sub><sup>+</sup> accumulates within the membrane over time due to cation selective behaviour and high porosity. This NH<sub>4</sub><sup>+</sup> is later released during the experiments, leading to the introduction of about 20-400 ppb, equivalent to about 1 – 25 nmol cm<sup>-2</sup> of extraneous NH<sub>4</sub><sup>+</sup>, depending strongly on the pre-treatment procedure.<sup>25,28,33</sup> Accumulation of atmospheric ammonia appears to be the main issue for the Nafion membrane,<sup>34</sup> but did not affect the Celgard (3401 and 3501) microporous membranes, which were considered as cleaner alternatives.<sup>25</sup> With our NO<sub>x</sub> determination procedure, we confirm that negligible amounts of NH<sub>3</sub> were released from Celgard membranes, as shown in **Figure 4.10**. However, 108 ± 18 ppb of NO<sub>2</sub><sup>-</sup> and 117 ± 18 ppb of NO<sub>3</sub><sup>-</sup> are released from a new Celgard membrane (2.5 cm x 2.5 cm). According to the manufacturer (Celgard), no sources of NO<sub>x</sub> were used during the production process, thus it is very likely that physisorption of atmospheric NO<sub>x</sub> occurred and accumulated over time. Yet, simply rinsing with H<sub>2</sub>O, or sonicating in 0.1 M KOH is sufficient to significantly reduce impurity levels below 40 ppb. Celgard membranes cannot be stored in liquid media, which might prevent air exposure, but have to be stored dry, otherwise it will lose the surfactant coated layer. Therefore, it is recommended to store Celgard membranes in a desiccator or Ar glovebox, especially for long term storage.

Anion exchange membranes (AEM) are also commonly applied in the nitrogen reduction field, especially in combination with alkaline electrolytes, due to their selective transport of OH<sup>-</sup> and negligible ammonia crossover. AEM ionomers consist of quaternary ammonium functional groups, which gives the membrane anion selective properties. One could expect that due to degradation and spontaneous protonation of the N-functional groups, ammonia formation occurs.<sup>30-32</sup> However, we did not observe any sign of ammonia contamination leaching from the AEM (**Figure 4.10**), even after 1 hour of sample collection (**Figure A.4.9**). Surprisingly, the amount of NO<sub>x</sub><sup>-</sup> species were negligible, which is most likely related to the wet storage of the membrane in a zip lock bag.

Catalyst materials, including used precursors containing N functional groups, might not release N-impurities directly, however, there is a tangible high risk of decomposition and protonation of these N groups into ammonia at electroreduction conditions.<sup>30-32</sup> The importance of such an evaluation is addressed in the following case as an example, wherein a copper catalyst was prepared by the electrodeposition of Cu on carbon paper (Cu EC) from a Cu<sup>2+</sup> solution, using a 0.5 M Cu(NO<sub>3</sub>)<sub>2</sub> electrolyte (method can be found in a previous

publication<sup>35</sup>). Directly after the electrodeposition, the Cu EC released  $21003 \pm 2608$  ppb  $\text{NO}_3^-$ , but also  $613 \pm 106$  ppb  $\text{NO}_2^-$ , which indicates that the  $\text{NO}_3^-$  from the electrolyte is still present and that it is partly reduced into  $\text{NO}_2^-$  during electrodeposition, while both remain in the Cu EC. The N contamination removal efficacy of two treatment methods for the Cu EC is evaluated. A heat treatment, consisting of heating the electrode at  $200^\circ\text{C}$  overnight (12 hours) in Ar; and a cyclic voltammetry treatment with 10 scans between  $-0.2$  V and  $-0.7$  V vs. RHE in  $0.1$  M KOH, more details can be found in the experimental section. The heat treatment appeared to be already effective for the removal of  $\text{NO}_3^-$  impurities in iron oxide powders.<sup>19</sup> Removal rates up to 99.2% were also achieved for the Cu EC, however, still non-negligible trace levels ( $>200$  ppb  $\text{NO}_x^-$ ) remained in the electrode. The cyclic voltammetry strategy is to some extent also effective reducing the  $\text{NO}_x^-$  level by 98.8%. We expect that the irremovable traces of impurities will continuously leach into the electrolyte during a typical NRR experiment because we observed an increase in the level of  $\text{NO}_x^-$  after 1 hour of sampling time (**Figure A.4.9**). Carbon paper (Alfa Aesar) is a commonly used catalyst substrate, but releases only negligible amounts of  $\text{NO}_2^-$  ( $41 \pm 23$  ppb and  $21 \pm 9$  ppb after alkaline pre-treatment), as shown in **Figure 4.10**.

Platinum is often used as an anode due its stability and low overpotential for the oxygen evolution reaction. To our surprise, after rinsing a Pt foil ( $2.5 \times 2.5 \times 0.025$  cm<sup>3</sup>, Mateck) multiple times with  $\text{H}_2\text{O}$ , the amount of released  $\text{NO}_2^-$  varied between 170-344 ppb and it is most likely related to the adsorption of atmospheric  $\text{NO}_x$ . Pt mononitrosyls can be formed when Pt is exposed to NO in an oxygen rich environment at room temperature.<sup>65</sup> Since the Pt foil was continuously exposed to low content of  $\text{NO}_x$  in the lab environment (**Figure 4.4**), the build-up of a surface layer of Pt mononitrosyls appears to be stable in  $\text{H}_2\text{O}$ , but could, to some extent, be removed in  $0.1$  M KOH (**Figure 4.10** and **Figure A.4.8**). This is confirmed from repeated measurements after prolonged exposure to air. The heat treatment on Pt was also successful, as only negligible amounts of  $\text{NO}_x^-$  are detected after this treatment. Interestingly, we observed that flame annealing, which is often used to remove organic impurities and to pre-oxidize the surface, provokes an increase in N impurities detected on a Pt foil (**Figure 4.10**). The butane flame torch can reach temperatures up to  $1430^\circ\text{C}$ , which is close to the activation of the thermal  $\text{NO}_x$  formation by air combustion occurring above  $\sim 1527^\circ\text{C}$ .<sup>66</sup> An alternative and more likely scenario is the “prompt” nitric oxide formation

via unburned hydrocarbon radicals and nitrogen. This reaction is less temperature dependent,<sup>66,67</sup> and might be the source of adsorbed  $\text{NO}_x$  species on the Pt surface.

**Implications for a typical NRR system.** In this paragraph, we discuss the overall effectiveness of the earlier stated cleaning procedures. In order to do this, concentrations stated in **Figure 4.10** were converted, using the geometric areas and control volumes into  $\text{nmol cm}^{-2}$  (**Figure A.4.8**). These conditions were taken from one of our previous studies,<sup>12</sup> which are summarized in **Figure 4.11**. We chose to exclude high sources of contaminated materials such as  $^{15}\text{N}_2$ , gloves and catalysts from the analysis because our aim is to qualitatively estimate the bare minimum background level for our system. From **Figure 4.11**, it becomes clear that in terms of our system, the background level (without applying any cleaning procedure) is roughly 140  $\text{nmol}$  consisting mostly of  $\text{NO}_x$  impurities. Assuming that most  $\text{NO}_x^-$  reduces into  $\text{NH}_3$ , the calculated yield of  $0.16 \text{ nmol s}^{-1} \text{ cm}^{-2}$  is enough for a NRR catalyst to be labelled as plausible.<sup>17</sup> Approximately 84% of the impurities were reduced to 23  $\text{nmol}$  by applying the most effective cleaning procedures, which is low enough to perform reliable NRR experiments. Moreover, the background level can be reduced even further by minimizing the exposed areas of membranes and electrodes using a more optimized cell design.

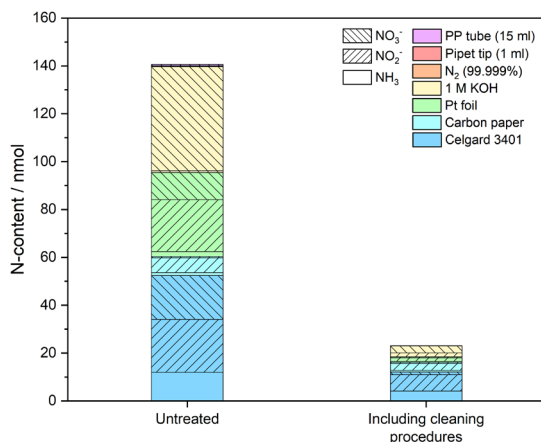


**Figure 4.11** Estimation of the minimum background level with and without the most effective cleaning procedures. Values were obtained from **Figure A.4.8** and **Table 4.1** assuming the  $\text{N}_2$  flow ( $20 \text{ ml min}^{-1}$ , 99.999%), membrane area (Celgard,  $10 \text{ cm}^2$ ), working electrode (carbon paper,  $1 \text{ cm}^2$ ), counter electrode (Pt foil,  $4 \text{ cm}^2$ ), electrolyte (1 M KOH, 10 ml), 1 pipet tip and 1 sample from our previous study tube with total experiment time of 15 min.<sup>12</sup> The applied cleaning procedure were: alkaline wash for Celgard 3401 membrane and carbon paper, heat treatment for Pt foil, long term storage of KOH salt in a desiccator, rinsing lab consumables with water. The corresponding N-content in ppb is given in **Figure A.4.11**.



## 4.4 Conclusions

In this work, we carried out a systematic investigation on the N contaminations derived from several sources and on the efficacy of multiple removal strategies, which should be used as benchmark to perform reliable electrochemical NRR studies. Notably, all the 99.999 % pure gases tested ( $N_2$ , He, Ar) were adequately clean as both  $NH_3$  and  $NO/NO_2$  were not detected ( $LOD_{NH_3}$ : 150 ppb,  $LOD_{NO_x}$ : 1 ppb). On the other hand,  $^{15}N_2$  gas contains relevant amounts of  $^{15}NH_3$  and therefore a more rigorous purification is required. Our analysis shows that commonly adopted liquid traps do not properly eliminate the  $NO_x$  contaminations from the feed gases, due to limited mass transport and reactivity. Importantly, the trapping efficiency should be evaluated at conditions close to experimental, as we show that factors like flow rate and duration of the experiment highly affect the removal efficiency. For these reasons we strongly recommend the application of commercial gas purifiers (evaluated herein), which exhibit the best performance at all relevant conditions.

The use of  $NH_3$  and  $NO_x$  as precursors in synthesis procedures should be avoided, as it was not possible to sufficiently remove the remaining  $NO_x^-$  from the Cu electrodeposited electrode from  $Cu(NO_3^-)$ . Another unresolvable observed issue is the  $NO_3^-$  content present in the chemical safety gloves. Even though its effect is difficult to assess in a quantitative manner, we consistently measured almost 1 ppm of  $NO_3^-$  after a short contact with a membrane.

The level of atmospheric  $NO_x$  in our laboratory was monitored, showing significant variations over time (1.5-27 ppb). These atmospheric  $NO_x$  species had a large impact on several materials commonly adopted in NRR experiments. As environmental exposure is inevitable, long term storage should be done in Ar gloveboxes or desiccators, which worked well for the electrolyte salts. To remove the already present N contaminations, the most effective treatments, depending on the material, include alkaline washing, heat treatment, and ultrapure water rinse. Based on our measurements, we estimated that a typical NRR experiment would have a minimum background level of about 1200 ppb, which can be reduced by about 87 %, to ~150 ppb, by properly implementing our recommendations (**Figure 4.11**). Thus, as an absolute control over these environmental N contaminations is challenging, experimentalists should become aware of the impact of these contaminations on NRR results, carrying out careful background quantifications and adopting the here

recommended strategies. A general minimum background level is rather difficult to address because of the large variety of experimental approaches within the research community. Nevertheless, we provided the experimentalists with recommendations and various tested cleaning procedures in order to reduce effect of impurities to a bare minimum.

## Appendix A.4

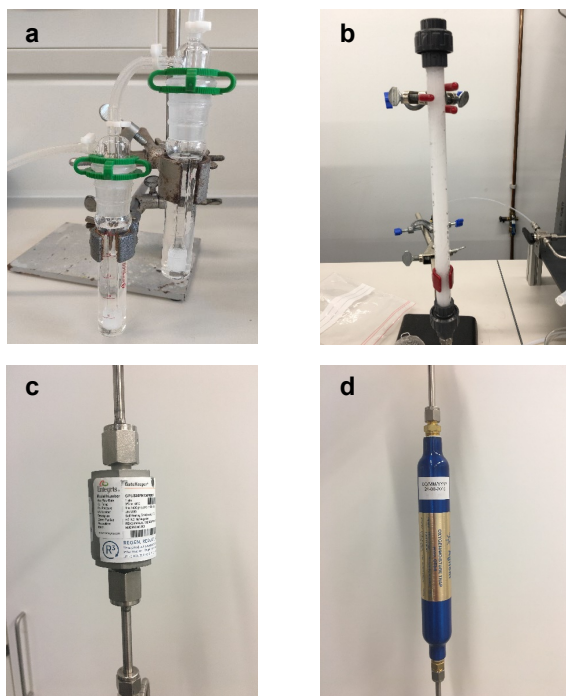


**Figure A.4.1** Pictures of the tested gas filters. (a) Two 20 mL scrubbers (Supelco Analytical, 6-4835) with liquid trap solution connected in series. (b) In-house made scrubber (30 cm length, diameter ..., PMMA) filled with inert 1/8" HDPE beads (McMaster) to increase tortuosity and 25 mL of either 0.1 M KOH or 0.1 M KOH + 0.1 M NaClO<sub>2</sub>. A hydrophobic frit (19.6 x 3.2mm, Biocomma) was inserted at the bottom of the column. (c) Entegris GPUS35FHX and (d) Agilent OT3-4 commercial packed gas filters.

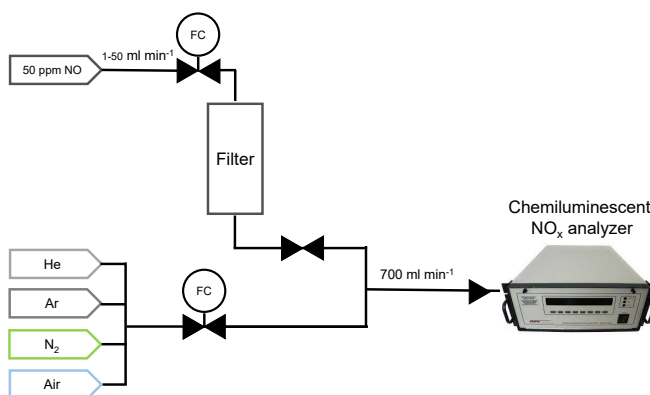


**Figure A.4.2** Simplified schematic of the gaseous NO<sub>x</sub> quantification measurements.

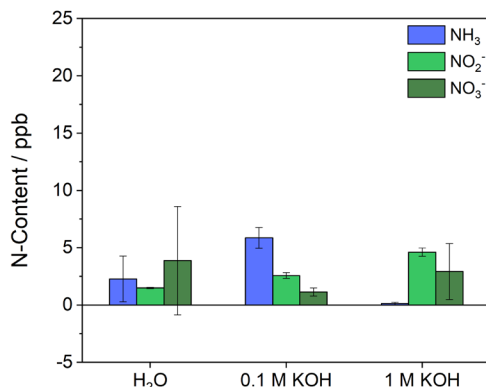


**Figure A.4.3** 24 hour open-to-air exposure of 2 ml  $\text{H}_2\text{O}$ , 0.1 M KOH and 1 M KOH in a 12 ml sample tube. The presented values are corrected with blank samples measured at  $t = 0$ . Error bar indicates the standard deviation of triplicates.

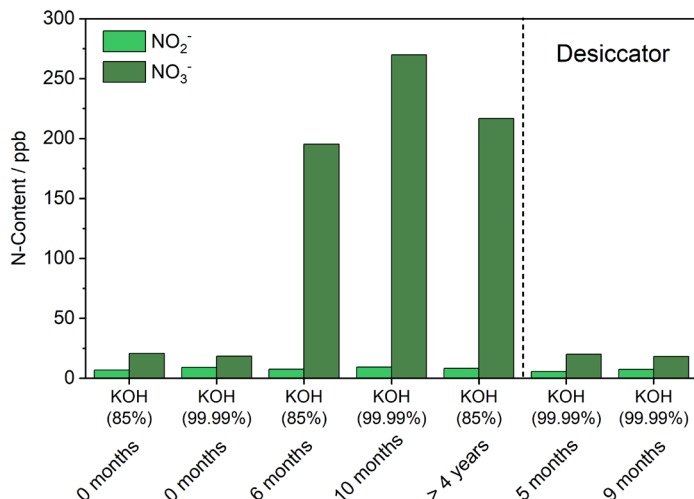


**Figure A.4.4** Comparison between KOH salt storage conditions in a chemical safety cabinet and vacuum desiccator (add brand here). The projected impurity concentrations were quantified by IC using freshly prepared 1 M KOH solutions.

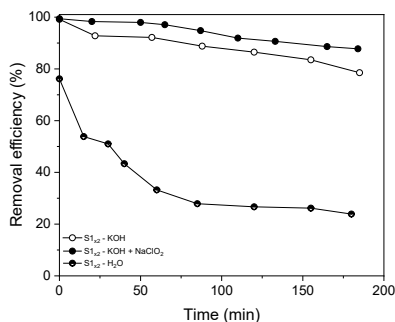


**Figure A.4.5**  $\text{NO}_x$  removal efficiency over time, measured at  $10 \text{ mL min}^{-1}$  for two 20 mL scrubbers (Supelco Analytical, 6-4835) connected in series containing MilliQ water (half-filled symbols), 0.1 M KOH (open symbols) and 0.1 M KOH + 0.1 M  $\text{NaClO}_2$  (solid symbols) as with liquid trap solution.

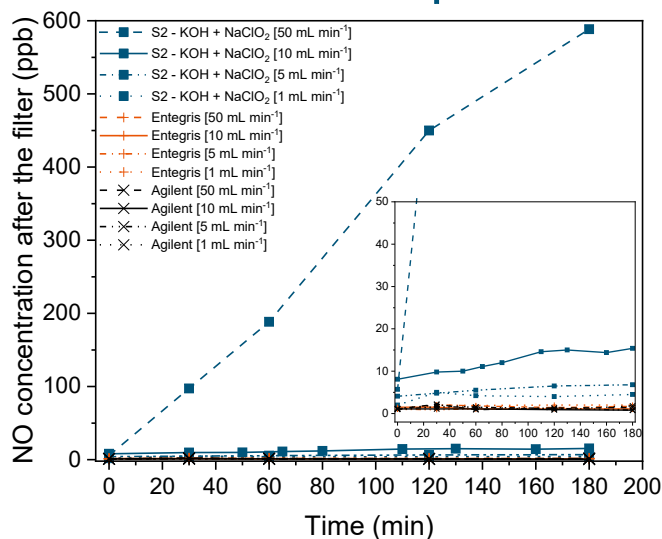


**Figure A.4.6** NO concentration measured over time at the outlet of each gas filter tested with an inlet gas mixture of 50 ppm NO in He at different flow rates (50 mL min<sup>-1</sup> dashed line, 10 mL min<sup>-1</sup> solid line, 5 mL min<sup>-1</sup> dash-dot line, and 1 mL min<sup>-1</sup> dotted line). In-house made scrubber (S2) filled with a 0.1 M KOH and 0.1 M NaClO<sub>2</sub> trapping solution is shown in blue, while the commercial Entegris and Agilent packed filters are shown in orange and black, respectively.

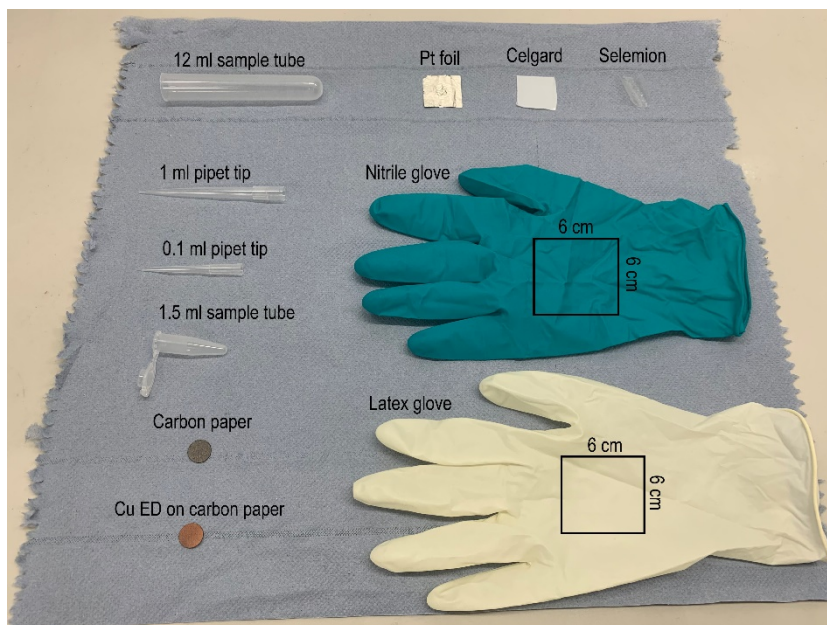


**Figure A.4.7** Photographic overview of the lab consumables and components used for screening.

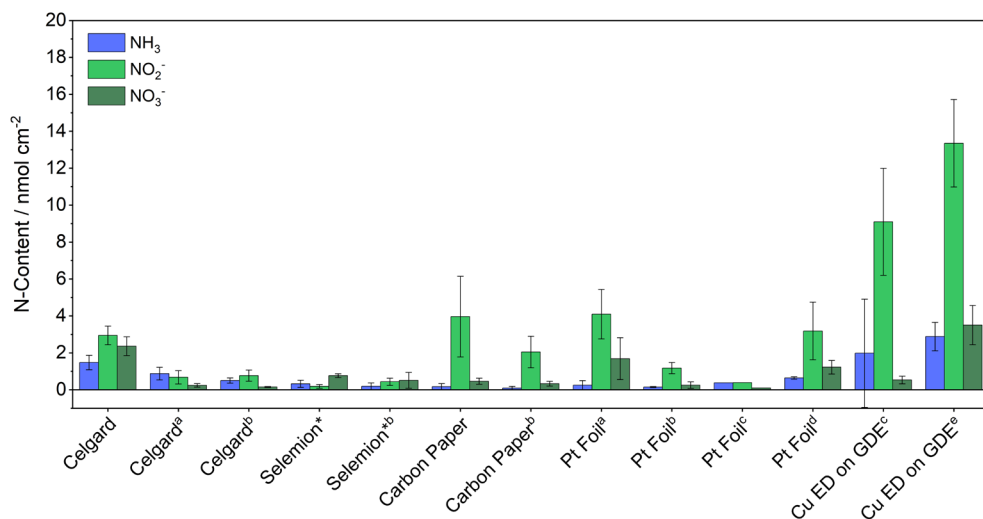


**Figure A.4.8** Screening of typical electrochemical cell components, N-impurities in nmol normalized by geometric area corresponding to Figure 4. Release of extraneous  $\text{NH}_3$ ,  $\text{NO}_2^-$  and  $\text{NO}_3^-$  sources from common used electrochemical cell components during ultra-sonicating in 5 ml of 0.1 M KOH for 15 min using different pre-treatment steps. All components, except the carbon paper had a 2.5 cm x 2.5 cm dimension. The carbon paper and Cu GDE were finely cut discs with a diameter of 1.2 cm. Indicated as unlabelled is untreated and fetched from the as received package. (a) rinsed excessively with  $\text{H}_2\text{O}$ , (b) sonicated for 15 min in 0.1 M KOH, (c) heat treatment in Ar at 200 °C overnight (12 hours), (d) sonicated for 15 min in 0.1 M KOH plus flame annealing with butane flame torch, (e) rinsed with  $\text{H}_2\text{O}$  and isopropanol, then electrochemical treatment by performing 10 cyclic voltammetry scans with only reductive currents (-0.2 V to -0.7 V vs. RHE) and rinsed with  $\text{H}_2\text{O}$  afterwards as elaborately described in ref.<sup>35</sup>. \*  $\text{NO}_2^-$  assay with the Griess test. Every component is measured in triplicates.

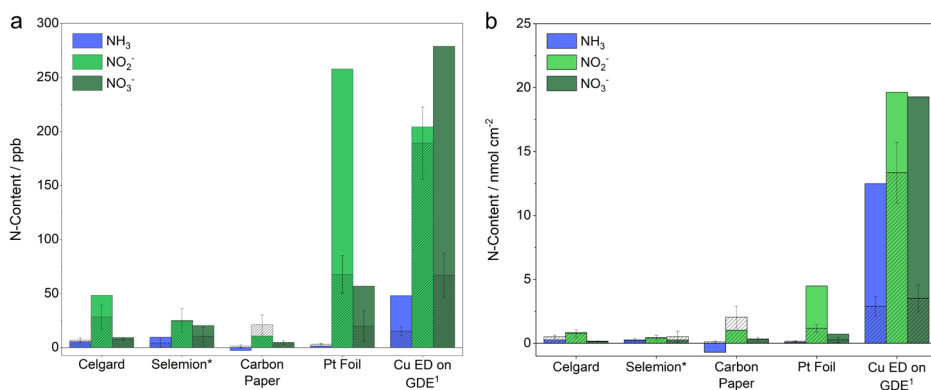


**Figure A.4.9** Release of N-impurities after 1 hour sonication in 0.1 M KOH after the following pre-treatment steps; 15 min of ultra-sonication in 0.1 M KOH; <sup>1</sup> rinsed with  $\text{H}_2\text{O}$  and isopropanol, then electrochemically reduced by performing 10 cyclic voltammetry scans with in a reduction regime (-0.2 V to -0.7 V vs. RHE) and rinsed with  $\text{H}_2\text{O}$  afterwards as elaborately described in ref.<sup>35</sup>. \*  $\text{NO}_2^-$  was quantified with the spectrophotometric Griess test due to identified  $\text{Cl}^-$  overlap in the ion chromatogram.

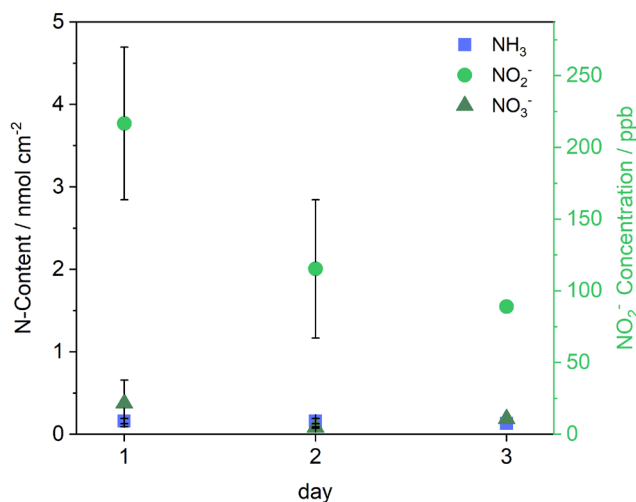


**Figure A.4.10** Pt foil (6.25 cm<sup>2</sup>) pre-treated with the alkaline wash at three subsequent days using a 5 ml test volume.

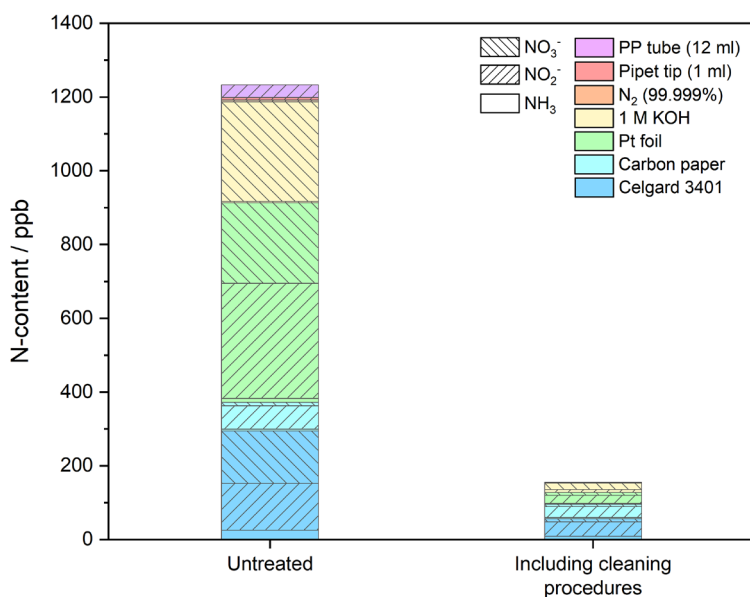


**Figure A.4.11** Estimation of N containing contamination derived from untreated commonly adopted electrochemical cell components and lab consumables and the resulting reduction of these N contamination achieved applying the most effective cleaning procedures discussed in this work. The applied cleaning procedure are: alkaline wash for Celgard 3401 membrane and carbon paper, heat treatment for Pt foil, storing the KOH in a desiccator, rinsing pipet tips and tubes with ultrapure water. With these precautions the N contamination level for a typical electrochemical NRR experiment can be limited to about 150 ppb. The corresponding N-content in nmol is given in **Figure 4.11**

## References

1. World fertilizer trends and outlook to 2022. *Food and Agriculture Organization of the United Nations* **2019**, 1-9.
2. Intelligence, M. *Ammonia Market - Growth, Trends, COVID-19 Impact, and Forecasts (2022 - 2027)*; 2021.
3. van der Ham, C. J. M.; Koper, M. T. M.; Hetterscheid, D. G. H., Challenges in reduction of dinitrogen by proton and electron transfer. *Chemical Society Reviews* **2014**, *43* (15), 5183-5191.
4. MacFarlane, D. R.; Cherepanov, P. V.; Choi, J.; Suryanto, B. H. R.; Hodgetts, R. Y.; Bakker, J. M.; Ferrero Vallana, F. M.; Simonov, A. N., A Roadmap to the Ammonia Economy. *Joule* **2020**, 1-20.
5. Arias, P. A., N. Bellouin, E. Coppola, R.G. Jones, G. Krinner, J. Marotzke, V. Naik, M.D. Palmer, G.-K. Plattner, J. Rogelj; M. Rojas, J. S., T. Storelvmo, P.W. Thorne, B. Trewin, K. Achuta Rao, B. Adhikary, R.P. Allan, K. Armour, G. Bala; R. Barimalala, S. B., J.G. Canadell, C. Cassou, A. Cherchi, W. Collins, W.D. Collins, S.L. Connors, S. Corti, F. Cruz; F.J. Dentener, C. D., A. Di Luca, A. Diongue Niang, F.J. Doblas-Reyes, A. Dosio, H. Douville, F. Engelbrecht; V. Eyring, E. F., P. Forster, B. Fox-Kemper, J.S. Fuglestad, J.C. Fyfe, N.P. Gillett, L. Goldfarb, I. Gorodetskaya; J.M. Gutierrez, R. H., E. Hawkins, H.T. Hewitt, P. Hope, A.S. Islam, C. Jones, D.S. Kaufman, R.E. Kopp, Y. Kosaka; J. Kossin, S. K., J.-Y. Lee, J. Li, T. Mauritsen, T.K. Maycock, M. Meinshausen, S.-K. Min, P.M.S. Monteiro; T. Ngo-Duc, F. O., I. Pinto, A. Pirani, K. Raghavan, R. Ranasinghe, A.C. Ruane, L. Ruiz, J.-B. Sallée, B.H. Samset; S. Sathyendranath, S. I. S., A.A. Sörensson, S. Szopa, I. Takayabu, A.-M. Tréguier, B. van den Hurk, R. Vautard; K. von Schuckmann, S. Z., X. Zhang, and K. Zickfeld, *Technical Summary. In Climate Change 2021: The Physical Science Basis. Contribution of Working Group I to the Sixth Assessment Report of the Intergovernmental Panel on Climate Change 2021*; pp 33-144.
6. Lim, J.; Fernández, C. A.; Lee, S. W.; Hatzell, M. C., Ammonia and Nitric Acid Demands for Fertilizer Use in 2050. *ACS Energy Letters* **2021**, *6* (10), 3676-3685.
7. Smith, C.; Hill, A. K.; Torrente-Murciano, L., Current and future role of Haber–Bosch ammonia in a carbon-free energy landscape. *Energy & Environmental Science* **2020**, *13* (2), 331-344.
8. Chatterjee, S., Limitations of Ammonia as a Hydrogen Energy Carrier for the Transportation Sector. **2021**.
9. Choi, J.; Suryanto, B. H. R.; Wang, D.; Du, H. L.; Hodgetts, R. Y.; Ferrero Vallana, F. M.; MacFarlane, D. R.; Simonov, A. N., Identification and elimination of false positives in electrochemical nitrogen reduction studies. *Nature Communications* **2020**, *11* (1), 1-10.
10. Choi, J.; Du, H.-L.; Nguyen, C. K.; Suryanto, B. H. R.; Simonov, A. N.; MacFarlane, D. R., Electroreduction of Nitrates, Nitrites, and Gaseous Nitrogen Oxides: A Potential Source of Ammonia in Dinitrogen Reduction Studies. *ACS Energy Letters* **2020**, *5* (6), 2095-2097.
11. Kolen, M.; Ripepi, D.; Smith, W. A.; Burdyny, T.; Mulder, F. M., Overcoming Nitrogen Reduction to Ammonia Detection Challenges: The Case for Leapfrogging to Gas Diffusion Electrode Platforms. *ACS Catalysis* **2022**, 5726-5735.



12. Izelaar, B.; Ripepi, D.; Asperti, S.; Dugulan, I. A.; Hendrikx, R. W. A.; Böttger, A. J.; Mulder, F. M.; Kortlever, R., Revisiting the Electrochemical Nitrogen Reduction on Molybdenum and Iron Carbides: Promising Catalysts or False Positives? *In Preparation*.
13. Choi, J.; Choi, J.; Du, H. L.; Du, H. L.; Nguyen, C. K.; Nguyen, C. K.; Suryanto, B. H. R.; Simonov, A. N.; Simonov, A. N.; MacFarlane, D. R.; MacFarlane, D. R., Electroreduction of Nitrates, Nitrites, and Gaseous Nitrogen Oxides: A Potential Source of Ammonia in Dinitrogen Reduction Studies. *ACS Energy Letters* **2020**, 5 (6), 2095-2097.
14. Ko, B. H.; Hasa, B.; Shin, H.; Zhao, Y.; Jiao, F., Electrochemical Reduction of Gaseous Nitrogen Oxides on Transition Metals at Ambient Conditions. *Journal of the American Chemical Society* **2022**, 144 (3), 1258-1266.
15. Dima, G. E.; De Vooy, A. C. A.; Koper, M. T. M., Electrocatalytic reduction of nitrate at low concentration on coinage and transition-metal electrodes in acid solutions. *Journal of Electroanalytical Chemistry* **2003**, 554-555 (1), 15-23.
16. Shibata, M.; Murase, K.; Furuya, N., Electroreduction of Nitrous Oxide to Nitrogen at Gas Diffusion Electrodes with Various Metal Catalysts. *Denki Kagaku oyobi Kogyo Butsuri Kagaku* **1997**, 65 (12), 1039-1043.
17. Choi, J.; Suryanto, B. H. R.; Wang, D.; Du, H.-L.; Hodgetts, R. Y.; Ferrero Vallana, F. M.; MacFarlane, D. R.; Simonov, A. N., Identification and elimination of false positives in electrochemical nitrogen reduction studies. *Nature Communications* **2020**, 11 (1), 5546.
18. It should be noted that atmospheric N<sub>2</sub>O is stable for about 115 years and is relatively inert, since it does not adsorb well on metal surfaces. Additionally, N<sub>2</sub>O solubility in water is also very low (1.24 g/L at 20 °C and 1 atm).
19. Chen, Y.; Liu, H.; Ha, N.; Licht, S.; Gu, S.; Li, W., Revealing nitrogen-containing species in commercial catalysts used for ammonia electrosynthesis. *Nature Catalysis* **2020**, 1-7.
20. Makela, S.; Yazdanpanah, M.; Adatia, I.; Ellis, G., Disposable Surgical Gloves and Pasteur (Transfer) Pipettes as Potential Sources of Contamination in Nitrite and Nitrate Assays. *Clinical Chemistry* **1997**, 43 (12), 2418-2420.
21. Ishibashi, T.; Himeno, M.; Imaizumi, N.; Maejima, K.; Nakano, S.; Uchida, K.; Yoshida, J.; Nishio, M., NO<sub>x</sub> Contamination in Laboratory Ware and Effect of Countermeasures. *Nitric Oxide* **2000**, 4 (5), 516-525.
22. Li, L.; Tang, C.; Yao, D.; Zheng, Y.; Qiao, S.-Z., Electrochemical Nitrogen Reduction: Identification and Elimination of Contamination in Electrolyte. *ACS Energy Letters* **2019**, 4 (9), 2111-2116.
23. Dabundo, R.; Lehmann, M. F.; Treibergs, L.; Tobias, C. R.; Altabet, M. A.; Moisan, P. H.; Granger, J., The Contamination of Commercial <sup>15</sup>N<sub>2</sub> Gas Stocks with <sup>15</sup>N-Labeled Nitrate and Ammonium and Consequences for Nitrogen Fixation Measurements. *PLOS ONE* **2014**, 9 (10), e110335-e110335.
24. Moreira-Coello, V.; Mouriño-Carballido, B.; Maraño, E.; Fernández-Carrera, A.; Pérez-Lorenzo, M.; Bode, A., Quantifying the overestimation of planktonic N<sub>2</sub> fixation due to contamination of <sup>15</sup>N<sub>2</sub> gas stocks. Oxford University Press: 2019.
25. Andersen, S. Z.; Čolić, V.; Yang, S.; Schwalbe, J. A.; Nielander, A. C.; McEnaney, J. M.; Enemark-Rasmussen, K.; Baker, J. G.; Singh, A. R.; Rohr, B. A.; Statt, M. J.; Blair, S. J.; Mezzavilla, S.; Kibsgaard, J.; Vesborg, P. C. K.; Cargnello, M.; Bent, S. F.; Jaramillo, T. F.; Stephens, I. E. L.; Nørskov, J. K.; Chorkendorff, I., A rigorous electrochemical ammonia synthesis protocol with quantitative isotope measurements. *Nature* **2019**, 570 (7762), 504-508.

26. Nielander, A. C.; McEnaney, J. M.; Schwalbe, J. A.; Baker, J. G.; Blair, S. J.; Wang, L.; Pelton, J. G.; Andersen, S. Z.; Enemark-Rasmussen, K.; Čolić, V.; Yang, S.; Bent, S. F.; Cargnello, M.; Kibsgaard, J.; Vesborg, P. C. K.; Chorkendorff, I.; Jaramillo, T. F., A Versatile Method for Ammonia Detection in a Range of Relevant Electrolytes via Direct Nuclear Magnetic Resonance Techniques. *ACS Catalysis* **2019**, 5797-5802.
27. Larson, T. V.; Covert, D. S.; Frank, R.; Charlson, R. J., Ammonia in the human airways: neutralization of inspired acid sulfate aerosols. *Science* **1977**, 197 (4299), 161-3.
28. Liu, H.; Zhang, Y.; Luo, J., The removal of inevitable NO<sub>x</sub> species in catalysts and the selection of appropriate membrane for measuring electrocatalytic ammonia synthesis accurately. *Journal of Energy Chemistry* **2020**, 49 (x), 51-58.
29. Yu, W.; Buabthong, P.; Read, C. G.; Dalleska, N. F.; Lewis, N. S.; Lewerenz, H.-J.; Gray, H. B.; Brinkert, K., Cathodic NH<sub>4</sub><sup>+</sup> leaching of nitrogen impurities in CoMo thin-film electrodes in aqueous acidic solutions †. **2020**.
30. Du, H. L.; Gengenbach, T. R.; Hodgetts, R.; Macfarlane, D. R.; Simonov, A. N., Critical Assessment of the Electrocatalytic Activity of Vanadium and Niobium Nitrides toward Dinitrogen Reduction to Ammonia. *ACS Sustainable Chemistry and Engineering* **2019**, 7 (7), 6839-6850.
31. Shipman, M. A.; Symes, M. D., A re-evaluation of Sn (II) phthalocyanine as a catalyst for the electrosynthesis of ammonia. *Electrochimica Acta* **2017**, 258, 618-622.
32. Hu, B.; Hu, M.; Seefeldt, L.; Liu, T. L., Electrochemical dinitrogen reduction to ammonia by Mo<sub>2</sub>N: catalysis or decomposition? *ACS Energy Letters* **2019**, 4 (5), 1053-1054.
33. Hanifpour, F.; Sveinbjörnsson, A.; Canales, C. P.; Skúlason, E.; Flosadóttir, H. D., Preparation of Nafion Membranes for Reproducible Ammonia Quantification in Nitrogen Reduction Reaction Experiments. *Angewandte Chemie International Edition* **2020**, 59 (51), 22938-22942.
34. Liu, H.; Zhang, Y.; Luo, J., The removal of inevitable NO<sub>x</sub> species in catalysts and the selection of appropriate membrane for measuring electrocatalytic ammonia synthesis accurately. *Journal of Energy Chemistry* **2020**, 49, 51-58.
35. Kani, N. C.; Prajapati, A.; Collins, B. A.; Goodpaster, J. D.; Singh, M. R., Competing Effects of pH, Cation Identity, H<sub>2</sub>O Saturation, and N<sub>2</sub> Concentration on the Activity and Selectivity of Electrochemical Reduction of N<sub>2</sub> to NH<sub>3</sub> on Electrodeposited Cu at Ambient Conditions. *ACS Catalysis* **2020**, 14592-14603.
36. Ripepi, D.; Zaffaroni, R.; Schreuders, H.; Boshuizen, B.; Mulder, F. M., Ammonia Synthesis at Ambient Conditions via Electrochemical Atomic Hydrogen Permeation. *ACS Energy Letters* **2021**, 3817-3823.
37. Ripepi, D.; Zaffaroni, R.; Schreuders, H.; Boshuizen, B.; Mulder, F., Ammonia Synthesis Via Electrochemical Atomic Hydrogen Permeation between 25 and 100 C. *ECS Meeting Abstracts* **2022**, MA2022-01 (36), 1545-1545.
38. Iriawan, H.; Andersen, S. Z.; Zhang, X.; Comer, B. M.; Barrio, J.; Chen, P.; Medford, A. J.; Stephens, I. E.; Chorkendorff, I.; Shao-Horn, Y., Methods for nitrogen activation by reduction and oxidation. *Nature Reviews Methods Primers* **2021**, 1 (1), 1-26.
39. Han, L.; Liu, X.; Chen, J.; Lin, R.; Liu, H.; Lü, F.; Bak, S.; Liang, Z.; Zhao, S.; Stavitski, E.; Luo, J.; Adzic, R. R.; Xin, H. L., Atomically Dispersed Molybdenum Catalysts for Efficient Ambient Nitrogen Fixation. *Angewandte Chemie* **2019**, 131 (8), 2343-2347.
40. Wang, T.; Kou, Z.; Zhang, J.; Wang, H.; Zeng, Y. J.; Wei, S.; Zhang, H., Boosting Faradic efficiency of dinitrogen reduction on the negatively charged Mo sites

modulated via interstitial Fe doping into a Mo<sub>2</sub>C nanowall catalyst. *Chemical Engineering Journal* **2021**, 417, 127924-127924.

41. Qin, B.; Li, Y.; Zhang, Q.; Yang, G.; Liang, H.; Peng, F., Understanding of nitrogen fixation electro catalyzed by molybdenum-iron carbide through the experiment and theory. *Nano Energy* **2020**.
42. Ripepi, D.; Zaffaroni, R.; Kolen, M.; Middelkoop, J.; Mulder, F. M., Operando isotope selective ammonia quantification in nitrogen reduction studies via gas chromatography-mass spectrometry. *Sustainable Energy & Fuels* **2022**, 6 (8), 1945-1949.
43. Zaffaroni, R.; Ripepi, D.; Middelkoop, J.; Mulder, F. M., Gas Chromatographic Method for In Situ Ammonia Quantification at Parts per Billion Levels. *ACS Energy Letters* **2020**, 5 (12), 3773-3777.
44. Weatherburn, M. W., Phenol-Hypochlorite Reaction for Determination of Ammonia. *Analytical Chemistry* **1967**, 39 (8), 971-974.
45. ThermoFisher Application Notes: 72481 IC trace anions concentrated bases. <https://assets.thermofisher.com/TFS-Assets/CMD/Application-Notes/an-72481-ic-trace-anions-concentrated-bases-an72481-en.pdf> (accessed 20-8).
46. Huijsmans, J. F.; Schils, R. L. In *Ammonia and nitrous oxide emissions following field-application of manure: state of the art measurements in the Netherlands*, International Fertiliser Society: 2009.
47. Greenlee, L. F.; Renner, J. N.; Foster, S. L., The Use of Controls for Consistent and Accurate Measurements of Electrocatalytic Ammonia Synthesis from Dinitrogen. *ACS Catalysis* **2018**, 8 (9), 7820-7827.
48. Milieu, R. v. V. e. luchtmeetnet - NH<sub>3</sub> and NO<sub>2</sub>. <https://www.luchtmeetnet.nl/componenten> (accessed 06-07).
49. de Castro, A.; Alegre, D.; Tabarés, F. L., Physisorption of ammonia on AISI 304L stainless steel at different surface temperature under high vacuum conditions. *Nuclear Materials and Energy* **2016**, 9, 1-5.
50. Dentener, F.; Stevenson, D.; Ellingsen, K. v.; Van Noije, T.; Schultz, M.; Amann, M.; Atherton, C.; Bell, N.; Bergmann, D.; Bey, I., The global atmospheric environment for the next generation. *Environmental Science & Technology* **2006**, 40 (11), 3586-3594.
51. Sivachandiran, L.; Thévenet, F.; Gravejat, P.; Rousseau, A., Investigation of NO and NO<sub>2</sub> adsorption mechanisms on TiO<sub>2</sub> at room temperature. *Applied Catalysis B: Environmental* **2013**, 142, 196-204.
52. Zhang, Q.; Li, Y.; Wang, M.; Wang, K.; Meng, F.; Liu, L.; Zhao, Y.; Ma, L.; Zhu, Q.; Xu, W., Atmospheric nitrogen deposition: A review of quantification methods and its spatial pattern derived from the global monitoring networks. *Ecotoxicology and Environmental Safety* **2021**, 216, 112180.
53. Haneef, S.; Johnson, J.; Dickinson, C.; Thompson, G.; Wood, G., Effect of dry deposition of NO<sub>x</sub> and SO<sub>2</sub> gaseous pollutants on the degradation of calcareous building stones. *Atmospheric Environment. Part A. General Topics* **1992**, 26 (16), 2963-2974.
54. Ciais, P.; Sabine, C.; Bala, G.; Bopp, L.; Brovkin, V.; Canadell, J.; Chhabra, A.; DeFries, R.; Galloway, J.; Heimann, M., Carbon and other biogeochemical cycles. Climate change 2013: the physical science basis. Contribution of Working Group I to the Fifth Assessment Report of the Intergovernmental Panel on Climate Change. **2013**.
55. Zhang, L.; Zhou, Q.; Liang, J.; Yue, L.; Li, T.; Luo, Y.; Liu, Q.; Li, N.; Tang, B.; Gong, F.; Guo, X.; Sun, X., Enhancing Electrocatalytic NO Reduction to NH<sub>3</sub> by the CoS Nanosheet with Sulfur Vacancies. *Inorganic Chemistry* **2022**, 61 (20), 8096-8102.

56. Young, C., IUPAC solubility data series. *Oxides of nitrogen (8)* **1981**.
57. Chameides, W. L., The photochemistry of a remote marine stratiform cloud. *Journal of Geophysical Research: Atmospheres* **1984**, 89 (D3), 4739-4755.
58. Joshi, J. B.; Mahajani, V. V.; Juvekar, V. A., Absorption of nox gases. *Chemical Engineering Communications* **1985**, 33 (1-4), 1-92.
59. Patwardhan, J. A.; Joshi, J. B., Unified Model for NOX Absorption in Aqueous Alkaline and Dilute Acidic Solutions. *AIChE Journal* **2003**, 49 (11), 2728-2748.
60. Chen, Y.; Liu, H.; Ha, N.; Licht, S.; Gu, S.; Li, W., Revealing nitrogen-containing species in commercial catalysts used for ammonia electrosynthesis. *Nature Catalysis* **2020**, 3 (12), 1055-1061.
61. Joe Eugene, L. S. M., Ferrenbach, Measurements of nitrogen fixation by direct means. In *Symbiotic Nitrogen Fixation Technology*, Taylor & Francis: 1987; pp 221-255.
62. Nielander, A. C.; Blair, S. J.; McEnaney, J. M.; Schwalbe, J. A.; Adams, T.; Taheri, S.; Wang, L.; Yang, S.; Cargnello, M.; Jaramillo, T. F., Readily Constructed Glass Piston Pump for Gas Recirculation. *ACS Omega* **2020**, 5 (27), 16455-16459.
63. Guo, R. T.; Hao, J. K.; Pan, W. G.; Yu, Y. L., Liquid Phase Oxidation and Absorption of NO from Flue Gas: A Review. *Separation Science and Technology (Philadelphia)* **2015**, 50 (2), 310-321.
64. Chu, H.; Chien, T. W.; Twu, B. W., The absorption kinetics of NO in NaClO<sub>2</sub>/NaOH solutions. *Journal of Hazardous Materials* **2001**, 84 (2-3), 241-252.
65. Prinetto, F.; Ghiotti, G.; Nova, I.; Lietti, L.; Tronconi, E.; Forzatti, P., FT-IR and TPD Investigation of the NO<sub>x</sub> Storage Properties of BaO / Al<sub>2</sub>O<sub>3</sub> and Pt - BaO. **2001**, (x), 12732-12745.
66. Correa, S. M., A review of NO<sub>x</sub> formation under gas-turbine combustion conditions. *Combustion Science and Technology* **1993**, 87 (1-6), 329-362.
67. Hayhurst, A.; Vince, I., The origin and nature of "prompt" nitric oxide in flames. *Combustion and Flame* **1983**, 50, 41-57.

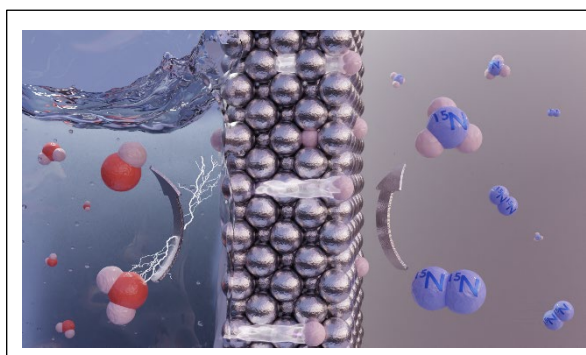


---

# Ammonia synthesis at ambient conditions via electrochemical atomic hydrogen permeation

# 5

Direct electrochemical nitrogen reduction holds the promise of enabling the production of carbon emission-free ammonia, which is an important intermediate in fertiliser industry and a candidate green energy carrier. Here we show a novel strategy for ambient condition ammonia synthesis using a hydrogen permeable nickel membrane electrode to spatially separate the electrolyte and hydrogen activation side from the nitrogen activation and hydrogenation sites. Ammonia is produced catalytically directly in the gas phase and in the absence of electrolyte on a polycrystalline nickel surface via hydrogenation of adsorbed nitrogen by electrochemically permeating atomic hydrogen from water reduction. Gaseous nitrogen activation at the nickel electrode is confirmed with  $^{15}\text{N}$  isotope labelling experiments and it is attributed to a Mars-van Krevelen mechanism enabled by the formation of N-vacancies upon hydrogenation of surface nitrides. We further show that gaseous hydrogen does not hydrogenate the adsorbed nitrogen, strengthening the benefit of having an atomic hydrogen permeable electrode. The proposed approach opens new directions towards green ammonia.



## 5.1 Introduction

The synthesis of ammonia ( $\text{NH}_3$ ) from nitrogen ( $\text{N}_2$ ) and hydrogen ( $\text{H}_2$ ) is widely considered one of the most important discoveries of the 20<sup>th</sup> century<sup>1</sup> as ammonia plays an essential role as intermediate in nitrogen-based fertiliser production, ultimately sustaining the exponential growth in human population<sup>2</sup>. Despite being abundant in Earth's atmosphere, dinitrogen is stable and relatively inert, requiring high temperature and pressure for its activation and conversion to ammonia. The current Haber-Bosch process, with an estimated annual global production of 150 million metric tons of  $\text{NH}_3$ <sup>3</sup>, consumes roughly 1-2 % of the global energy demand<sup>4</sup> and 5 % of the yearly extracted methane as hydrogen source<sup>5</sup> via steam-methane reforming. As consequence, this process alone is responsible for about 1.4 % of the worldwide  $\text{CO}_2$  emissions<sup>6</sup>. In a world aiming to become  $\text{CO}_2$  neutral and renewable energy based by 2050, such fossil derived ammonia must be replaced by an alternative renewable option<sup>6</sup>. In addition to the current primary use as fertiliser intermediate, liquid ammonia is also regarded as a potential high-density energy carrier (22.5 MJ kg<sup>-1</sup>, liquid at 8 bar and RT, or 1 bar and -33° C)<sup>7, 8</sup>, yet its production with the current state of the art fossil based technology would be largely unsustainable.

Electrochemical ammonia synthesis is an attractive solution as it can produce carbon free  $\text{NH}_3$  in a flexible and scalable manner from the intermittent surplus of electricity generated by decentralised renewables<sup>9</sup>. However, despite considerable growing interest and recent developments<sup>10-13</sup>, electrochemical ammonia production at near ambient conditions remains unpractical and multiple challenges have to be tackled to further enable direct electrolytic ammonia synthesis. First, the nitrogen reduction reaction to ammonia is in competition with the relatively easier hydrogen evolution reaction (HER). The activation of dinitrogen is an arduous process due to the stable  $\text{N}\equiv\text{N}$  bond (941 kJ mol<sup>-1</sup>) and due to the absence of a permanent dipole in the  $\text{N}_2$  molecule, thus involving only neutral species. In contrast, hydrogen evolution proceeds according to the Volmer mechanism, involving charged hydrogen species (protons or polar water molecules). Conventional electrochemistry is carried out in the presence of an aqueous electrolyte, which contains an excess of hydrogen species (as  $\text{H}_2\text{O}$ ,  $\text{H}^+$  or  $\text{OH}^-$ ) and therefore, in an aqueous solution, at negative potential, hydrogen reduction and adsorption on the catalyst's active sites easily prevails over nitrogen adsorption and activation<sup>14-17</sup>. The adsorbed H readily recombines on

the catalyst surface to form  $H_2$ , rather than being employed in the production of ammonia; consequently, the electrochemical process is characterised by low faradaic efficiency. Second, the solubility of dinitrogen in aqueous electrolytes is rather low (0.7mM at ambient conditions<sup>15</sup>), thus the availability of nitrogen at the catalyst surface becomes limiting. Third,  $NH_3$  is produced in contact with the electrolyte and partitioned between gas phase and liquid phase, demanding appropriate product separation. Fourth, the catalyst surface preferentially adsorbs oxygen traces from the electrolyte; this poisons nitrogen activation sites and deactivates the catalyst<sup>17, 18</sup>.

Substantial efforts have been recently made to develop new strategies to overcome the mentioned challenges in direct electrochemical nitrogen reduction to ammonia at ambient conditions. In particular, studies suggested that  $NH_3$  selectivity could be improved by engineering the catalyst-electrolyte interface<sup>14, 15, 19-22</sup> or using non-aqueous electrolytes<sup>14, 21, 23-25</sup> to increase nitrogen concentration and limit the proton and electron transfer at the catalyst interface. However, both approaches do not ensure a complete separation from the electrolyte nor do they prevent the competition of different adsorbate species at the catalyst surface, as previously discussed.

In this contribution, we present an unconventional electrochemical design to perform catalytic nitrogen reduction to ammonia by separating the electrolytic hydrogen activation from the catalytic dinitrogen activation and hydrogenation at the two opposite sides of a dense metallic hydrogen permeable electrode. The working principle is demonstrated using a thin nickel foil as hydrogen permeable electrode. Ammonia is produced catalytically at ambient conditions via the unprecedented reaction between electrochemically permeating atomic hydrogen and adsorbed nitrogen, brought together in the absence of the electrolyte through this Ni electrode. The formation of N-vacancies, enabled by the hydrogenation of surface nitrogen atoms, shows a clear effect on the catalytic cycle, indicating the occurrence of a Mars-van Krevelen mechanism for  $N_2$  activation. We also show that the presence of active nitrogen on the Ni surface hinders the activation of gaseous  $H_2$  that is typically needed for  $NH_3$  synthesis. This finding corroborates the benefit of applying permeating atomic hydrogen for the hydrogenation of adsorbed N. The demonstrated reaction pathway represents a novel mechanism for direct electrolytic ammonia production at ambient conditions, which has the potential to be an effective strategy to overcome most of the challenges in electrochemical ammonia synthesis.



## 5.2 Experimental

**Materials.** Polycrystalline nickel foil (99.9 %) with a thickness of 0.0125 mm was purchased from Goodfellow and used as dense hydrogen permeable working electrode. A nickel wire (> 99 %) with a diameter of 1 mm was purchased from MaTeck GmbH and used as counter electrode. Electrolyte solution was prepared by dissolving potassium hydroxide (99.9 % from VWR International) in Milli-Q water. Nickel, Yttrium and Palladium sputtering targets (99.9 %) were purchased from Mateck GmbH.

**Sample preparation.** All samples were first extensively cleaned in an AJA ultra-high vacuum magnetron sputtering system with an Ar/H<sub>2</sub> plasma treatment for 30 minutes. Prior to the plasma process, the base pressure of the UHV chamber was about 10<sup>-8</sup> mbar. Ar (6N - 35 sccm) and H<sub>2</sub> (6N - 5 sccm) were constantly fed in the process chamber, held at a pressure of 5 µbar, while plasma was generated at 20W RF power.

Surface nitrides were prepared by an additional plasma nitriding step using RF power supplies in an Ar:N<sub>2</sub> mixture (2:1) at a total pressure of 20 µbar. Ten minutes exposure at 40W RF power were sufficient to obtain a stable thin surface nitride layer.

**X-ray Photoelectron Spectroscopy.** XPS spectra were recorded with a Thermo Scientific K-alpha spectrometer using an Al K $\alpha$  monochromator. The base pressure of the UHV XPS analysis chamber was 2·10<sup>-9</sup> mbar. For all the measurements the spot size was set to 400 µm and the HR-XPS spectra were acquired with a pass energy of 50 eV and step size of 0.1 eV. The C 1s adventitious carbon at 284.8 eV was used for calibration and Shirley background was applied.

Freshly prepared samples were transferred from the AJA UHV chamber to the XPS load lock via a sealed sample holder to prevent contamination from air. For the XPS nitrogen exposure experiment, the Ar/H<sub>2</sub> cleaned Ni surface was further *in-situ* cleaned for 30 seconds via Ar ion bombardment (1keV) in the XPS analysis chamber (**Figure 5.2a**). The sample was then placed back in the XPS load lock (10<sup>-7</sup> mbar base pressure), where purified N<sub>2</sub> gas was dosed until reaching a pressure of 1 bar, followed by immediate evacuation of the load lock. Once reaching a base pressure of about 10<sup>-7</sup> mbar, the sample was transferred back to the analysis chamber for the final measurement (**Figure 5.2b**). The

XPS N 1s peak of chemisorbed atomic nitrogen ( $N^{ad}$ ) on transition metals is typically reported to be in a binding energy range between 396 and 398 eV<sup>26, 27</sup>, while molecular nitrogen has been found at higher binding energies, from about 400 eV<sup>28</sup>.

XPS depth profiles were acquired alternating *in-situ* Ar ions (1 keV) etch cycles with XPS measurements in snapshot mode (150eV pass energy). The estimation of the etching rate is obtained from the complete etching of 50 nm Ni thin film on a SiO<sub>2</sub>/Si substrate (**Figure A.5.15**).

**Electrochemical setup.** Ni foils were cut with diameter of 28 mm and fit into the custom-made electrochemical cell with a geometrical active area of 2.5 cm<sup>2</sup> (18 mm inner diameter). An aqueous solution of 1 M KOH was used as electrolyte and circulated through the electrochemical cell. A peristaltic pump (Masterflex) provided a continuous electrolyte flow of 6.5 mL/min. The feed of N<sub>2</sub>, He and H<sub>2</sub> in the cathodic gas compartment was regulated by means of dedicated mass flow controllers (EL Flow Prestige - Bronkhorst). Prior inlet to the cell the gases were passed through a gas purifier (Agilent OT3-4). SilcoNert®2000 tubing was used for all the gas connections. A Parstat MC 1000 potentiostat was used in a two-electrode configuration for the galvanostatic charging of 5 mA cm<sup>-2</sup>.

**Ammonia detection.** Ammonia detection was carried out directly from the gas phase with an *in-line* gas chromatographic method with about 5 minutes analysis time and a lower detection limit of about 150 ppb<sup>29</sup>. A TRACE™ 1300 Gas Chromatograph (from Interscience BV - Thermo Fisher Scientific) was equipped with Agilent Select Low Ammonia column located in the GC oven chamber, a pulse discharge detector and two secondary thermal conductivity detectors. Calibration curve was carried out by dosing certificated calibration gas mixtures of 13.8 ppm and 2.2 ppm NH<sub>3</sub> in N<sub>2</sub> and dilute them with pure N<sub>2</sub> to the chosen concentration (**Figure A.5.16**).

The described chromatographic method was coupled with a single quadrupole mass spectrometer (from Interscience BV - Thermo Fisher Scientific) to *in-situ* detect isotopologues of NH<sub>3</sub>. The adoption of the Agilent Select Low Ammonia column for water/ammonia separation made possible to circumvent the notorious challenge of <sup>14</sup>NH<sub>3</sub>/OH<sup>-</sup> and <sup>15</sup>NH<sub>3</sub>/H<sub>2</sub>O overlapping *m/z* ratios. The <sup>14</sup>NH<sub>3</sub> is characterised by *m/z* equal

to 16 (80%) and 17 (100%), while  $^{15}\text{NH}_3$  by  $m/z$  equal to 17 (80%) and 18 (100%). The quantification of the produced ammonia was carried out based on the peak area of the  $m/z$  17 at the retention time corresponding to ammonia (1.83 min). The contributions from  $^{15}\text{NH}_3$  and  $^{14}\text{NH}_3$  were resolved from the known fragmentation ratio, which results fall within the experimental error. The calibration curve of  $m/z$  17 was carried out by dosing a certificated calibration gas mixture of 13.8 ppm  $\text{NH}_3$  in  $\text{N}_2$  and dilute them with pure  $\text{N}_2$  to the chosen concentration (**Figure A.5.8**).

**Control experiments.** The need for a rigorous assessment on the gas purity was recently outlined in the context of  $\text{NH}_3$  synthesis<sup>23, 30-32</sup>. All the high purity gases, He (Linde - 5N),  $\text{N}_2$  (Linde - 5N) and  $^{15}\text{N}_2$  (98 atom %  $^{15}\text{N}$ , Sigma-Aldrich), used in the electrochemical tests were additionally purified with an *in-line* trap (Agilent OT3-4), before entering the cell, ensuring a contaminants-free reaction environment. The *in-line* GC ammonia detection method<sup>29</sup> used in this work shows no sign of  $\text{NH}_3$  contaminations in our setup above the detection limit of 150 ppb in the gas phase when  $1 \text{ mL min}^{-1}$  of purified carrier gas flows through the system at open circuit conditions. No  $^{15}\text{NH}_3$  was detected with GC-MS during control experiments (using He or  $^{14}\text{N}_2$ ), while the  $^{15}\text{NH}_3$  produced during  $^{15}\text{N}$  experiments confirmed the catalytic process. Moreover, the direct sampling of the gas stream from the cathodic gas compartment of the electrolytic cell ensures the elimination of external sources of contamination, for instance due to laborious sample handling typical of the most common liquid detection methods used for  $\text{NH}_3$  determination (i.e. Nessler's reagent and  $^1\text{H}$  NMR, which rely on concentration of the  $\text{NH}_3$  in an acid trap, and that can also accumulate impurities present in the feed gas flow).

Oxidised forms of nitrogen ( $\text{NO}_x$ ) represent another potential source of contamination in  $\text{NH}_3$  synthesis experiments<sup>31, 32</sup>. From the HR-XPS analysis of the N 1s spectrum (**Figure 5.2**), we verified the absence of nitrogen-containing impurities in the electrode material. In particular,  $\text{NO}_x$  are characterised by XPS signals at high binding energies in the N 1s spectrum, typically higher than 400 eV<sup>33, 34</sup>.  $\text{NO}_x$  contaminations can also be found in research grade purity (5N)  $\text{N}_2$  and Ar, up to about a level of 220 ppb and 170 ppb, respectively<sup>31</sup>. These small contaminations can lead to false positives especially in electrochemical cells where high flowrate nitrogen gas is in contact with a liquid alkaline electrolyte, which can absorb and accumulate  $\text{NO}_x$ . However, the  $\text{NH}_3$  synthesis in the

present work is carried out directly in the gas phase (at 1 mL min<sup>-1</sup> feed gas flow rate), in the absence of electrolyte and with direct gaseous NH<sub>3</sub> detection via GC. A quadrupole mass spectrometer (MS) with secondary electron multiplier, from Hiden Analytics, was used to test the NO<sub>x</sub> removal action of the gas purifier. A certified calibration gas containing 100 ppm of nitric oxide in He was analysed into the MS, monitoring the mass-to-charge ratio ( $m/z$ ) equal to 30 (**Figure A.5.17**). When after about 35 minutes the gas mixture was fed through the *in-line* gas purifier before reaching the MS inlet, one observes the drop in  $m/z=30$  signal, indicating the complete NO absorption and removal.

The level of NO<sub>x</sub> contaminations in the feed gases and the efficacy of the N<sub>2</sub> gas purification was also assessed via nitrite and nitrate spectrophotometric determination (**Figure A.5.18** and **Figure A.5.19**). The gases were continuously bubbled (40 mL min<sup>-1</sup>), for a prolonged period of time, through two 0.1 M KOH solutions (20 mL) connected in series. For nitrite determination, 1 mL of sample was transfer to a glass vial followed by 10 mL HCl (10 mM) and 0.2 mL of reagent to produce a diazide compound with a red colour; successively incubated for 20 min at ambient temperature and immediately after analysed at the UV-vis at 540 nm. The reagent stock solution was prepared by adding sulphanilamide (0.2 g) and N-(1-naphtyl)ethylenediamine dihydrochloride (0.01 g) to 2.5 mL of MilliQ water and 0.5 mL of phosphoric acid. For nitrate determination, 3.5 mL of sample was transfer to a glass vial followed by 505  $\mu$ L of HCl (1.2 M) and 10  $\mu$ L of 0.8 wt% sulfamic acid. The resulting solution was incubated for 20 min at ambient temperature and immediately after analysed at the UV-vis at 220 and 275 nm. Traces of NO<sub>x</sub> were measured from not purified gases; however, the *in-line* gas purifier showed no detectable amount of NO<sub>x</sub> contamination above ppb levels (**Table A.5.1**), which excludes NO<sub>x</sub> reduction by permeated H to be responsible for the > 150 ppb up to about 6 ppm NH<sub>3</sub> signals.

**Electrochemical hydrogen permeation.** The electrochemical hydrogen permeation through the Ni foil was measured using the method developed by Devanathan and Stachurski<sup>35</sup>. Both compartments of the Devanathan-Stachurski cell were filled with 1M KOH, to match the ammonia synthesis experimental conditions. In the cathodic compartment, atomic hydrogen is generated at the cathode surface by water dissociation (5 mA cm<sup>-2</sup>), subsequently the adsorbed hydrogen is absorbed into the bulk and diffuses through the lattice of the sample. In the anodic compartment, permeating atomic hydrogen

is oxidised at constant potential (+0.3 V vs SHE). The resulting anodic current is directly proportional to the hydrogen permeating through the sample. The Ni foil working electrode was physically grounded and the multichannel potentiostat (Parstat MC 1000) set in floating mode. To accurately measure the permeation current electrochemically, a protective Pd thin layer of 20 nm was sputter deposited at the hydrogen exit side; this approach is widely used in literature for electrochemical hydrogen permeation measurements<sup>36</sup> (the Pd layer is absent during NH<sub>3</sub> synthesis on an equivalent Ni foil). The background oxidation current was allowed to reach a value of lower than 1  $\mu\text{A cm}^{-2}$ , prior the starting of the experiment. The transient electro-permeation of hydrogen gives the characteristic s-shaped curve (**Figure A.5.2**).

**Hydrogenography.** The hydrogen adsorption and dissociation (i.e. hydrogen spillover) on the metal catalyst was studied with a metal hydride based optical hydrogen sensor<sup>37</sup>. A thin yttrium layer of about 60 nm was sputter deposited on top of a transparent quartz substrate, in turn coated with a 20 nm layer of nickel. After, when required, surface nitrides were prepared by an additional plasma nitriding step. The multilayer thin film samples are then placed in a sealed chamber, which is first evacuated and then kept under a constant hydrogen pressure of 1 bar. A white light LED lamp, placed underneath the hydrogen loading chamber, is used for illumination through the samples. Upon hydrogen exposure, the hydrogen can dissociate on the top layer of the metal surface under investigation. Hence, atomic hydrogen diffuses through the thin metal, reaching the yttrium layer and forming an yttrium hydride phase. The hydrogenation of Y results in a visible change in optical transmittance<sup>38</sup>, monitored with a digital camera (Canon EOS 550D).

**Figure A.5.5** shows the comparison between a pure Ni surface and a Ni surface pre-exposed to nitrogen plasma. Only the pure nickel surface showed significant yttrium hydride formation after 7 hours of exposure to 1 bar of H<sub>2</sub> at room temperature; indicating that pre-chemisorbed nitrogen blocks H<sub>2</sub> spillover. Eventually, noticeable yttrium hydride formation on nitride Ni surface was observed only after about 280 hours.

To rule out the possibility that the surface nitride layer would strongly affect the hydrogen permeation, preventing the atomic hydrogen to reach the underlying Yttrium layer, we repeated the same experiment by adding to two new samples (i.e. nitrided nickel and pure nickel) a Pd top layer of 20 nm, which acts as hydrogen spillover catalyst. In this

case, the complete transformation of Y in yttrium hydride was achieved after less than 2 seconds for both samples, showing no significant differences in hydrogen permeability.

### 5.3 Results and discussion

**System design.** To limit the competition between nitrogen and hydrogen, a dense hydrogen permeable electrode is used to separate two independent compartments dedicated to the spatially decoupled hydrogen activation and nitrogen adsorption respectively, as shown in **Figure 5.1**.

The liquid compartment contains the aqueous electrolyte required for the coupled electrochemical water oxidation and reduction reactions, driven by the applied potential. Here, the hydrogen is electrochemically inserted in the lattice of the negatively charged thin metallic electrode, permeable only to atomic hydrogen via a solution-diffusion mechanism<sup>39</sup>. Importantly, the hydrogen atoms flux can be tuned, by a large extent, by changing the cathodic charging and water reduction driving force, which is a potential advantage of a hydrogen permeable electrode<sup>40</sup>. Thus, the dense hydrogen permeable electrode provides a controlled access of protons and electrons, delivered as atomic hydrogen to the nitrogen active sites, preventing at the same time the poisoning of the catalyst by blocking the access of O<sub>2</sub>, H<sub>2</sub>O and electrolyte.

In the gas compartment, the electrode is only in contact with gaseous nitrogen, which can chemisorb onto the catalyst surface in the absence of competing adsorbate molecules from the electrolyte. Despite the stable N≡N bond, dissociative chemisorption of dinitrogen at room temperature has been reported to happen spontaneously on several clean transition metal surfaces<sup>28, 41-45</sup>. However, one of the major limitations of ambient condition (catalytic) ammonia synthesis is the formation of stable intermediates at the catalyst surface that hinder the advancement of the reaction, due to the lack of available active sites for both H<sub>2</sub> and N<sub>2</sub> dissociation<sup>46, 47</sup>. To overcome such issue, we propose an electrochemical cell configuration where the hydrogenation of the adsorbed nitrogen (and its intermediates) to ammonia proceeds via hydrogen atoms emerging from the bulk of a thin metallic electrode. Therefore, the feeding of reactive hydrogen atoms from the bulk circumvents the necessity of available active sites for H<sub>2</sub> activation on the catalyst surface. In this case, the catalytic hydrogenation reactions can continue upon NH<sub>3</sub> formation and desorption; hence a free

active site becomes available exclusively for further dinitrogen adsorption. Moreover,  $\text{NH}_3$  is produced directly in the gas phase in a separate compartment, facilitating product separation and preventing  $\text{NH}_3$  back diffusion to the anode surface and subsequent  $\text{NH}_3$  oxidation. The following sections will address in detail each step: nitrogen adsorption, hydrogen permeation and nitrogen hydrogenation to ammonia.

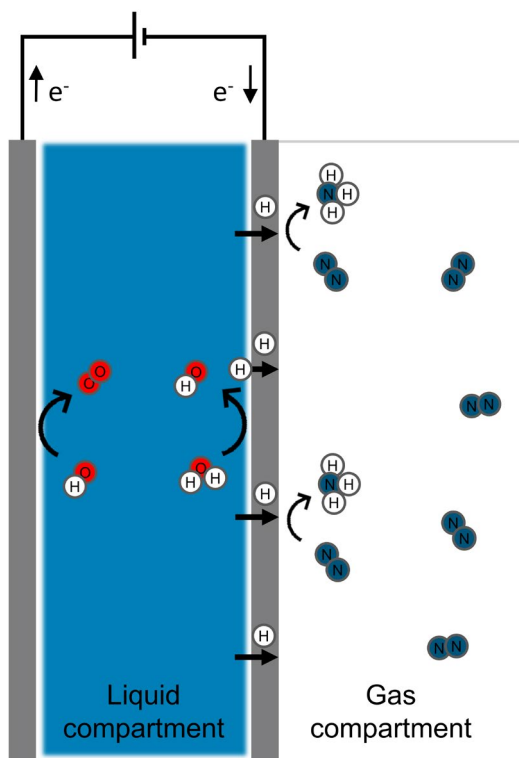


**Figure 5.1** Schematic representation of the proposed system for direct electrolytic ammonia synthesis via electrochemically generated and permeated atomic hydrogen. The cathode is a thin dense metallic electrode permeable to atomic hydrogen and characterised by two active interfaces: an electrode-electrolyte interface dedicated to the electrochemical hydrogen activation (liquid compartment side), and an electrode-gas interface dedicated to the dinitrogen activation and hydrogenation (gas compartment side). Ammonia is generated directly in the gas compartment from the interaction between adsorbed nitrogen and permeating atomic hydrogen.

**Nitrogen adsorption.** Dissociative nitrogen chemisorption occurs at room temperature on Ni surfaces<sup>28, 42-44</sup>. Moreover, the formation of “bulk-like” surface nitrides subsequent to nitrogen adsorption has been suggested for Ni<sup>44</sup>, similarly to the one proposed for Fe<sup>48</sup>. X-ray photoelectron spectroscopy (XPS) was used to characterise nitrogen adsorption on a rigorously Ar/H<sub>2</sub> plasma cleaned Ni foil (**Figure A.5.1a**). The N 1s spectra before and after the exposure to 1 bar N<sub>2(g)</sub> at room temperature (**Figure 5.2a** and **Figure 5.2b**) were compared to the spectrum obtained for a Ni foil exposed to a low-pressure plasma nitriding process (**Figure 5.2c**; the nitriding treatment is described in the Experimental section). The appearance of a main peak centred at 397.8 eV, ascribed to atomic nitrogen (N<sup>ad</sup>)<sup>26, 27</sup>, confirms the formation of surface nitrides and thus that N<sub>2(g)</sub> is activated on a sufficiently clean Ni surface. However, the Ar/H<sub>2</sub> cleaned nickel foil rapidly oxidizes to form surface hydroxides when exposed to air (**Figure A.5.1c**), while the formed surface nitrides provide a protective layer against nickel oxidation from molecular oxygen and moisture (**Figure A.5.1b**). Moreover, during the electrochemical ammonia production experiments, the hydrogenation of surface nitrides generates *in-situ* highly active sites on the Ni surface without the necessity of an ultra-high vacuum (UHV) and oxygen-free controlled environment, used for nitrogen adsorption. As such, in this contribution we deliberately use nitrided protected nickel surfaces with the aim of preventing unwanted nickel oxidation that would hamper the possibility of demonstrating that nitrogen can be catalytically hydrogenated to ammonia by electrochemically permeating hydrogen at ambient conditions.



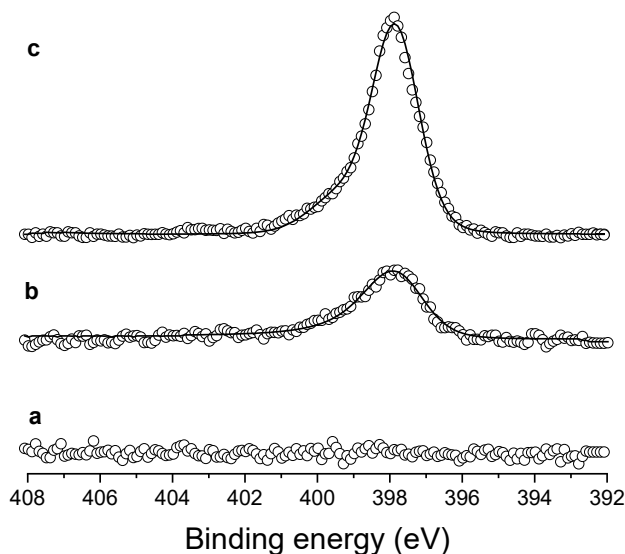


**Figure 5.2** Comparison between the N 1s XPS spectra of: an Ar/H<sub>2</sub> cleaned polycrystalline nickel surface (a) before and (b) after the exposure to 1 bar gaseous molecular nitrogen, and (c) an Ar/H<sub>2</sub> cleaned polycrystalline nickel surface after the exposure to low-pressure nitrogen plasma. The difference in peak intensity can be attributed to the additional contribution of nitrogen found in the subsurface of the plasma treated sample. The open circles are the measured values. The fitting is shown as a continuous black line, LA(1.3, 2.4, 69). Pass energy: 50 eV.

**Hydrogen permeation and nitrogen reduction to ammonia.** Nickel has a good hydrogen permeability (**Figure A.5.2**), and does not form very stable hydrides due to its only marginally negative enthalpy of formation<sup>49</sup>. The 12.5  $\mu\text{m}$  thin dense Ni electrode (2.5  $\text{cm}^2$ ) was placed in the cell with the nitrided surface oriented towards the gas side of the electrochemical cell (**Figure 5.1**). A simple two-electrode setup was used, in which the counter electrode was a Ni wire of 6.5  $\text{cm}^2$ . All the experiments were carried out at ambient conditions and with a constant N<sub>2</sub> flow of 1  $\text{mL min}^{-1}$  supplied at the cathodic gas compartment, unless otherwise stated. The inlet gas was sufficiently purified with an *in-line* filter before entering the cell to remove possible contaminations<sup>50</sup> (**Table A.5.1**). The outlet gases were constantly monitored with *in-line* TRACE™ 1300 gas chromatography (GC). Details of the *in-line* detection method have been reported elsewhere<sup>29</sup>. The insertion of

atomic hydrogen into the metal lattice of the electrode was achieved with a constant cathodic charging current density of  $5 \text{ mA cm}^{-2}$  in 1 M potassium hydroxide aqueous solution, resulting in a cell potential between 1.9 and 2.0 V and corresponding to an overall energy input of about  $9.2 \text{ kWh kg}_{\text{NH}_3}^{-1}$  (**Figure A.5.3**). It is acknowledged that electrolytic ammonia synthesis at reduced cell potentials represents a craved energetic requirement, sometimes difficult to achieve even for some of the most promising studies<sup>21, 51</sup>. We investigated the ammonia production in response to the electrochemical hydrogen permeation, by alternating open circuit and cathodic charging conditions, while continuously analysing the composition of the gas compartment (**Figure 5.3a**). No detectable amounts of ammonia were found during open circuit conditions, indicating that no contaminations nor other sources of ammonia were present in the cathodic gas compartment of the electrolytic cell. Upon electrochemical charging, hydrogen is generated at the electrode-electrolyte interface and hydrogen atoms permeate through the nickel lattice. Gaseous ammonia is then produced by the reaction between active adsorbed nitrogen and the permeating lattice hydrogen, as revealed from the appearance of a distinct peak in the gas chromatograms. When interrupting the charging current, the resulting decay of the permeating hydrogen flux follows a characteristic diffusion profile as a function of time<sup>35</sup>. Consequently, the synthesis of ammonia ceases until a successive cathodic charging current is applied, when both hydrogen permeation and ammonia production are restored. Therefore, this result shows the hydrogenation of  $\text{N}^{\text{ad}}$  to ammonia via electrochemical atomic hydrogen permeation at ambient conditions.

To elucidate the impact of atomic H on the hydrogenation pathway, the surface nickel nitride was exposed to two different concentrations of gaseous hydrogen in the absence of electrochemical hydrogen permeation, i.e. open circuit conditions. An  $\text{Ar:H}_2$  (98:2 □) mixture and pure  $\text{H}_2$  were sequentially fed with a flow rate of  $1 \text{ mL min}^{-1}$  in the cathodic gas compartment. In both cases, no ammonia was recorded at the GC. This is consistent with the reported stability of nickel nitrides under hydrogen gas up to a temperature of 430 K<sup>52</sup>. Exclusively after switching to electrochemical hydrogen permeation, ammonia production was restored and detected with the *in-line* GC (**Figure A.5.4**). This observation evidences that the formation of  $\text{NH}_{3(\text{g})}$  requires dissociated  $\text{H}_2$  to be present and that  $\text{H}_2$  dissociation does not occur from the gas phase on the nitrated Ni surface. Hydrogenography measurements (**Figure A.5.5**) confirmed that pre-adsorbed nitrogen on

Ni hinders  $H_2$  spillover, therefore preventing the hydrogenation reaction to proceed and form  $NH_3$ . However, the direct hydrogenation of  $N^{ad}$  does become enabled when electrochemical inserted and permeated lattice hydrogen atoms are present.

Long term experiments under a constant charging current show that the  $NH_3$  production decreases in time; yet, when  $N_2$  gas is present in the gas compartment  $NH_3$  production lasts up to 9 hours longer and about three times more  $NH_3$  is produced compared to having He gas atmosphere in the gas compartment (**Figure 5.3b** and **Figure 5.4**). The decay of  $NH_3$  synthesis suggests that the available  $N^{ad}$  for hydrogenation decreases with time; while the larger production achieved with  $N_2$  atmosphere and the isotope labelled experiment indicate that gas phase  $N_2$  does participate in the catalysis, replenishing surface nitrides by dissociative adsorption (vide infra). Overall in the long term, three times higher ammonia production under  $N_2$  atmosphere suggests that  $N^{ad}$  already present on the surface is contributing to a lesser extent than the activation of  $N_2$  from the gas phase. These results were obtained consistently for multiple experiments (**Figure 5.4**, **Figure A.5.6** and **Figure A.5.7**).

The activation of gaseous nitrogen, and its subsequent hydrogenation to ammonia, was confirmed using isotopically labelled  $^{15}N_2$  as feed gas. Prior to be introduced to the electrolytic cell,  $^{15}N_2$  gas was purified with an *in-line* filter to remove possible contaminations, as previously done for inlet  $^{14}N_2$  gas.  $^{15}NH_3$  was detected by coupling an *in-line* TRACE<sup>TM</sup> 1300 GC with a ISQ<sup>TM</sup> single quadrupole mass spectrometer (**Figure A.5.8**). With this method we were capable of distinguishing isotopologues of  $NH_3$  via mass spectroscopy ( $^{14}NH_3$   $m/z = 16, 17$  and  $^{15}NH_3$   $m/z = 17, 18$ ), thanks to the water/ammonia separation achieved with a suitable separation column<sup>29</sup>. Once again, no  $NH_3$  ( $^{14}N$  or  $^{15}N$ ) was detected during open circuit conditions, i.e. in the absence of H-permeation (**Figure A.5.9-A.5.12**). Ammonia production was observed solely in response to electrochemical H-permeation and in close agreement with the amount of ammonia produced with  $^{14}N_2$  in **Figure 5.3**, proving the consistency of the experimental results, independently of the isotope used (**Table A.5.2**). Under electrochemical hydrogen permeation, the appearance of a peak at the retention time corresponding to ammonia, at mass-to-charge ( $m/z$ ) ratio equal to 18 (fragment 100%), and a confirmation peak at  $m/z$  ratio equal to 17 (fragment 80%), confirmed that  $^{15}NH_3$  was produced via the catalytic reaction between activated gaseous  $^{15}N_2$  and atomically permeating hydrogen.

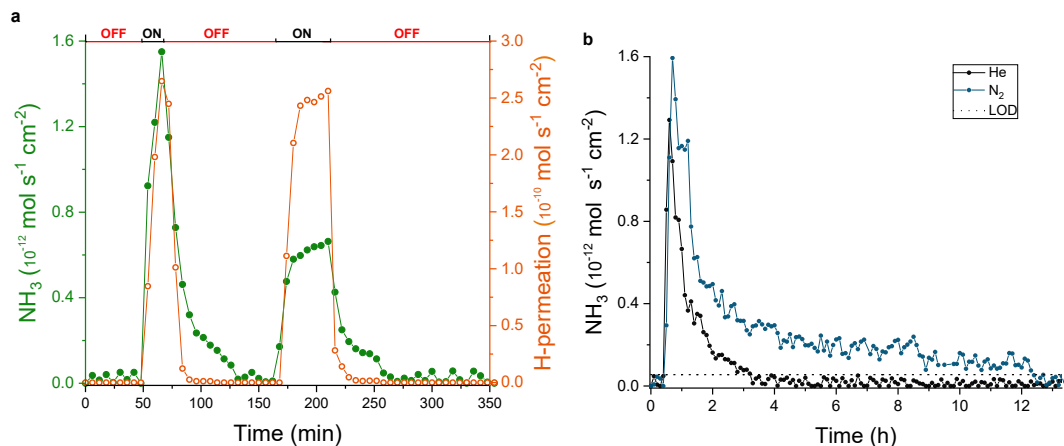


**Figure 5.3** (a) The rate of ammonia synthesis (solid green symbols) and electrochemical hydrogen permeation (open orange symbols) through a 0.0125 mm thick Ni electrode as function of time, while alternating open circuit condition (top horizontal axis: OFF) and cathodic charging (top horizontal axis: ON). (b) Long term ammonia production rate under  $\text{N}_2$  (blue) and He (black) atmosphere. Higher synthesis rate and up to 9 hours longer  $\text{NH}_3$  production is measured under  $\text{N}_2$  atmosphere. The black dotted line indicates the limit of detection (LOD).

On the other hand, the production of  $^{14}\text{NH}_3$  (**Figure A.5.12** and **Table A.5.2**) is attributed to the hydrogenation of pre-adsorbed nitrogen ( $^{14}\text{N}$ ), which also leads to the expected *in-situ* generation of active N vacancy sites (vide infra). The mechanism for the  $\text{N}_2$  activation depends on the nature and the abundance of available surface sites. The contribution of N-vacancies to the  $\text{NH}_3$  synthesis reaction is discussed in the following section.

**N mobility and vacancies.** As a consequence of the nitrogen plasma pre-treatment, small traces of nitrogen were also found in the subsurface layer of the nickel electrode. The XPS N 1s depth profile in **Figure 5.5** shows the nitrogen distribution over the sample thickness after the nitrogen plasma pre-treatment and after electrochemical hydrogen permeation. The penetration depth of nitrogen was about 40 nm. Interestingly, upon electrochemical hydrogen permeation, we observed the consumption of the nitrogen from both surface and the subsurface. Eventually, after 12 h operation nearly all nitrogen atoms in the bulk reacted to form  $\text{NH}_3$ . No  $\text{N}_2$  was detected during the experiments under inert He carrier gas, suggesting that all the implanted nitrogen was selectively converted to  $\text{NH}_3$ .

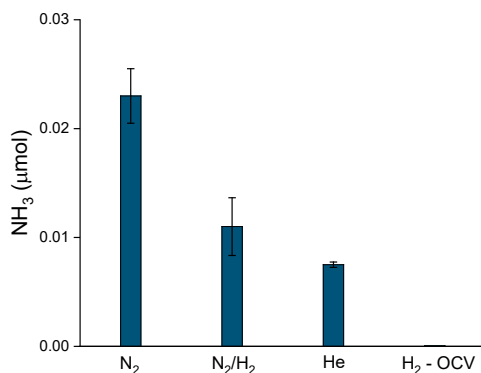


**Figure 5.4** Amount of ammonia generated under N<sub>2</sub>, N<sub>2</sub>:H<sub>2</sub> (96:4 %) or He after 12 hours of electrochemical hydrogen permeation at ambient conditions. The NH<sub>3</sub> amount under N<sub>2</sub> atmosphere increases about 3-fold compared to He. No ammonia has been detected under pure H<sub>2</sub> without electrochemical hydrogen permeation. Error bars correspond to the standard deviation of three or more measurements with fresh samples.

The N 1s signal measured at the Ni surface after prolonged H-permeation shows the formation of a small shoulder around 399.9 eV, indicating a distinct N species, which could be ascribed to the presence of N-vacancies<sup>53</sup> (**Figure A.5.13**). The produced nickel nitride thin film is stable under ambient conditions; however, the hydrogenation of surface nitrogen atoms to ammonia results in the formation of nitrogen vacancies<sup>54</sup>. These vacancies exhibit a low activation barrier for N migration in nickel nitrides<sup>17</sup>. Therefore, the created N-vacancies can be exchanged for nitrogen available from the bulk, accounting for the observed depletion of nitrogen atoms from the subsurface layers. Still, as stated above, N<sub>2</sub> readily reacts with the vacancies. The presence of a pre-existing surface nitride layer and the role of N-vacancies, points in the direction of molecular nitrogen activation via a Mars-van Krevelen mechanism<sup>55</sup>. The N-vacancy, formed at the catalyst surface upon ammonia production from surface nitrogen atoms, represents an energetically more favourable active site for nitrogen adsorption and activation compared to a bare Ni surface<sup>17, 54, 56, 57</sup>; although the latter also activates N<sub>2</sub> when sufficiently clean as shown in **Figure 5.2**. However, in the long term of the experiment, poisoning apparently results in the reduction of available N-

vacancy active sites. Migration of N from the subsurface also plays a role, but does not seem to deactivate the vacancy formation, but rather extend the  $\text{NH}_3$  formation from the plasma pre-adsorbed N. Thus, the prolonged reaction could benefit from strategies to increase N-vacancy stability on the surface<sup>58, 59</sup>.

The surface sites can also interact with molecular or atomic hydrogen or other potential adsorbates that might preferentially occupy them over adsorbed N, preventing a persistent and more efficient  $\text{N}_{2(\text{g})}$  activation<sup>18, 47, 57, 60</sup>. To investigate whether the presence of  $\text{H}_2$  gas would help in creating a more reductive environment, or suppress oxide impurities, or interact with the active sites, we also carried out the  $\text{NH}_3$  synthesis using a mixture of 4 %  $\text{H}_2$  in  $\text{N}_2$  in the gas compartment (**Figure A.5.14**). In this case, the resulting produced ammonia ( $0.011 \mu\text{mol}$ ) was less than obtained under pure nitrogen, but higher when compared to He atmosphere (**Figure 5.4**); this evidences that the competing action of  $\text{H}_2$  on the N-adsorption sites<sup>57</sup> is more prominent than the potential reducing and surface protection action on e.g. oxygen impurities. Therefore, it becomes relevant that, under reaction conditions, the surface is sufficiently contaminant free, as adsorbed N was observed with XPS in a well-controlled environment and after *in-situ* Ar ion cleaning. This also suggests that the  $\text{N}_2$  activation on the polycrystalline Ni surface controls the reaction rate.

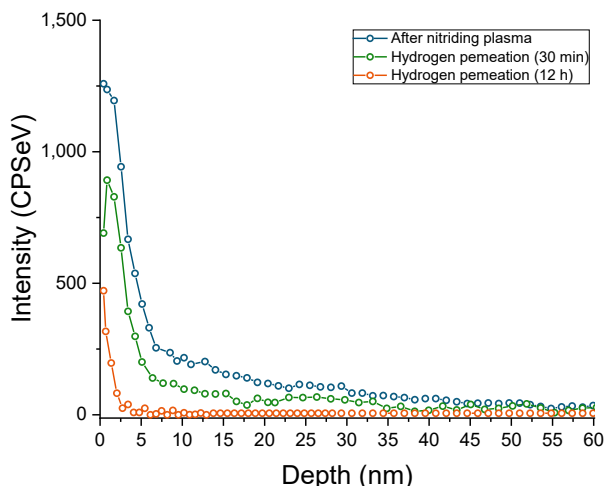


**Figure 5.5** Intensity of the N 1s nitrogen signal as function of the depth of the sample, resulting from X-ray Photoelectron Spectroscopy depth-profiling measurements: after  $\text{N}_2$ -plasma exposure (blue), after 30 min (green) and 12h (orange) of electrochemical hydrogen permeation under  $\text{N}_2$ .

## 5.4 Conclusion

Through the adoption of a hydrogen permeable electrode, we have demonstrated a novel strategy for direct electrolytic ammonia synthesis from  $N_2$ ,  $H_2O$  and renewable electricity at room temperature and pressure. The proposed system uses cheap and abundant materials and it is in line with the paramount need of innovative electrode designs for electrochemical ammonia synthesis<sup>14, 19</sup>. The dense metallic electrode ensures a complete separation of the nitrogen active sites from the electrolyte, while reactive atomic hydrogen is electrochemically fed from the bulk of the electrode. Hydrogenography and gas chromatography measurements revealed that adsorbed nitrogen on a polycrystalline Ni surface does not react with gaseous  $H_2$ , hindering the hydrogen spillover essential for the  $NH_3$  synthesis reaction. Nonetheless,  $NH_3$  synthesis was enabled upon atomic hydrogen permeation, showing that the hydrogenation of active nitrogen via permeating hydrogen circumvents the mutual competition between nitrogen and hydrogen activation. Our results indicate the occurrence of a Mars-van Krevelen dinitrogen activation mechanism, in which N-vacancies play a significant role in the catalytic process facilitating  $N_2$  adsorption.

This work highlights the role of the hydrogen permeable electrode and the electrochemical atomic hydrogen permeation in the catalytic hydrogenation of  $N^{ad}$  to ammonia at ambient conditions, demonstrating the feasibility of this reaction. We envision that the presented work will encourage further developments towards a more efficient direct electrolytic ammonia synthesis.

## Appendix A.5

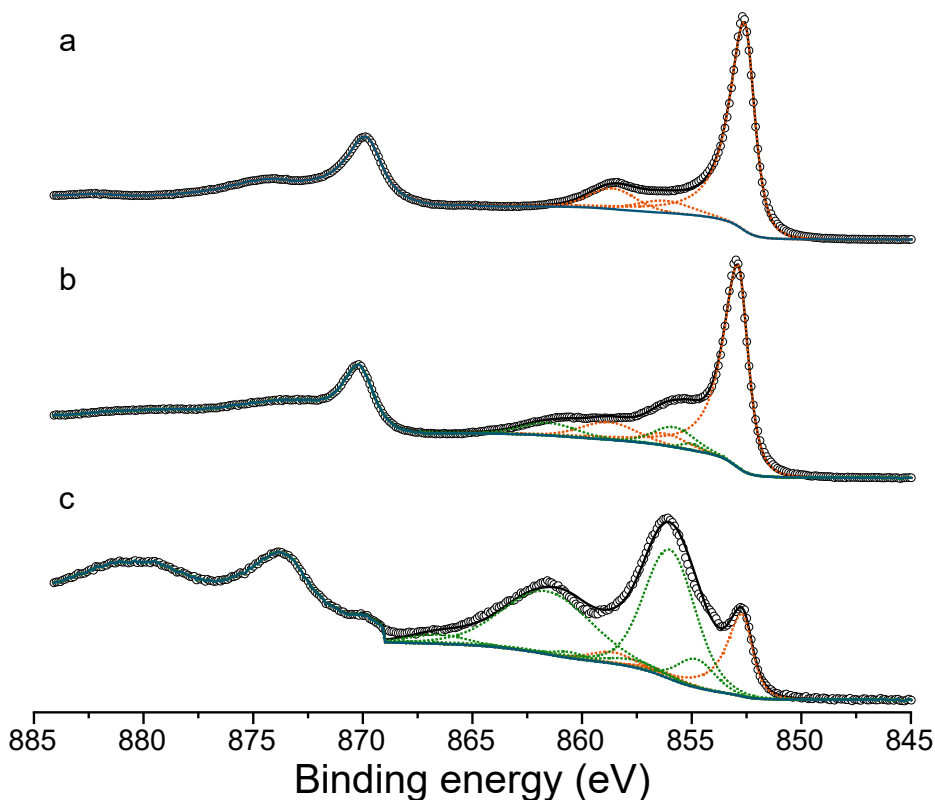


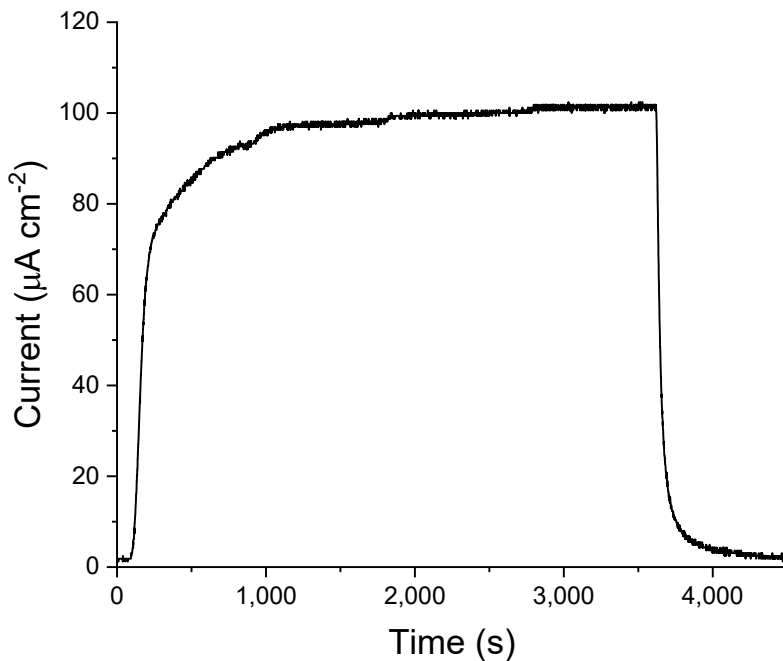
**Figure A.5.1** Comparison between the Ni 2p XPS spectra of: (a) a nickel surface after the Ar/H<sub>2</sub> plasma cleaning treatment not exposed to air, (b) a nickel nitrided surface after air exposure and (c) a nickel surface Ar/H<sub>2</sub> plasma cleaned and subsequently exposed to air. The air exposure of a reduced Ni surface results in the significant formation of surface hydroxides, while the presence of a surface nitride layer ensures protection against nickel oxidation. A standard Shirley background was used as baseline for the 2p<sub>3/2</sub> portion of the spectra. For the sample where substantial mixed nickel metal/hydroxide is present, a slight baseline offset at higher binding energies was applied to improve the fitting<sup>61</sup>. The 2p<sub>3/2</sub> spectrum of Ni metal is characterised by three peaks: a main metallic peak at 852.6 eV, fitted with asymmetrical line shape, LA(1.1, 2.2, 10), and two satellite peaks at 856.3 and 858.7 eV, fitted with a mixed Gaussian-Lorentzian profile, GL(30)<sup>61</sup>. The 2p<sub>3/2</sub> spectrum of nickel hydroxide consists of six components, which have been reported elsewhere<sup>61</sup>. The convolutions and the backgrounds are shown as continuous black and blue lines, respectively. Nickel metal components are shown as orange dotted line, while nickel hydroxide components are shown as green dotted line. The open circles are the measured values. Pass energy: 50 eV.



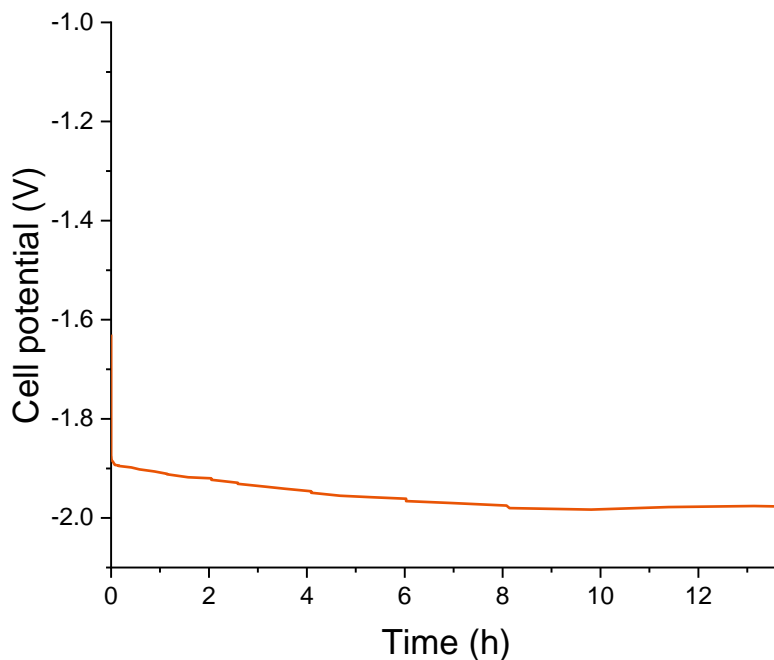
### Electrochemical hydrogen permeation

The electrochemical hydrogen permeation was measured using the method developed by Devanathan and Stachurski<sup>35</sup>. **Figure A.5.2** shows the atomic hydrogen permeation rate through the 0.0125 mm thick Ni foil, resulting from a cathodic charging current density of 5 mA cm<sup>-2</sup>. The steady state hydrogen flux ( $\Phi_H$ ) is equal to 100  $\mu\text{A cm}^{-2}$ . At the electrode surface, this corresponds to approximately 0.4 H/Ni per second, as calculated in equation (A.5.1), where  $N_a$  is the Avogadro's number,  $F$  is the Faraday's constant,  $N_{100}$  is the Ni atoms per unit cell area and  $a$  is the Ni lattice constant<sup>62</sup>.

$$\frac{H}{Ni} = \frac{\Phi_H \cdot N_a / F}{N_{100} / a^2} = \frac{\frac{(100 \cdot 10^{-6}) \times 6.022 \cdot 10^{23}}{96500}}{\frac{2}{(3.5 \cdot 10^{-8})^2}} \cong 0.4 \quad (\text{A.5.1})$$



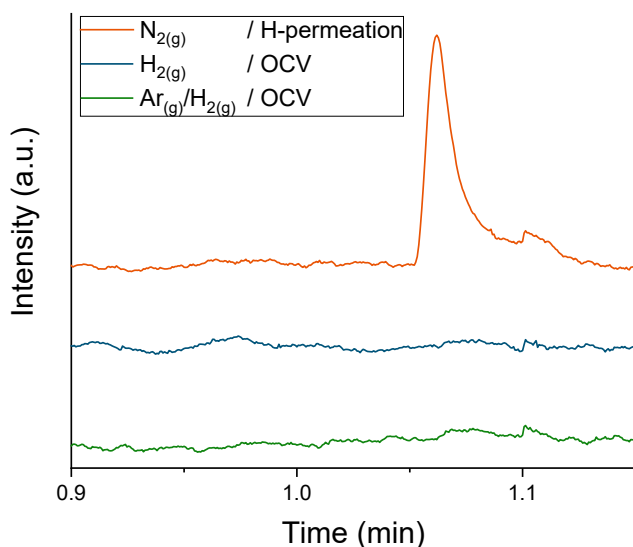
**Figure A.5.2** Measured atomic hydrogen permeation rate through 0.0125 mm nickel foil at ambient condition as a function of time. After 50 seconds, the Ni foil was cathodically polarized in 1 M KOH solution at 5 mA cm<sup>-2</sup>. The cathodic charging current was interrupted after 3600 seconds, resulting in the consequent decay of permeated hydrogen. The measured hydrogen permeation transient shows the characteristic s-shaped profile.



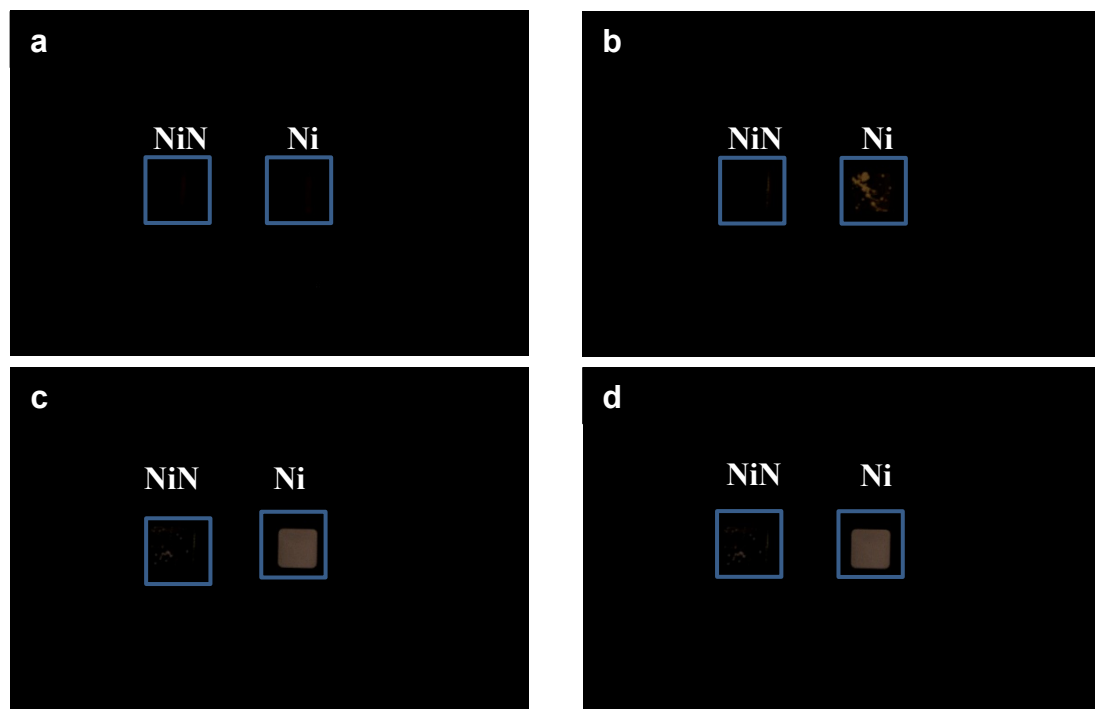
**Figure A.5.3** Measured potential between working electrode and counter electrode at constant cathodic charging current density of  $5 \text{ mA cm}^{-2}$  in 1 M potassium hydroxide aqueous solution and under  $\text{NH}_3$  synthesis conditions.  $\text{NH}_3$  is formed in the gas stream while the cell potential is between 1.9 and 2.0 V, which results in an energy investment of  $9.2 \text{ kWh kg}_{\text{NH}_3}^{-1}$  or 144% of the higher heating value of ammonia of  $6.25 \text{ kWh kg}_{\text{NH}_3}^{-1}$ .

### Comparison between atomic hydrogen permeation and molecular hydrogen gas

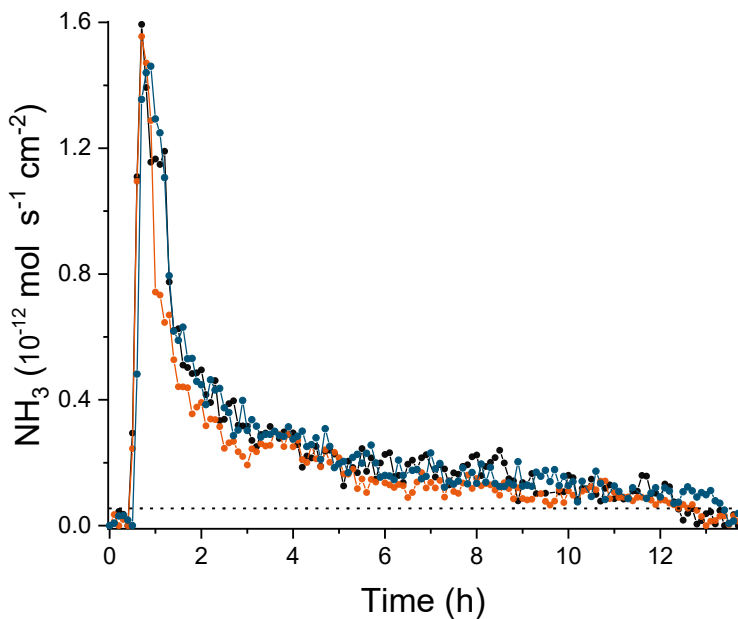
The surface nickel nitride was sequentially exposed to a gas mixture of Ar:H<sub>2</sub> (98:2 %) and pure H<sub>2</sub> with a flow rate of 1 ml/min under open circuit conditions (i.e. no hydrogen permeation). The sample was exposed to each of the gas mixtures for more than 1 hour, during which no ammonia was detected with the *in-line* GC. Exclusively after activating the electrochemical hydrogen permeation, ammonia was detected. This experiment indicates that the hydrogenation of active nitrogen to ammonia does not occur in the presence of only gaseous hydrogen, while permeating lattice hydrogen is able to form ammonia under the same operating conditions, with or without gaseous H<sub>2</sub>.



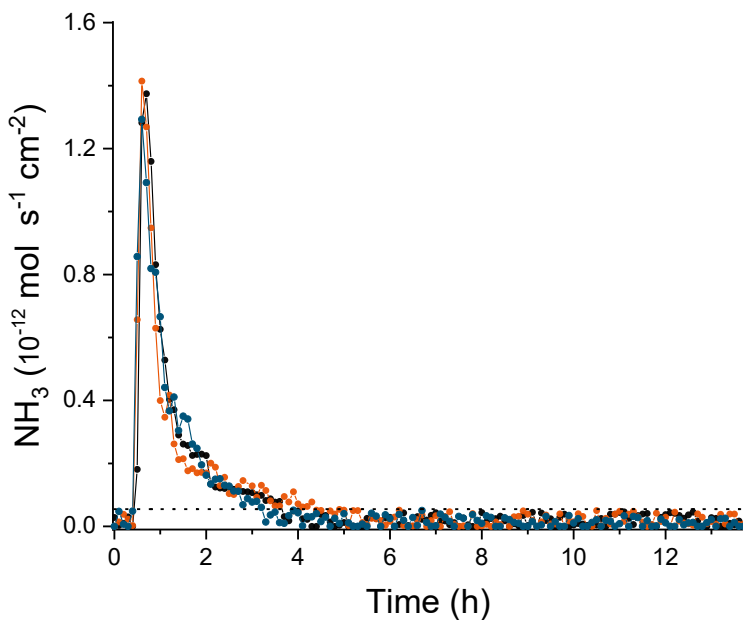
**Figure A.5.4** Stacked partial chromatograms, at the NH<sub>3</sub> retention time, corresponding to a nickel electrode after plasma nitriding treatment and sequentially exposed to a gas mixture of 2% H<sub>2</sub> in Ar (green), pure H<sub>2</sub> (blue) and under electrochemical hydrogen permeation in N<sub>2</sub> (orange). A distinct peak corresponding to NH<sub>3</sub> is only visible when electrochemical hydrogen permeation is active. No ammonia is produced with gaseous hydrogen at the equal experimental conditions.



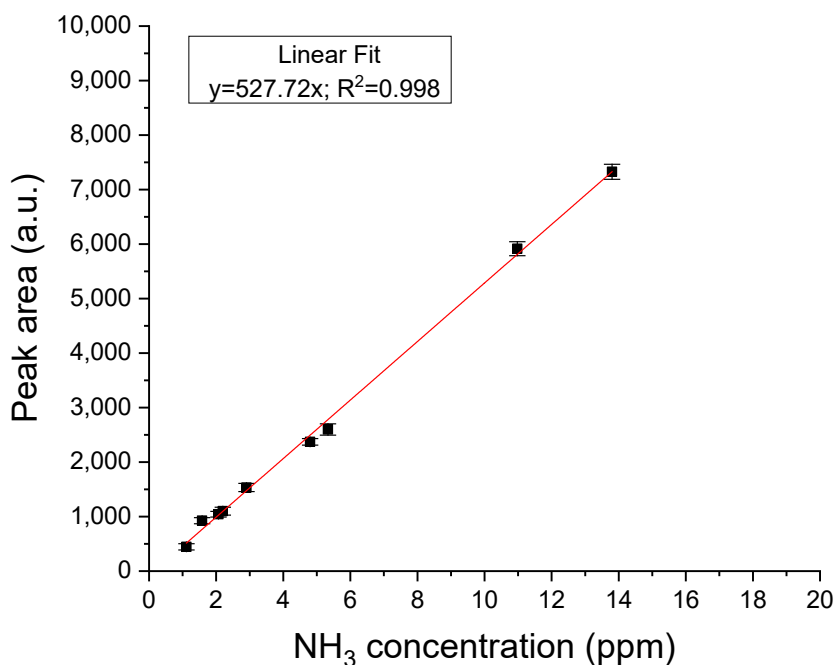
**Figure A.5.5** The blue boxes identify the position of the nickel surface (Ni) and the nickel surface pre-exposed to nitrogen plasma (NiN). The two samples before (a), and after 7 (b), 34 (c) and 72 (d) hours exposure to 1 bar of  $H_2$  at room temperature. The formation of the yttrium hydride resulting from hydrogen spillover on the metal surface is shown by a brighter colour due to the transmission of a light source underneath the samples. The pure nickel surface shows significant yttrium hydride formation after 7 hours, while no sign of significant yttrium hydride formation was observed after 72 hours for the nickel surface pre-exposed to nitrogen plasma.



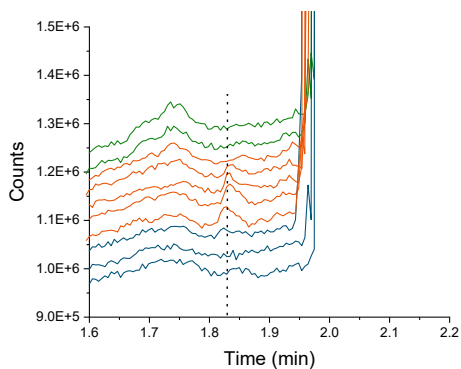
**Figure A.5.6** Long term ammonia production rate under  $\text{N}_2$  for repeated for three separate but identically treated samples. The black dotted line indicates the limit of detection (LOD).



**Figure A.5.7** Long term ammonia production rate under He for repeated for three separate but identically treated samples. The black dotted line indicates the limit of detection (LOD).



**Figure A.5.8** GC-MS calibration curve ( $m/z=17$ ) was carried out by dosing 13.8ppm NH<sub>3</sub> certificated calibration gas (rest N<sub>2</sub>) and dilute it with pure N<sub>2</sub> to the chosen concentration. Error bars correspond to the standard deviation of three or more repeated measurements

**$^{15}\text{N}$  isotope labelling experiment**

**Figure A.5.9** Signal at MS detector for  $m/z=18$  before (green), during (orange) and after (blue) electrochemical hydrogen permeation under  $^{15}\text{N}_2$  gas. Ammonia is eluted at 1.83 min, while water at about 1.95 min.

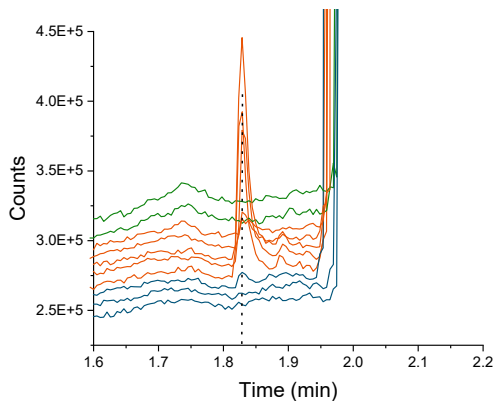


**Figure A.5.10** Signal at MS detector for  $m/z=17$  before (green), during (orange) and after (blue) electrochemical hydrogen permeation under  $^{15}\text{N}_2$  gas. Ammonia is eluted at 1.83 min, while water at about 1.95 min.

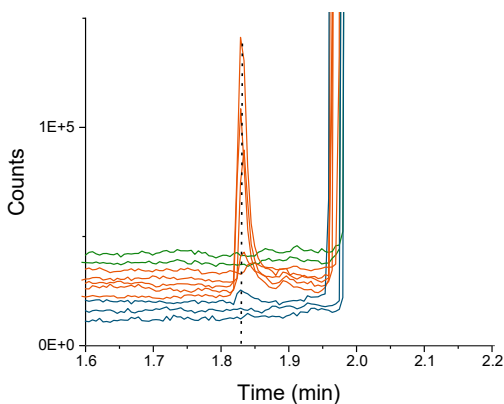


**Figure A.5.11** Signal at MS detector for  $m/z=16$  before (green), during (orange) and after (blue) electrochemical hydrogen permeation under  $^{15}\text{N}_2$  gas. Ammonia is eluted at 1.83 min, while water at about 1.95 min.

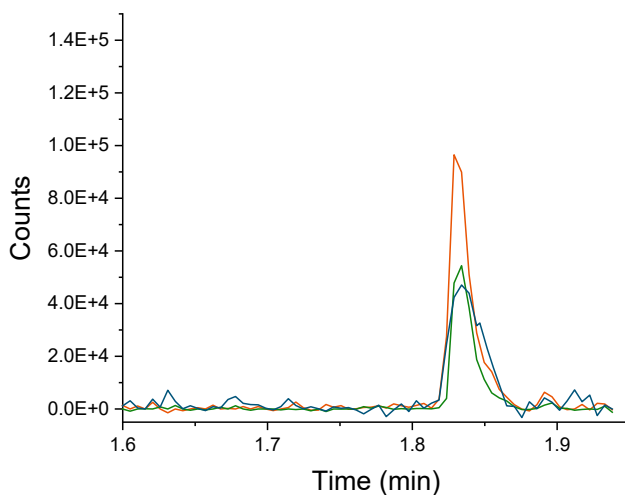


**Figure A.5.12** Overlay of the background subtracted GC-MS signals from  $m/z$  ratio equal to 18 (blue), 17 (orange) and 16 (green) detected simultaneously during electrochemical hydrogen permeation and exposure to  $^{15}\text{N}_2$ .

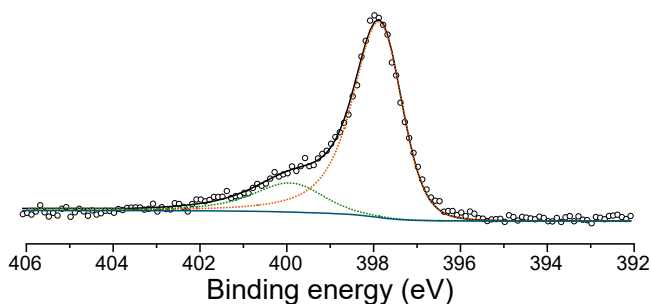


**Figure A.5.13** N 1s HR-XPS spectra of the surface of the electrode after 12 hours of electrochemical hydrogen permeation under  $\text{N}_2$ . A shoulder with limited intensity is observable at around 399.9 eV (green dotted line), which could be ascribed to the presence of N-vacancies.  $\text{N}^{\text{ad}}$  component is shown as orange dotted line. Line shape: LA(1.3, 2.4, 69). A standard Shirley background was used as baseline (continuous blue line). The convolution is shown as continuous black. The open circles are the measured values. Pass energy: 50 eV.



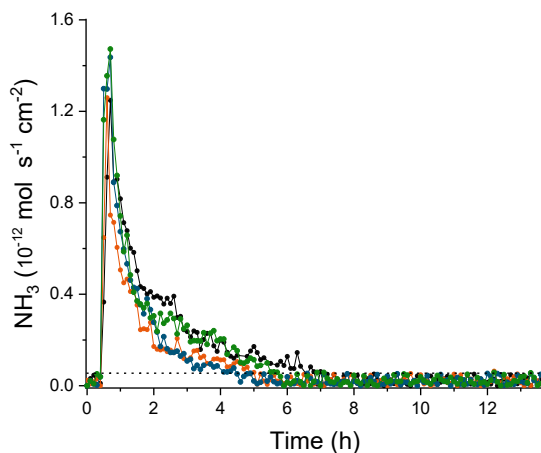


**Figure A.5.14** Long term ammonia production rate under a gas mixture of 4%  $\text{H}_2$  in  $\text{N}_2$  for repeated for four separate but identically treated samples. The black dotted line indicates the limit of detection (LOD).

#### Estimation of etching rate for XPS depth profiling

The etching rate was extrapolated from extended etching cycles of a 50 nm nickel thin film, upon  $\text{SiO}_2/\text{Si}$  substrate detection (**Figure A.5.15**). The estimated etching rate at 1 keV beam energy is  $0.085 \text{ nm s}^{-1} \pm 0.004 \text{ nm s}^{-1}$ , calculated from equation (A.5.2).

$$\text{etching rate} = \frac{\text{film thickness}}{\text{etch time}} \quad (\text{A.5.2})$$

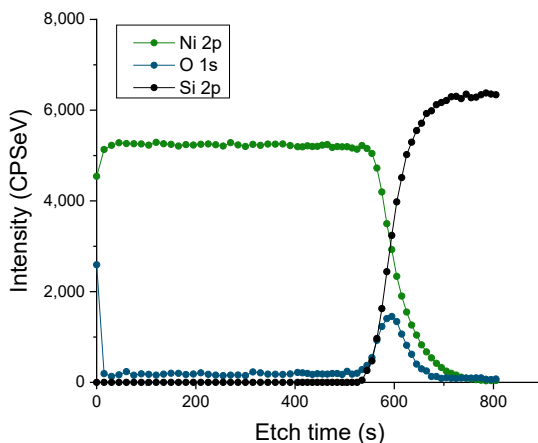


**Figure A.5.15** XPS depth profiling of a 50 nm nickel thin film sputter deposited on a  $\text{SiO}_2/\text{Si}$  substrate. Ar ions with a beam energy of 1 KeV were used to remove atoms from the sample surface.

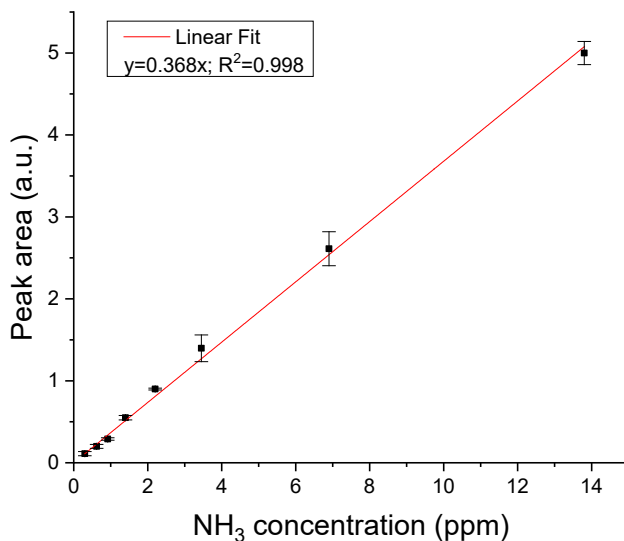


**Figure A.5.16** GC calibration curve was carried out by dosing certificated calibration gases (NH<sub>3</sub> in N<sub>2</sub>) and dilute them with pure N<sub>2</sub> to the chosen concentration. Error bars correspond to the standard deviation of three or more repeated measurements. Details of the *in-line* detection method have been reported elsewhere<sup>29</sup>.

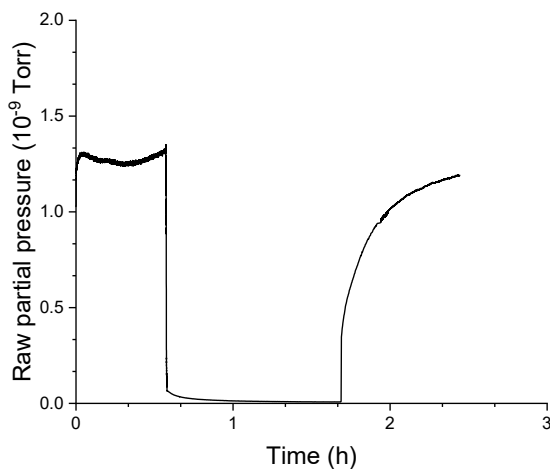


**Figure A.5.17** Detection of mass-to-charge ratio 30 by quadrupole mass spectrometer with secondary electron multiplier (Hidden Analytics). Initially, 100 ppm of nitric oxide in He was fed directly in the mass spectrometer. After about 35 minutes the gas mixture was fed through the *in-line* gas purifier (Agilent OT3-4) before reaching the MS inlet. The sudden decrease of  $m/z=30$  shows the NO removal. After about 100 minutes the filter was bypassed again, and the NO signal level restored.

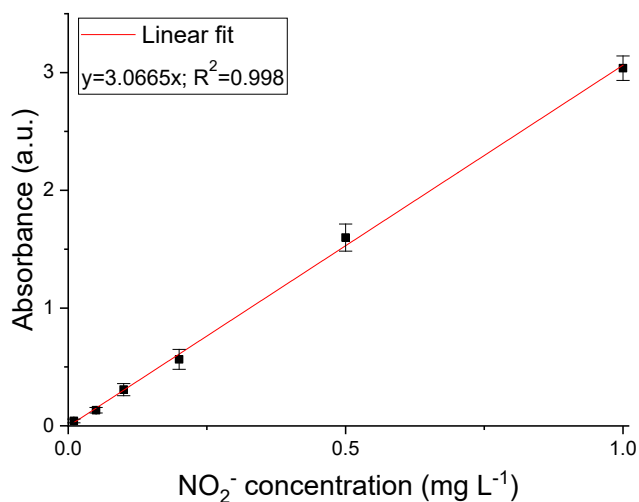


**Figure A.5.18**  $\text{NO}_2^-$  calibration curve was carried out by dilutions of 5 mg/L  $\text{KNO}_2$  stock solution. Absorbance was measured at 540 nm. Error bars correspond to the standard deviation of three or more repeated measurements.

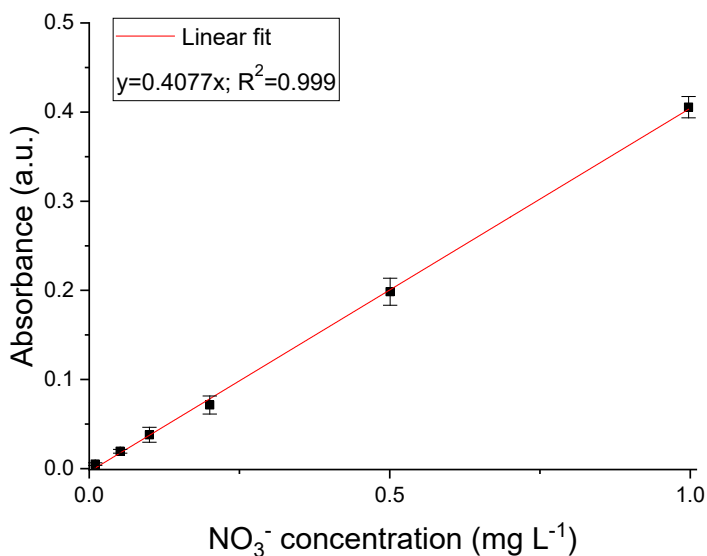


**Figure A.5.19**  $\text{NO}_3^-$  calibration curve was carried out by dilutions of 5 mg/L  $\text{KNO}_3$  stock solution. The total absorbance was calculated as following:  $A_{220} - 2A_{275}$ . Error bars correspond to the standard deviation of three or more repeated measurements.

**Table A.5.1** Determination of NO<sub>x</sub> from carrier gases and gas purification. After 24h of purified gas accumulation at 40 mL min<sup>-1</sup>, only NO<sub>x</sub> at ppb level within the experimental error were detected. Considering that during electrochemical ammonia synthesis experiments NH<sub>3</sub> detection was carried out directly with *in-line* GC measurements under a constant gas flow (i.e. no accumulation), once can estimate that only less than ppb level of NO<sub>x</sub> is present in the purified gas stream. Therefore NO<sub>x</sub> reduction the permeated H would not be detectable (GC LOD=150 ppb).

	24h N <sub>2</sub>			24h He				24h N <sub>2</sub> + Purifier		
	NO <sub>3</sub> A <sub>220</sub> -2*A <sub>275</sub> [A]	NO <sub>2</sub> A <sub>540</sub> [A]	Total NO <sub>x</sub> [mg L <sup>-1</sup> ]	NO <sub>3</sub> A <sub>220</sub> -2*A <sub>275</sub> [A]	NO <sub>2</sub> A <sub>540</sub> [A]	Total [mg L <sup>-1</sup> ]	NO <sub>x</sub>	NO <sub>3</sub> A <sub>220</sub> -2*A <sub>275</sub> [A]	NO <sub>2</sub> A <sub>540</sub> [A]	Total NO <sub>x</sub> [mg L <sup>-1</sup> ]
<b>Bubbler 1</b>	0.0657	0.0120	0.165 ±0.005	0.0024	0.0065	0.009 ±0.005		0.0015	0.0004	0.004 ±0.005
<b>Bubbler 2</b>	0.0136	0.0015	0.034 ±0.005	0.0017	0.0017	0.005 ±0.005		0.0014	0.0002	0.003 ±0.005

### Estimation of NO<sub>x</sub> concentration in purified gas stream

The concentration of NO<sub>x</sub> in the purified gas stream can be calculated as follow:

$$concentration\ NO_{x(gas)} = \frac{concentration\ NO_{x(sol)} \times V_{(l)}}{MW_{NO_x} \times t \times \phi} < ppb \quad (A.5.3)$$

Where  $V_{(l)}$  is the volume of the liquid trap,  $MW$  is the molecular weight of NO<sub>2</sub> or NO<sub>3</sub>,  $t$  is the duration of the experiment (86400 s), and  $\phi$  is the total molar flow (3E-5 mol s<sup>-1</sup>).

**Table A.5.2** Quantification of  $^{15}\text{NH}_3$  from  $^{15}\text{N}$  isotope labelling experiment. Summary of integrated peak area of  $m/z$  ratio equal to 16, 17 and 18 from GC-MS signal before, during and after electrochemical hydrogen permeation. Ammonia retention time is 1.83 min. The obtained  $\text{NH}_3$  is in agreement with the amount obtained from GC detection during  $^{14}\text{N}$  experiments.

	Retention time (min)	Peak area [ $m/z=16$ ] (counts*min)	Peak area [ $m/z=17$ ] (counts*min)	Peak area [ $m/z=18$ ] (counts*min)	$\text{NH}_3$ rate ( $10^{-12} \text{ mol s}^{-1} \text{ cm}^{-2}$ )	$\frac{^{15}\text{NH}_3}{^{14}\text{NH}_3 + ^{15}\text{NH}_3}$ (%)
OCV-before [1]	-	-	-	-	-	-
OCV-before [1]	-	-	-	-	-	-
H-perm [1]	1.84	125.7	220.7	-	0.13	-
H-perm [2]	1.83	231.2	565.4	434.3	0.3	$60.9 \pm 6.5$
H-perm [3]	1.83	1990.6	2979.5	827.0	1.74	$23.0 \pm 3.3$
H-perm [4]	1.83	1012.1	1985.5	1040.5	1.22	$44.5 \pm 2.9$
H-perm [5]	1.83	1287.4	2244.4	1009.0	1.36	$37.1 \pm 4.1$
OCV-after [1]	1.83	241.2	362.6	-	0.21	-
OCV-after [2]	-	-	-	-	-	-
OCV-after [3]	-	-	-	-	-	-

**Energetic calculations.** As result of the electrochemical hydrogen insertion into the Ni lattice, after permeation the emerging H can either react with the active nitrogen to form  $\text{NH}_3$  or recombine and desorb as  $\text{H}_2$  at the gas compartment. The formation of the  $\text{H}_2$  in the gas compartment was measured with the TCD detector. **Figure 5.3** shows the total hydrogen permeation, sum of the recombining hydrogen and the hydrogen reacting with N. Therefore, a hydrogenation efficiency ( $H.E.$ ) can be defined as the ratio of ammonia production rate ( $\dot{N}\text{H}_3$ ) and the total permeating hydrogen ( $H_{perm}$ ), both express in  $\text{mol s}^{-1} \text{cm}^{-2}$ :

$$H.E. (\%) = \frac{3 \times \dot{N}\text{H}_3}{H_{perm}} \times 100 \quad (\text{A.5.4})$$

The maximum recorded H.E. is 1.92 %. Considering that all the electrochemical experiments were conducted with a constant charging current density ( $i_{ch}$ ) of  $5 \text{ mA cm}^{-2}$ , one can also define a faradaic efficiency ( $FE$ ) for the presented process as follow:

$$FE = \frac{(3e^-) \times \dot{N}\text{H}_3}{i_{ch}} \times F \times 100 \quad (\text{A.5.5})$$

It was not attempted here to optimise the H permeation current ( $0.1 \text{ mA cm}^{-2}$ ) over the  $\text{H}_2$  evolution ( $5 \text{ mA cm}^{-2}$ ) at the charging side (liquid compartment), which resulted in a maximum recorded FE of 0.009 %. For H reduced, inserted, permeated and reacted to  $\text{NH}_3$ , the corresponding cell potential is about 1.95 V (**Figure A.5.3**), resulting in an overall energy input of  $9.2 \text{ kWh kg}_{\text{NH}_3}^{-1}$ , calculated as:

$$\text{energy input} = (3e^-) \times (1.95 \text{ V}) \times (4.45 \times 10^{-26} \frac{\text{kWh}}{\text{eV}}) \times N_a \times \frac{1}{M_{\text{NH}_3}} \quad (\text{A.5.6})$$

Here the  $\text{NH}_3$  reaction is a three electron reaction,  $N_a$  is the Avogadro's number and  $M_{\text{NH}_3}$  is the molar mass of ammonia. The theoretical minimum energy investment corresponding to 1.17eV equilibrium potential for the reaction  $3\text{H}_2\text{O} + \text{N}_2 \rightarrow 2\text{NH}_3 + 1.5\text{O}_2$  under standard conditions would be  $5.5 \text{ kWh kg}_{\text{NH}_3}^{-1}$ . However, the intermediate  $\text{NiH}_x$  has a slightly negative enthalpy of formation of  $-5 \text{ kJ mol}^{-1}$ <sup>63</sup>, which makes that the equilibrium potential for the  $\text{NiH}_x$  formation will bring the potential closer towards 1.23 V; water splitting to produce  $\text{H}_2$  in equilibrium with  $\text{NiH}_x$ . Therefore, in theory the minimum energy investment is above  $5.5 \text{ kWh kg}_{\text{NH}_3}^{-1}$ , but below  $5.8 \text{ kWh kg}_{\text{NH}_3}^{-1}$  corresponding to 1.23 V. The averaged energy requirement for current Haber-Bosch processes is  $9.8 \text{ kWh kg}_{\text{NH}_3}^{-1}$ <sup>5</sup>, while the more energy-intensive Li mediated ammonia synthesis process requires an energy input of about  $22 \text{ kWh kg}_{\text{NH}_3}^{-1}$  practical and  $14 \text{ kWh kg}_{\text{NH}_3}^{-1}$  theoretical minimum related to the required intermediate  $\text{Li}^+$  reduction to Li metal<sup>64</sup>. Therefore, the proposed approach, which separates the hydrogen and nitrogen activation steps, has considerable promise and we envision this will stimulate future developments.

## References

1. Smil, V., Detonator of the population explosion. *Nature* **1999**, *400* (6743), 415-415.
2. Erisman, J. W.; Sutton, M. A.; Galloway, J.; Klimont, Z.; Winiwarter, W., How a century of ammonia synthesis changed the world. *Nature Geoscience* **2008**, *1*, 636.
3. Bernhardt, D.; Reilly, J. F., Mineral Commodity Summaries 2020. *U.S. Geological Survey* **2020**, *1*, 116-117.
4. Jiao, F.; Xu, B., Electrochemical Ammonia Synthesis and Ammonia Fuel Cells. *Advanced Materials* **2019**, *31* (31), 1805173.
5. Rouwenhorst, K. H. R.; Krzywda, P. M.; Benes, N. E.; Mul, G.; Lefferts, L., Ammonia, 4. Green Ammonia Production. In *Ullmann's Encyclopedia of Industrial Chemistry*, 2020; pp 1-20.
6. MacFarlane, D. R.; Cherepanov, P. V.; Choi, J.; Suryanto, B. H. R.; Hodgetts, R. Y.; Bakker, J. M.; Ferrero Vallana, F. M.; Simonov, A. N., A Roadmap to the Ammonia Economy. *Joule* **2020**, *4* (6), 1186-1205.
7. Avery, W. H., A role for ammonia in the hydrogen economy. *International Journal of Hydrogen Energy* **1988**, *13* (12), 761-773.
8. Lan, R.; Irvine, J. T. S.; Tao, S. W., Ammonia and related chemicals as potential indirect hydrogen storage materials. *International Journal of Hydrogen Energy* **2012**, *37* (2), 1482-1494.
9. Mulder, F. M., Implications of diurnal and seasonal variations in renewable energy generation for large scale energy storage. *Journal of Renewable and Sustainable Energy* **2014**, *6* (3), 033105.
10. Guo, X.; Du, H.; Qu, F.; Li, J., Recent progress in electrocatalytic nitrogen reduction. *Journal of Materials Chemistry A* **2019**, *7* (8), 3531-3543.
11. Cao, N.; Zheng, G., Aqueous electrocatalytic N<sub>2</sub> reduction under ambient conditions. *Nano Research* **2018**, *11* (6), 2992-3008.
12. Soloveichik, G., Electrochemical synthesis of ammonia as a potential alternative to the Haber–Bosch process. *Nature Catalysis* **2019**, *2* (5), 377-380.
13. Qing, G.; Ghazfar, R.; Jackowski, S. T.; Habibzadeh, F.; Ashtiani, M. M.; Chen, C.-P.; Smith, M. R.; Hamann, T. W., Recent Advances and Challenges of Electrocatalytic N<sub>2</sub> Reduction to Ammonia. *Chemical Reviews* **2020**, *120* (12), 5437-4416.
14. Singh, A. R.; Rohr, B. A.; Schwalbe, J. A.; Cargnello, M.; Chan, K.; Jaramillo, T. F.; Chorkendorff, I.; Nørskov, J. K., Electrochemical Ammonia Synthesis—The Selectivity Challenge. *ACS Catalysis* **2017**, *7* (1), 706-709.
15. Hu, L.; Xing, Z.; Feng, X., Understanding the Electrocatalytic Interface for Ambient Ammonia Synthesis. *ACS Energy Letters* **2020**, *5* (2), 430-436.
16. Kibsgaard, J.; Nørskov, J. K.; Chorkendorff, I., The Difficulty of Proving Electrochemical Ammonia Synthesis. *ACS Energy Letters* **2019**, *4* (12), 2986-2988.
17. Abghoui, Y.; Skúlason, E., Computational Predictions of Catalytic Activity of Zincblende (110) Surfaces of Metal Nitrides for Electrochemical Ammonia Synthesis. *The Journal of Physical Chemistry C* **2017**, *121* (11), 6141-6151.
18. Ertl, G.; Huber, M., Interaction of Nitrogen and Oxygen on Iron Surfaces. *Zeitschrift für Physikalische Chemie* **1980**, *119* (1), 97.
19. Ampelli, C., Electrode design for ammonia synthesis. *Nature Catalysis* **2020**, *3* (5), 420-421.

20. Shi, R.; Zhang, X.; Waterhouse, G. I. N.; Zhao, Y.; Zhang, T., The Journey toward Low Temperature, Low Pressure Catalytic Nitrogen Fixation. *Advanced Energy Materials* **2020**, *10* (19), 2000659.
21. Lazouski, N.; Chung, M.; Williams, K.; Gala, M. L.; Manthiram, K., Non-aqueous gas diffusion electrodes for rapid ammonia synthesis from nitrogen and water-splitting-derived hydrogen. *Nature Catalysis* **2020**, *3* (5), 463-469.
22. Liu, S.; Qian, T.; Wang, M.; Ji, H.; Shen, X.; Wang, C.; Yan, C., Proton-filtering covalent organic frameworks with superior nitrogen penetration flux promote ambient ammonia synthesis. *Nature Catalysis* **2021**, *4* (4), 322-331.
23. Suryanto, B. H. R.; Du, H.-L.; Wang, D.; Chen, J.; Simonov, A. N.; MacFarlane, D. R., Challenges and prospects in the catalysis of electroreduction of nitrogen to ammonia. *Nature Catalysis* **2019**, *2* (4), 290-296.
24. Singh, A. R.; Rohr, B. A.; Statt, M. J.; Schwalbe, J. A.; Cargnello, M.; Nørskov, J. K., Strategies toward Selective Electrochemical Ammonia Synthesis. *ACS Catalysis* **2019**, *9* (9), 8316-8324.
25. Zhou, F.; Azofra, L. M.; Ali, M.; Kar, M.; Simonov, A. N.; McDonnell-Worth, C.; Sun, C.; Zhang, X.; MacFarlane, D. R., Electro-synthesis of ammonia from nitrogen at ambient temperature and pressure in ionic liquids. *Energy & Environmental Science* **2017**, *10* (12), 2516-2520.
26. Moulder, J. F.; Stickle, W. F.; Sobol, P. E.; Bomben, K. D., *Handbook of X-ray Photoelectron Spectroscopy: a reference book of standard spectra for identification and interpretation of XPS data*. Perkin-Elmer Corporation: Eden Prairie, Minnesota, 1992.
27. Galtayries, A.; Laksono, E.; Siffre, J.-M.; Argile, C.; Marcus, P., XPS study of the adsorption of NH<sub>3</sub> on nickel oxide on Ni(111). *Surface and Interface Analysis* **2000**, *30* (1), 140-144.
28. Rao, C. N. R.; Ranga Rao, G., Nature of nitrogen adsorbed on transition metal surfaces as revealed by electron spectroscopy and cognate techniques. *Surface Science Reports* **1991**, *13* (7), 223-263.
29. Zaffaroni, R.; Ripepi, D.; Middelkoop, J.; Mulder, F. M., Gas Chromatographic Method for In Situ Ammonia Quantification at Parts per Billion Levels. *ACS Energy Letters* **2020**, *5* (12), 3773-3777.
30. Andersen, S. Z.; Čolić, V.; Yang, S.; Schwalbe, J. A.; Nielander, A. C.; McEnaney, J. M.; Enemark-Rasmussen, K.; Baker, J. G.; Singh, A. R.; Rohr, B. A.; Statt, M. J.; Blair, S. J.; Mezzavilla, S.; Kibsgaard, J.; Vesborg, P. C. K.; Cargnello, M.; Bent, S. F.; Jaramillo, T. F.; Stephens, I. E. L.; Nørskov, J. K.; Chorkendorff, I., A rigorous electrochemical ammonia synthesis protocol with quantitative isotope measurements. *Nature* **2019**, *570* (7762), 504-508.
31. Choi, J.; Suryanto, B. H. R.; Wang, D.; Du, H.-L.; Hodgetts, R. Y.; Ferrero Vallana, F. M.; MacFarlane, D. R.; Simonov, A. N., Identification and elimination of false positives in electrochemical nitrogen reduction studies. *Nature Communications* **2020**, *11* (1), 5546.
32. Chen, Y.; Liu, H.; Ha, N.; Licht, S.; Gu, S.; Li, W., Revealing nitrogen-containing species in commercial catalysts used for ammonia electrosynthesis. *Nature Catalysis* **2020**, *3* (12), 1055-1061.
33. Tolman, C. A.; Riggs, W. M.; Linn, W. J.; King, C. M.; Wendt, R. C., Electron spectroscopy for chemical analysis of nickel compounds. *Inorganic Chemistry* **1973**, *12* (12), 2770-2778.



34. Brundle, C. R.; Carley, A. F., XPS and UPS studies of the adsorption of small molecules on polycrystalline Ni films. *Faraday Discussions of the Chemical Society* **1975**, *60* (0), 51-70.
35. Devanathan, M. A. V.; Stachurski, Z.; Tompkins, F. C., The adsorption and diffusion of electrolytic hydrogen in palladium. *Proceedings of the Royal Society of London. Series A. Mathematical and Physical Sciences* **1962**, *270* (1340), 90-102.
36. Manolatos, P.; Jerome, M.; Galland, J., Necessity of a palladium coating to ensure hydrogen oxidation during electrochemical permeation measurements on iron. *Electrochimica Acta* **1995**, *40* (7), 867-871.
37. Soroka, O.; Sturm, J. M.; Lee, C. J.; Schreuders, H.; Dam, B.; Bijkerk, F., Hydrogen diffusion through Ru thin films. *International Journal of Hydrogen Energy* **2020**, *45* (29), 15003-15010.
38. Ngene, P.; Longo, A.; Mooij, L.; Bras, W.; Dam, B., Metal-hydrogen systems with an exceptionally large and tunable thermodynamic destabilization. *Nature Communications* **2017**, *8* (1), 1846.
39. Uemiy, S., State-of-the-Art of Supported Metal Membranes for Gas Separation. *Separation and Purification Methods* **1999**, *28* (1), 51-85.
40. Sherbo, R. S.; Delima, R. S.; Chiykowski, V. A.; MacLeod, B. P.; Berlinguette, C. P., Complete electron economy by pairing electrolysis with hydrogenation. *Nature Catalysis* **2018**, *1* (7), 501-507.
41. Dietrich, H.; Geng, P.; Jacobi, K.; Ertl, G., Sticking coefficient for dissociative adsorption of N<sub>2</sub> on Ru single-crystal surfaces. *The Journal of Chemical Physics* **1996**, *104* (1), 375-381.
42. Rao, G. R.; Rao, C. N. R., Adsorption of nitrogen on clean and modified single-crystal Ni surfaces. *Applied Surface Science* **1990**, *45* (1), 65-69.
43. Wedler, G.; Alshorachi, G., Adsorption of Nitrogen on Polycrystalline Nickel Films between 77 K and 333 K. *Berichte der Bunsengesellschaft für physikalische Chemie* **1980**, *84* (3), 277-281.
44. Grunze, M.; Driscoll, R. K.; Burland, G. N.; Cornish, J. C. L.; Pritchard, J., Molecular and dissociative chemisorption of N<sub>2</sub> on Ni(110). *Surface Science* **1979**, *89* (1), 381-390.
45. Ertl, G.; Lee, S. B.; Weiss, M., Kinetics of nitrogen adsorption on Fe(111). *Surface Science* **1982**, *114* (2), 515-526.
46. Vojvodic, A.; Medford, A. J.; Studt, F.; Abild-Pedersen, F.; Khan, T. S.; Bligaard, T.; Nørskov, J. K., Exploring the limits: A low-pressure, low-temperature Haber–Bosch process. *Chemical Physics Letters* **2014**, *598*, 108-112.
47. Ertl, G.; Huber, M.; Lee, S. B.; Paál, Z.; Weiss, M., Interactions of nitrogen and hydrogen on iron surfaces. *Applications of Surface Science* **1981**, *8* (4), 373-386.
48. Bozso, F.; Ertl, G.; Grunze, M.; Weiss, M., Interaction of nitrogen with iron surfaces: I. Fe(100) and Fe(111). *Journal of Catalysis* **1977**, *49* (1), 18-41.
49. Tkacz, M., Enthalpies of formation and decomposition of nickel hydride and nickel deuteride derived from (p, c, T) relationships. *J. Chem. Thermodyn.* **2001**, *33* (8), 891-897.
50. Hodgetts, R. Y.; Du, H.-L.; MacFarlane, D. R.; Simonov, A. N., Electrochemically Induced Generation of Extraneous Nitrite and Ammonia in Organic Electrolyte Solutions During Nitrogen Reduction Experiments. *ChemElectroChem* **2021**, *8* (9), 1596-1604.

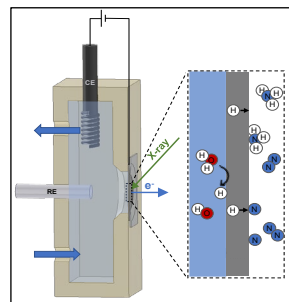
51. Suryanto, B. H. R.; Matuszek, K.; Choi, J.; Hodgetts, R. Y.; Du, H.-L.; Bakker, J. M.; Kang, C. S. M.; Cherepanov, P. V.; Simonov, A. N.; MacFarlane, D. R., Nitrogen reduction to ammonia at high efficiency and rates based on a phosphonium proton shuttle. *Science* **2021**, 372 (6547), 1187-1191.
52. Baiker, A.; Maciejewski, M., Formation and thermal stability of copper and nickel nitrides. *Journal of the Chemical Society, Faraday Transactions 1: Physical Chemistry in Condensed Phases* **1984**, 80 (8), 2331-2341.
53. Liu, B.; He, B.; Peng, H.-Q.; Zhao, Y.; Cheng, J.; Xia, J.; Shen, J.; Ng, T.-W.; Meng, X.; Lee, C.-S.; Zhang, W., Unconventional Nickel Nitride Enriched with Nitrogen Vacancies as a High-Efficiency Electrocatalyst for Hydrogen Evolution. *Advanced Science* **2018**, 5 (8), 1800406.
54. Ye, T.-N.; Park, S.-W.; Lu, Y.; Li, J.; Sasase, M.; Kitano, M.; Tada, T.; Hosono, H., Vacancy-enabled N<sub>2</sub> activation for ammonia synthesis on an Ni-loaded catalyst. *Nature* **2020**, 583 (7816), 391-395.
55. Mars, P.; van Krevelen, D. W., Oxidations carried out by means of vanadium oxide catalysts. *Chemical Engineering Science* **1954**, 3, 41-59.
56. Zeinalipour-Yazdi, C. D.; Hargreaves, J. S. J.; Catlow, C. R. A., Nitrogen Activation in a Mars–van Krevelen Mechanism for Ammonia Synthesis on Co<sub>3</sub>Mo<sub>3</sub>N. *The Journal of Physical Chemistry C* **2015**, 119 (51), 28368-28376.
57. Michalsky, R.; Avram, A. M.; Peterson, B. A.; Pfromm, P. H.; Peterson, A. A., Chemical looping of metal nitride catalysts: low-pressure ammonia synthesis for energy storage. *Chemical Science* **2015**, 6 (7), 3965-3974.
58. Jin, H.; Li, L.; Liu, X.; Tang, C.; Xu, W.; Chen, S.; Song, L.; Zheng, Y.; Qiao, S.-Z., Nitrogen Vacancies on 2D Layered W<sub>2</sub>N<sub>3</sub>: A Stable and Efficient Active Site for Nitrogen Reduction Reaction. *Advanced Materials* **2019**, 31 (32), 1902709.
59. Abghoui, Y.; Skúlason, E., Transition Metal Nitride Catalysts for Electrochemical Reduction of Nitrogen to Ammonia at Ambient Conditions. *Procedia Computer Science* **2015**, 51, 1897-1906.
60. Abghoui, Y.; Garden, A. L.; Hlynsson, V. F.; Björgvinsdóttir, S.; Ólafsdóttir, H.; Skúlason, E., Enabling electrochemical reduction of nitrogen to ammonia at ambient conditions through rational catalyst design. *Physical Chemistry Chemical Physics* **2015**, 17 (7), 4909-4918.
61. Biesinger, M. C.; Payne, B. P.; Lau, L. W. M.; Gerson, A.; Smart, R. S. C., X-ray photoelectron spectroscopic chemical state quantification of mixed nickel metal, oxide and hydroxide systems. *Surface and Interface Analysis* **2009**, 41 (4), 324-332.
62. Davey, W. P., Precision Measurements of the Lattice Constants of Twelve Common Metals. *Physical Review* **1925**, 25 (6), 753-761.
63. Griessen, R.; Driessen, A., Heat of formation and band structure of binary and ternary metal hydrides. *Physical Review B* **1984**, 30 (8), 4372-4381.
64. Wang, M.; Khan, M. A.; Mohsin, I.; Wicks, J.; Ip, A. H.; Sumon, K. Z.; Dinh, C.-T.; Sargent, E. H.; Gates, I. D.; Kibria, M. G., Can sustainable ammonia synthesis pathways compete with fossil-fuel based Haber–Bosch processes? *Energy & Environmental Science* **2021**, 14 (5), 2535-2548.



# In situ study of hydrogen permeable electrodes for electrolytic ammonia synthesis using near ambient pressure XPS

6

Hydrogen permeable electrodes can be utilised for electrolytic ammonia synthesis from dinitrogen, water and renewable electricity at ambient conditions, providing a promising route towards sustainable ammonia. The understanding of the interactions of adsorbing N and permeating H at the catalytic interface is a critical step towards the optimization of this  $\text{NH}_3$  synthesis process. In this study, we conducted a unique *in situ* near ambient pressure X-ray photoelectron spectroscopy experiment to investigate the solid-gas interface of a Ni hydrogen permeable electrode under conditions relevant for ammonia synthesis. Here we show that the formation of a Ni oxide surface layer blocks the chemisorption of gaseous dinitrogen. However, the Ni 2p and O 1s XPS spectra reveal that electrochemically driven permeating atomic hydrogen effectively reduces the Ni surface at ambient temperature, while  $\text{H}_2$  does not. Nitrogen gas chemisorbs on the generated metallic sites, followed by hydrogenation via permeating H, as adsorbed N and  $\text{NH}_3$  are found on the Ni surface. Our findings suggest that the first hydrogenation step to NH and the  $\text{NH}_3$  desorption might be limiting at the operating conditions. The study was then extended to Fe and Ru surfaces. The formation of surface oxide and nitride species on iron blocks the H permeation and prevents the reaction to advance; while on ruthenium the stronger Ru-N bond might favour the recombination of permeating hydrogen to  $\text{H}_2$  over the hydrogenation of adsorbed nitrogen. This work provides insightful results to aid the rational design of efficient electrolytic  $\text{NH}_3$  synthesis processes based on but not limited to hydrogen permeable electrodes.



## 6.1 Introduction

Ammonia ( $\text{NH}_3$ ) is an essential source of activated nitrogen, required for the global production of N-based fertilisers (more than 180 million tonnes per year).<sup>1</sup> In addition, the demand for ammonia is expected to grow because of its potential application as future energy carrier.<sup>2, 3</sup> The negative environmental impact of the current fossil based industrial  $\text{NH}_3$  synthesis process,<sup>4</sup> the Haber-Bosch process, operating at high temperatures and pressures, urges for a more sustainable alternative. The renewable energy driven electrosynthesis of ammonia from dinitrogen ( $\text{N}_2$ ) and water at mild conditions may represent an attractive solution to produce fossil-energy-free  $\text{NH}_3$ .<sup>2</sup> Although the electrocatalytic reduction of nitrogen to ammonia has gained large scientific interest,<sup>5</sup> the hydrogen evolution reaction (HER) strongly dominates over the nitrogen reduction reaction (NRR) in aqueous environments, due to the preferential hydrogen activation.<sup>6-9</sup> The lack of a selective catalyst for nitrogen activation drove the scientific community to explore other approaches to minimize and suppress the competition with HER.<sup>10-14</sup>

In this context, the adoption of a hydrogen permeable electrode proved to be a successful strategy to spatially separate the aqueous electrolyte and the hydrogen reduction side from the  $\text{N}_2$  activation and hydrogenation sites (**Figure 6.1a**).<sup>11</sup> In this way,  $\text{N}_2$  can bond onto the catalytic surface in the absence of other competing adsorbate molecules from the electrolyte.  $\text{NH}_3$  is then formed on the catalyst surface from the hydrogenation of adsorbed N via electrochemically permeating atomic hydrogen at ambient conditions. In this way, when the  $\text{NH}_3$  desorbs, it becomes available directly in the gas phase, without the necessity of further separation from a liquid electrolyte. While the catalytic reaction was demonstrated as a proof of principle with strict isotope labelling control experiments using a Ni hydrogen permeable electrode,<sup>11</sup> other materials might speed up the rate of the reaction. Iron and ruthenium are among the most promising catalysts, according to their reported activity toward nitrogen activation<sup>15-19</sup> and hydrogen permeability<sup>20, 21</sup> at near ambient conditions. Moreover, in our previous study, we have seen how the presence of surface nitrides, besides protecting the reactive Ni surface against oxidation, may act as precursor for a low temperature Mars-van Krevelen (MvK) mechanism.<sup>11</sup> This two stages mechanism consists of, first, the hydrogenation of lattice N to yield  $\text{NH}_3$  and a nitrogen vacancy ( $\text{N}^{\text{vac}}$ ), and second, the filling of the  $\text{N}^{\text{vac}}$  with gaseous dinitrogen.<sup>22</sup> The use of metal nitrides (MN) as ammonia synthesis

catalysts has been proposed and offers several advantages, such as a limited H adsorption.<sup>22-24</sup> Even though recently there have been some concerns on certain MN used as electrocatalysts for nitrogen reduction reaction (NRR) in aqueous electrolytes,<sup>25</sup> the catalytic activity of MN was demonstrated with isotope exchange experiments, revealing the occurrence of a Mars-van Krevelen mechanism.<sup>23, 26</sup> Density functional theory (DFT) calculations showed that such surface nitrogen vacancies can activate N<sub>2</sub> by weakening of the triple bond (N-N bond elongation), lowering the barrier for nitrogen activation.<sup>27-29</sup> However, the catalytic MvK nitrogen activation typically requires high temperatures to hydrogenate the surface lattice N with reactive H<sub>2</sub> gas. In contrast, electrochemically inserted and permeating atomic hydrogen reduces surface N to form NH<sub>3</sub> and N<sup>vac</sup> at ambient temperature.<sup>11</sup>

Yet, the ammonia production rates achieved till now using H permeable electrodes remain far from commercially relevant applications,<sup>30</sup> and thus further mechanistic understanding and technical developments are needed. Consequently, understanding how N<sub>2</sub> and permeating H interact on the catalytic surface during the reaction can aid the rational design and development of better catalysts. Surface sensitive *operando* and *in situ* techniques, such as near ambient pressure X-ray photoelectron spectroscopy (NAP-XPS), can provide such information, as has been shown for several systems recently in the literature,<sup>31-34</sup> including palladium hydrogen membranes.<sup>35</sup> XPS commonly operates under ultra high vacuum (UHV) conditions due to the short inelastic mean free path length of photoelectrons in a gas atmosphere. Recent technological advances have made it possible to operate XPS under more realistic conditions, bridging the gap between UHV and operating pressure.<sup>36, 37</sup> NAP-XPS can thus measure modifications in the surface electronic structure of the catalyst and the nature of adsorbed molecules in an element specific manner. Numerous spectroscopic studies on nitrogen adsorption and catalytic ammonia synthesis have been carried out over the years.<sup>15, 38-41</sup> As a result, various adsorbed N species and reaction intermediates have been identified using XPS (**Table 6.1**). Remarkably, while extensive studies on the adsorption of N<sub>2</sub> with XPS are available for Ni and Fe, less work has focused on XPS of nitrogen adsorption on Ru.

In this study, synchrotron-based soft X-ray photoelectron spectroscopy was used to investigate the solid-gas interface of nickel, iron and ruthenium polycrystalline surfaces, and their corresponding nitride phases, under electrochemical hydrogen permeation and

dinitrogen atmosphere. This *in situ* XPS study shows that the first hydrogenation step to NH and the NH<sub>3</sub> desorption on Ni might be limiting at the operating conditions. We also provide further evidence of how electrochemically inserted and permeating atomic hydrogen can reduce the surface lattice N on Ni, to form NH<sub>3</sub> and N<sup>vac</sup> at ambient temperature, while the same process is not observed on Fe and Ru..

## 6.2 Experimental

**Materials and methods.** Potassium hydroxide pellets (Sigma-Aldrich, 99.99% trace metals basis) and Milli-Q water were used for the preparation of the electrolyte solution (0.1 M). The polycrystalline nickel foil with a thickness of 12.5  $\mu\text{m}$  and 99.9 % purity was purchased from Goodfellow. The polycrystalline iron foil with a thickness of 25.0  $\mu\text{m}$  and 99.5 % purity was purchased from Advent Research Materials Ltd. All the samples were thoroughly cleaned in an ultra-high vacuum chamber under Ar/H<sub>2</sub> plasma for 30 min. The Ru thin film was deposited on the cleaned polycrystalline Ni foil by reactive magnetron sputtering (AJA International Inc.) at 100 W DC power in Ar (6N) atmosphere. Ruthenium sputtering target was purchased from Mateck GmbH (purity 99.9 %). Prior to the deposition the pressure of the ultra high vacuum chamber was about  $10^{-8}$  mbar. During the deposition a constant Ar flow of 35 sccm was used and the pressure held to  $3 \cdot 10^{-3}$  mbar by mean of a butterfly reducing valve mounted at the inlet of the pumping stage. The deposition time was adjusted to obtain a film thickness of 20 nm, as determined by surface profilometry (with a relative uncertainty of about 10 %). Analogously to the Ru sputtering deposition, also the protective 20 nm Pd layer for the hydrogen permeation experiments in the Devanathan-Stachurski setup was prepared by reactive magnetron sputtering, using a 2-inch metal target (MaTeck, 99.9 % purity) at 100 W DC power in an Ar atmosphere.

**Sample preparation.** A total of six types of electrodes were prepared for this study, respectively Ni, Fe, Ru, and their corresponding surface nitrides. The Ni and Fe electrodes consist of a polycrystalline nickel (12.5  $\mu\text{m}$ ) and iron (25  $\mu\text{m}$ ) foil, respectively. The Ru electrode consists of a polycrystalline nickel foil (12.5  $\mu\text{m}$ ) coated with 20 nm of sputter deposited ruthenium. All the samples were thoroughly cleaned in an ultra-high vacuum chamber under Ar/H<sub>2</sub> plasma for 30 min. The plasma was generated with a radio frequency power supply at 20 W under a constant flow of Ar (35 sccm) and H<sub>2</sub> (5 sccm). A pressure of

$5 \cdot 10^{-3}$  mbar was held in the reaction chamber by mean of a butterfly reducing valve mounted at the inlet of the pumping stage. Surface nitrides were prepared by exposing the cleaned sample surface to an additional plasma nitriding step consisting of an Ar/N<sub>2</sub> plasma (in 2 to 1 ratio) at  $2 \cdot 10^{-2}$  mbar for ten minutes. This results in about 30 nm thick nickel nitride layer.<sup>11</sup> The described sample preparation steps were carried out *ex situ*, prior mounting the electrode in the electrochemical cell. More details on the materials and methods can be found in the Supporting Information (SI). The structural properties of the prepared samples were analysed with X-ray diffraction (XRD). XRD analysis was performed with a Bruker D8 ADVANCE ECO equipped with a Cu K $\alpha$  source (1.54060 Å, 40 kV and 25 mA). The Bragg-Brentano measurement geometry was applied with a fixed sample illumination slit of 5.0 mm and a LynxEye XE-T detector. The data was collected at 0.01° step size in the range of 5-110°. The Fe sample was characterised using a Bruker D8 ADVANCE diffractometer equipped with a Co K $\alpha$  source, to avoid the characteristic fluorescence emitted by iron when using a Cu K $\alpha$  source. The obtained results are included in the SI (**Figure A.6.1-A.6.3**).

**Electrochemical hydrogen permeation.** The electrochemical hydrogen permeation rate of the different electrodes under investigation is measured using the Devanathan-Stachurski (DS) method<sup>42</sup> (**Figure A.6.4**). Electrochemical hydrogen insertion is carried out in 0.1 M KOH solution with a galvanostatic cathodic charging current density of 5 mA cm<sup>-2</sup>. The permeating atomic hydrogen is then oxidised at the anodic compartment (hydrogen exit side of the DS cell) at a constant electrode potential of +0.3 V vs SHE in a 0.1 M KOH electrolyte. The measured anodic current is directly proportional to the atomic hydrogen permeation through the specimen. The sample was physically grounded and the multichannel potentiostat set in floating mode.



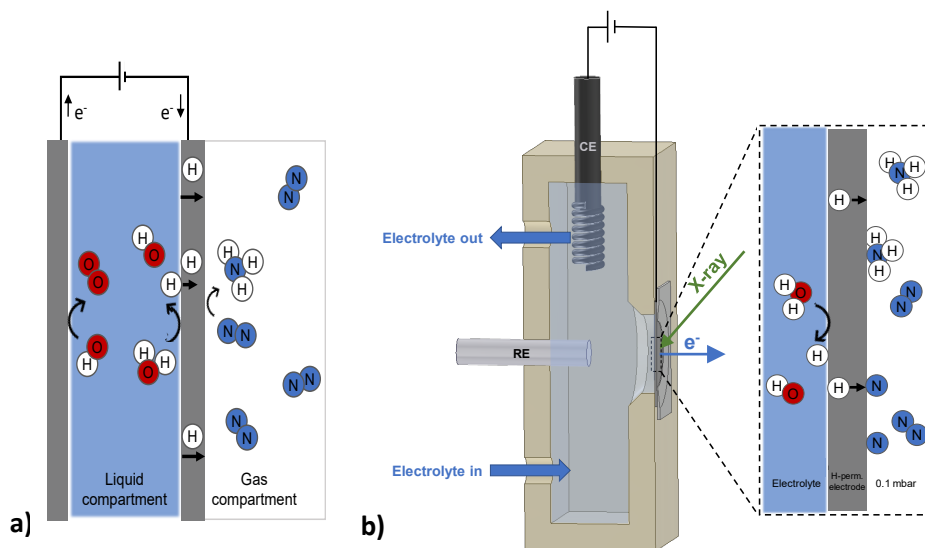


**Figure 6.1** On the left, a schematic representation of the electrolytic cell for ammonia synthesis under investigation, which uses a hydrogen permeable electrode (a). Reproduced from *ACS Energy Lett.* 2021, 6, 11, 3817–3823. Copyright 2021 The Authors. Published by American Chemical Society. A detailed description of the working principle can be found elsewhere.<sup>11</sup> Schematic cross section of the *in situ* electrochemical flow cell for near ambient pressure X-ray photoelectron spectroscopy used in this study (b). The electrolyte is continuously circulated through the cell. Soft X-ray photoelectron spectroscopy was used to investigate the solid-gas interface (right side of the electrode). The enclosure highlights the main steps involved in electrochemical hydrogen insertion, dinitrogen activation and nitrogen reduction to ammonia.

**Ammonia quantification.** Ammonia quantification is carried out directly in the gas phase with a gas chromatography (GC) method, previously developed in our group. Details of the detection method are available elsewhere.<sup>43, 44</sup> The electrodes under investigation in this study were mounted in a two compartments polyether ether ketone (PEEK) electrochemical flow cell (**Figure 6.1a** and **Figure 6.2**). One side of the electrode, in the liquid compartment, is in contact with the aqueous electrolyte (0.1 M KOH), while the other side, in the gas compartment, is in contact with only N<sub>2</sub> at ambient pressure flowing at 1 ml min<sup>-1</sup> (the electrode geometrical active area is 2.5 cm<sup>2</sup>). The gas composition of the gas compartment is continuously analysed via GC. The detection of ammonia was not possible directly at the near ambient pressure XPS setups, mainly because of the small surface area and the large volume of the stainless steel analysis chamber, which is known for high NH<sub>3</sub> physisorption.<sup>45, 46</sup>

**Spectroscopy.** The *in situ* XPS spectra were collected at two different synchrotron facilities. The ISISS beamline of BESSY II employs bending magnet (D41) and a plane grating monochromator (PGM), tuneable photon energy 80-2000 eV, detection of photoelectrons normal to surface, 0.1 mm x 0.08 mm beam spot size and  $6 \cdot 10^{10}$  photons/s/0.1 Å at a 0.111 mm exit slit. The NAP-XPS end-station is equipped with a SPECS PHOIBOS 150 NAP hemispherical XPS analyser. The spectra were collected using 10 eV pass energy (20 eV for survey scan) and 0.1 eV step, with an experimental resolution of about 0.55 eV. All the gases (N<sub>2</sub>, O<sub>2</sub>, H<sub>2</sub>) were supplied by Westfalen AG and had a purity of 99.9999%. The *in situ* electrochemical cell is made of polyether ether ketone (PEEK). The sample size for the H permeable electrode was 10 x 10 mm, with a geometrical active area of about 50 mm<sup>2</sup>, defined as the inner area of the O-ring that contains the electrolyte. The *in situ* electrochemical near ambient pressure X-ray photoelectron spectroscopy experiments were performed at the ISISS beamline at the BESSY II electron storage ring operated by the Helmholtz-Zentrum Berlin für Materialien und Energie, using the existing electrochemical flow cell,<sup>47</sup> shown in **Figure 6.1b** and **Figure 6.2**. The electrolyte (0.1 M KOH) was flown in the electrochemical cell via a peristaltic pump with a flow rate of 1 ml min<sup>-1</sup>. The electrochemical experiments were carried out using a Pt counter electrode and a saturated Ag/AgCl reference electrode. The electrochemical insertion and permeation of atomic hydrogen through the metal lattice of the working electrode was achieved with a constant negative polarization of -1.5 V vs SHE (not iR corrected), using a Biologic SP-300 potentiostat. The applied potential matches the operating conditions of our previous work,<sup>11</sup> resulting in similar charging current density (**Figure A.6.5**). The operation under potentiostatic conditions was preferred due to better electrochemical stability using the *in situ* electrochemical cell, compared to galvanostatic operation. The pressure of the XPS analysis chamber reached 10<sup>-7</sup> mbar prior to starting the experiment. Dosing of the gases in the near ambient pressure XPS chamber was carried out with a set of dedicated mass flow controllers (Bronkhorst) to a pressure of 0.1 mbar. A potential of 90 V was applied to the nozzle of the analyser to eliminate the gas phase contributions in XPS measurements. The solid Ni hydrogen permeable electrode provides a complete, physical separation between the aqueous electrolyte and the NAP side. Yet, hydrogen atoms can selectively diffuse through the lattice of the Ni electrode, via electrochemical insertion under negative polarization. With this

configuration the reaction between permeating absorbed hydrogen and surface species at the solid-gas interface can be studied in near ambient pressure in the absence of liquid electrolyte.

The BL24-CIRCE beamline at the ALBA Synchrotron Light Source uses tuneable photon energy 90-2000 eV, beam incident angle  $80^\circ$  from normal to surface, beam spot size 0.1 mm horizontally and 0.03 mm vertically. The NAP-XPS end-station is equipped with a SPECS PHOIBOS 150 NAP hemispherical XPS analyser. More details on the BL24-CIRCE are also available elsewhere.<sup>48</sup> The spectra were collected using 10 eV pass energy (20 eV for survey scan) and 0.1 eV step, with an experimental resolution of 0.29 eV. All the gases ( $N_2$ ,  $H_2$  and  $O_2$ ) used had 6.0 purity grade. Near ambient pressure X-ray photoelectron spectroscopy experiments were performed at BL24-CIRCE beamline at the ALBA Synchrotron Light Source, Spain, using a laser heated sample holder (**Figure 6.2**).<sup>37</sup> The sample was heated from behind using an infrared laser, while the sample temperature was monitored by a K-Type thermocouple. The pressure of the XPS analysis chamber prior starting the experiment was about  $6 \cdot 10^{-8}$  mbar and gases were introduced by dedicated mass flow controllers (Brooks). To prevent beam damage effects, each spectrum was recorded on a fresh spot on the surface.

Additional *ex situ* XPS measurements were collected with a Thermo Scientific K-alpha spectrometer with Al K $\alpha$  monochromator, using a sealed sample holder to avoid air exposure of the samples.

All the spectra in the present manuscript were collected with a photoelectron kinetic energy of 200 eV, by adjusting the incident excitation energy accordingly, unless stated otherwise. The XPS intensity was normalised by the ring current and photon flux to compensate for slight variations in incident X-ray. Data analysis was performed using CasaXPS software. For each core shell, a valence band spectrum was recorded at the respective photon energy for a proper energy calibration.<sup>49</sup> The absolute binding energy values were allowed to vary by  $\pm 0.1$  eV. Because of spin-orbit coupling, Ni 2p, Fe 2p and Ru 3p spectra are split in two parts ( $p_{3/2}$  and  $p_{1/2}$ ), with a defined intensity ratio. In this case, only one part of the spectrum ( $p_{3/2}$ ) is used for fitting of the components, as common practice.<sup>50</sup> All fitting parameters are given in Table A.6.1-A.6.5.

**Quantitative model for overlayer thickness calculations.** The kinetic energy of the emitted photoelectrons depends on the incident photon energy. Therefore, photoelectrons with different escape depth can be collected varying the incident photon energy. Variable

synchrotron incident photon energy can thus be used to measure the thickness of overlayers in a non-destructive way.<sup>51, 52</sup> The film thickness is derived from the integrated XPS signal intensities and the effective attenuation length (EAL) at different kinetic energies, assuming an uniform overlayer of finite thickness over a semi infinite substrate, from the following equation:

$$\frac{I_o}{I_s} = \frac{F_o \rho_o \sigma_o \lambda_{EAL_o}}{F_s \rho_s \sigma_s \lambda_{EAL_s}} \cdot \left[ 1 - e^{-\frac{t}{\lambda_{EAL_o} \cos \alpha}} \right] e^{\frac{t}{\lambda_{EAL_o} \cos \alpha}} \quad (6.1)$$

where  $F$  is a value that depends on the emitted electron energy and includes various instrumental parameters,  $\rho$  is the atomic density,  $\sigma$  the differential cross-section,  $\lambda_{EAL}$  is the effective attenuation length,  $t$  the overlayer thickness,  $\alpha$  the photoelectron emission angle measured with respect to the surface normal, and  $I$  the XPS intensity from the substrate (s) and overlayer (o). More details on the quantification model are available elsewhere.<sup>52</sup> The effective attenuation length can be approximated to the inelastic mean free path (IMFP) for kinetic energies above 200 eV.<sup>51</sup> The values of the IMFP are obtained from the NIST Electron Inelastic-Mean-Free-Path Database (NSRD 71 version 1.2).<sup>53</sup> The parameters  $F$  and  $\sigma$  are considered equals for both substrate and overlayer. The calculate  $I_o/I_s$  values are fitted against the measured ones by stepwise varying the overlayer thickness, till reaching the minimum standard deviation.

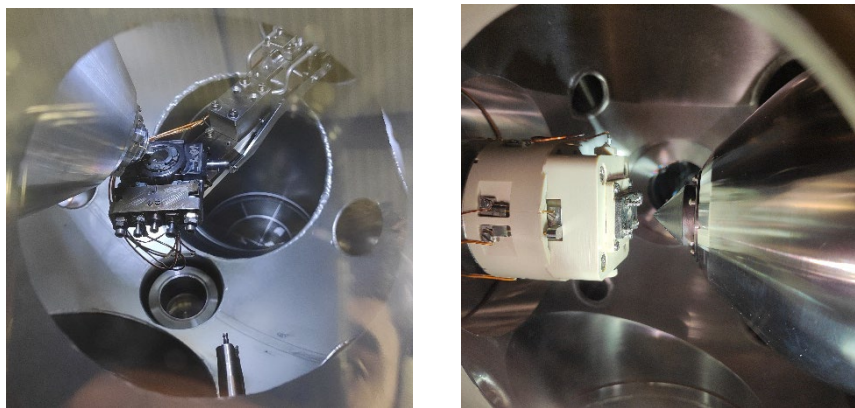


**Figure 6.2** On the left, a picture of the sample holder for back laser heating experiments in the analysis chamber of the BL24-CIRCE beamline (ALBA, Barcelona). On the right, a picture of the in situ electrochemical cell within the analysis chamber of the ISISS beamline (BESSY II, Berlin).

### 6.3 Results and discussion

**Nickel.** Nitrogen chemisorption occurs on reduced surfaces of various transition metals, even at ambient temperature and pressure.<sup>15</sup> However, the presence of other reactive species that compete for adsorption sites, affects the dinitrogen activation negatively.<sup>6, 8, 54, 55</sup> Chemisorbed atomic nitrogen has been observed on metallic Ni.<sup>11, 15, 39, 56, 57</sup> In contrast, from our NAP XPS measurements, we found that a NiO layer grown on the polycrystalline Ni does not present any reactivity towards N<sub>2</sub> adsorption (**Figure A.6.6**). From these results, it follows, that preserving an oxide-free Ni metal catalytic surface is important to effectively activate N<sub>2</sub>. However, this is a challenge as Ni readily forms surface oxide species even in the presence of traces of oxygen or water, due to the highly negative and spontaneous oxide formation energy (about -240 kJ mol<sup>-1</sup>).<sup>58, 59</sup> Hence, it is no surprise that XPS measurements performed on the initially clean metallic Ni foil reveal the formation of a thin mixed oxide/hydroxide surface layer, due to the brief exposure to air during sample mounting in the *in situ* electrochemical setup. The Ni 2p<sub>3/2</sub> spectrum shows the components corresponding to metallic, oxide and hydroxide species (**Figure 6.3**). The data were fitted according to literature (details are available in Table A.6.1-A.6.2).<sup>60</sup>

Consistent with this, the corresponding O 1s spectrum reveals the components characteristic of oxide (529.3 eV), hydroxide (531.1 eV) and adsorbed water (532.9 eV).<sup>60, 61</sup> The thickness of the oxide layer can be estimated using a non-destructive depth profile analysis based on variable synchrotron incident radiation energy.<sup>51, 52</sup> By fitting the experimental data with the simplified model described in equation 6.1, the thickness of the oxide overlayer is estimated to be approximately 0.75 nm (**Figure 6.3**). Details on the quantitative model are available in the experimental section. Our *in situ* observations reveal that, once formed, surface Ni oxides are stable in both vacuum and under gaseous H<sub>2</sub> (0.1 mbar) at temperatures below 100 °C (**Figure 6.4** and **Figure A.6.7**). As such, very stringent gas purity would be necessary to maintain a metallic Ni catalytic surface at temperatures close to ambient. However, here we show that it is possible to apply electrochemical permeating atomic hydrogen to effectively reduce the surface Ni oxides and hydroxides at room temperature (**Figure 6.3**). Under electrochemical hydrogen loading, the initial oxidized state of the surface changes.

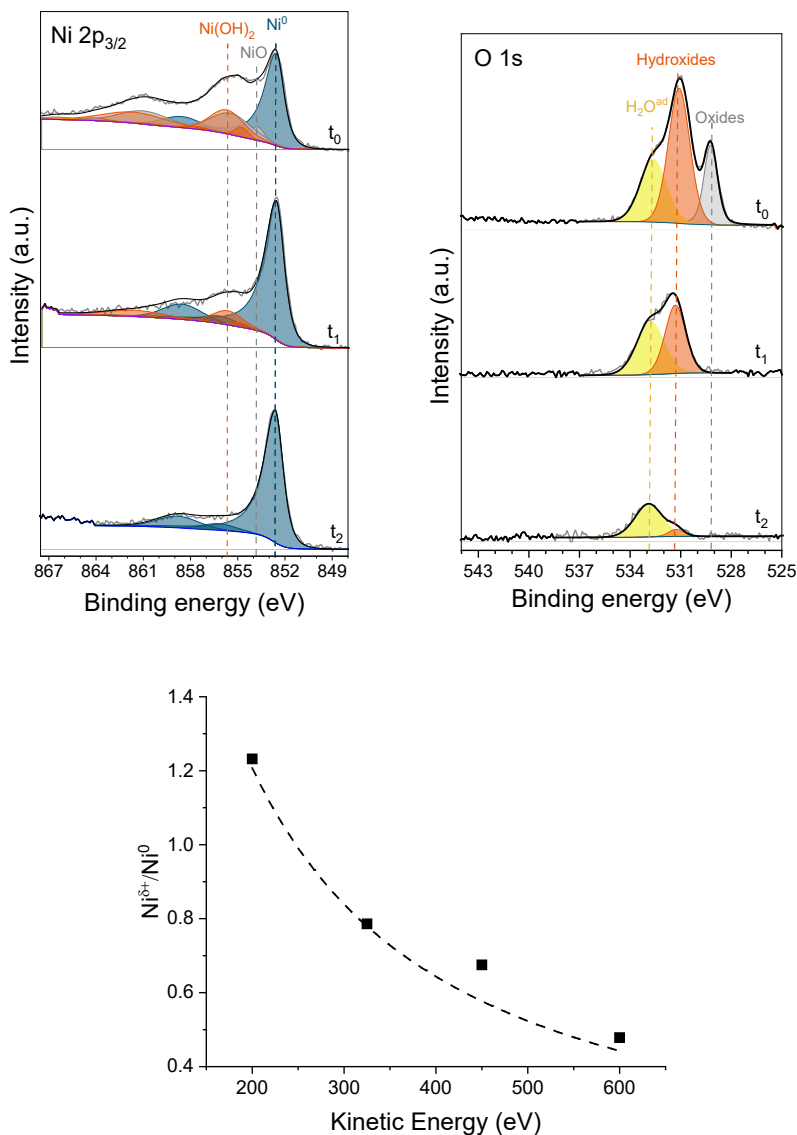


**Figure 6.3** On the top, the Ni 2p<sub>3/2</sub> (left) and O 1s (right) XPS spectra show, over time (t<sub>0</sub>= 0 min, t<sub>1</sub>= +15 min and t<sub>2</sub>= +75 min), the *in situ* reduction of Ni oxide/hydroxide via electrochemically permeating atomic hydrogen at room temperature under vacuum. Fit model using Ni<sup>0</sup> (blue), metal oxide (grey), metal hydroxide (orange) and adsorbed water (yellow). On the bottom, the ratio of the Ni 2p<sub>3/2</sub> XPS peak areas of oxidised and metallic species, at t<sub>0</sub>= 0 min, as function of photoelectron kinetic energy (between 200 and 600 eV). Measured values (symbols) and calculated fit (dotted line). From this, the initial thickness of the oxidised surface layer is estimated to be 0.75 ± 0.02 nm.

The  $\text{Ni}^0$  contributions become increasingly dominant, ultimately replacing all  $\text{Ni}^{+\delta}$  components. It was observed that Ni oxides are the first species to be reduced, followed by hydroxide components, until a metallic Ni surface is obtained. Oxide decomposition by X-ray or vacuum was ruled out with prolonged measurements under open circuit potential (OCP), which do not show any signs of reduction. This result is expected as the enthalpy of formation of the surface oxides and hydroxides is rather negative, which indicates that these compounds are relatively stable. Although the reductive action of continuously fed atomic hydrogen maintains a metallic catalytic surface, re-oxidation is observed upon interruption of electrochemical H permeation (**Figure A.6.8**). This is due to the presence of residual vacuum contaminants, as traces of oxygen and water vapor (the pressure in the analysis chamber prior starting the experiment was about  $7 \cdot 10^{-7}$  mbar).

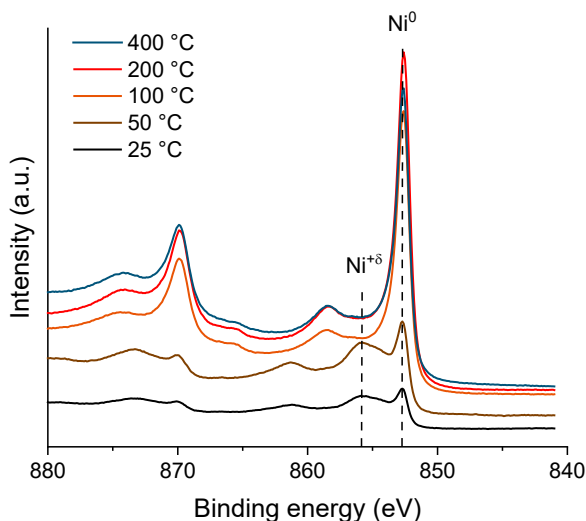


**Figure 6.4** Ni 2p XPS spectra of the polycrystalline Ni foil in presence of 1 mbar of  $\text{H}_2$  heated up from room temperature (25 °C) to 400 °C. The position main metallic and oxide components is indicated by the dashed lines. Reduction of the Ni surface is achieved from 100 °C. Photoelectron kinetic energy was 200 eV.

Having established how electrochemically permeating atomic hydrogen can *in situ* reduce the Ni surface under room temperature conditions, we now turn our attention to the interaction of this reduced surface with dinitrogen gas. **Figure 6.5a** shows that a clean metallic Ni surface exposed to  $\text{N}_2$  results in a dominant N 1s peak centred at 397.8 eV

corresponding to chemisorbed atomic nitrogen.<sup>41, 62-65</sup> When also electrochemical hydrogen permeation is active, an additional component at higher binding energy (BE, 400.3 eV), assigned to adsorbed  $\text{NH}_3$ ,<sup>41, 62, 66</sup> appears in the N 1s spectrum (**Figure 6.5b**). Other nitrogen species on Ni surfaces have been detected at comparable BE, as reported in **Table 6.1**. However, molecular dinitrogen on Ni has only been observed at temperatures  $\leq 80$  K.<sup>39, 63, 67</sup> While NO species can also be excluded, as they have been observed at appreciable lower BE (399.8-399.4 eV) and because of the absence of the respective O 1s component at about 530.3 eV<sup>63, 64, 68</sup> (**Figure A.6.9**). The assignment of this peak to adsorbed  $\text{NH}_3$  is also confirmed from gaseous ammonia detected from a sample with higher N coverage, where a peak at 400.3 eV is also observed upon electrochemical H permeation (vide infra).

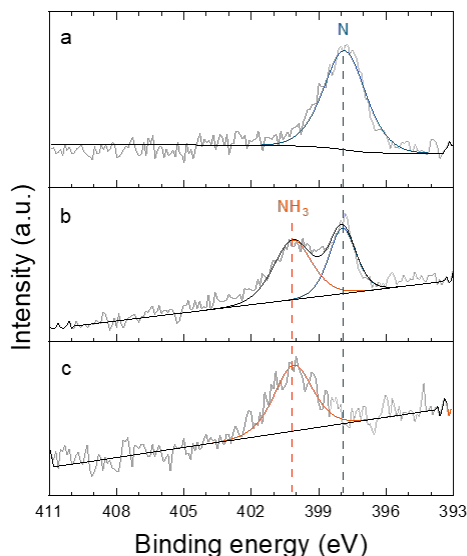


**Figure 6.5** N 1s XPS spectra of clean metallic Ni surface (a) after exposure to  $\text{N}_2$  in OCP, measured *ex situ* using a sealed XPS sample holder to avoid contact with air (which would hinder the N chemisorption), (b) during the exposure to 0.1 mbar of  $\text{N}_2$  under electrochemical atomic hydrogen permeation and (c) after subsequent evacuation to UHV under electrochemical atomic hydrogen permeation. The reference spectrum (a) is obtained using a K-alpha spectrometer, while the spectra (b) and (c) are measured *in situ* at the ISSS beamline. The larger width of the peak at 400.3 eV might be due to disorder, which includes different adsorption sites.

Ammonia is thus formed on the Ni surface as result of hydrogenation of chemisorbed nitrogen. However, in this case, on a flat Ni surface with limited N coverage, the ammonia



production rate is estimated to be lower than  $10^{-13}$  mol cm<sup>-2</sup> s<sup>-1</sup> (corresponding to the instrument detection limit), as no gaseous ammonia was detected with in-line GC in a separate experiment. Reaction intermediates NH and NH<sub>2</sub>, reported on Ni at around 398.5 eV,<sup>62, 66</sup> cannot be discriminated in the N 1s spectra, this indicates that the hydrogenation rate of NH to NH<sub>2</sub> and NH<sub>3</sub> is much faster than the hydrogenation of N and the desorption of NH<sub>3</sub>. The persistent presence of atomic nitrogen species at 397.8 eV on the catalyst surface exposed to N<sub>2</sub> and constant H-permeation (**Figure 6.5b**), possibly indicates that atomic N is constantly replenished by newly adsorbed and dissociated dinitrogen. The subsequent evacuation of the N<sub>2</sub> present in the analysis chamber in OCP (i.e. vacuum conditions without H-permeation) does not alter the N 1s spectrum (**Figure A.6.10**), indicating that both the N and NH<sub>3</sub> are stably bound on the surface. However, in the absence of gaseous N<sub>2</sub> to replenish the reacting adsorbed nitrogen (i.e. under vacuum), the N 1s peak at 397.8 eV progressively disappears when electrochemical hydrogen permeation is restored; leaving NH<sub>3</sub> as the only N species on the surface (**Figure 6.5c**). From these observations, it becomes evident how the presence of stable intermediates and adsorbed reaction products, such as adsorbed NH<sub>3</sub>, limits the availability of the active sites for high rate catalysis. This indicates that NH<sub>3</sub> desorption and the first hydrogenation step to NH might be limiting factors for the studied process at room temperature. The ammonia adsorption energy on Ni is reported to be about 80 kJ mol<sup>-1</sup><sup>69, 70</sup> and it desorbs at around 100 °C.<sup>71, 72</sup> Therefore, a slight increase in the operating temperature is expected to significantly improve the performance of the reaction, which will be part of future work.

Following the above rationale, the observed overall reaction on Ni<sup>0</sup> might still be kinetically slow due to the large activation barrier for the first nitrogen hydrogenation step and NH<sub>3</sub> desorption. Remarkably, the N<sub>2</sub> adsorption on Ni<sup>0</sup> occurs spontaneously until a certain coverage is reached. To overcome these barriers, we extended our *in situ* study to a modified Ni electrode with a nitrated surface layer, which acts as precursor for a low temperature Mars-van Krevelen (MvK) mechanism. Here, the rationale is to have a higher density of surface N to facilitate the apparently difficult first hydrogenation step, while the permeating atomic hydrogen *in situ* generates NH<sub>3</sub> and a large number of highly active surface N<sup>vac</sup>, accelerating the activation of gaseous nitrogen compared to a metallic Ni site, as described in the following section.

**Table 6.1** Review of N 1s assignments of adsorbed nitrogen species on nickel surfaces.

Species	Surface	BE (eV)	Reference
N <sup>ad</sup>	Ni(110)	397.0	[ <sup>39</sup> ]
	Ni(100), Ni(110)	397.0	[ <sup>66</sup> ]
	Ni(111)	397.8	[ <sup>62</sup> ]
	Ni(110)	398.0	[ <sup>65</sup> ]
	Ni(poly)	397.8	[ <sup>63</sup> , <sup>64</sup> ]
	Ni(poly)	397.3	[ <sup>73</sup> ]
N <sub>2</sub> <sup>phys</sup>	Ni(111)	405.5 <sup>a</sup>	[ <sup>67</sup> ]
	Ni(110)	405.3 <sup>a</sup>	[ <sup>39</sup> ]
	Ni(poly)	405.7 <sup>a</sup>	[ <sup>63</sup> ]
N <sub>2</sub> <sup>chem</sup>	Ni(111)	401.0 <sup>a</sup>	[ <sup>67</sup> , <sup>74</sup> ]
	Ni(110)	399.4 <sup>a</sup>	[ <sup>39</sup> ]
	Ni(poly)	400.6 <sup>a</sup>	[ <sup>63</sup> , <sup>64</sup> ]
N <sub>2</sub> O	Ni(poly)	402.0 <sup>a</sup> , 406.0 <sup>a</sup>	[ <sup>63</sup> , <sup>64</sup> ]
NO	Ni(111)	399.8	[ <sup>68</sup> ]
	Ni(poly)	399.5	[ <sup>63</sup> , <sup>64</sup> ]
	Ni(poly)	399.4	[ <sup>73</sup> ]
NO <sub>2</sub>	Ni(poly)	403.0	[ <sup>63</sup> ]
NH <sub>x</sub> (x=1,2)	Ni(100), Ni(110)	398.5	[ <sup>66</sup> ]
	Ni(111)	399.7	[ <sup>62</sup> ]
	Ni(110)	398.4	[ <sup>65</sup> ]
NH <sub>3</sub>	Ni(100), Ni(110)	400.5	[ <sup>66</sup> ]
	Ni(110)	400.9	[ <sup>65</sup> ]

<sup>a</sup> At temperature  $\leq 80$  K.

**Surface nickel nitride.** Nickel nitrides are characterised by low nitrogen vacancy formation energy and relatively low barriers for  $\text{NH}_3$  synthesis,<sup>27, 75, 76</sup> making this material a good candidate for the process under investigation. We first verified the stability of the surface nickel nitride under investigation with *in situ* NAP XPS measurements under  $\text{H}_2$  atmosphere (0.1 mbar) at room temperature (**Figure A.6.11**). The stability of the nitrated Ni electrode was also tested at higher temperatures, up to 150 °C, under 1 bar hydrogen atmosphere in a sealed PEEK cell, while monitoring the gas composition with a GC. No detectable amounts of ammonia were found within the instrument detection limit (of the order of  $10^{-13} \text{ mol cm}^{-2} \text{ s}^{-1}$ ), suggesting that the nitride surface is also stable at these conditions. These results are consistent with the previously reported inability of a nitrated Ni surface to dissociate  $\text{H}_2$ ,<sup>11</sup> and other stability reports.<sup>77, 78</sup>

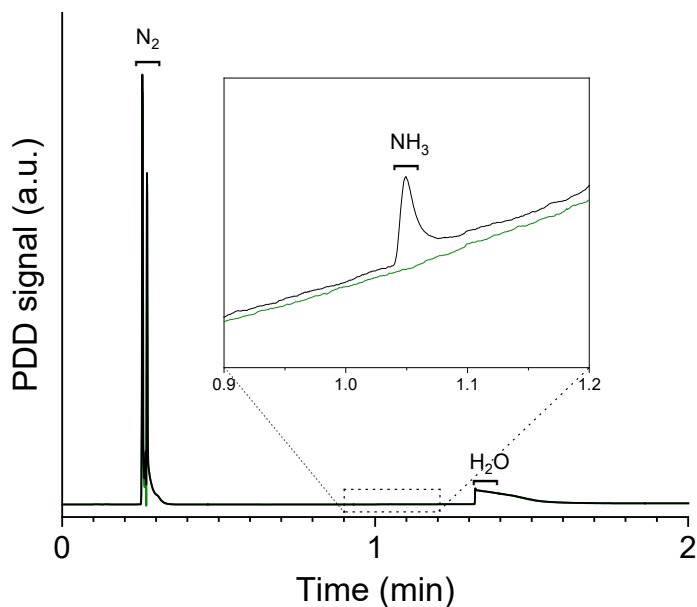


**Figure 6.6** Full chromatographs of the nitrated Ni surface electrode during  $\text{NH}_3$  synthesis experiment. Permanent gases are eluted at 0.25 min, ammonia at 1.05 min, and water at 1.3 min. The enclosure highlights the region of the chromatograph around the ammonia elution time. Ammonia is produced when the electrochemical atomic hydrogen permeation through the electrode is initiated (black line). On the other hand, no  $\text{NH}_3$  is detected in OCP (green line), i.e. no H permeation.

On the other hand, the surface lattice nitrogen (dominant component at 397.8 eV in the N 1s spectrum) reacts with the electrochemically inserted hydrogen atoms to form  $\text{NH}_3$ , leading to the appearance of a peak at 400.3 eV in the N 1s XPS spectrum (**Figure 6.7**), as observed earlier for gaseous  $\text{N}_2$  adsorbed and activated on a clean Ni. However, in this case, the production rate of gaseous ammonia is high enough and is confirmed with GC detection in a separate electrochemical experiment (**Figure 6.6**). The presence of stable  $\text{NH}_3$ , which remains on the metal surface even after the interruption of hydrogen permeation, indicates that also in this case product desorption is limiting. However, the high density of adsorbed surface N makes the limiting NH formation step to occur more often and therefore  $\text{NH}_3$  can be produced at a faster rate than with a lower N coverage. In addition, during the hydrogenation of the surface nickel nitride layer, a distinctive new contribution at 399.1 eV appears. This peak is tentatively assigned to N atoms in the proximity of the formed N vacancies on the Ni surface, which results in a shift towards higher binding energy due to the redistribution of electrons left after the hydrogenation of lattice N to  $\text{NH}_3$ .<sup>79-83</sup> The peak appears slightly broader, which might indicate the contribution from N in the proximity of a different number of vacancies. Even though it is difficult to determine the exact nature of this component, we cannot entirely exclude the contribution from some  $\text{NH}_x$  species (with  $x=1, 2$ ), which have been reported on Ni in a similar energy range (**Table 6.1**).<sup>65, 66</sup> Moreover, a peak with limited intensity at 399.1 eV is noticeable in the pristine sample (**Figure 6.7**), indicating that few  $\text{N}^{\text{vac}}$  might be initially present on the subsurface of the nitrated Ni as result of the plasma nitridation process. Thus, with *in situ* XPS it appears possible to directly observe the room temperature formation of  $\text{NH}_3$  and  $\text{N}^{\text{vac}}$  from reduction of nitrogen adsorbed on Ni via electrochemical atomic hydrogen permeation, while the activation of  $\text{N}_2$  was proven earlier with  $^{15}\text{N}_2$  isotope labeling experiments.<sup>11</sup>

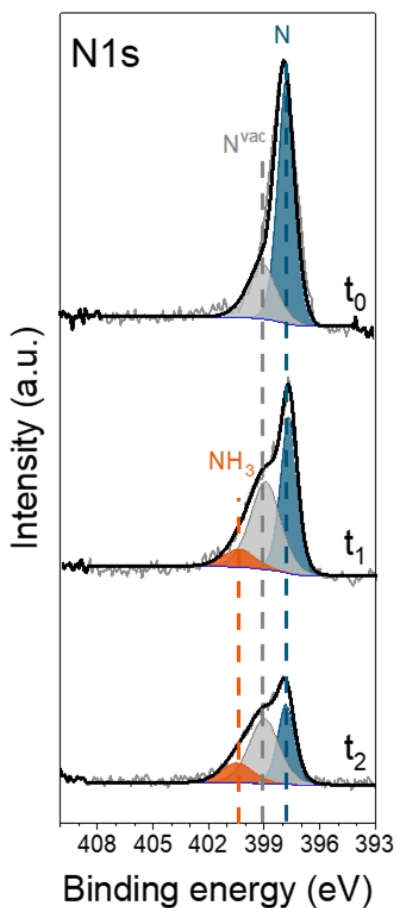


**Figure 6.7** N 1s XPS spectra of the pristine nitrated Ni electrode ( $t_0 = 0$  min) and during electrochemical insertion of hydrogen under vacuum conditions ( $t_1 = +15$  min,  $t_2 = +90$  min). The three components are colour coded and corresponding to surface and subsurface atomic N (blue), to N in the proximity of N<sup>vac</sup> (grey) and to NH<sub>3</sub> (orange).

**Iron.** Iron has been extensively studied for nitrogen chemistry over the last century, and metallic Fe is well known to activate dinitrogen even at ambient conditions, but still in competition with oxygen and limited by oxidised species.<sup>55</sup> It is therefore interesting to study a polycrystalline Fe surface under electrochemical hydrogen permeation and N<sub>2</sub> atmosphere. The initial oxide layer formed on the Fe foil after a short exposure to air or traces of oxygen represents one of the major limitations in using Fe as nitrogen activation catalyst in a hydrogen permeable electrode system. This layer drastically blocks the atomic hydrogen permeation (**Figure A.6.12**), preventing the reduction of surface species (i.e., oxides and adsorbed nitrogen) by permeating H. In our case, we measured a reduction in H permeation flux of more than 100-fold (**Figure A.6.4**). As a consequence, *in situ* XPS measurements carried out during electrochemical hydrogen loading do not show any significant reduction of the oxide overlayer, nor the formation of metallic Fe (**Figure A.6.13**). Only a slight shift towards lower binding energy is noticeable from the Fe 2p spectra and it can be associated to a limited partial reduction of some Fe<sup>+3</sup> species to Fe<sup>+2</sup>. Moreover, the highly negative iron oxide formation energy might represent an additional barrier for the oxide removal by permeating atomic hydrogen, compared to nickel oxides.<sup>59</sup> The higher stability of iron oxide species is also confirmed by our *in situ* XPS experiments, where temperatures higher than 250 °C under hydrogen atmosphere (1 mbar) are required to fully reduce the Fe surface (**Figure 6.8**). The presence of only a minor metallic Fe<sup>0</sup> component after cooling of the thermally reduced iron surface under H<sub>2</sub>, indicates that the reoxidation of iron reaches a thicker layer, compared to the oxygen exposed Ni which still shows a strong Ni<sup>0</sup> contribution (**Figure 6.4**). Therefore, contrary to what observed with Ni, the electrochemical insertion of atomic H did not successfully reduce the surface of the iron electrode.

Remarkably, although no metallic Fe<sup>0</sup> could be observed, when the oxidised iron surface is exposed to N<sub>2</sub> (0.1 mbar) in OCP, the N 1s XPS spectrum reveals the formation of two nitrogen species (**Figure 6.9a**). Adsorbed molecular nitrogen on Fe surfaces has been observed only at extremely low temperatures.<sup>16</sup> Moreover, as no H<sub>2(g)</sub> nor permeating atomic H are available (only unavoidable traces of water are present), we do not expect the formation of hydrogenated forms of N. Recently, Degaga et al. reported analogous N 1s peaks on a Fe<sub>3</sub>O<sub>4</sub>(001) surface exposed to N<sub>2</sub>.<sup>38</sup> Based on their observations and theoretical calculations, these N 1s contributions detected on the Fe oxide surface were assigned to N-O (400.6 eV) and N-Fe<sup>3+</sup> (399.1 eV) bonds.<sup>38</sup> This reveals that nitrogen activation is possible also on

oxidised Fe surface. However, upon electrochemical hydrogen insertion, we did not observe any hydrogenation of the adsorbed N species, possibly due to the H blockage by the iron oxide layer, which strongly limits the access of reactive atomic hydrogen to the surface.

A nitride surface layer, generated via plasma nitridation, on a reduced Fe surface can act both as protective layer against oxidation<sup>84</sup> and as precursor for a MvK N<sub>2</sub> activation mechanism. However, the formation of a thin iron nitride surface layer also blocks the atomic hydrogen permeation (**Figure A.6.4**). As such, no hydrogenation of surface iron nitride is observed during *in situ* XPS, due to the insufficient H flux or too stable Fe-N bond.

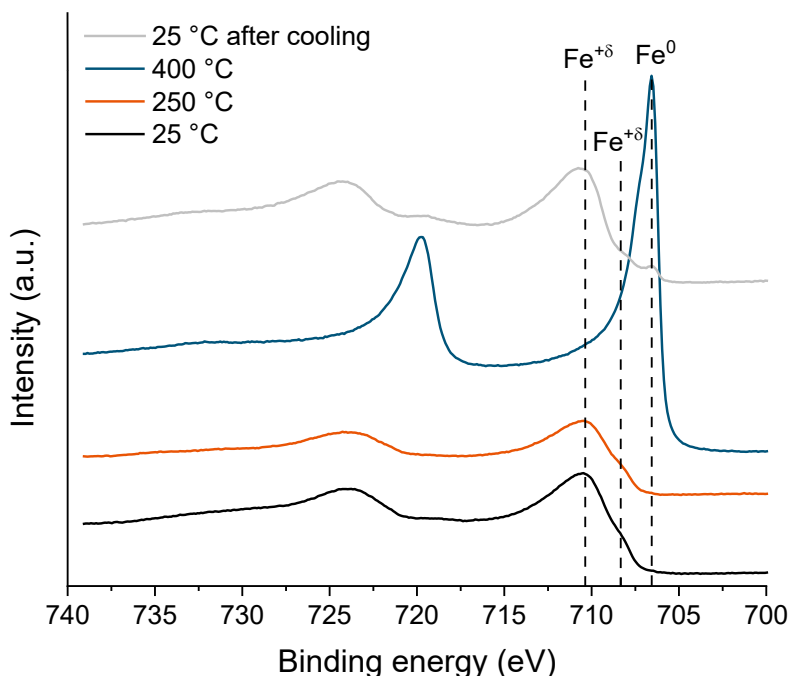


**Figure 6.8** Fe 2p XPS spectra of the polycrystalline Fe foil in presence of 1 mbar of H<sub>2</sub> heated up from room temperature (25 °C) to 400 °C and then cooled down again to 25 °C (grey line). The position of the main metallic and oxide components is indicated by the dashed lines. Reduction of the Fe surface is achieved for temperatures higher than 250 °C. Photoelectron kinetic energy was 200 eV.

**Ruthenium.** Both the materials investigated so far (Ni and Fe) are prone to oxidation when exposed to air or water, which blocks N active sites and obstructs the permeation of atomic hydrogen. For this reason it is interesting to extend our study to more noble metals, such as ruthenium, which is a well established ammonia synthesis catalyst.<sup>85</sup> The

electrochemical insertion of H through the Ru (and Ru nitride) coated Ni electrode results in a moderate H permeation flux in comparison to the uncoated Ni (**Figure A.6.4**).

As expected, the Ru 3p and 3d spectra reveal a metallic surface and the absence of contributions from higher oxidation states (**Figure A.6.10**). During the exposure to N<sub>2</sub> (0.1 mbar in OCP), the N 1s spectrum shows two contributions, indicating the presence of dissociated N adsorbed on the polycrystalline Ru surface (397.3 eV) and a second N species at 399.0 eV (**Figure 6.9b**). The latter appears at a binding energy close to adsorbed N<sub>2</sub>, whose cleavage is established to be the limiting step for N<sub>2</sub> activation on Ru catalytic surfaces.<sup>85-88</sup> However, the acquired data did not provide an unambiguous identification of the nature of this species. Yet, the N 1s spectrum remains nearly unchanged upon electrochemical hydrogen permeation, showing no signs of other N species on the Ru surface in the course of the experiment. Similarly, no substantial variations in the N 1s spectrum are observed for the nitrided ruthenium electrode under electrochemical H loading, although the H-permeation is not blocked by the presence of a surface nitride layer (**Figure A.6.4**). In both cases, no NH<sub>3</sub> was detected with gas chromatography in separate electrochemical experiments. Thus, the formation of H<sub>2</sub> from surface recombination of permeating H prevails over the hydrogenation of the adsorbed N. The stronger Ru-N bond, compared to Ni,<sup>89</sup> might be too stable to be hydrogenated by H-permeation under these conditions; aggravating the barrier to the first hydrogenation. In fact, Ni has the least negative adsorption energy of nitrogen, among the tested materials, which indicates that the N-M bond follows the trend: Ni<Ru<Fe.<sup>90</sup> This may be the underlying reason why only Ni shows appreciable NH<sub>3</sub> formation in this study, next to the more persistent presence of iron oxide. We thus envision that rational design of catalysts with optimal nitrogen-surface interactions is needed to deploy the full potential of H permeable electrodes for electrolytic ammonia synthesis at near ambient conditions.



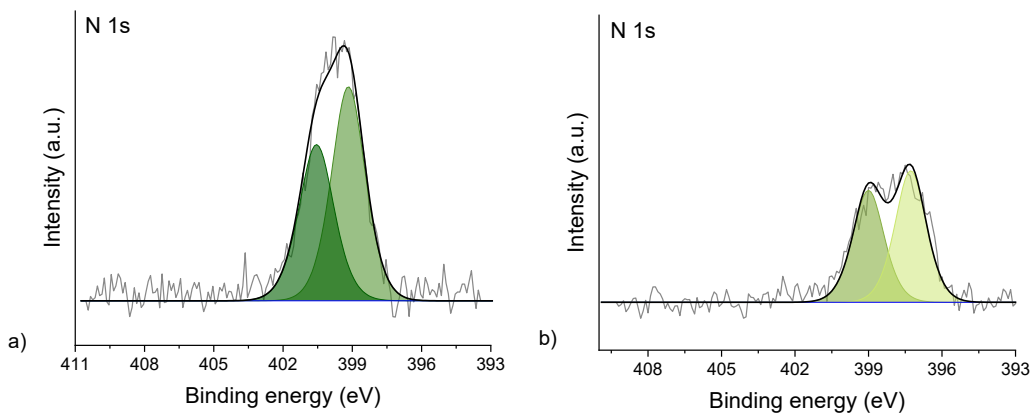


**Figure 6.9** (a) N 1s XPS spectrum of the oxidized polycrystalline Fe under 0.1 mbar  $N_2$  atmosphere in open circuit (i.e. no H loading). The N 1s shows two adsorbed nitrogen species at 400.6 and 399.1 eV. (b) N 1s XPS spectrum of the polycrystalline Ru surface under 0.1 mbar  $N_2$  atmosphere in open circuit (i.e. no H loading). The N 1s shows two components at 399.0 and 397.3 eV. Photoelectron kinetic energy was 300 eV.

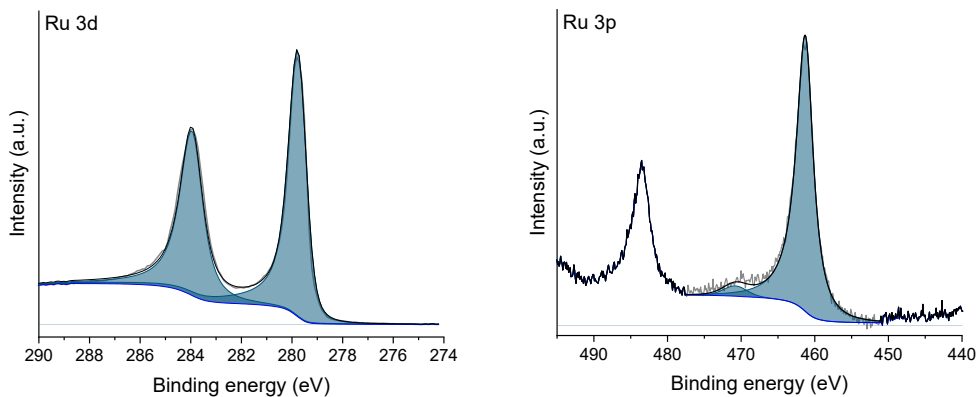


**Figure 6.10** Ru 3d (left) and Ru 3p (right) XPS spectra showing a metallic ruthenium surface, with peak fitting in agreement with literature.<sup>91</sup> Photoelectron kinetic energy was 300 eV.

## 6.4 Conclusions

In this study, we used *in situ* near ambient pressure XPS to investigate the solid-gas interphase of polycrystalline Ni electrode under electrochemical H permeation and N<sub>2</sub> atmosphere for NH<sub>3</sub> synthesis. The availability of surface Ni<sup>0</sup> sites is a primary requirement for the chemisorption of gaseous N<sub>2</sub>, as we verified that fully oxidised Ni surface does not present any reactivity towards dinitrogen adsorption. We showed how electrochemically inserted and permeating atomic hydrogen can reduce surface Ni oxide and hydroxide species, under conditions at which gaseous H<sub>2</sub> alone does not. Chemisorbed nitrogen is then detected on the metallic Ni surface under N<sub>2</sub> atmosphere, followed by the formation of NH<sub>3</sub> from the reaction with permeating H. The presence of stable adsorbed NH<sub>3</sub> on the Ni surface, indicates that product desorption might be limiting at room temperature, thus reducing the availability of active sites. The first hydrogenation step to NH may also be limiting, as higher production of NH<sub>3</sub> is observed when more N is present on the surface. When a thin nitride layer is present, the electrochemically permeating atomic hydrogen reduces the surface lattice nitrogen to form NH<sub>3</sub> and N<sup>vac</sup> at ambient temperature, as observed on the surface of the electrode with *in situ* XPS. These defective sites (i.e. N<sup>vac</sup>) promote the activation of dinitrogen compared to the slower N<sub>2</sub> activation on Ni. Importantly, the hydrogenation of surface lattice nitrogen was not observed with H<sub>2</sub> at temperatures up to 150 °C, emphasizing the benefit of electrochemically permeating atomic H.

We extended the study of hydrogen permeable electrodes for NH<sub>3</sub> synthesis to Fe and Ru catalytic surfaces. The presence of either Fe oxides or nitrides severely inhibits permeating H from accessing the catalytic surface, hindering the advancement of the reaction. Dinitrogen activation is observed on polycrystalline Ru surface. Still, no evidence of hydrogenation of the adsorbed nitrogen species upon H permeation is found under near ambient conditions. Based on these results, it emerges that H permeability and M-N bond strength are two key parameters to be taken in consideration in the design of an optimal N activation catalyst using H permeable electrodes.

In conclusion, our findings demonstrate the dual benefit of H permeable nickel electrodes, which *in situ* generate active sites by oxide and nitride reduction at the catalytic solid-gas interface, while providing controllable flux of H atoms available for hydrogenation of adsorbed N. Moreover, we show how *in situ* NAP-XPS can be applied to investigate

processes based on hydrogen permeable electrodes, providing invaluable insights needed for their efficient design.

## Appendix A.6

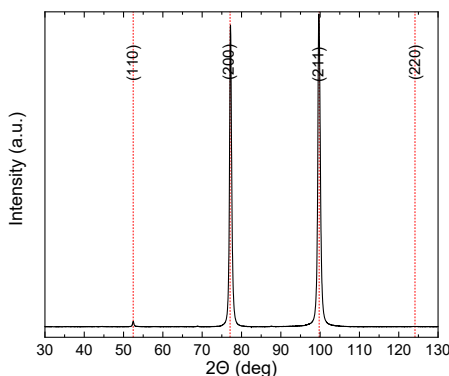


**Figure A.6.1** XRD pattern of polycrystalline Fe foil. The reference diffraction pattern of the  $\alpha$ -Fe metal cubic phase (PDF 04-014-0360), is shown as red dotted vertical lines (Co  $K_\alpha$  source).

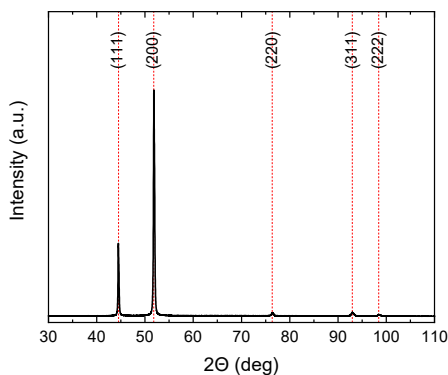


**Figure A.6.2** XRD pattern of polycrystalline Ni foil. The reference diffraction pattern of the Ni metal cubic phase (JCPDS #04-0850) is shown as red dotted vertical lines.

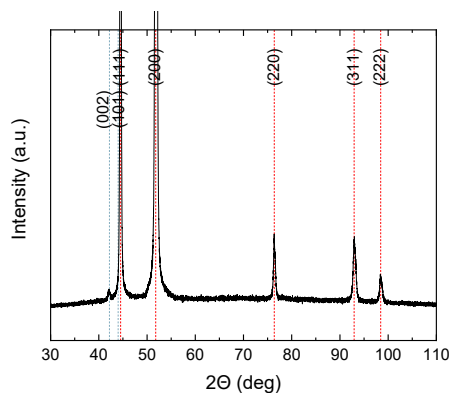


**Figure A.6.3** XRD pattern of polycrystalline Ni foil coated with 20 nm of sputter deposited Ru. The reference diffraction pattern of the Ni metal cubic phase (JCPDS #04-0850) and hexagonal close-packed Ru metal (JCPDS #06-663) are shown as red and blue dotted vertical lines respectively.

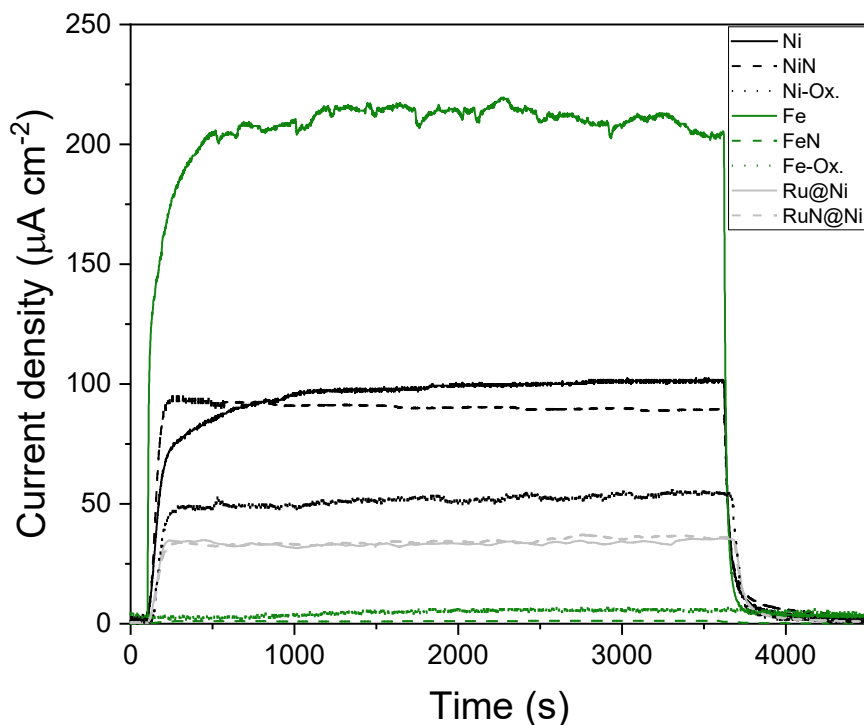


**Figure A.6.4** Measured electrochemical atomic hydrogen permeation rate through different specimens at ambient conditions as a function of time. The y-axis represents the measured current resulting from the oxidation of permeating atomic hydrogen to a proton and an electron at the exit side of the sample; thus this current corresponds to the atomic hydrogen permeation flux. After 100 seconds, the specimen was cathodically polarised in 0.1 M KOH solution at 5 mA cm<sup>-2</sup>, resulting in the increase in measured oxidation current. The cathodic current was interrupted after 3600 seconds, resulting in the consequent decay of permeated hydrogen. The measured hydrogen permeation transient shows the characteristic s-shaped profile. Further details on the electrochemical hydrogen permeation experiments are available in the experimental section of the manuscript. The analysed specimens are: 12.5 μm nickel foil (black), 25 μm Fe foil (green), and 12.5 μm nickel foil coated with 20 nm Ru (grey). Different line styles indicate the condition of the surface of the specimen: oxidised in air (dotted line), metallic surface (solid line), or with a surface nitride top-layer (dashed black). The clean metallic Ni and Fe surfaces (black and green solid lines) were obtained through a Ar/H<sub>2</sub> plasma treatment described in the experimental session of the manuscript (sample preparation subsection). A protective 20 nm Pd layer was sputter deposited (only for hydrogen permeation measurements) on the hydrogen exit side of all the electrodes after either the oxidation, cleaning or nitriding step. The adoption of a protective Pd layer is common practice in electrochemical hydrogen permeation measurements using a Devanathan-Stachurski cell.<sup>92</sup>

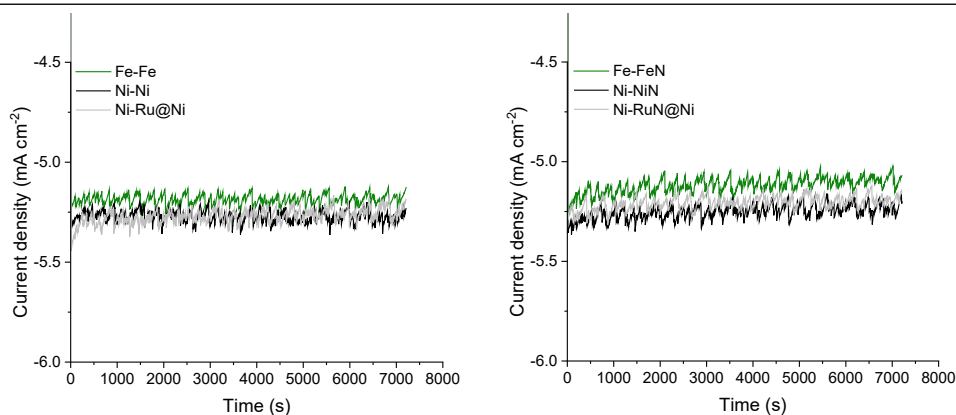


**Figure A.6.5** Electroanalytical measurements from the six types of electrodes tested in this study. All the electrochemical tests were carried out in potentiostatic condition (-1.5 V vs SHE) in a flowing 0.1 M KOH electrolyte solution, using a Pt counter electrode and a saturated Ag/AgCl reference electrode. The material at the electrode-electrolyte interface (either Ni or Fe) is specified in the legend in the left side of the dash, while the material at the electrode-gas interface (Fe, Ni, Ru or their corresponding nitrided surfaces) is indicated on the right side of the dash (so e.g. Ni-RuN@Ni indicates a Ni electrode-electrolyte interface and a RuN@Ni electrode-gas interface).

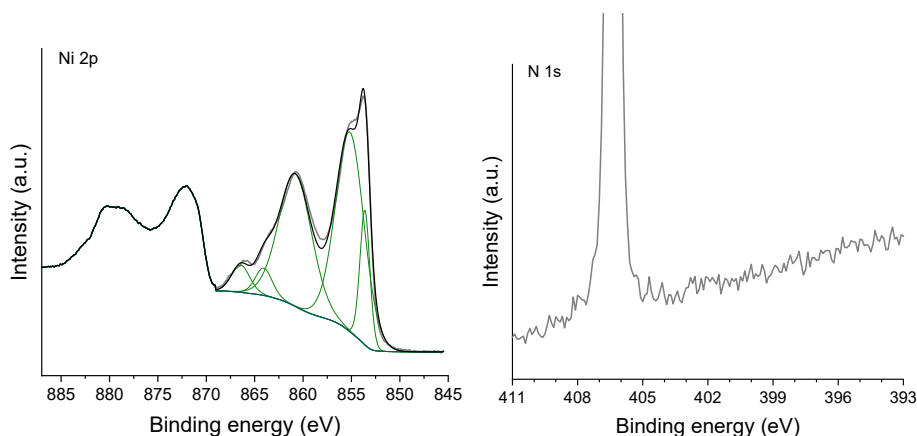


**Figure A.6.6** Ni 2p (left) and N 1s (right) XPS spectra of a nickel oxide layer grown onto a clean Ni foil via in situ exposure to O<sub>2</sub> at 200 °C and subsequently exposed to N<sub>2</sub> (1 mbar). Peak fitting (in green) of Ni 2p spectrum shows a fully oxidised (NiO) nickel surface. The N 1s spectrum does not show any reactivity towards N<sub>2</sub> adsorption. The large peak around 406.5 eV is due to the presence of dinitrogen gas.<sup>93</sup> Photoelectron kinetic energy was 200 eV.

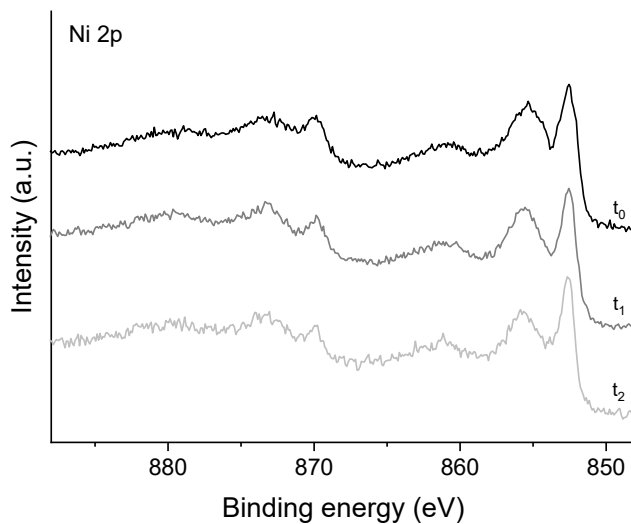


**Figure A.6.7** Stacked Ni 2p XPS spectra of the polycrystalline Ni foil under vacuum and X-ray illumination over time ( $t_0=0$  min,  $t_1=20$  min and  $t_2=45$  min). No noticeable reduction of the Ni surface is observable after 45 min. Photoelectron kinetic energy was 200 eV.

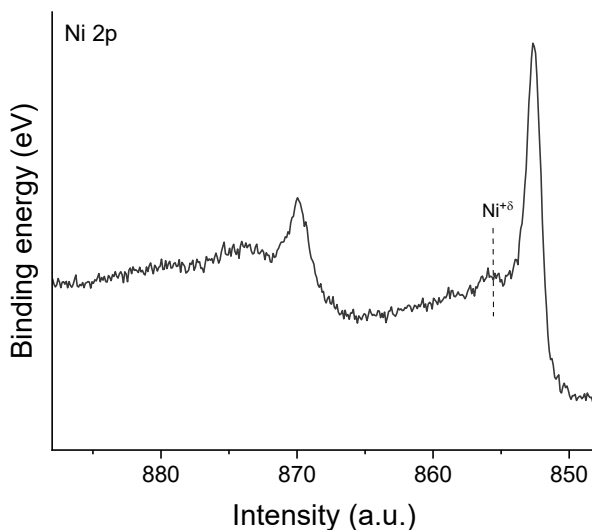


**Figure A.6.8** Ni 2p XPS spectra the polycrystalline Ni foil held for about 15 minutes in OCP under vacuum, after full reduction by permeating atomic hydrogen. Re-oxidation of the electrode surface is noticeable from the distinctive oxide component, here indicated with a dashed line. This is attributed to the presence of residual traces of oxygen and water vapour in the analysis chamber (the pressure of the analysis chamber prior starting the experiment was about  $7 \cdot 10^{-7}$  mbar). Photoelectron kinetic energy was 200 eV.

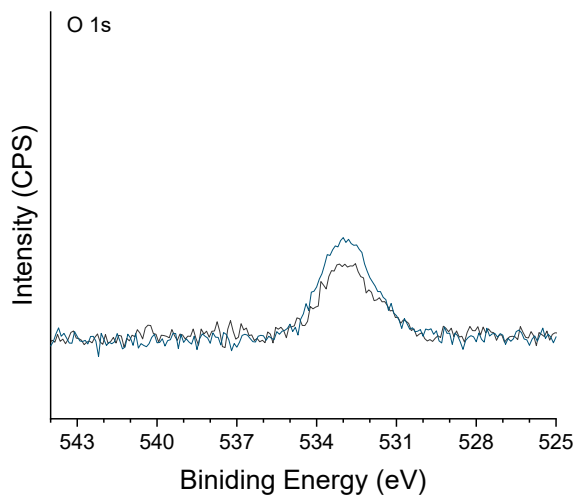


**Figure A.6.9** Comparison of the O 1s spectra of the Ni surface before (black) and after (blue) the exposure to N<sub>2</sub> (0.1 mbar). Photoelectron kinetic energy was 200 eV.

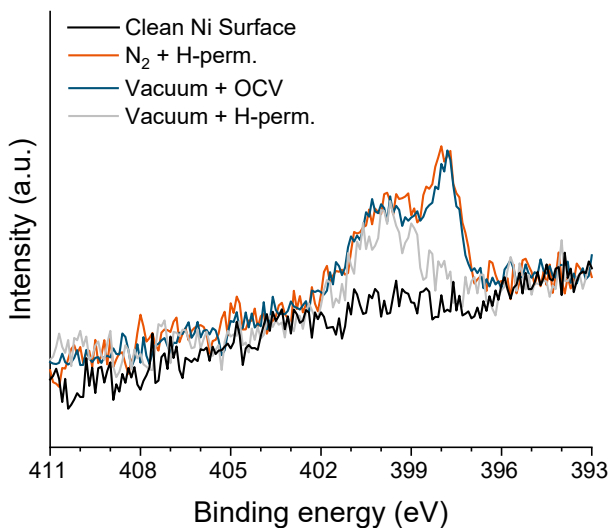


**Figure A.6.10** N 1s XPS spectra of the reduced metallic Ni electrode before the exposure to N<sub>2</sub> showing the absence of initial N on the surface (black), after the exposure to 0.1 mbar of N<sub>2</sub> during electrochemical atomic hydrogen permeation (orange), after subsequent evacuation to UHV and interruption of the hydrogen permeation (blue) and after restoring the electrochemical atomic hydrogen permeation in UHV (grey). Photoelectron kinetic energy was 200 eV.



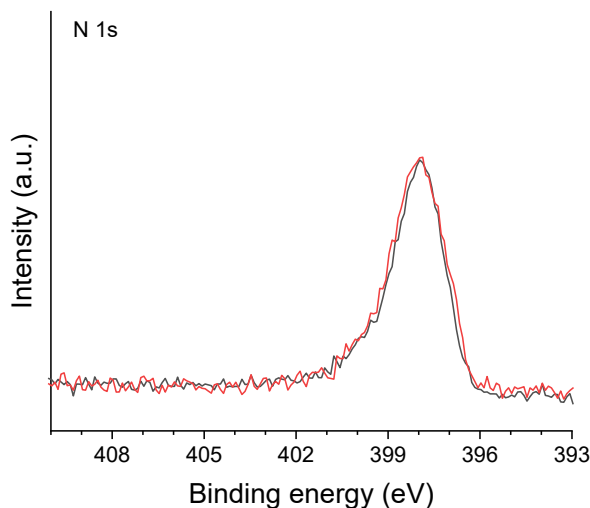


**Figure A.6.11** N 1s XPS spectra of the surface nickel nitride before (black) and after (orange) H<sub>2</sub> exposure (0.1 mbar) at room temperature.

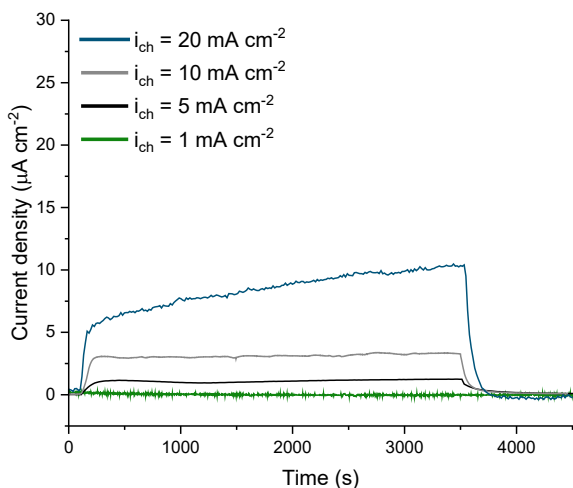


**Figure A.6.12** Measured electrochemical atomic hydrogen permeation rate through 25  $\mu\text{m}$  Fe foil oxidised in air at different charging current densities (1 to 20  $\text{mA cm}^{-2}$ ). The y-axis represents the measured current resulting from the oxidation of permeating atomic hydrogen to a proton and an electron at the exit side of the sample; thus this current corresponds to the atomic hydrogen permeation flux. After about 100 seconds, the specimen was cathodically polarised in 0.1 M KOH solution, resulting in the increase in measured oxidation current. The cathodic current was interrupted after 3600 seconds, resulting in the consequent decay of permeated hydrogen. The measured hydrogen permeation transient shows the characteristic s-shaped profile. A protective 20 nm Pd layer was sputter deposited (only for hydrogen permeation measurements) on the hydrogen exit side of all the electrodes. Further details on the electrochemical hydrogen permeation experiments are available in the experimental section of the manuscript. Slightly higher H permeation are achieved at higher charging current. However, because of the presence of an oxide surface layer, even at 20  $\text{mA cm}^{-2}$  charging current density, the H permeation remain still substantially low ( $< 10 \mu\text{A cm}^{-2}$ ) and more than 20 times lower than a reduced Fe electrode (**Figure A.6.4**).

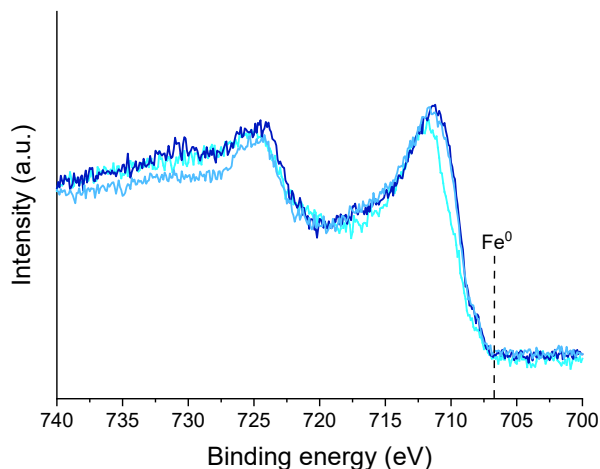


**Figure A.6.13** Fe 2p XPS spectra as received and after about one and two hours of electrochemical hydrogen loading under vacuum (lighter to darker colour indicates increasing time). Metallic Fe species are not observed. Only a slight shift towards lower binding energy is notable, which can be associated to a limited partial reduction of some  $\text{Fe}^{+3}$  species to  $\text{Fe}^{+2}$ . Photoelectron kinetic energy was 200 eV.

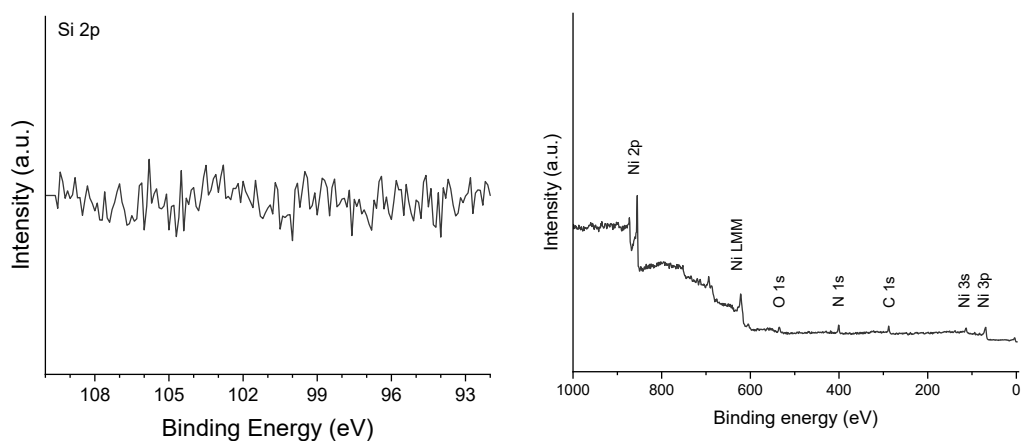


**Figure A.6.14** Additional XPS spectra. On the left, Si 2p XPS spectrum of the Ni foil shows the absence of Si in the sample. On the right, XPS survey spectrum of the surface nickel nitride sample, collected with 1467 eV excitation energy. Traces of adventitious C and O are a consequence of unavoidable air exposure.

**Table A.6.1** Parameters used for the Ni 2p<sub>3/2</sub> XPS fits using CasaXPS software package: binding energy (BE), line shape, full width at half-maximum (FWHM) and relative peak area. A Shirley background was used as baselines.

Component	BE (eV)	Line shape	FWHM (eV)	Relative area (%)
Ni <sup>0</sup>	852.6	LA(1.1,2.2,10)	1.0	100
	856.3	GL(30)	2.5	7.0
	858.7	GL(30)	2.8	16.8
NiO	853.7	GL(30)	1.1	28.4
	855.4	GL(30)	3.0	100
	860.9	GL(30)	3.7	76.9
	864.0	GL(30)	2.0	8.1
	866.4	GL(30)	2.4	8.8
Ni(OH) <sub>2</sub>	854.9	GL(30)	1.1	16.3
	855.7	GL(30)	2.2	100
	857.7	GL(30)	1.9	6.6
	860.5	GL(30)	1.1	3.1
	861.5	GL(30)	4.4	86.5
	866.5	GL(30)	3.0	8.2

**Table A.6.2** Parameters used for the O1s XPS fits using CasaXPS software package: binding energy (BE), line shape and full width at half-maximum (FWHM). A Shirley background was used as baselines.

Component	BE (eV)	Line shape	FWHM (eV)
Oxides	529.3	GL(30)	1.0
Hydroxides	531.1	GL(30)	1.9
H <sub>2</sub> O <sup>ad</sup>	532.9	GL(30)	1.3

**Table A.6.3** Parameters used for the N 1s XPS fits using CasaXPS software package: binding energy (BE), line shape, full width at half-maximum (FWHM). A Shirley background was used as baselines.

Conditions	Component	BE (eV)	Line shape	FWHM (eV)
Ni <sup>0</sup> , OCP, N <sub>2</sub>	N <sup>atom</sup>	397.8	GL(50)	1.8
Ni <sup>0</sup> , -1.5 V vs RHE/H-perm, N <sub>2</sub>	N <sup>atom</sup>	397.8	GL(50)	1.0
	NH <sub>3</sub>	400.3	GL(50)	2.4
Ni <sup>0</sup> , -1.5 V vs RHE/H-perm, vacuum	NH <sub>3</sub>	400.3	GL(50)	2.4
NiN, OCP, vacuum	N <sup>atom</sup>	397.8	GL(50)	1.0
	N <sup>vac</sup>	399.1	GL(50)	1.9
NiN, -1.5 V vs RHE/H-perm, vacuum	N <sup>atom</sup>	397.8	GL(50)	1.0
	N <sup>vac</sup> /NH <sub>x</sub>	399.1	GL(50)	1.9
	NH <sub>3</sub>	400.3	GL(50)	2.4
Fe <sup>+2/+3</sup> , OCP, N <sub>2</sub>	N-Fe <sup>3+</sup>	399.1	GL(50)	1.5
	N-O	400.6	GL(50)	1.5
Ru, OCP, N <sub>2</sub>	N-Ru	397.3	GL(50)	1.5
	N <sub>2</sub> <sup>ad</sup>	399.0	GL(50)	1.5

**Table A.6.4** Parameters used for the Ru 3d XPS fits using CasaXPS software package: binding energy (BE), line shape, full width at half-maximum (FWHM) and relative peak area. A Shirley background was used as baselines.

Component	BE (eV)	Line shape	FWHM (eV)	Relative area (%)
Ru <sup>0</sup> 3d <sub>5/2</sub>	279.8	LF(0.8,1.25,500,180)	0.7	100
Ru <sup>0</sup> 3d <sub>3/2</sub>	284.0	LF(1.01,1.25,500,50)	1.0	70.0

**Table A.6.5** Parameters used for the Ru 3p<sub>3/2</sub> XPS fits using CasaXPS software package: binding energy (BE), line shape, full width at half-maximum (FWHM) and relative peak area. A Shirley background was used as baselines.

Component	BE (eV)	Line shape	FWHM (eV)	Relative area (%)
Ru <sup>0</sup> 3p <sub>3/2</sub>	461.2	LF(1,1.2,25,5)	2.6	100
	470.8	GL(30)	3.7	3.5

## References

1. World fertilizer trends and outlook to 2022. *Food and Agriculture Organization of the United Nations* **2019**, 1-9.
2. MacFarlane, D. R.; Cherepanov, P. V.; Choi, J.; Suryanto, B. H. R.; Hodgetts, R. Y.; Bakker, J. M.; Ferrero Vallana, F. M.; Simonov, A. N., A Roadmap to the Ammonia Economy. *Joule* **2020**, *4* (6), 1186-1205.
3. Mulder, F. M., Implications of diurnal and seasonal variations in renewable energy generation for large scale energy storage. *Journal of Renewable and Sustainable Energy* **2014**, *6* (3), 033105.
4. Rouwenhorst, K. H. R.; Krzywda, P. M.; Benes, N. E.; Mul, G.; Lefferts, L., Ammonia, 4. Green Ammonia Production. In *Ullmann's Encyclopedia of Industrial Chemistry*, 2020; pp 1-20.
5. Yang, B.; Ding, W.; Zhang, H.; Zhang, S., Recent progress in electrochemical synthesis of ammonia from nitrogen: strategies to improve the catalytic activity and selectivity. *Energy & Environmental Science* **2021**, *14* (2), 672-687.
6. Kibsgaard, J.; Nørskov, J. K.; Chorkendorff, I., The Difficulty of Proving Electrochemical Ammonia Synthesis. *ACS Energy Letters* **2019**, *4* (12), 2986-2988.
7. Hu, L.; Xing, Z.; Feng, X., Understanding the Electrocatalytic Interface for Ambient Ammonia Synthesis. *ACS Energy Letters* **2020**, *5* (2), 430-436.
8. Singh, A. R.; Rohr, B. A.; Schwalbe, J. A.; Cargnello, M.; Chan, K.; Jaramillo, T. F.; Chorkendorff, I.; Nørskov, J. K., Electrochemical Ammonia Synthesis—The Selectivity Challenge. *ACS Catalysis* **2017**, *7* (1), 706-709.
9. Lim, J.; Fernández, C. A.; Lee, S. W.; Hatzell, M. C., Ammonia and Nitric Acid Demands for Fertilizer Use in 2050. *ACS Energy Letters* **2021**, *6* (10), 3676-3685.
10. Suryanto, B. H. R.; Matuszek, K.; Choi, J.; Hodgetts, R. Y.; Du, H.-L.; Bakker, J. M.; Kang, C. S. M.; Cherepanov, P. V.; Simonov, A. N.; MacFarlane, D. R., Nitrogen reduction to ammonia at high efficiency and rates based on a phosphonium proton shuttle. *Science* **2021**, *372* (6547), 1187-1191.
11. Ripepi, D.; Zaffaroni, R.; Schreuders, H.; Boshuizen, B.; Mulder, F. M., Ammonia Synthesis at Ambient Conditions via Electrochemical Atomic Hydrogen Permeation. *ACS Energy Letters* **2021**, 3817-3823.
12. Ampelli, C., Electrode design for ammonia synthesis. *Nature Catalysis* **2020**, *3* (5), 420-421.
13. Lazouski, N.; Chung, M.; Williams, K.; Gala, M. L.; Manthiram, K., Non-aqueous gas diffusion electrodes for rapid ammonia synthesis from nitrogen and water-splitting-derived hydrogen. *Nature Catalysis* **2020**, *3* (5), 463-469.
14. Liu, S.; Qian, T.; Wang, M.; Ji, H.; Shen, X.; Wang, C.; Yan, C., Proton-filtering covalent organic frameworks with superior nitrogen penetration flux promote ambient ammonia synthesis. *Nature Catalysis* **2021**, *4* (4), 322-331.
15. Rao, C. N. R.; Ranga Rao, G., Nature of nitrogen adsorbed on transition metal surfaces as revealed by electron spectroscopy and cognate techniques. *Surface Science Reports* **1991**, *13* (7), 223-263.
16. Bozso, F.; Ertl, G.; Grunze, M.; Weiss, M., Interaction of nitrogen with iron surfaces: I. Fe(100) and Fe(111). *Journal of Catalysis* **1977**, *49* (1), 18-41.

17. Dietrich, H.; Geng, P.; Jacobi, K.; Ertl, G., Sticking coefficient for dissociative adsorption of N<sub>2</sub> on Ru single-crystal surfaces. *The Journal of Chemical Physics* **1996**, *104* (1), 375-381.
18. Shi, H.; Jacobi, K.; Ertl, G., Interaction of hydrogen with nitrogen atoms chemisorbed on a Ru(0001) surface. *The Journal of Chemical Physics* **1995**, *102* (3), 1432-1439.
19. Montoya, J. H.; Tsai, C.; Vojvodic, A.; Nørskov, J. K., The Challenge of Electrochemical Ammonia Synthesis: A New Perspective on the Role of Nitrogen Scaling Relations. *ChemSusChem* **2015**, *8* (13), 2180-2186.
20. Soroka, O.; Sturm, J. M.; Lee, C. J.; Schreuders, H.; Dam, B.; Bijkerk, F., Hydrogen diffusion through Ru thin films. *International Journal of Hydrogen Energy* **2020**, *45* (29), 15003-15010.
21. Steward, S. A. *Review of Hydrogen Isotope Permeability Through Materials*; United States, 1983; p Medium: ED; Size: 28 p.
22. Hargreaves, J. S. J., Nitrides as ammonia synthesis catalysts and as potential nitrogen transfer reagents. *Applied Petrochemical Research* **2014**, *4* (1), 3-10.
23. Ye, T.-N.; Park, S.-W.; Lu, Y.; Li, J.; Sasase, M.; Kitano, M.; Tada, T.; Hosono, H., Vacancy-enabled N<sub>2</sub> activation for ammonia synthesis on an Ni-loaded catalyst. *Nature* **2020**, *583* (7816), 391-395.
24. Dražević, E.; Skúlason, E., Are There Any Overlooked Catalysts for Electrochemical NH<sub>3</sub> Synthesis—New Insights from Analysis of Thermochemical Data. *iScience* **2020**, *23* (12), 101803.
25. Du, H.-L.; Gengenbach, T. R.; Hodgetts, R.; MacFarlane, D. R.; Simonov, A. N., Critical Assessment of the Electrocatalytic Activity of Vanadium and Niobium Nitrides toward Dinitrogen Reduction to Ammonia. *ACS Sustainable Chemistry & Engineering* **2019**, *7* (7), 6839-6850.
26. Hunter, S. M.; Gregory, D. H.; Hargreaves, J. S. J.; Richard, M.; Duprez, D.; Bion, N., A Study of 15N/14N Isotopic Exchange over Cobalt Molybdenum Nitrides. *ACS Catalysis* **2013**, *3* (8), 1719-1725.
27. Zeinalipour-Yazdi, C. D.; Hargreaves, J. S. J.; Catlow, C. R. A., Nitrogen Activation in a Mars–van Krevelen Mechanism for Ammonia Synthesis on Co<sub>3</sub>Mo<sub>3</sub>N. *The Journal of Physical Chemistry C* **2015**, *119* (51), 28368-28376.
28. Abghoui, Y.; Garden, A. L.; Hlynsson, V. F.; Björgvinsdóttir, S.; Ólafsdóttir, H.; Skúlason, E., Enabling electrochemical reduction of nitrogen to ammonia at ambient conditions through rational catalyst design. *Physical Chemistry Chemical Physics* **2015**, *17* (7), 4909-4918.
29. Zeinalipour-Yazdi, C. D.; Hargreaves, J. S. J.; Catlow, C. R. A., DFT-D3 Study of Molecular N<sub>2</sub> and H<sub>2</sub> Activation on Co<sub>3</sub>Mo<sub>3</sub>N Surfaces. *The Journal of Physical Chemistry C* **2016**, *120* (38), 21390-21398.
30. DOE, U. S., *Renewable Energy to Fuels Through Utilization of Energy-Dense Liquids (REFUEL) Program Overview* **2016**.
31. Arrigo, R., In situ X-ray spectroscopic characterization techniques for electrocatalysis. *Current Opinion in Green and Sustainable Chemistry* **2022**, *34*, 100601.
32. Velasco-Vélez, J.-J.; Falling, L. J.; Bernsmeier, D.; Sear, M. J.; Clark, P. C. J.; Chan, T.-S.; Stotz, E.; Hävecker, M.; Kraehnert, R.; Knop-Gericke, A.; Chuang, C.-H.; Starr, D. E.; Favaro, M.; Mom, R. V., A comparative study of electrochemical cells for in situ x-ray spectroscopies in the soft and tender x-ray range. *Journal of Physics D: Applied Physics* **2021**, *54* (12), 124003.

33. Borgschulte, A.; Sambalova, O.; Delmelle, R.; Jenatsch, S.; Hany, R.; Nüesch, F., Hydrogen reduction of molybdenum oxide at room temperature. *Scientific Reports* **2017**, 7 (1), 40761.
34. Zhang, C.; Grass, M. E.; McDaniel, A. H.; DeCaluwe, S. C.; Gabaly, F. E.; Liu, Z.; McCarty, K. F.; Farrow, R. L.; Linne, M. A.; Hussain, Z.; Jackson, G. S.; Bluhm, H.; Eichhorn, B. W., Measuring fundamental properties in operating solid oxide electrochemical cells by using in situ X-ray photoelectron spectroscopy. *Nature Materials* **2010**, 9 (11), 944-949.
35. Kerger, P.; Vogel, D.; Rohwerder, M., Electrochemistry in ultra-high vacuum: The fully transferrable ultra-high vacuum compatible electrochemical cell. *Review of Scientific Instruments* **2018**, 89 (11), 113102.
36. Salmeron, M.; Schlögl, R., Ambient pressure photoelectron spectroscopy: A new tool for surface science and nanotechnology. *Surface Science Reports* **2008**, 63 (4), 169-199.
37. Pérez-Dieste, V.; Aballe, L.; Ferrer, S.; Nicolàs, J.; Escudero, C.; Milán, A.; Pellegrin, E., Near Ambient Pressure XPS at ALBA. *Journal of Physics: Conference Series* **2013**, 425 (7), 072023.
38. Degaga, G. D.; Trought, M.; Nemsak, S.; Crumlin, E. J.; Seel, M.; Pandey, R.; Perrine, K. A., Investigation of N<sub>2</sub> adsorption on Fe<sub>3</sub>O<sub>4</sub>(001) using ambient pressure X-ray photoelectron spectroscopy and density functional theory. *The Journal of Chemical Physics* **2020**, 152 (5), 054717.
39. Rao, G. R.; Rao, C. N. R., Adsorption of nitrogen on clean and modified single-crystal Ni surfaces. *Applied Surface Science* **1990**, 45 (1), 65-69.
40. Madey, T. E.; Yates, J. T.; Erickson, N. E., X-ray photoelectron spectroscopic study of the adsorption of N<sub>2</sub> and NO on tungsten. *Surface Science* **1974**, 43 (2), 526-544.
41. Ertl, G.; Thiele, N., XPS studies with ammonia synthesis catalysts. *Applications of Surface Science* **1979**, 3 (1), 99-112.
42. Devanathan, M. A. V.; Stachurski, Z.; Tompkins, F. C., The adsorption and diffusion of electrolytic hydrogen in palladium. *Proceedings of the Royal Society of London. Series A. Mathematical and Physical Sciences* **1962**, 270 (1340), 90-102.
43. Ripepi, D.; Zaffaroni, R.; Kolen, M.; Middelkoop, J.; Mulder, F. M., Operando isotope selective ammonia quantification in nitrogen reduction studies via gas chromatography-mass spectrometry. *Sustainable Energy & Fuels* **2022**, 6 (8), 1945-1949.
44. Zaffaroni, R.; Ripepi, D.; Middelkoop, J.; Mulder, F. M., Gas Chromatographic Method for In Situ Ammonia Quantification at Parts per Billion Levels. *ACS Energy Letters* **2020**, 5 (12), 3773-3777.
45. de Castro, A.; Alegre, D.; Tabarés, F. L., Physisorption of ammonia on AISI 304L stainless steel at different surface temperature under high vacuum conditions. *Nuclear Materials and Energy* **2016**, 9, 1-5.
46. Danielson, L. R.; Dresser, M. J.; Donaldson, E. E.; Dickinson, J. T., Adsorption and desorption of ammonia, hydrogen, and nitrogen on ruthenium (0001). *Surface Science* **1978**, 71 (3), 599-614.
47. Streibel, V.; Hävecker, M.; Yi, Y.; Velasco Vélez, J. J.; Skorupska, K.; Stotz, E.; Knop-Gericke, A.; Schlögl, R.; Arrigo, R., In Situ Electrochemical Cells to Study the Oxygen Evolution Reaction by Near Ambient Pressure X-ray Photoelectron Spectroscopy. *Topics in Catalysis* **2018**, 61 (20), 2064-2084.

48. Divins, N. J.; Angurell, I.; Escudero, C.; Pérez-Dieste, V.; Llorca, J., Influence of the support on surface rearrangements of bimetallic nanoparticles in real catalysts. *Science* **2014**, *346* (6209), 620-623.
49. Miller, A. C.; Powell, C. J.; Gelius, U.; Anderson, C. R., Energy calibration of X-ray photoelectron spectrometers. Part III: Location of the zero point on the binding-energy scale. *Surface and Interface Analysis* **1998**, *26* (8), 606-614.
50. Briggs, D.; Grant, J. T.; Limited, S., *Surface Analysis by Auger and X-ray Photoelectron Spectroscopy*. SurfaceSpectra: 2003.
51. Imamura, M.; Matsubayashi, N.; Fan, J.; Kojima, I.; Sasaki, M., The determination of the thickness of the silicon oxide film by synchrotron radiation x-ray photoelectron spectroscopy (SR-XPS) analysis. *Measurement Science and Technology* **2010**, *22* (2), 024007.
52. Cimino, A.; Gazzoli, D.; Valigi, M., XPS quantitative analysis and models of supported oxide catalysts. *Journal of Electron Spectroscopy and Related Phenomena* **1999**, *104* (1), 1-29.
53. Powell, C. J.; Jabloski, A., *NIST Electron Inelastic-Mean-Free-Path Database version 1.2, SRD 71*. NIST: Gaithersburg, MD, 2010.
54. Ertl, G.; Huber, M.; Lee, S. B.; Paál, Z.; Weiss, M., Interactions of nitrogen and hydrogen on iron surfaces. *Applications of Surface Science* **1981**, *8* (4), 373-386.
55. Ertl, G.; Huber, M., Interaction of Nitrogen and Oxygen on Iron Surfaces. *Zeitschrift für Physikalische Chemie* **1980**, *119* (1), 97.
56. Wedler, G.; Alshorachi, G., Adsorption of Nitrogen on Polycrystalline Nickel Films between 77 K and 333 K. *Berichte der Bunsengesellschaft für physikalische Chemie* **1980**, *84* (3), 277-281.
57. Grunze, M.; Driscoll, R. K.; Burland, G. N.; Cornish, J. C. L.; Pritchard, J., Molecular and dissociative chemisorption of N<sub>2</sub> on Ni(110). *Surface Science* **1979**, *89* (1), 381-390.
58. Holmes, R. D.; O'Neill, H. S. C.; Arculus, R. J., Standard Gibbs free energy of formation for Cu<sub>2</sub>O, NiO, CoO, and Fe<sub>x</sub>O: High resolution electrochemical measurements using zirconia solid electrolytes from 900–1400 K. *Geochimica et Cosmochimica Acta* **1986**, *50* (11), 2439-2452.
59. Medford, A. J.; Vojvodic, A.; Hummelshøj, J. S.; Voss, J.; Abild-Pedersen, F.; Studt, F.; Bligaard, T.; Nilsson, A.; Nørskov, J. K., From the Sabatier principle to a predictive theory of transition-metal heterogeneous catalysis. *Journal of Catalysis* **2015**, *328*, 36-42.
60. Biesinger, M. C.; Payne, B. P.; Lau, L. W. M.; Gerson, A.; Smart, R. S. C., X-ray photoelectron spectroscopic chemical state quantification of mixed nickel metal, oxide and hydroxide systems. *Surface and Interface Analysis* **2009**, *41* (4), 324-332.
61. Dupin, J.-C.; Gonbeau, D.; Vinatier, P.; Levasseur, A., Systematic XPS studies of metal oxides, hydroxides and peroxides. *Physical Chemistry Chemical Physics* **2000**, *2* (6), 1319-1324.
62. Galtayries, A.; Laksono, E.; Siffre, J.-M.; Argile, C.; Marcus, P., XPS study of the adsorption of NH<sub>3</sub> on nickel oxide on Ni(111). *Surface and Interface Analysis* **2000**, *30* (1), 140-144.
63. Brundle, C. R., XPS and UPS studies of the interaction of nitrogen-containing molecules with nickel: The use of binding energy patterns and relative intensities to diagnose surface species. *Journal of Vacuum Science and Technology* **1976**, *13* (1), 301-309.



64. Brundle, C. R.; Carley, A. F., XPS and UPS studies of the adsorption of small molecules on polycrystalline Ni films. *Faraday Discussions of the Chemical Society* **1975**, 60 (0), 51-70.
65. Grunze, M.; Golze, M.; Driscoll, R.; Dowben, P. A., Ammonia adsorption and decomposition on a Ni (110) surface. *Journal of Vacuum Science and Technology* **1981**, 18 (2), 611-615.
66. Kulkarni, G. U.; Rao, C. N. R.; Roberts, M. W., Nature of the Oxygen Species at Ni(110) and Ni(100) Surfaces Revealed by Exposure to Oxygen and Oxygen-Ammonia Mixtures: Evidence for the Surface Reactivity of O- Type Species. *The Journal of Physical Chemistry* **1995**, 99 (10), 3310-3316.
67. Breitschafter, M. J.; Umbach, E.; Menzel, D., Characterization of mixed N<sub>2</sub>-layers on Ni(111) in the temperature range 20–100 K. *Surface Science* **1986**, 178 (1), 725-734.
68. Breitschafter, M. J.; Umbach, E.; Menzel, D., An electron spectroscopic investigation of the adsorption of NO on Ni(111). *Surface Science* **1981**, 109 (2), 493-511.
69. Chattopadhyay, A.; Yang, H.; Whitten, J. L., Adsorption of ammonia on nickel(111). *The Journal of Physical Chemistry* **1990**, 94 (16), 6379-6383.
70. Van Santen, R. A.; Neurock, M., Concepts in Theoretical Heterogeneous Catalytic Reactivity. *Catalysis Reviews* **1995**, 37 (4), 557-698.
71. Baiker, A.; Monti, D., Interaction of Ammonia with Metallic Copper, Nickel and Cobalt Catalysts Studied by Temperature Programmed Desorption. *Berichte der Bunsengesellschaft für physikalische Chemie* **1983**, 87 (7), 602-605.
72. Verhaak, M. J. F. M.; van Dillen, A. J.; Geus, J. W., Measuring the acid-base properties of supported nickel catalysts using temperature-programmed desorption of ammonia. *Applied Catalysis A: General* **1993**, 105 (2), 251-269.
73. Carley, A. F.; Rassias, S.; Roberts, M. W.; Tang-Han, W., Chemisorption of nitric oxide by nickel. *Surface Science* **1979**, 84 (1), L227-L230.
74. Umbach, E., Electronic structure and interactions in well-defined coadsorbate layers. *Applied Physics A* **1988**, 47 (1), 25-36.
75. Ye, T.-N.; Park, S.-W.; Lu, Y.; Li, J.; Sasase, M.; Kitano, M.; Hosono, H., Contribution of Nitrogen Vacancies to Ammonia Synthesis over Metal Nitride Catalysts. *Journal of the American Chemical Society* **2020**, 142 (33), 14374-14383.
76. Abghoui, Y.; Skúlason, E., Computational Predictions of Catalytic Activity of Zincblende (110) Surfaces of Metal Nitrides for Electrochemical Ammonia Synthesis. *The Journal of Physical Chemistry C* **2017**, 121 (11), 6141-6151.
77. Baiker, A.; Maciejewski, M., Formation and thermal stability of copper and nickel nitrides. *Journal of the Chemical Society, Faraday Transactions 1: Physical Chemistry in Condensed Phases* **1984**, 80 (8), 2331-2341.
78. Alexander, A.-M.; Hargreaves, J. S. J.; Mitchell, C., The Reduction of Various Nitrides under Hydrogen: Ni<sub>3</sub>N, Cu<sub>3</sub>N, Zn<sub>3</sub>N<sub>2</sub> and Ta<sub>3</sub>N<sub>5</sub>. *Topics in Catalysis* **2012**, 55 (14), 1046-1053.
79. Wu, H.; Jiang, H.; Yang, Y.; Hou, C.; Zhao, H.; Xiao, R.; Wang, H., Cobalt nitride nanoparticle coated hollow carbon spheres with nitrogen vacancies as an electrocatalyst for lithium–sulfur batteries. *Journal of Materials Chemistry A* **2020**, 8 (29), 14498-14505.
80. Guo, S.; Zhang, H.; Yang, P.; Chen, Y.; Yu, X.; Yu, B.; Zhao, Y.; Yang, Z.; Liu, Z., Visible-light-driven photoreduction of CO<sub>2</sub> to CO over porous nitrogen-deficient carbon nitride nanotubes. *Catalysis Science & Technology* **2019**, 9 (10), 2485-2492.

81. Ketteler, G.; Yamamoto, S.; Bluhm, H.; Andersson, K.; Starr, D. E.; Ogletree, D. F.; Ogasawara, H.; Nilsson, A.; Salmeron, M., The Nature of Water Nucleation Sites on TiO<sub>2</sub>(110) Surfaces Revealed by Ambient Pressure X-ray Photoelectron Spectroscopy. *The Journal of Physical Chemistry C* **2007**, *111* (23), 8278-8282.
82. Jackman, M. J.; Thomas, A. G.; Murn, C., Photoelectron Spectroscopy Study of Stoichiometric and Reduced Anatase TiO<sub>2</sub>(101) Surfaces: The Effect of Subsurface Defects on Water Adsorption at Near-Ambient Pressures. *The Journal of Physical Chemistry C* **2015**, *119* (24), 13682-13690.
83. Liu, B.; He, B.; Peng, H.-Q.; Zhao, Y.; Cheng, J.; Xia, J.; Shen, J.; Ng, T.-W.; Meng, X.; Lee, C.-S.; Zhang, W., Unconventional Nickel Nitride Enriched with Nitrogen Vacancies as a High-Efficiency Electrocatalyst for Hydrogen Evolution. *Advanced Science* **2018**, *5* (8), 1800406.
84. Umeda, K.; Kawashimo, Y.; Nakasone, M.; Harada, S.; Tasaki, A., Iron-Nitride Thin Films Prepared by Arc-Discharge-Type Ion-Plating. *Japanese Journal of Applied Physics* **1984**, *23* (Part 1, No. 12), 1576-1579.
85. Muhler, M.; Rosowski, F.; Hinrichsen, O.; Hornung, A.; Ertl, G., Ruthenium as catalyst for ammonia synthesis. In *Studies in Surface Science and Catalysis*, Hightower, J. W.; Nicholas Delgass, W.; Iglesia, E.; Bell, A. T., Eds. Elsevier: 1996; Vol. 101, pp 317-326.
86. van der Ham, C. J. M.; Koper, M. T. M.; Hetterscheid, D. G. H., Challenges in reduction of dinitrogen by proton and electron transfer. *Chemical Society Reviews* **2014**, *43* (15), 5183-5191.
87. Jacobi, K., Nitrogen on Ruthenium Single-Crystal Surfaces. *Physica Status Solidi (a)* **2000**, *177*, 37-51.
88. Hinrichsen, O.; Rosowski, F.; Hornung, A.; Muhler, M.; Ertl, G., The Kinetics of Ammonia Synthesis over Ru-Based Catalysts: 1. The Dissociative Chemisorption and Associative Desorption of N<sub>2</sub>. *Journal of Catalysis* **1997**, *165* (1), 33-44.
89. Vojvodic, A.; Medford, A. J.; Studt, F.; Abild-Pedersen, F.; Khan, T. S.; Bligaard, T.; Nørskov, J. K., Exploring the limits: A low-pressure, low-temperature Haber-Bosch process. *Chemical Physics Letters* **2014**, *598*, 108-112.
90. Jacobsen, C. J. H.; Dahl, S.; Clausen, B. S.; Bahn, S.; Logadottir, A.; Nørskov, J. K., Catalyst Design by Interpolation in the Periodic Table: Bimetallic Ammonia Synthesis Catalysts. *Journal of the American Chemical Society* **2001**, *123* (34), 8404-8405.
91. Morgan, D. J., Resolving ruthenium: XPS studies of common ruthenium materials. *Surface and Interface Analysis* **2015**, *47* (11), 1072-1079.
92. Manolatos, P.; Jerome, M.; Galland, J., Necessity of a palladium coating to ensure hydrogen oxidation during electrochemical permeation measurements on iron. *Electrochimica Acta* **1995**, *40* (7), 867-871.
93. Shah, D.; Bahr, S.; Dietrich, P.; Meyer, M.; Thißen, A.; Linford, M. R., Nitrogen gas (N<sub>2</sub>), by near-ambient pressure XPS. *Surface Science Spectra* **2019**, *26* (1), 014023.

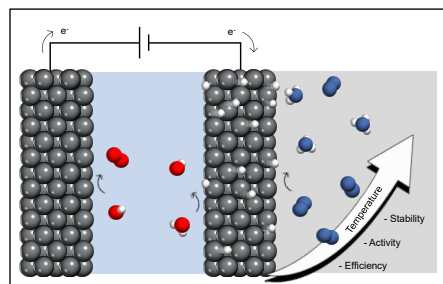


---

# Effect of temperature and H flux on the $\text{NH}_3$ synthesis via electrochemical hydrogen permeation

7

Ammonia is an indispensable commodity in the fertiliser industry and a potential global carbon free energy and hydrogen carrier. Thus, the implementation of a technology for the production of green ammonia from renewable electricity, which can replace the fossil fuel based Haber-Bosch process, is paramount. The use of hydrogen permeable electrodes to synthesise ammonia from dinitrogen, water and electricity, provides a promising alternative strategy, albeit reaction rate, faradaic efficiency and long term stability require improvements. Here, this H permeation system is investigated in the operating temperature range 25 to 120 °C, and varying the rate of electrochemical atomic hydrogen permeation. In this study, we show how these parameters impact the  $\text{NH}_3$  synthesis performance and how a suitable increase in temperature considerably improves the reaction rate, the faradaic efficiency and the stability of the nitrogen reduction reaction via electrochemical atomic hydrogen permeation. At 120 °C, a steady reaction is achieved for over 12 h with a 10 times higher cumulative  $\text{NH}_3$  production and almost 40-fold increase in faradaic efficiency compared to the room temperature operation previously reported.<sup>1</sup> The produced  $\text{NH}_3$  is formed with a cell potential of 1.4 V, which correspond to an attractive theoretical minimum electrical energy investment of 6.6 kWh  $\text{kg}_{\text{NH}_3}^{-1}$ . The stable operation is attributed to a balanced control over the population of N,  $\text{NH}_x$  and H species at the catalyst surface. The findings present in this study extend the understanding on the mechanisms involved in the nitrogen reduction reaction and may facilitate the development of an efficient green ammonia synthesis process.



## 7.1 Introduction

With the increasing share in renewable energy generation, the electrification of large industrial chemical processes, such as the production of ammonia ( $\text{NH}_3$ ), is considered a primary requirement to mitigate the climate crisis and reduce the dependency from fossil fuels. Electrocatalytic ammonia synthesis from dinitrogen ( $\text{N}_2$ ) reduction is currently regarded as a potential alternative to the current energy intensive and environmentally impactful, fossil powered, Haber-Bosch process.<sup>2-5</sup> Conventional aqueous electrochemical  $\text{NH}_3$  synthesis appears extremely challenging and the field is plagued with unreproducible results, due to mainly ammonia and nitrate impurities traces that obscure the dinitrogen reduction.<sup>6-11</sup>

Alternatively, an unconventional approach, based on hydrogen permeable electrodes, has been proven to be an attractive solution for the production of  $\text{NH}_3$  from dinitrogen and water at ambient conditions.<sup>1</sup> This method uses a solid, non-porous, metal electrode to physically separate the electrochemical hydrogen generation from the catalytic dinitrogen activation and hydrogenation to ammonia. Because of this particular configuration, the two distinct catalytic surfaces can be independently optimised for the hydrogen generation and the nitrogen reduction, respectively. The approach harnesses the ability of certain reactive metal surfaces, like Ni, to spontaneously activate dinitrogen. This is possible when  $\text{N}_2$  is not in competition with other adsorbate molecules, as hydrogen or oxygen species from the electrolyte.<sup>12-16</sup> The hydrogenation of adsorbed nitrogen is then carried out by atomic hydrogen generated from water electroreduction and permeating through the bulk of the solid metallic electrode. This design effectively limits and regulates the availability of H, which otherwise could dominate the catalytic interface in a conventional aqueous electrochemical environment, resulting in the suppression of  $\text{N}_2$  activation.

Regrettably, the performance achieved using H permeable electrodes up to this point remains well below the metrics established by the US Department of Energy, aiming at a  $\text{NH}_3$  production rate of  $10^{-6} \text{ mol cm}^{-2} \text{ s}^{-1}$ .<sup>17</sup> One factor limiting the potential of this system is the decay in  $\text{NH}_3$  yield rate observed after few hours of operation, indicating the occurrence of a deactivation process.<sup>1</sup> This mechanism is not yet well understood, however, a recent *in situ* study suggested that ambient temperature operation might be limited by slow N hydrogenation to NH and  $\text{NH}_3$  desorption (Chapter 6).

On this basis, the present work provides a systematic investigation of the effect of operating temperature (in the range 25 to 120 °C, in which concentrated a KOH solution can be used as liquid electrolyte) and H permeation flux on the N<sub>2</sub> reduction reaction, leading to a considerably improved NH<sub>3</sub> synthesis process.

## 7.2 Experimental

**Materials.** Polycrystalline nickel foil (Goodfellow, 99.9 % purity) with a thickness of 0.0125 mm was used as hydrogen permeable electrode. A nickel wire (MaTeck GmbH, > 99 % purity) with a diameter of 1 mm and total wetted geometrical area of about 5 cm<sup>2</sup> was used as counter electrode.

The electrolyte was prepared dissolving KOH (Sigma-Aldrich, 99.99 % purity) in MilliQ water with 45 % w/w concentration (solution boiling point 132.5 °C). Such concentrated electrolyte solution was necessary to operate the electrochemical cell at temperatures up to 120 °C and ambient pressure.

High purity N<sub>2</sub> (Linde, 5N) and Ar (Linde, 5N), was used. Although analysis for NO<sub>x</sub> and NH<sub>3</sub> impurities using methods in Chapter 4, showed that the concentration of these contaminants did not exceed the lower detection limit (LOD<sub>NH<sub>3</sub></sub>: 150 ppb, LOD<sub>NO<sub>x</sub></sub>: 10 ppb), all the gases were cleaned with gas purifiers (Agilent OT3-4) prior introduction to the electrochemical cell, ensuring an efficient removal of all the possible NO<sub>x</sub> and NH<sub>3</sub> contaminations.<sup>1, 18</sup> This additional purification step was also applied to <sup>15</sup>N<sub>2</sub> (99 atom % <sup>15</sup>N, Sigma-Aldrich) used for isotope labelled experiments, as <sup>15</sup>N<sub>2</sub> might also contain traces of extraneous N species.<sup>18, 19</sup>

**Sample preparation.** The sample preparation is analogous to the one carried out in our previous work.<sup>1</sup> In short, the Ni foil was extensively cleaned with a Ar:H<sub>2</sub> plasma (7:1) for 30 min at 5 μbar, generated at 20 W RF power. Subsequently, a protective surface nitride layer against oxidation<sup>1, 20</sup> was generated by nitrogen plasma nitridation using an Ar:N<sub>2</sub> mixture (2:1) at 20 μbar and 40 W RF power for ten minutes. The stability of the Ni nitrided surface was tested at temperatures up to 150 °C under H<sub>2</sub>, showing no formation NH<sub>3</sub> or N<sub>2</sub>, thus underlining the benefit of the H permeable electrode.

**Electrochemical setup.** In this study, a two compartments electrochemical flow cell made of polyether ether ketone (PEEK) for all the electrochemical experiments. The

hydrogen permeable Ni electrode separates the two sides of the electrochemical cell. In one side of the cell containing the counter electrode, the electrolyte solution is circulated using a Masterflex peristaltic pump. At the other side, the feed gas flow is controlled by means of dedicated mass flow controllers (EL Flow Prestige – Bronkhorst). Silconert®2000 inert tubing was used for all the gas connections to minimize ammonia physisorption. All the  $\text{NH}_3$  synthesis experiments were carried out using a Parstat MC 1000 potentiostat in galvanostatic conditions, with a constant charging current density of  $0.25 \text{ mA cm}^{-2}$ , unless otherwise stated.

This work focuses on the synthesis of  $\text{NH}_3$  in the temperature range between 25 and 120 °C. To operate at these temperatures, the electrochemical cell, a large electrolyte reservoir (150 mL), the PTFE tubing and Kapton insulated electric cables were installed inside a Carbolite™ PF Fan convection laboratory oven. Enough time was allowed for thermal equilibration of all the system components inside the oven. Prior to starting the electrochemical experiments the temperature of the electrolyte reservoir was measured with a K-Type thermocouple, to ensure the equilibration time was sufficient ( $\pm 2$  °C the setpoint temperature).

**Gas analysis.** Gas analysis was carried out in real time, connecting directly the outlet of the gas compartment of the electrochemical cell to the GC/GC-MS, without any external sample manipulation. An extensive description of the ammonia quantification methods via GC and via isotope sensitive GC-MS are available from our previous publications.<sup>21, 22</sup> The hydrogen permeated and recombined to  $\text{H}_2$  at the gas compartment side was quantified using a dedicated channel equipped with Haysep N, Molsieve 5A and a thermal conductivity detector (TCD). A calibration curve for the  $\text{H}_2$  quantification is provided in **Figure A.7.1**.

**Electrochemical Impedance Spectroscopy.** Variations in ohmic, kinetic and mass transport resistance were identified and quantified using electrochemical impedance spectroscopy (EIS). This technique has been widely applied to study various electrochemical processes.<sup>23-25</sup> The EIS measurements were performed with a VersaSTAT 4 potentiostat (AMETEK) at -1.6 V cell voltage (potentiostatic EIS) over a frequency range from 100 kHz to 0.2 Hz with an AC amplitude ( $w$ ) of 10 mV.

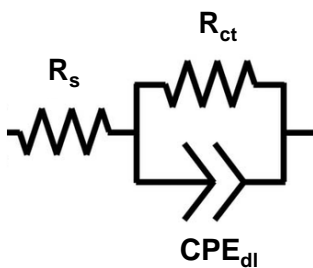


**Figure 7.1** Equivalent circuit model used for fitting EIS data.

The EIS measurements were fitted with a simple Randel's electronic equivalent circuit (**Figure 7.1**) using the ZView software. A constant phase element (CPE) replaces the double layer capacitor to account for the non-ideal capacitance behaviour, influenced by surface roughness, inhomogeneity and porosity.<sup>26, 27</sup> The CPE is characterised by a pseudo-capacitance ( $Q$ ) and a coefficient ( $n$ ), which can vary between 0 and 1 ( $n=1$  for an ideal capacitor), as shown in equation 7.1.<sup>27</sup>

$$C_{\text{NH}_4^+} = \frac{I_{\text{NH}_4^+}}{I_{std}} \frac{N_{std}}{N_{\text{NH}_4^+}} C_{std} \quad (7.1)$$



## 7.3 Results and discussion

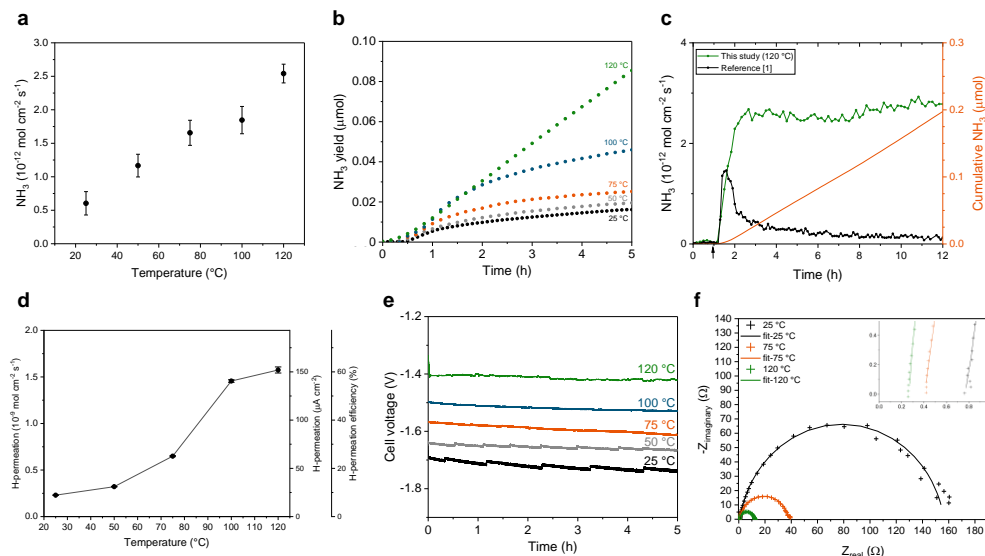


**Figure 7.2** (a) Average ammonia production rate at different temperatures (during the first hour of measurement). (b) Cumulative ammonia production as function of time at different temperatures. (c) Long term experiments carried out at  $120^\circ\text{C}$  from this study (green and orange lines) and at  $25^\circ\text{C}$  from previous report<sup>1</sup> (black line). The arrow indicates the start of the cathodic charging. (d) Variation of the electrochemical hydrogen permeation flux as function of temperature reported in different units and permeation efficiency intended as ratio between the charging current density ( $0.25 \text{ mA cm}^{-2}$ ) and the rate of permeated hydrogen. (e) Effect of the temperature on the cell potential recorded at a constant current density of  $0.25 \text{ mA cm}^{-2}$  (chronopotentiometry) over time. (f) Nyquist plot of electrochemical impedance spectroscopy measurements carried out at different temperatures. Symbols and solid lines indicate the measured values and the electronic equivalent circuit fittings respectively. The enclosure highlights the region of the Nyquist plot at the intersection of the impedance curve with the x-axis (real part of the impedance), which identifies the solution resistance.

Increasing the operating temperature results in a faster initial rate of  $\text{NH}_3$  formation (Figure 7.2a). The highest  $\text{NH}_3$  yield rate of  $2.5 \cdot 10^{-12} \text{ mol cm}^{-2} \text{ s}^{-1}$  is obtained at  $120^\circ\text{C}$ , corresponding to a 4-fold improvement compared to room temperature operation. The higher catalytic dinitrogen reduction is confirmed by alternating  $\text{N}_2$  and Ar as feed gas, and through the reduction of purified  $^{15}\text{N}_2$ , while *in operando* measuring the production of gaseous ammonia with sensitive gas chromatography-mass spectrometry (GC-MS)<sup>21, 22</sup> (Figure A.7.2-A.7.3 and Table A.7.1). The  $^{15}\text{N}_2$  is activated and reduced to  $^{15}\text{NH}_3$ , by gradually

replenishing the <sup>14</sup>N already present on the surface and hydrogenated to form <sup>14</sup>NH<sub>3</sub> and N vacancies.

Remarkably, in addition to the pronounced enhancement in NH<sub>3</sub> yield rate, the increase in temperature has a beneficial impact on the stability of the reaction. This trend is clearly visualised in **Figure 7.2b**, where the amount of NH<sub>3</sub> produced is reported during 5 h experiments. Over time, at temperature below 120 °C, the ammonia production rate gradually declines, suggesting the occurrence of a deactivation mechanism. However, the latter appears to progressively vanish with increasing temperatures, until reaching a steady ammonia production at 120 °C. Long term experiments carried out at 120 °C reveal a constant yield rate and a total of 0.2 μmol of produced NH<sub>3</sub> after 12 h (**Figure 7.2c** and **Figure A.7.4**). This is equivalent to 10 times larger cumulative NH<sub>3</sub> production, compared to our previously reported study (**Figure 7.2c**).<sup>1</sup>

Multiple factors might be responsible for the observed trend. The deactivation mechanism occurring at lower temperatures might be related to the coverage dependence of activation barriers.<sup>28-31</sup> The adoption of an initial protective nitride layer results in a high starting N surface coverage.<sup>1</sup> However, operating in a regime where the H permeation rate is much faster than the rate of N replenishment on the catalyst surface, leads to the depletion of N available at the Ni surface. Therefore, as the N bond strength significantly increases with reducing N coverage,<sup>29, 32</sup> the rate of the first hydrogenation (N to NH), which is considered the limiting step with the largest activation energy,<sup>30</sup> drops; slowing down the NH<sub>3</sub> synthesis.<sup>31-33</sup> Rising the operating temperature of several tens of degrees accelerates the rate of adsorption of nitrogen a few orders of magnitude.<sup>28, 34</sup> Consequently, the enhanced nitrogen activation creates a more balanced catalytic cycle, maintaining apparently a constant N surface coverage through the NH<sub>3</sub> synthesis and N activation cycle. Additionally, higher temperatures promote the desorption of ammonia,<sup>35-37</sup> which can limit the availability of sites for dinitrogen activation at ambient temperature.

An increase in operating temperature accelerates the reaction kinetics and improves ionic conductivity and diffusion processes in (electro-)catalytic systems. As a result, the galvanostatic charging, applied for the generation of atomic hydrogen from water reduction, demands a lower cell potential at higher temperatures (**Figure 7.2e**). The cell potential represents the sum of the equilibrium potential and overpotential associated with multiple resistances.<sup>38</sup> Both the Gibbs free energy change (thus the equilibrium potential) and the

overpotential of the overall water dissociation reaction decrease with the increasing temperatures.<sup>38, 39</sup> The reduction of electrochemical resistances is measured by EIS measurements (**Figure 7.2f**). In the Nyquist plot, the intersection point of the impedance curve with the x-axis (real part of the impedance) identifies the solution resistance ( $R_s$ ), which decreases from 0.78  $\Omega$  at room temperature, to 0.24  $\Omega$  at 120 °C (**Figure 7.2f** and **Table 7.1**). This is a direct consequence of the improved ionic conductivity of the KOH solution at higher temperatures.<sup>40, 41</sup> At intermediate frequencies, the double layer capacitance and the charge transfer resistance are represented by a depressed semi-circle. The EIS results indicate an improved charge transfer rate as the operating temperature increases (**Figure 7.2f** and **Table 7.1**).

**Table 7.1** Equivalent circuit model parameters applied for the fitting of the EIS measurements of **Figure 7.2f** using the Randel's circuit shown in **Figure 7.1**.

Temperature (°C)	$R_s$ ( $\Omega$ )	CPE		$R_{ct}$ ( $\Omega$ )
		Q (F)	$n$	
<b>25</b>	0.78	5.64E-05	0.899	156.6
<b>75</b>	0.41	5.95E-05	0.899	37.6
<b>120</b>	0.24	4.40E-05	0.899	12.0

Ultimately, the temperature also affects the hydrogen transport rate through the electrode. It should be noted that, during electrochemical hydrogen permeation, only a fraction of the generated atomic hydrogen from water electroreduction (Volmer reaction) permeates through the electrode, while the remaining fraction recombines to  $H_2$  via the Tafel or the Heyrovský reaction. The applied galvanostatic charging ensures that the atomic hydrogen formation rate at the electrode-electrolyte interface remains constant. However, the aliquot of permeated H sharply increases with temperature (**Figure 7.2d**), which is essentially associated with the temperature dependence of the hydrogen permeability (product of diffusivity and solubility).<sup>42</sup> An Arrhenius relationship correlates temperature and permeability;<sup>43</sup> however, deviations from the Arrhenius behaviour have been reported and are often attributed to surface effects.<sup>44</sup> Therefore, the temperature has a direct impact on the permeation efficiency, intended as ratio between the total hydrogen generated (i.e. equal to the galvanostatic current) and the permeated hydrogen. Other approaches to increase the

electrochemical hydrogen permeation include the modification of the electrode bulk material (with higher H permeability),<sup>45-47</sup> the reduction of the electrode thickness,<sup>48-50</sup> or the adoption of H permeation promoters in the electrolyte.<sup>51-56</sup> We observed a substantial increase in hydrogen permeation efficiency, reaching  $60 \pm 2\%$  at  $120^\circ\text{C}$  (**Figure 7.2d** and **Table A.7.4**). The following section will discuss the implications of enhanced hydrogen permeation on the overall reaction efficiency. An in-depth investigation and optimization on the electrochemical hydrogen permeation mechanisms fall out of the scope of the present work.

To evaluate the effect of the hydrogen permeation rate on the N reduction reaction under investigation, further experiments were carried out varying the charging current. Higher current densities result in faster H permeation, although at a lower permeation efficiency (**Table A.7.5**). Consequently, the larger availability of reactive H at the catalytic surface increases the chance for hydrogenation of adsorbed N to  $\text{NH}$ ,  $\text{NH}_2$  and  $\text{NH}_3$ , thus accelerating the formation of  $\text{NH}_3$  (**Figure 7.3**). However, the hydrogenation efficiency, defined as the ratio of the  $\text{NH}_3$  synthesis rate ( $\dot{N}\text{H}_3$ ) and the atomic hydrogen permeation rate ( $H_{\text{perm}}$ ), decreases at higher  $H_{\text{perm}}$ . This is because a larger aliquot of permeating H recombines at the side of the catalyst surface exposed to dinitrogen, indicating that the hydrogenation of adsorbed N is a slower process compared to the  $2\text{H}$  recombination into  $\text{H}_2$  on Ni. Furthermore, a too large H flux might result in the catalyst surface to be covered mostly by  $\text{H}/\text{H}_2$ , obstructing nitrogen adsorption, since direct competition for active sites has been observed.<sup>1, 15</sup>

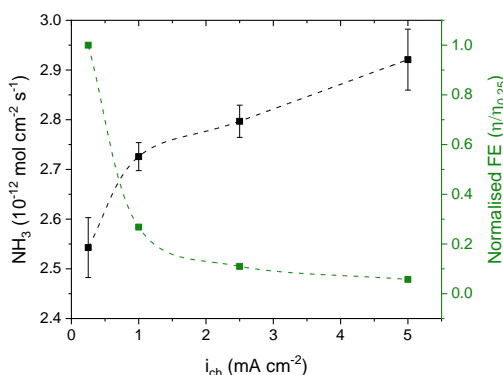


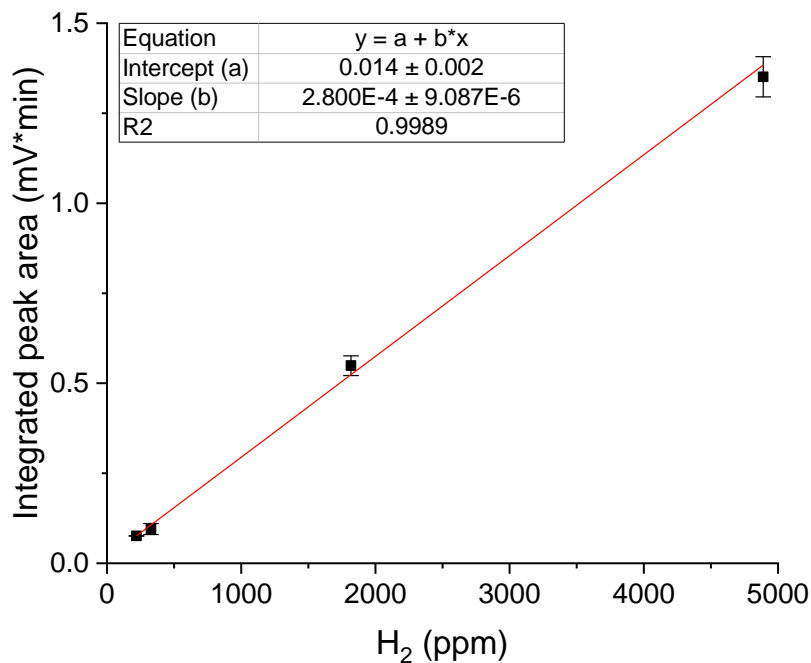
**Figure 7.3** Ammonia production rate measured at  $120^\circ\text{C}$  at different charging current densities (closed symbols). The corresponding faradaic efficiency is reported normalized to the faradaic efficiency obtained at  $0.25 \text{ mA cm}^{-2}$  (open symbols). Lines are a guide for the eyes.

Both the permeation and hydrogenation efficiency directly affect the faradaic efficiency (FE) of the overall process (**Table A.7.4-A.7.5** and equation A.7.1-A.7.4). Operating the electrolytic cell at 120 °C and 0.25 mA cm<sup>-2</sup> results in almost 40-fold improvement in FE compared to our previous report.<sup>1</sup> Even though, so far, the overall FE remains fairly low (0.1 %), the produced NH<sub>3</sub> is formed with a cell potential of 1.4 V (**Figure A.7.4**), which correspond to an attractive theoretical minimum electrical energy investment of 6.6 kWh kg<sup>-1</sup><sub>NH<sub>3</sub></sub> (equation A.7.4).

## Conclusions

The NH<sub>3</sub> synthesis using Ni hydrogen permeable electrode was investigated in the temperature range between 25 and 120 °C. Our results indicate that the increase in operating temperature improves considerably the NH<sub>3</sub> reaction rate, while also sustaining a stable catalytic cycle. This is possibly the result of enhanced nitrogen adsorption and NH<sub>3</sub> desorption, which maintain a steady N surface coverage throughout the NH<sub>3</sub> synthesis cycle, preventing the catalyst deactivation. Hence, to operate the nitrogen reduction reaction in a stable and efficient manner, a critical control over the population of N, NH<sub>x</sub> and H species at the catalyst surface is necessary. Because of the adoption of H permeable electrodes, N activation and H permeation can be independently controlled, by a large extent, as shown here. Increased operating temperatures also favour a more efficient electrochemical hydrogen insertion, consequently leading to an increase in faradaic efficiency by a factor of 37 compared to the previous room temperature report.<sup>1</sup>

Our investigation reveals a complex NH<sub>3</sub> synthesis mechanism resulting from the interplay of multiple processes involved in the electrolytic NH<sub>3</sub> production via electrochemical atomic hydrogen permeation. We anticipate that the scientific insights into the NH<sub>3</sub> synthesis mechanism and into the deactivation process will facilitate the design of suitable catalysts and the selection of operating conditions for the development of improved NH<sub>3</sub> yields.

**Appendix A.7**

**Figure A.7.1** GC calibration curve of H<sub>2</sub> carried out by dosing a certified calibration gases (4 % H<sub>2</sub> in N<sub>2</sub>) and dilute it with N<sub>2</sub> to the chosen concentration. Error bars correspond to the standard deviation of three or more repeated measurements.

## Control experiments.

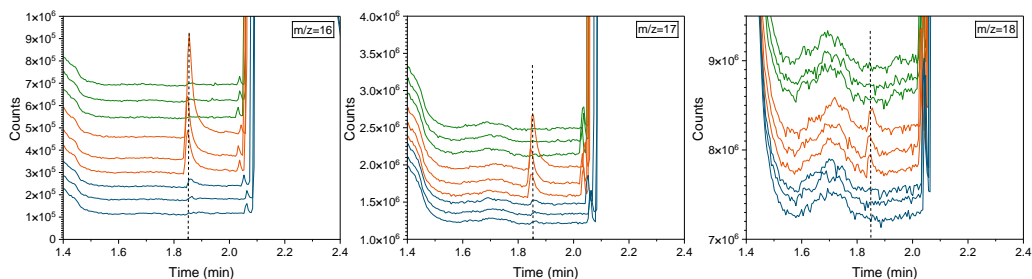


**Figure A.7.2** GC-MS chromatograms, around the ammonia retention time (1.83 min), corresponding to the ionized fragments with mass-to-charge ratio equal to 16, 17 and 18, before (green), during (orange) and after (blue) electrochemical hydrogen permeation under  $^{15}\text{N}_2$  gas. Higher noise level in  $m/z=18$  is due to the effect of water background.

**Table A.7.1** Integrated peak areas of the GC-MS chromatographs of **Figure A.7.2** and the calculated ammonia yield rate. Initially, the hydrogenation of preadsorbed nitrogen ( $^{14}\text{N}$ ) leads to the formation of  $^{14}\text{NH}_3$  and N-vacancy active sites. Subsequently, the gaseous  $^{15}\text{N}_2$  is activated, replacing the  $^{14}\text{N}$  on the surface and forming  $^{15}\text{NH}_3$ .

Injection	Time	I <sub>18</sub>	I <sub>17</sub>	I <sub>16</sub>	r <sub>NH<sub>3</sub></sub>	$^{15}\text{NH}_3$
	[min]	[counts x min]	[counts x min]	[counts x min]	[ $10^{-12}$ mol s $^{-1}$ cm $^{-2}$ ]	[%]
H-perm. [1]	1.85	10457	19631	11500	4.20	42.6 $\pm$ 5
H-perm. [2]	1.84	8418	13085	6598	2.80	51.5 $\pm$ 6
H-perm. [3]	1.84	8408	9598	3192	2.05	70.1 $\pm$ 4

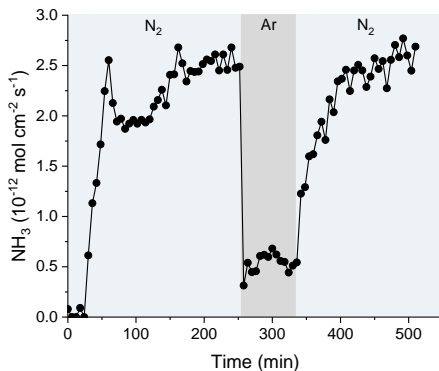


**Figure A.7.3** The successful dinitrogen activation to ammonia is verified by alternating the  $\text{N}_2$  (blue background) and Ar (grey background) feeding gases during electrochemical hydrogen insertion, while in operando monitoring the gas composition with GC.<sup>21, 22</sup> As a result, ammonia production is detected when dinitrogen gas is available, while the rate suddenly drops when Ar is flown to the system.  $\text{NH}_3$  production is then restore to the initial rate, once the  $\text{N}_2$  is reintroduced into the system. A minimum level of ammonia (5 times lower than with  $\text{N}_2$ ) is still detected under Ar, mainly due to the marginal reduction of surface nitrides to  $\text{NH}_3$ . However, in the absence of  $\text{N}_2$  to replenish the reacted surface nitrogen the  $\text{NH}_3$  production will eventually cease once all the nitrogen is consumed. On the other hand, when  $\text{N}_2$  gas is present the catalytic reaction is sustained at a steady rate for more than 12 h (**Figure 7.2c**), indicating that dinitrogen is continuously reduced to  $\text{NH}_3$ .

### Hydrogen permeation data set.

**Table A.7.2** Electrochemical hydrogen permeation data set of GC measurements for the detection of recombined permeating H to H<sub>2</sub>, carried out with a 45 % w/w KOH solution at 0.25 mA cm<sup>-2</sup> and at different temperatures.

T [°C]	Retention time [min]	Area [mV*min]	STD	Average area [mV*min]	H <sub>2</sub> [ppm]	H <sub>2</sub> [mol cm <sup>-2</sup> s <sup>-1</sup> ]	H [mol cm <sup>-2</sup> s <sup>-1</sup> ]	H [uA cm <sup>-2</sup> ]	Efficiency [%]
25	2.12	0.1117	0.002	0.110	392.7	1.15E-10	2.30E-10	22.2	8.9
	2.11	0.1099							
	2.12	0.1087							
	2.12	0.113							
	2.12	0.1065							
50	2.12	0.1533	0.002	0.154	548.8	1.61E-10	3.22E-10	31.0	12.4
	2.12	0.1517							
	2.12	0.153							
	2.12	0.1583							
	2.12	0.152							
75	2.11	0.303	0.005	0.310	1108.0	3.25E-10	6.49E-10	62.6	25.1
	2.12	0.306							
	2.12	0.315							
	2.12	0.314							
	2.12	0.314							
100	2.12	0.699	0.013	0.696	2485.3	7.28E-10	1.46E-09	140.5	56.2
	2.12	0.705							
	2.12	0.711							
	2.12	0.692							
	2.12	0.673							
120	2.12	0.811	0.031	0.752	2687.4	7.87E-10	1.57E-09	151.9	60.8
	2.12	0.747							
	2.12	0.745							
	2.12	0.739							
	2.12	0.721							



**Table A.7.3** Electrochemical hydrogen permeation data set of measurements carried out with 45 % w/w KOH solution at 120 °C and at different charging current densities ( $i_{ch}$ ).

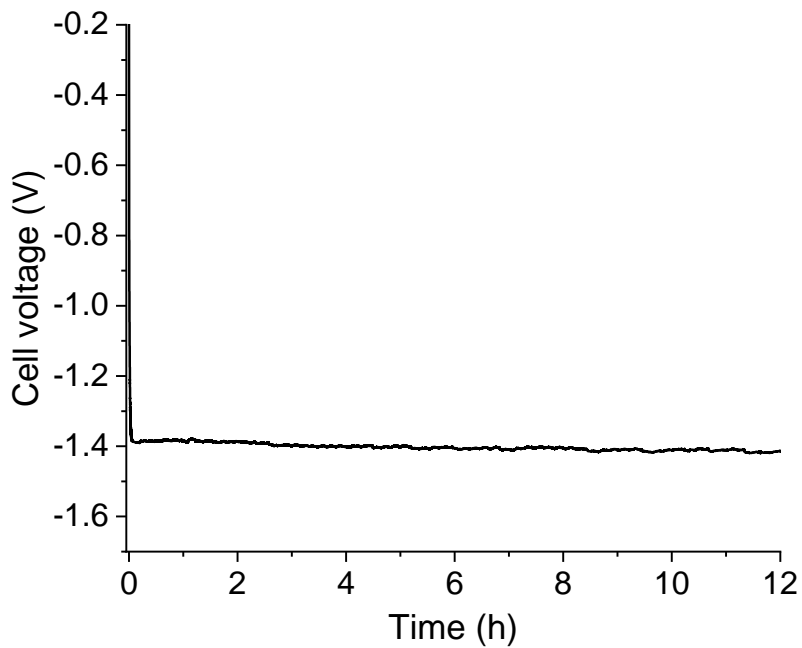
T [°C]	Retention time [min]	Area [mV*min]	$i_{ch}$ [ $\mu\text{A cm}^{-2}$ ]	STD	Average area [mV*min]	H <sub>2</sub> [ppm]	H <sub>2</sub> [ $\text{mol cm}^{-2} \text{s}^{-1}$ ]	H [ $\text{mol cm}^{-2} \text{s}^{-1}$ ]	H [ $\mu\text{A cm}^{-2}$ ]	Efficiency [%]
120	2.12	0.811	250	0.031	0.75	2687.4	7.87E-10	1.57E-09	151.9	60.8
	2.12	0.747								
	2.12	0.745								
	2.12	0.739								
	2.12	0.721								
120	2.12	1.040	1000	0.010	1.05	3735.8	1.09E-09	2.19E-09	211.2	21.1
	2.11	1.051								
	2.12	1.062								
	2.12	1.042								
	2.12	1.035								
120	2.12	1.485	2500	0.006	1.60	5714.3	1.67E-09	3.35E-09	323.1	12.9
	2.12	1.479								
	2.12	1.479								
	2.11	1.491								
	2.12	1.474								
120	2.11	1.964	5000	0.005	1.96	7006.1	2.05E-09	4.10E-09	396.1	7.9
	2.12	1.955								
	2.12	1.957								
	2.12	1.967								
	2.12	1.965								

**Table A.7.4** Summary table of NH<sub>3</sub> synthesis experiments carried out at different temperatures.

<b><math>i_{ch}=0.25 \text{ A cm}^{-2}</math></b>					
<b>Temperature</b> [°C]	<b>NH<sub>3</sub></b> [mol cm <sup>-2</sup> s <sup>-1</sup> ]	<b>H-perm.</b> [mol cm <sup>-2</sup> s <sup>-1</sup> ]	<b>H-perm. efficiency</b> [%]	<b>Hydrogenation efficiency</b> [%]	<b>FE</b> [%]
<b>120</b>	2.54E-12	1.57E-09	60.8	0.48	0.30
<b>100</b>	1.85E-12	1.46E-09	56.2	0.38	0.21
<b>75</b>	1.66E-12	6.49E-10	25.1	0.77	0.19
<b>50</b>	1.17E-12	3.22E-10	12.4	1.09	0.14
<b>25</b>	6.04E-13	2.30E-10	8.9	0.79	0.07

**Table A.7.5** Summary table of NH<sub>3</sub> synthesis experiments carried out at different charging current densities ( $i_{ch}$ ).

<b>T=120 °C</b>					
<b><math>i_{ch}</math></b> [mA cm <sup>-2</sup> ]	<b>NH<sub>3</sub></b> [mol cm <sup>-2</sup> s <sup>-1</sup> ]	<b>H-perm.</b> [mol cm <sup>-2</sup> s <sup>-1</sup> ]	<b>H-perm. efficiency</b> [%]	<b>Hydrogenation efficiency</b> [%]	<b>FE</b> [%]
<b>0.25</b>	2.54E-12	1.57E-09	60.8	0.48	0.30
<b>1.00</b>	2.73E-12	2.19E-09	21.1	0.37	0.08
<b>2.50</b>	2.80E-12	3.35E-09	12.9	0.25	0.03
<b>5.00</b>	2.92E-12	4.10E-09	7.92	0.21	0.02

**Cell potential – 12 h experiment.**

**Figure A.7.4** Cell voltage measured between cathode and anode during 12 h operation at  $0.25 \text{ mA cm}^{-2}$  and  $120^\circ\text{C}$ .

### Efficiency calculation.

The H permeation efficiency is defined as ratio between the permeated hydrogen current density ( $H_{perm}$ ) and the galvanostatic charging current density ( $i_{ch}$ ).

$$H \text{ permeation efficiency} = \frac{H_{perm}}{i_{ch}} \times 100 \quad (A.7.1)$$

The hydrogenation efficiency is calculated as ratio of the ammonia yield rate ( $NH_3$ ) to the product of the number of moles (three moles of H forming one mole of  $NH_3$ ) and the hydrogen permeation flux.

$$\text{Hydrogenation efficiency} = \frac{3 \times NH_3}{H_{perm}} \times 100 \quad (A.7.2)$$

The faradaic efficiency (FE) is calculated as ratio of the ammonia yield rate to the product of the number of electrons ( $n=3$ ), the Faraday constant ( $F$ ) and the galvanostatic charging current density.

$$FE = \frac{n \times NH_3 \times F}{i_{ch}} \times 100 \quad (A.7.3)$$

The overall energy input (excluding the contribution of thermal energy) is calculated from the measured cell potential of about 1.40 V (**Figure A.7.4**).

$$\text{Energy input} = (3e^-) \times (1.40 \text{ V}) \times \left( 4.45 \times 10^{-26} \frac{kWh}{eV} \right) \times \frac{N_a}{M_{NH_3}} \quad (A.7.4)$$

Where the  $N_a$  is the Avogadro's number and  $M_{NH_3}$  is the ammonia molar mass.

## References

1. Ripepi, D.; Zaffaroni, R.; Schreuders, H.; Boshuizen, B.; Mulder, F. M., Ammonia Synthesis at Ambient Conditions via Electrochemical Atomic Hydrogen Permeation. *ACS Energy Letters* **2021**, 3817-3823.
2. MacFarlane, D. R.; Cherepanov, P. V.; Choi, J.; Suryanto, B. H. R.; Hodgetts, R. Y.; Bakker, J. M.; Ferrero Vallana, F. M.; Simonov, A. N., A Roadmap to the Ammonia Economy. *Joule* **2020**, 4 (6), 1186-1205.
3. Shi, R.; Zhang, X.; Waterhouse, G. I. N.; Zhao, Y.; Zhang, T., The Journey toward Low Temperature, Low Pressure Catalytic Nitrogen Fixation. *Advanced Energy Materials* **2020**, 10 (19), 2000659.
4. Service, R. F., Liquid sunshine. *Science* **2018**, 361 (6398), 120-123.
5. Soloveichik, G., Electrochemical synthesis of ammonia as a potential alternative to the Haber–Bosch process. *Nature Catalysis* **2019**, 2 (5), 377-380.
6. Kolen, M.; Ripepi, D.; Smith, W. A.; Burdyny, T.; Mulder, F. M., Overcoming Nitrogen Reduction to Ammonia Detection Challenges: The Case for Leapfrogging to Gas Diffusion Electrode Platforms. *ACS Catalysis* **2022**, 5726-5735.
7. Choi, J.; Suryanto, B. H. R.; Wang, D.; Du, H.-L.; Hodgetts, R. Y.; Ferrero Vallana, F. M.; MacFarlane, D. R.; Simonov, A. N., Identification and elimination of false positives in electrochemical nitrogen reduction studies. *Nature Communications* **2020**, 11 (1), 5546.
8. Andersen, S. Z.; Čolić, V.; Yang, S.; Schwalbe, J. A.; Nielander, A. C.; McEnaney, J. M.; Enemark-Rasmussen, K.; Baker, J. G.; Singh, A. R.; Rohr, B. A.; Statt, M. J.; Blair, S. J.; Mezzavilla, S.; Kibsgaard, J.; Vesborg, P. C. K.; Cargnello, M.; Bent, S. F.; Jaramillo, T. F.; Stephens, I. E. L.; Nørskov, J. K.; Chorkendorff, I., A rigorous electrochemical ammonia synthesis protocol with quantitative isotope measurements. *Nature* **2019**, 570 (7762), 504-508.
9. Singh, A. R.; Rohr, B. A.; Schwalbe, J. A.; Cargnello, M.; Chan, K.; Jaramillo, T. F.; Chorkendorff, I.; Nørskov, J. K., Electrochemical Ammonia Synthesis—The Selectivity Challenge. *ACS Catalysis* **2017**, 7 (1), 706-709.
10. Shahid, U. B.; Chen, Y.; Gu, S.; Li, W.; Shao, M., Electrochemical nitrogen reduction: an intriguing but challenging quest. *Trends in Chemistry* **2022**, 4 (2), 142-156.
11. Hu, L.; Xing, Z.; Feng, X., Understanding the Electrocatalytic Interface for Ambient Ammonia Synthesis. *ACS Energy Letters* **2020**, 5 (2), 430-436.
12. Abghoui, Y.; Garden, A. L.; Hlynsson, V. F.; Björgvinsdóttir, S.; Ólafsdóttir, H.; Skúlason, E., Enabling electrochemical reduction of nitrogen to ammonia at ambient conditions through rational catalyst design. *Physical Chemistry Chemical Physics* **2015**, 17 (7), 4909-4918.
13. Howalt, J. G.; Vegge, T., The role of oxygen and water on molybdenum nanoclusters for electro catalytic ammonia production. *Beilstein Journal of Nanotechnology* **2014**, 5, 111-120.
14. Shi, H.; Jacobi, K.; Ertl, G., Interaction of hydrogen with nitrogen atoms chemisorbed on a Ru(0001) surface. *The Journal of Chemical Physics* **1995**, 102 (3), 1432-1439.
15. Ertl, G.; Huber, M.; Lee, S. B.; Paál, Z.; Weiss, M., Interactions of nitrogen and hydrogen on iron surfaces. *Applications of Surface Science* **1981**, 8 (4), 373-386.

16. Ertl, G.; Huber, M., Interaction of Nitrogen and Oxygen on Iron Surfaces. *Zeitschrift für Physikalische Chemie* **1980**, *119* (1), 97.
17. Soloveichik, G. In *Arpa-e refuel program: Distributed production of ammonia and its conversion to energy*, 2019 AIChE Annual Meeting, AIChE, 2019.
18. Ripepi, D.; Izelaar, B.; van Noordenne, D.; Jungbacker, P.; Kortlever, R.; Mulder, F. M., Determination and Effective NO<sub>x</sub> and NH<sub>3</sub> removal for reliable electrochemical nitrogen reduction. *In preparation*.
19. Dabundo, R.; Lehmann, M. F.; Treibergs, L.; Tobias, C. R.; Altabet, M. A.; Moisaner, P. H.; Granger, J., The Contamination of Commercial 15N<sub>2</sub> Gas Stocks with 15N-Labeled Nitrate and Ammonium and Consequences for Nitrogen Fixation Measurements. *PLOS ONE* **2014**, *9* (10), e110335.
20. Vasconcellos, M. A. Z.; Hinrichs, R.; de Andrade, A. M. H.; da Cunha, J. B. M.; Baumvol, I. J. R., Phase characterization of iron-nitride formed by reactive pulsed magnetron sputtering. *Surface and Coatings Technology* **2020**, *392*, 125753.
21. Ripepi, D.; Zaffaroni, R.; Kolen, M.; Middelkoop, J.; Mulder, F. M., Operando isotope selective ammonia quantification in nitrogen reduction studies via gas chromatography-mass spectrometry. *Sustainable Energy & Fuels* **2022**, *6* (8), 1945-1949.
22. Zaffaroni, R.; Ripepi, D.; Middelkoop, J.; Mulder, F. M., Gas Chromatographic Method for In Situ Ammonia Quantification at Parts per Billion Levels. *ACS Energy Letters* **2020**, *5* (12), 3773-3777.
23. Yuan, X. Z.; Song, C.; Wang, H.; Zhang, J., *Electrochemical Impedance Spectroscopy in PEM Fuel Cells: Fundamentals and Applications*. Springer London: 2009.
24. Blommaert, M. A.; Vermaas, D. A.; Izelaar, B.; in 't Veen, B.; Smith, W. A., Electrochemical impedance spectroscopy as a performance indicator of water dissociation in bipolar membranes. *Journal of Materials Chemistry A* **2019**, *7* (32), 19060-19069.
25. Zhuang, Q.-C.; Qiu, X.-Y.; Xu, S.-D.; Qiang, Y.-H.; Su, S., Diagnosis of electrochemical impedance spectroscopy in lithium-ion batteries. *Lithium Ion Batteries—New Developments* **2012**, *8*, 189-227.
26. Brug, G. J.; van den Eeden, A. L. G.; Sluyters-Rehbach, M.; Sluyters, J. H., The analysis of electrode impedances complicated by the presence of a constant phase element. *Journal of Electroanalytical Chemistry and Interfacial Electrochemistry* **1984**, *176* (1), 275-295.
27. Shoar Abouzari, M. R.; Berkemeier, F.; Schmitz, G.; Wilmer, D., On the physical interpretation of constant phase elements. *Solid State Ionics* **2009**, *180* (14), 922-927.
28. Scholten, J. J. F.; Zwietering, P.; Konvalinka, J. A.; de Boer, J. H., Chemisorption of nitrogen on iron catalysts in connection with ammonia synthesis. Part 1.—The kinetics of the adsorption and desorption of nitrogen. *Transactions of the Faraday Society* **1959**, *55* (0), 2166-2179.
29. Diekhöner, L.; Mortensen, H.; Baurichter, A.; Luntz, A. C., Coverage dependence of activation barriers: Nitrogen on Ru(0001). *Journal of Vacuum Science & Technology A* **2000**, *18* (4), 1509-1513.
30. Ertl, G., Surface Science and Catalysis—Studies on the Mechanism of Ammonia Synthesis: The P. H. Emmett Award Address. *Catalysis Reviews* **1980**, *21* (2), 201-223.
31. Dumesic, J. A.; Huber, G. W.; Boudart, M., Principles of Heterogeneous Catalysis. In *Handbook of Heterogeneous Catalysis*.
32. Chorkendorff, I.; Niemantsverdriet, J. W., *Concepts of modern catalysis and kinetics*. John Wiley & Sons: 2017.

33. Ripepi, D.; Izelaar, B.; van Noordenne, D.; Jungbacker, P.; Kolen, M.; Karanth, P.; Cruz, D.; Zeller, P.; Pérez-Dieste, V.; Villar-Garcia, I. J.; Smith, W. A.; Mulder, F. M., In situ study of hydrogen permeable electrodes for electrolytic ammonia synthesis using near ambient pressure XPS. *In preparation*. **2022**.
34. Ertl, G.; Lee, S. B.; Weiss, M., Kinetics of nitrogen adsorption on Fe(111). *Surface Science* **1982**, *114* (2), 515-526.
35. Al-Shammeri, K. K.; Saleh, J. M., Adsorption and decomposition of ammonia on metal films of nickel, palladium, tungsten and aluminum. *The Journal of Physical Chemistry* **1986**, *90* (13), 2906-2910.
36. Chattopadhyay, A.; Yang, H.; Whitten, J. L., Adsorption of ammonia on nickel(111). *The Journal of Physical Chemistry* **1990**, *94* (16), 6379-6383.
37. Verhaak, M. J. F. M.; van Dillen, A. J.; Geus, J. W., Measuring the acid-base properties of supported nickel catalysts using temperature-programmed desorption of ammonia. *Applied Catalysis A: General* **1993**, *105* (2), 251-269.
38. Bard, A. J.; Faulkner, L. R., *Electrochemical Methods: Fundamentals and Applications, 2nd Edition*. John Wiley & Sons, Incorporated: 2000.
39. Grigoriev, S. A.; Fateev, V. N., Hydrogen Production by Water Electrolysis. In *Hydrogen Production Technologies*, 2017; pp 231-276.
40. Feng, W.; Pang, W.; Xu, Y.; Guo, A.; Gao, X.; Qiu, X.; Chen, W., Transition Metal Selenides for Electrocatalytic Hydrogen Evolution Reaction. *ChemElectroChem* **2020**, *7* (1), 31-54.
41. Gilliam, R. J.; Graydon, J. W.; Kirk, D. W.; Thorpe, S. J., A review of specific conductivities of potassium hydroxide solutions for various concentrations and temperatures. *International Journal of Hydrogen Energy* **2007**, *32* (3), 359-364.
42. Otsuka, T.; Shinohara, M.; Horinouchi, H.; Tanabe, T., Hydrogen permeation in iron and nickel alloys around room temperature. *Journal of Nuclear Materials* **2013**, *442* (1, Supplement 1), S726-S729.
43. Steward, S. Review of hydrogen isotope permeability through materials; Lawrence Livermore National Lab.(LLNL), Livermore, CA (United States): 1983.
44. Shupe, D. S., Effect of surface processes on hydrogen and nitrogen permeation. I. Adsorption. *The Journal of Chemical Physics* **1978**, *68* (6), 2612-2620.
45. Delima, R. S.; Sherbo, R. S.; Dvorak, D. J.; Kurimoto, A.; Berlinguette, C. P., Supported palladium membrane reactor architecture for electrocatalytic hydrogenation. *Journal of Materials Chemistry A* **2019**, *7* (46), 26586-26595.
46. Yukawa, H.; Nambu, T.; Matsumoto, Y., 13 - Design of group 5 metal-based alloy membranes with high hydrogen permeability and strong resistance to hydrogen embrittlement. In *Advances in Hydrogen Production, Storage and Distribution*, Basile, A.; Iulianelli, A., Eds. Woodhead Publishing: 2014; pp 341-367.
47. Boes, N.; Züchner, H., Electrochemical methods for studying diffusion, permeation and solubility of hydrogen in metals. *Journal of the Less Common Metals* **1976**, *49*, 223-240.
48. Jayaraman, V.; Lin, Y. S., Synthesis and hydrogen permeation properties of ultrathin palladium-silver alloy membranes. *Journal of Membrane Science* **1995**, *104* (3), 251-262.
49. Elhamid, M. H. A.; Ateya, B. G.; Pickering, H. W., Determination of the Rate Constants of Hydrogen Absorption into Metals. *Journal of The Electrochemical Society* **2000**, *147* (8), 2959-2963.

50. Athayde, A. L.; Baker, R. W.; Nguyen, P., Metal composite membranes for hydrogen separation. *Journal of Membrane Science* **1994**, *94* (1), 299-311.
51. Flis, J., *Corrosion of metals and hydrogen-related phenomena: selected topics*. Elsevier: 2016.
52. Newman, J.; Shreir, L., Role of hydrides in hydrogen entry into steel from solutions containing promoters. *Corrosion Science* **1969**, *9* (8), 631-641.
53. Qian, S.; Conway, B., Electrochemical sorption of H into Fe and mild-steel: kinetic conditions for enhancement or inhibition by adsorbed HS. *Physical Chemistry Chemical Physics* **1999**, *1* (11), 2805-2813.
54. Akiyama, E.; Li, S., Electrochemical hydrogen permeation tests under galvanostatic hydrogen charging conditions conventionally used for hydrogen embrittlement study. *Corrosion Reviews* **2016**, *34* (1-2), 103-112.
55. Ichiba, M.; Takai, K.; Sakai, J. i., Effects of test conditions on corrosion reactions and hydrogen absorption in hydrogen embrittlement tests using an ammonium thiocyanate solution. *ISIJ International* **2016**, *56* (3), 397-404.
56. Dull, D.; Nobe, K., Effect of thioureas and triazoles on hydrogen penetration rates in iron. *Corrosion* **1979**, *35* (12), 535-540.





## Summary

In the last century, the indiscriminate use of fossil energy to power the industrial revolution and technological progress of humankind, has led to the depletion of limited natural resources and, most importantly, the emission and accumulation of alarming levels of pollutants and greenhouse gases (GHG) in the atmosphere. One of the major consequences of these emissions is the climate crisis that we are currently facing. As our society is in constant need for energy to live and progress, we are urged to find more sustainable and renewable energy sources, and to decrease the environmental impact of industrial processes. Electrochemistry can be used to temporarily store intermittent renewable electricity, to then be reconverted back to electrons, or it can be used to produce chemicals. As such, the electrification of the chemical industry offers the opportunity to reduce its GHG footprint. The variable supply of renewable electricity can be used by the chemical industry to generate artificial fuel and feedstock. In this way, the synergy between the chemical industry and the energy sector can boost market access, scale and competitiveness.

In particular, this thesis focuses on one of the largest processes in chemical industry, i.e. the ammonia production. An introduction on the topic is given in Chapter 1. Ammonia is produced at large scale (178 million tons per year) and it is a commodity essential for the fertiliser and food sector. The current production of ammonia, via the Haber-Bosch process, relies on fossil fuels and hydrogen derived from steam-methane reforming. Consequently the sector is responsible for releasing 1.4 % of the global CO<sub>2</sub> emissions. The implementation of a fully renewable powered Haber-Bosch process is limited by its large reactor scale and its continuous and steady operation, which clashes with the intrinsic intermittency of sources such as solar and wind. This is one of the reasons why a direct electrochemical route for ammonia synthesis has recently attracted significant attention in the scientific and industrial communities. The concept entails the direct synthesis of ammonia from water, dinitrogen and renewable electricity. Moreover, the possibility of producing ammonia in a sustainable manner may enable a new scenario where ammonia can also be used as carbon free energy carrier, thus playing a key role in a decarbonised energy landscape powered by renewables. However, the lack of a selective catalyst and the arduous competition with side reactions, as the hydrogen evolution reaction, make this process extremely challenging.

The aim of this thesis is to expand the current understanding of the nitrogen reduction reaction at near ambient conditions, addressing both fundamental and practical challenges. The first part of this thesis (Chapter 2-4) provides insights on the implementation of reliable electrochemical nitrogen reduction experiments and sensitive *operando* ammonia detection. Chapter 2 provides a fast and reliable ammonia detection method to speed-up catalyst screening and development of novel sustainable ammonia evolution devices, as it requires significantly less sample handling and preparation compared to other reported methods. The proposed method is based on a gas chromatography technique, and it allows for *in situ* monitoring of ammonia evolution, down to 150 ppb, from -but not limited to- electrochemical devices. Chapter 3 presents an isotope sensitive gas chromatography-mass spectrometry method for the quantification of  $\text{NH}_3$  at low concentration level, typically encountered in electrochemical ammonia synthesis applications. This method allows the discrimination of  $^{15/14}\text{NH}_3$ , necessary for the required  $^{15}\text{N}_2$  isotope labelling control experiments. Additionally, this method can directly and simultaneously measure other species in the analyte, thus it allows researchers to directly assess reaction selectivity by measuring reaction by-products, as well as the presence of gaseous/volatile contaminants in the experimental setup. Chapter 4 investigates the impact of contaminations on electrochemical nitrogen reduction experiments, with the aid of multiple analytical techniques and instrumentation, such as ion chromatography, gas chromatography, mass spectrometry,  $\text{NO}_x$  chemiluminescence analyser and UV-Vis spectrophotometry. This chapter not only provides a comprehensive identification and quantification of the contaminations, but it also critically analyses the effectiveness of different cleaning strategies, establishing a series of guidelines to perform reliable experiments.

The second part of this thesis (Chapter 5-7) investigates the room temperature spontaneous dinitrogen activation on selected metallic surfaces and its hydrogenation to ammonia via electrochemical atomic hydrogen permeation, using a solid metallic hydrogen permeable membrane electrode. Chapter 5 demonstrates a novel strategy for ambient condition ammonia synthesis from water and dinitrogen, designed to limit the competition between nitrogen activation and other competing adsorbates at the catalytic surface. As such, a hydrogen permeable nickel membrane electrode is used to spatially separate the electrolyte and the hydrogen activation side from the nitrogen activation and hydrogenation sites. With this approach, ammonia is produced catalytically directly in the gas phase and in

the absence of electrolyte. Gaseous nitrogen activation at the nickel electrode is confirmed with  $^{15}\text{N}$  isotope labelling control experiments and it is attributed to a Mars-van Krevelen mechanism enabled by the formation of N-vacancies upon hydrogenation of surface nitrides. Chapter 6 reports on the interactions of adsorbing N and permeating H at the catalytic interface of nickel, iron and ruthenium based hydrogen permeable electrodes during electrolytic ammonia synthesis. *In situ* near ambient pressure X-ray photoelectron spectroscopy (XPS) is used to measure modifications in the surface electronic structure of the catalyst and the nature of the adsorbed molecules. This chapter shows that permeating atomic hydrogen reduces surface Ni oxide and hydroxide species, under conditions at which gaseous  $\text{H}_2$  does not. Moreover, the results demonstrate that the availability of surface  $\text{Ni}^0$  sites is a primary requirement for the chemisorption of gaseous  $\text{N}_2$ . *In situ* XPS measurements reveal that nitrogen gas chemisorbs on the generated metallic sites, followed by hydrogenation via permeating H, as adsorbed N and  $\text{NH}_3$  are found on the Ni surface. Our findings indicate that the first hydrogenation step to NH and the last  $\text{NH}_3$  desorption step might be limiting at the utilised operating conditions. Finally, the study was then extended to Fe and Ru surfaces. However, the formation of surface iron oxide and nitride species on iron blocks the H permeation and prevents the reaction to advance; while on ruthenium the stronger Ru-N bond might favour the recombination of permeating hydrogen to  $\text{H}_2$  over the hydrogenation of adsorbed nitrogen. Chapter 7 provides a systematic investigation of the effect of operating temperature (in the range 25 to 120 °C) and H permeation flux on the  $\text{N}_2$  reduction reaction on Ni, leading to a considerably improved  $\text{NH}_3$  synthesis process. At 120 °C a stable operation was achieved for over 12 h with a 10 times higher cumulative  $\text{NH}_3$  production and almost 40-fold increase in faradaic efficiency compared to the room temperature operation reported in chapter 5. The results obtained in this chapter indicate that increasing operating temperatures enhances nitrogen adsorption and  $\text{NH}_3$  desorption, maintaining a steady N surface coverage throughout the  $\text{NH}_3$  synthesis cycle. Moreover, to operate the nitrogen reduction reaction in a stable and efficient manner, the control over the population of N,  $\text{NH}_x$  and H species at the catalyst surface is critical, as well as the capability of oxides to be reduced by permeating H. As such, the adoption of H permeable electrodes allows to independently control the N activation and H permeation, by a large extent.



# Samenvatting

Fossiele brandstoffen zijn in de laatste eeuw essentieel geweest voor het ontketenen van de industriële revolutie en brachten technologische vooruitgang voor de mensheid. Dit heeft geleid tot het uitputten van beperkt beschikbare natuurlijke bronnen en resulteerde in de uitstoot van broeikasgassen (BKG) en de opbouw van alarmerende concentraties van verontreinigende stoffen en broeikasgassen (BKG) in de atmosfeer. Een van de grote gevolgen van deze ophoping van BKG is de recente klimaatproblematiek. Onze samenleving heeft een voortdurende behoefte aan energie, waardoor we genoodzaakt zijn om onderzoek te gaan naar duurzamere alternatieven, zodat we de negatieve milieu-impact van industriële processen kunnen verminderen. Elektrochemie kan worden gebruikt om duurzame intermitterend opgewekte elektriciteit tijdelijk op te slaan. Vervolgens kan de elektriciteit terug worden omgezet in elektronen, of kan het worden gebruikt om chemicaliën te produceren. Hierdoor biedt de elektrificatie van de chemische industrie de mogelijkheid om haar BKG voetafdruk te verkleinen. De fluctuerende stroom van duurzame elektriciteit kan door de chemische industrie gebruikt worden om hernieuwbare brandstoffen en grondstoffen te produceren. Door de synergie tussen de chemische industrie en de energiesector wordt de markttoegang, schaalgrootte en concurrentievermogen gestimuleerd.

Dit proefschrift richt zich in het bijzonder op een van de grootste processen in de chemische industrie, namelijk de ammoniakproductie. Een inleiding over het onderwerp wordt gegeven in hoofdstuk 1. Ammoniak wordt op grote schaal geproduceerd (178 miljoen ton per jaar) en is een grondstof die essentieel is voor de kunstmest- en voedingssector. De huidige productie van ammoniak verloopt via het Haber-Bosch-proces wat afhankelijk is van fossiele brandstoffen en waterstof gemaakt door stoomreforming van methaan. De sector is hierdoor verantwoordelijk voor 1,4 % van de wereldwijde CO<sub>2</sub>-uitstoot. De implementatie van een volledig duurzaam Haber-Bosch proces wordt beperkt door de schaalgrootte. De continuïteit en stabiliteit botst namelijk met de wisselende energie toevoer van zon en wind. Dit is een van de redenen waarom een directe elektrochemische route voor ammoniaksynthese recent veel aandacht heeft gekregen in de wetenschappelijke en industriële gemeenschappen. Het concept omvat de directe synthese van ammoniak uit water, stikstof en hernieuwbare elektriciteit. Als ammoniak op een

duurzame manier kan worden geproduceerd, heeft het de potentie om te dienen als een koolstofvrije energiedrager. Waardoor het een sleutelrol speelt in een koolstofvrij energielandschap dat wordt aangedreven door hernieuwbare energiebronnen. Desalniettemin heeft de elektrochemische route nog veel uitdagingen, vanwege het ontbreken van een selectieve katalysator en het optreden van ongewenste reacties, zoals de waterstofevolutiereactie.

Het doel van dit proefschrift is om het huidige begrip van de stikstofreductiereactie bij omgevingscondities uit te breiden, door zowel te kijken naar fundamentele aspecten als praktische problemen. Het eerste deel van dit proefschrift (hoofdstuk 2-4) geeft inzicht in de implementatie van het betrouwbaar uitvoeren van elektrochemische stikstofreductie-experimenten en *operando* detecteren van ammoniak.

Hoofdstuk 2 biedt een snelle en betrouwbare ammoniak detectiemethode om de katalysator analyse en de ontwikkeling van nieuwe duurzame ammoniak synthese apparaten te versnellen, omdat het aanzienlijk minder materiaalverwerking en -voorbereidingstijd kost in vergelijking met andere gerapporteerde methoden. De voorgestelde methode is gebaseerd op een gaschromatografie en maakt het mogelijk om *in situ* de ammoniakevolutie te monitoren, met een ondergrens van 150 ppb.

Hoofdstuk 3 presenteert een isotoopgevoelige gaschromatografie-massaspectrometrie methode voor de kwantificering van lage concentraties  $\text{NH}_3$  die typerend zijn voor elektrochemische ammoniak experimenten. Deze methode maakt het onderscheid tussen  $^{15/14}\text{NH}_3$ , wat noodzakelijk is voor het uitvoeren van  $^{15}\text{N}_2$  controle experimenten. Bovendien kan deze methode direct, maar ook tegelijkertijd andere componenten in het analyt meten, waardoor onderzoekers de selectiviteit van de reactie kunnen beoordelen, evenals de aanwezigheid van vluchtige verontreinigingen in de experimentele opstelling.

Hoofdstuk 4 onderzoekt de invloed van vervuilingen op elektrochemische stikstof reductie experimenten, met behulp van meerdere analytische technieken en instrumenten, zoals ion chromatografie, gas chromatografie, massa spectrometrie,  $\text{NO}_x$  chemiluminescentie -analysator en UV-Vis spectroscopie. Dit hoofdstuk geeft niet alleen een omvangrijk overzicht van identificatie en kwantificatie van de contaminaties, maar analyseert ook kritisch de effectiviteit van verschillende schoonmaak strategieën. Hiermee wordt een reeks richtlijnen opgesteld om betrouwbare experimenten uit te voeren.

Het tweede deel van deze thesis (Hoofdstuk 5-7) onderzoekt de spontane distikstof activatie bij kamer temperatuur op geselecteerde metallische oppervlakte en de hydrogenatie naar ammonia via elektrochemische atomische waterstof permeatie, gebruikmakende van een vast metallische waterstof permeabel membraan elektrode.

Hoofdstuk 5 demonstreert een nieuwe strategie voor ammonia synthese onder standaardcondities vanuit water en distikstof, ontworpen om de concurrentie tussen stikstofactivering en andere concurrerende geadsorbeerde stoffen aan het katalytische oppervlak te beperken. Als zodanig, is een waterstof permeabele nikkel membraan elektrode gebruikt om het elektrolyt en de waterstof activatie zijde, ruimtelijk te scheiden van de stikstof activatie en hydrogenatie sites. Met deze aanpak wordt ammonia direct katalytisch geproduceerd in de gas fase en in afwezigheid van elektrolyt. Stikstofgas activatie op de nikkel elektrode was bevestigd met  $^{15}\text{N}$  isotoop gelabelde controle experimenten en het wordt toegeschreven aan een Mars-van Krevelen-mechanisme dat mogelijk wordt gemaakt door de vorming van N-vacancies bij hydrogenering van oppervlaktenitriden.

Hoofdstuk 6 beschrijft de interacties tussen geadsorbeerd stikstof en doordringend waterstof op het katalytische grensvlak van op nikkel, ijzer en ruthenium gebaseerde waterstof permeabele elektroden tijdens elektrolytische ammoniaksynthese. *In situ* near ambient pressure X-ray photoelectron spectroscopy (XPS) wordt gebruikt om modificaties in de elektronische oppervlaktestructuur van de katalysator en de aard van de geadsorbeerde moleculen te meten. Dit hoofdstuk laat zien dat permeatie van atomaire waterstof het oppervlak van Ni-oxide en -hydroxide reduceert, onder omstandigheden waarbij waterstof gas dat niet doet. Bovendien tonen de resultaten aan dat de beschikbaarheid van  $\text{Ni}^0$  sites aan het oppervlak een primaire vereiste is voor de chemisorptie van gasvormig  $\text{N}_2$ . *In situ* XPS-metingen laten zien dat stikstofgas chemisch adsorbeert op de gegenereerde metallische sites, gevolgd door hydrogenering via permeatie van atomaire waterstof, aangezien geadsorbeerde N en  $\text{NH}_3$  worden gevonden op het Ni-oppervlak. Onze bevindingen geven aan dat de eerste hydrogenatiestap tot  $\text{NH}$  en de laatste  $\text{NH}_3$ -desorptiestap mogelijk limiterend zijn bij de gebruikte reactie condities. Ten slotte werd het onderzoek uitgebreid naar Fe- en Ru-oppervlakken. De vorming van ijzeroxide en ijzernitriden op het ijzer oppervlak blokkeert echter de H-permeatie en voorkomt dat de reactie verder gaat; terwijl op ruthenium de sterkere Ru-N-binding de recombinatie van



doordringende waterstof tot  $H_2$  zou kunnen begunstigen boven de hydrogenering van geadsorbeerde stikstof.

Hoofdstuk 7 geeft een systematisch onderzoek naar het effect van reactietemperatuur (in het bereik van 25 tot 120 °C) en H-permeatieflux op de  $N_2$ -reductiereactie op Ni, wat leidt tot een aanzienlijk verbeterd  $NH_3$ -syntheseprocess. Bij 120 °C werd een stabiele werking bereikt gedurende meer dan 12 uur met een 10 keer hogere cumulatieve  $NH_3$ -productie en een bijna 40-voudige toename van de Faraday-efficiëntie in vergelijking met de werking op kamertemperatuur gerapporteerd in hoofdstuk 5. De resultaten verkregen in dit hoofdstuk geven aan dat toenemende reactietemperaturen de stikstofadsorptie en  $NH_3$ -desorptie verbeteren, waardoor een constante N-oppervlakte dekking gedurende de hele  $NH_3$ -synthesecyclus behouden blijft. Om de stikstofreductiereactie op een stabiele en efficiënte manier te laten verlopen, is bovendien de controle over de populatie van N-,  $NH_x$ - en H-stoffen aan het katalysatoroppervlak van cruciaal belang, evenals het vermogen van oxiden om te worden gereduceerd door permeatie van waterstof. Als zodanig, maakt het gebruik van H-permeabele elektroden het mogelijk om de N-activering en H-permeatie grotendeels onafhankelijk te regelen.

## Acknowledgements

A PhD is an incredible life-changing and formative experience. Now that it comes to an end, I feel that this journey could not have been possible without the support of the people that I have encountered along the road, that in a way or another had an impact on my life. This section of the dissertation is dedicated to those persons who, even unconsciously, have contributed to my personal and professional growth, which has brought me here today.

This research project would not be possible without **Prof. Fokko Mulder**. Thank you for giving me the opportunity to work on this project, for your support and guidance throughout the PhD. Your work and intuition have been an example for me. Your constant interests towards the project and mutual curiosity in finding out more, have been often the seed for endless conversations, as well as inspiration and motivation throughout these years. I must add that it is hard to see a professor, or a PI, running experiments in the lab, but you are a pleasant surprise in this. Finally, you teach me how the “Friday afternoon experiments” are often the most interesting and surprising ones! **Prof. Wilson Smith**, thank you for your help during these years. Even though it has been harder to keep frequent contacts due to your relocation in Colorado, US, you have been a great motivator for me, and I admire your ability to infuse loads of energy and optimism to the people around you. Your scientific contributions have also improved the quality of this work.

A sincere thanks goes also to the members of the doctoral committee for reading this dissertation, providing feedbacks and participating in the defence ceremony.

To the MECS group. It was a great privilege to be part of such a wonderful research group, full of bright people. Thank you for all the moments we have shared inside and outside working hours. The soul of the MECS group, **Joost** and **Herman**. You have been of tremendous help, and I have learn so much from you. I will miss the fun small talks in your office and during coffee break! Coffee breaks, borrels and the countless cakes for every possible occasion have delighted my days (and compensate my daily sugar dose), throughout the PhD rollercoaster. Thanks also to **Bart**, who introduced me to XPS (which

became a central tool in my research) and has been of great support with LabVIEW. **Audrey**, you have been the first person of the group I met, which happened to be during my first interview with Fokko. You helped me starting up in the lab. Thank you for the good time outside the lab and the enjoyable conversations. **Erdem**, thank you for all the great time and for being a great colleague, friend and sport/music buddy. **Riccardo**, you have been of a great help in a crucial phase of the project. Thank you for all your inputs and discussions, result of your great knowledge and competences. It is always nice to catch up with you. **Martin**, we shared office, but more importantly we shared the frustration and challenges of researching on the electrochemical ammonia synthesis, but gladly we both made it alive! Thank you for the nice discussions. **Dylan and Peter**, the dynamic duo! You are the new generation of nitrogen people in MECS, keep up this title with honour. Thank you also for your help during the synchrotron campaign in Berlin. We have seen endless nights, but bringing back home great results. **Anirudh**, you are so kind and always ready to help. It has been a pleasure working with you and to spend fun time playing beach volley. **Sid**, a great band singer and a sweet friend and colleague. **Aaron and Kailun** thank you for being such lovely colleagues and for all the small things we did together. **Maryam**, I am thankful and glad to have been taken on board of some of your exciting projects on CO<sub>2</sub> reduction. Thank you to all the other colleagues in MECS that have been part of this journey: **Bernhard, Diana, Fahimeh, Giorgio** (it is always nice to have an Italian around), **Hugo** (thank you for the nice time we shared in Canada!), **Kai, Marijn, Mark S.** (one of the most cheerful person I ever met), **Mark W.** (thank you for sharing your enthusiasm and knowledge on batteries), **Nate, Nienke, Pranav, Recep, Robin** (fun time back in Toulouse!), **Sanjana**. A special thanks goes to the bachelor and master students I had the pleasure to supervise during their final projects: **Daan, Kevin, Laura, Tamara and Maria**. I have learnt a lot from you and from your remarkable work. It makes me proud to have seen each one of you flourish in a few months. I wish you all the best for your future! **Prof. Bernard Dam, Prof. Hans Geerlings and Dr. Tom Burdyny**, thank you for your inputs and feedbacks throughout these years, and thank you for keeping the MECS group at high standards and an open environment. **Wim**, thank you for being always prompt to ask questions. **Roos and Rajshree**, thank you for the enormous support in all those administrative matters.

During these years I had the pleasure of interacting with many others wonderful people in TU Delft: **Angie, Donato, Min Li, Lars B., Robbert, Kostadin, Hozanna Miro, Dr. Ruud Kortlever**. A special thanks goes to **Boaz**, with whom I spent countless time working together over these years. It has been a pleasure to work with you, always with some funny notes here and there! I will keep nice memories from the synchrotron trip in Barcelona.

My gratitude goes also like to some people outside the TU Delft umbrella, with whom I had the pleasure to interact: **Dr. Virginia Pérez-Dieste, Dr. Ignacio Villar-Garcia, Ana Martinez, Dr. Patrick Zeller, Dr. Daniel Cruz, Dr. Rick Mom, Dr. Michael Hävecker, Dr. Juan-Jesús Velasco-Vélez**. Thank you all for your helpful discussions and support during the beamtimes.

Warm-hearted thanks to all the friends that supported me in these years, beyond the science. Friends in The Netherlands: **Kenji, Leslie, Hemant, Lučka, Andres, Rita, Simone** (now you are also part of this group, even our friendship dates back to before kindergarten!), **Sebastien** and **Edoardo** (the padel master). **Matteo** thank you for being such an invaluable friend, for all the memorable time spent together, big laughs, concerts, dinners, countless adventures and stimulating discussions. Friends from far away, the “**Geriatrics group**” (I feel so lucky to have met such wonderful people in my life!) **Alessandro P., Mic** and **Mattia**, which continue to be present and supportive, despite the distance. Life brought us apart, but our connection is enduring.

**Clelia**, my big sis! Thank you for the constant support, for the last-minute English-grammar checks, to be always there. Just knowing you will be there for me makes me stronger. **Mamma e papà**, grazie per il vostro supporto incondizionato, i vostri immensi sacrifici, il vostro amore e la vostra fiducia, per avermi insegnato a guardare avanti e per avermi sempre lasciato libero di scegliere e costruirmi un futuro, anche quando questo avrebbe significato vivere a migliaia di chilometri di distanza. Se oggi sono qui è anche merito vostro.

**Adriana**, I will never be able to express all my gratitude in these few lines, but probably I do not need to. You already know precisely, down to the last detail, how these years have been. Yet, you have always been there for me, a parachute in a free fall, fuel for a rocket. I am grateful to share my life with you. Thank you!

Another chapter of life is completed, but exactly as this booklet, I will proudly look back at it and use this experience for the future ahead. Thanks to everyone, and to whom I might have forgotten to mention, for being a part of this achievement!

*Davide*

*Delft, September 2022*

# List of publications

## Publications

14. **D. Ripepi**, H. Schreuders, F.M. Mulder. Effect of temperature and H flux on the  $\text{NH}_3$  synthesis via electrochemical hydrogen permeation. *In preparation*.
13. **D. Ripepi**,\* B. Izelaar,\* D. van Noordenne, P. Jungbacker, R. Kortlever, F.M. Mulder. Determination and Effective  $\text{NO}_x$  and  $\text{NH}_3$  removal for reliable electrochemical nitrogen reduction. *In preparation*.
12. **D. Ripepi**, B. Izelaar, D. van Noordenne, P. Jungbacker, M. Kolen, P. Karanth, D. Cruz, P. Zeller, V. Pérez-Dieste, I.J. Villar-Garcia, W.A. Smith, F.M. Mulder. In situ study of hydrogen permeable electrodes for electrolytic ammonia synthesis using near ambient pressure XPS. *ACS Catal.* **2022**, 12, 13781-13791.
11. B. Izelaar, **D. Ripepi**, S. Asperti, I.A. Dugulan, R.W.A. Hendrikx, A.J. Böttger, F.M. Mulder, R. Kortlever. Revisiting the Electrochemical Nitrogen Reduction on Molybdenum and Iron Carbides: Promising Catalysts or False Positives?. *ACS Catal.* **2022**. *Under review*.
10. M. Abdinejad, S. Subramanian, M.K. Motlagh, M. Noroozifar, **D. Ripepi**, D. Pinto, M. Li, K. Tang, J. Middelkoop, A. Urakawa, H.B. Kraatz, T. Burdyny. Insertion of Cu-Pd into 3-Dimensional MXene-based Aerogels for Highly-efficient Electroreduction of  $\text{CO}_2$ . *In preparation*.
9. M.J. Weijers, P. Karanth, **D. Ripepi**, F.G.B. Ooms, F.M. Mulder. Thick NMC811 electrodes enabled by nonsolvent induced phase inversion. *In preparation*.
8. M. Kolen, G. Antoniadis, H. Schreuders, B. Boshuizen, D. van Noordenne, **D. Ripepi**, W.A. Smith, F.M. Mulder. Combinatorial Screening of Bimetallic Electrocatalysts for Nitrogen Reduction to Ammonia Using a High-Throughput Gas Diffusion Electrode Cell Design. *J. Electrochem. Soc.* **2022**. 169, 124506.

7. M. Abdinejad, E. Irtem, A. Farzi, M. Sussenburg, S. Subramanian, H.P.I. van Montfort, **D. Ripepi**, M. Li, J. Middelkoop, A. Seifitokaldani, T. Burdyny. CO<sub>2</sub> Electrolysis via Surface-Engineering Electrografted Pyridines on Silver Catalyst. *ACS Catal.* **2022**, *12*, 7862-7876.
6. **D. Ripepi**, R. Zaffaroni, H. Schreuders, B. Boshuizen, F.M. Mulder. Ammonia Synthesis via Electrochemical Atomic Hydrogen Permeation between 25 and 100 °C. *ECS Meetings Abstract* **2022**, 1545.
5. M. Sassenburg, R. de Rooij, N.T. Nesbitt, R. Kas, S. Chandrashekar, N.J. Firet, K. Yang, K. Liu, M.A. Blommaert, M. Kolen, **D. Ripepi**, W.A. Smith, T. Burdyny. Characterizing CO<sub>2</sub> Reduction Catalysts on Gas Diffusion Electrodes: Comparing Activity, Selectivity, and Stability of Transition Metal Catalysts. *ACS Appl. Energy Mater.* **2022**, *5* (5), 5983-5994.
4. M. Kolen, **D. Ripepi**, W.A. Smith, F.M. Mulder. Overcoming Nitrogen Reduction to Ammonia Detection Challenges: The Case for Leapfrogging to Gas Diffusion Electrode Platforms. *ACS Catal.* **2022**, *12*, 5726-5735.
3. **D. Ripepi**, R. Zaffaroni, M. Kolen, J. Middelkoop, F.M. Mulder. Operando isotope selective ammonia quantification in nitrogen reduction studies via gas chromatography-mass spectrometry. *Sustainable Energy Fuels* **2022**, *6* (8), 1945-1949.
2. **D. Ripepi**, R. Zaffaroni, H. Schreuders, B. Boshuizen, F.M. Mulder. Ammonia Synthesis at Ambient Conditions via Electrochemical Atomic Hydrogen Permeation. *ACS Energy Lett.* **2021**, *6*, 3817-3823. [Featured Journal Cover]
1. R. Zaffaroni, **D. Ripepi**, J. Middelkoop, F.M. Mulder. Gas Chromatographic Method for In situ Ammonia Quantification at Parts per Billion Levels. *ACS Energy Lett.* **2020**, *5* (12), 3773-3777.

\*These authors contributed equally.

## Curriculum Vitae

Davide Ripepi was born on 2<sup>nd</sup> of May 1993 in Reggio di Calabria, Italy. In 2012 he graduated from the technical high school Istituto Augusto Righi of Reggio di Calabria, receiving the award of best student for the years 2009-2012. He continued his education at the Politecnico di Torino, Italy, where he received his bachelor degree in Energy and Nuclear Engineering in 2015. In the same year, Davide moved to Delft, the Netherlands and in December 2017 he received his master degree in Sustainable Energy Technology, following a specialised track in hydrogen and energy storage. During his master studies he also took a one-year experience as Fuel Cell Engineer in the TU Delft student team Eco-Runner, building an energy-efficient hydrogen racing car and participating at the Shell eco-marathon in London. In 2018 he joined the Materials for Energy Conversion and Storage (MECS) group as PhD candidate under the supervision of Prof. Fokko M. Mulder, and the co-supervision of Prof. Wilson A. Smith, at the Chemical Engineering department, faculty of Applied Science, of the Technical university of Delft. He is currently a post-doctoral researcher in the same group. His research focused on the direct electrochemical ammonia synthesis at near ambient condition using hydrogen permeable electrodes. He has given several talks in national and international scientific conferences. He won the TU Delft Best Energy Paper Awards in 2021 and he received a travel grant by the Energy Technology Division of The Electrochemical Society in 2022. During his time in the MECS group, he also actively collaborated in different electrochemical areas, such as CO<sub>2</sub> reduction and Li-ion batteries. The most relevant results of his doctoral research are presented in this dissertation.